

IMPERIAL

Development of an Acoustic Dose-Profile Measurement Technique for Short Pulse Proton and Ion Beams

MARIA MAXOUTI

Department of Physics
Imperial College London
High Energy Physics Research Group

*A thesis submitted in partial fulfilment of the requirements for the
degree of Doctor of Philosophy
at Imperial College London*

April 2025

Contents

Abstract	vii
Declaration	x
Copyright	x
Acknowledgements	xii
List of Figures	xv
List of Tables	xxxix
Abbreviations	xl
1 Introduction	1
1.1 Context	1
1.2 Summary	2
2 Background Theory	5
2.1 Particle Therapy	5
2.1.1 The Bragg Peak	5
2.1.2 Energy Loss & Linear Energy Transfer	8
2.1.3 FLASH Dose Rates & Minibeams	11
2.2 Dosimetry	12
2.3 Ion-Acoustic Imaging	15
2.4 Scintillators	17

2.4.1	Scintillating Fibres	18
2.4.2	Liquid Scintillators	18
3	LhARA	20
3.1	Facility	20
3.2	Stage 1	21
3.2.1	Laser-Driven Source	21
3.2.2	Ion Capture	23
3.2.3	Beam Transport	24
3.2.4	Transfer Line	25
3.3	Stage 2	26
3.3.1	Post-Acceleration	26
3.3.2	Beam Transport	27
3.3.3	Extraction Line	27
3.4	Dosimetry System	28
3.5	The SmartPhantom	32
4	LION Beamline	36
4.1	Particle Source	36
4.1.1	Source Energy Spectrum	37
4.1.2	Source Angular Distribution	41
4.2	Quadrupole Doublet	43
4.3	Configuration	46
4.4	PMQ Focus	48
4.5	Electron Background	50

4.6	Electromagnetic Pulse & Bremsstrahlung	54
5	Ion-Acoustic Signal	56
5.1	SmartPhantom	56
5.1.1	Energy Depositions	56
5.1.2	Pressure Distribution	60
5.2	Acoustic Transducers	64
5.3	Signal Evaluation	68
5.4	Image Reconstruction	74
5.4.1	Iterative Time-Reversal Reconstruction	74
5.4.2	Model-Based Minimization Reconstruction	77
5.4.3	Back-Projection Reconstruction	79
5.5	Kapton Transmission Loss	81
6	Liquid Scintillator	89
6.1	Scintillating Liquid	89
6.2	Scintillation Correction	89
6.3	Fluorescent Dye and UV Source	91
6.4	Optical Absorption	95
6.5	Response and Saturation	98
7	Scintillating Fibre Detectors	105
7.1	Simulation	105
7.1.1	Two-Dimensional Reconstruction	106
7.1.2	Bragg Peak Reconstruction	110

7.1.3	Acoustic Wave Distortion	112
7.1.4	Beam Divergence	117
7.2	Construction	120
7.3	Response	124
8	SmartPhantom Evaluation	134
8.1	Synchronized Data Acquisition	134
8.2	Scintillating Fibre Detectors	136
8.2.1	Energy Response	138
8.2.2	Beam Profile	143
8.3	Radiochromic Films	144
8.4	Liquid Scintillator and Transducers	150
8.4.1	Effective Range	169
8.4.2	Mean Energy	175
8.4.3	Beam Width	177
8.4.4	Particle Number	184
9	Conclusion	189
9.1	Discussion	189
9.2	Future Work	196
9.3	Towards Clinical Application	198
A	Two-Dimensional Model	200
B	Image Reconstruction: Hemispherical Cup	205
C	Ion-Acoustics in Human Physiology	209

Abstract

Cancer is the second leading cause of death globally, with radiotherapy treating about 50% of patients. Conventional radiotherapy uses photons, however, it often irradiates healthy cells surrounding the cancerous region. New treatment facilities are turning to protons and light ions, which deposit a maximum dose within a small volume at the end of their range.

This thesis introduces LhARA, the Laser-hybrid Accelerator for Radiobiological Applications, which aims to advance radiobiology by exploring how different particle beam characteristics affect therapeutic outcomes. Using pulsed proton and light-ion beams, LhARA offers flexibility in ion species, beam widths, and pulse duration.

To minimize uncertainties, real-time dose delivery monitoring is essential. This work presents the SmartPhantom, a novel detector for monitoring three-dimensional dose accumulation delivered using nanosecond-scale ion beam pulses. Unlike existing devices that provide only relative dose values, the SmartPhantom delivers calibrated feedback.

The detector uses ultrasound waves induced by the transient pressure increase as the beam propagates through matter. Due to the high speed of ultrasound, feedback is nearly instantaneous. To calibrate the acoustic response, a liquid scintillator is used as the propagating medium inside the detector. The scintillation light emitted during beam propagation, combined with known photon yields, enables absolute dose reconstruction.

The SmartPhantom was evaluated at the MC40 cyclotron in Birmingham and the LION accelerator at CALA in Munich. To optimize the design, a simulation pipeline was developed using Python for source parametrization, BDSIM for particle tracking, Geant4

for energy deposition calculations, and Matlab for acoustic modeling.

The results revealed strong correlation between optical and acoustic measurements, validating the detector's potential. This lays the foundation for a clinically viable, real-time dose monitoring system.

Declaration

I hereby declare that the material presented in this thesis is my own work unless otherwise stated or referenced.

Maria Maxouti

March 2025

Copyright

The copyright of this thesis rests with the author. Unless otherwise indicated, its contents are licensed under a Creative Commons Attribution-NonCommercial 4.0 International Licence (CC BY- NC). Under this licence, you may copy and redistribute the material in any medium or format. You may also create and distribute modified versions of the work. This is on the condition that: you credit the author and do not use it, or any derivative works, for a commercial purpose. When reusing or sharing this work, ensure you make the licence terms clear to others by naming the licence and linking to the licence text. Where a work has been adapted, you should indicate that the work has been changed and describe those changes. Please seek permission from the copyright holder for uses of this work that are not included in this licence or permitted under UK Copyright Law.

Acknowledgements

Firstly, I would like to express my deepest gratitude to my supervisor, Professor Ken Long, for his unwavering guidance, encouragement and dedication throughout this journey. His constant support, from daily communication to hands-on help in the lab, has been invaluable. He has always treated us as colleagues, showing respect and genuine care.

I would also like to extend my gratitude to the entire LhARA collaboration, and especially to the ion-acoustics group for their guidance and insightful feedback. I would like to especially thank Professor Peter Hobson for his exceptional support and hands-on assistance in the labs at Imperial and Birmingham. I would also like to sincerely thank him for developing the optical simulations, selecting the liquid scintillator and designing the imaging optics, all of which played a crucial role in achieving great results. In addition, I would like to thank Professor Jeff Bamber for his invaluable support and guidance in the acoustics part of the project and for his assistance with the experiments conducted at ICR and Munich. I am also deeply thankful to Nick Dover for his assistance with the laser-driven source simulation and RCF stack analysis. I would also like to thank Tony Price for his help in the initial evaluation of the SmartPhantom in Birmingham, as well as the entire LMU group for their extensive support during the experiments at the LION beamline in Munich.

I am also deeply grateful to Oliver Jeremy, the mastermind behind the design of the SmartPhantom, and the Imperial workshop for bringing it to life. Our weekly discussions, design modifications and brainstorming sessions were truly enjoyable. I would also like to express my heartfelt gratitude to Josie McGariggle for making my PhD journey one filled with joy and laughter, and for transforming room 1113 the best office anyone could have

wished for. I would also like to thank her for the invaluable help in building the scintillating fibre detectors, for providing the Topas simulations and for the memorable travels we had during collaboration meetings.

Last but certainly not least, I am eternally grateful to my parents, Pantelis and Lena, and my brother, Charalampos, without whom I would not be where I am today. To my grandmother, Maroulla, for teaching me the values of unconditional love, hard work, and the pursuit of knowledge. Finally, to my partner, Constantinos, who stood by my side from the very beginning to the very end of this journey, offering constant support, encouragement, and patience. This thesis is dedicated to you all.

List of Figures

1	Relative depth-dose distribution for x-rays (photons) versus protons [17]. . .	6
2	Comparison of the Bragg peak shapes resulting from proton beams at different energies travelling through water [21].	7
3	Schematic diagram of the ion-acoustic wave generation and detection. . . .	15
4	Schematic diagram of the LhARA beamlines [4].	21
5	Schematic diagram illustrating the Target Normal Sheath Acceleration mechanism.	22
6	Schematic diagram of the Gabor lens to be used in LhARA. The orange arrow shows the direction of the beam, the red circles indicate the direction of the current within the coils, and the green represents the electron cloud [53].	24
7	Schematic diagram of the LhARA Stage 1 beamline [4].	25
8	Fixed-field alternating (FFA) gradient acceleration scheme to be used in LhARA, with parts of the injection and extraction lines shown at the bottom and top left, respectively [4].	28
9	Computer-Aided Design of the final version of the SmartPhantom, evaluated at the LION beamline, featuring four windows for mounting the optical and acoustic systems. Left: front view. Right: near view.	32
10	Computer-Aided Design of the final version of the SmartPhantom, featuring the optical systems and the transducer housings attached onto the designated windows, along with the Olympus V303 transducer secured at the bottom. .	34

11	Computer-Aided Design of the interior of the SmartPhantom. Left and middle: entrance window with the scintillating fibre detectors attached. Right: entrance window without the scintillating fibre detectors, featuring only the attachment flange.	35
12	Parametrised energy distribution of the laser-driven protons generated at the LION beamline source, based on the specific laser and foil target parameters listed in Table 5. The solid black line represents Equation 4.1 and the blue area is a histogram of the generated spectrum.	40
13	Comparison of the generated envelope divergence angles for the parametrized angular distribution of the LION beamline source (blue) with the theoretical linear relationship described in Equation 4.5 (black).	42
14	Histograms of the divergence angle (left), generated from a Gaussian distribution, and the azimuthal angle (right), uniformly distributed between 0 and 2π , representing the parametrized angular distribution of 100000 particles at the LION beamline source.	42
15	Two-dimensional cross-section of the LION beamline parametrised beam consisting of 1 million particles. The simulated distribution is symmetric, with a Gaussian profile that has a FWHM diameter of $10\text{ }\mu\text{m}$	43
16	Sketch of the magnetic field lines within a quadrupole magnet. The blue arrows illustrate the Lorentz force, indicating a focusing effect in the x-plane and a defocusing effect in the y-plane [68].	45
17	Elliptical aluminium collimator used for shielding to ensure radiation protection for the quadrupole magnets. The specific aperture size is selected for focusing a proton beam with a nominal energy of approximately 20 MeV. .	47

18	Annotated diagram of the LION beamline simulated in BDSIM, showing the accelerator elements and their drifts designed to focus a beam with a modal energy of approximately 20 MeV.	48
19	Proton depletion as a function of distance when the parametrised particles at the laser-driven source of the LION beamline propagate through the beamline elements. Vacuum section (top) and air section (bottom).	49
20	Histogram of the final energy spectrum of the particles after passing through all accelerator elements in the LION beamline and focused onto the SmartPhantom. The peak energy is approximately 20.43 MeV.	50
21	Two-dimensional histogram of the spatial distribution of particles at the LION beamline focus for a nominal beam energy of 20.43 MeV. The focused beam has a FWHM of 0.77 mm and 0.39 mm along each axis and a total diameter of approximately 2 mm.	51
22	Parametrised energy distribution of the laser-driven electrons generated at the LION beamline source. The solid black line represents Equation 4.14 and the blue area is a histogram of the generated spectrum of 100000 electrons.	52
23	Histogram of the electron divergence angle distribution generated using Equation 4.16, showing 100 thousand electrons at the LION beamline source.	53
24	Time-of-flight distributions for source-generated protons (purple) and electrons (blue) as they propagate through the LION beamline.	54
25	Geant4 simulation of the SmartPhantom. Angled view (left), cross-section view (right). The beam, given by the BDSIM simulation, is incident from the left.	57

26	Energy depositions, along the three orthogonal axes, caused by particles emerging from the LION beamline and entering the SmartPhantom, for three cases: the entire volume filled with water, a 50-50 mixture of water and liquid scintillator and 100% liquid scintillator.	58
27	Energy depositions in the liquid scintillator inside the SmartPhantom, caused by the passage of protons emerging from the LION beamline. Voxel size: 0.1 mm.	59
28	Energy depositions in the liquid scintillator inside the SmartPhantom, caused by the passage of source-generated electrons emerging from the LION beamline. Voxel size: 0.1 mm.	59
29	Secondary particles produced from the interactions between the incoming beam and the solution in the inner volume of the SmartPhantom.	60
30	Energy depositions in the liquid scintillator caused by secondary particles produced in the SmartPhantom. Voxel size: 0.1 mm.	61
31	Total pressure distribution of particles depositing energy as they propagate through the SmartPhantom, shown in three orthogonal planes. Voxel size: 0.1 mm.	62
32	Ion-acoustic signal generation and evolution within the SmartPhantom, simulated using k-Wave. Two pressure waves are generated at $t = 0$ originating from the Bragg peak and the entrance window. Both waves propagate outwards, with the second one reflected off the liquid-air interface at the Kapton foil due to acoustic impedance mismatch.	63

33	An illustration of the two distinct waves emitted as the beam propagates through the SmartPhantom. The α -wave is emitted laterally in the pre- BP region and the γ -wave is emitted at the BP in all directions. The particles travel from left to right.	64
34	k-Wave simulation illustrating the acoustic transducers and their location relative to the beam energy depositions, indicated by the yellow region. The energy depositions depicted are generated by a beam exiting the LION beam-line, optimized for a modal energy of 20 MeV, as it passes through the liquid scintillator.	68
35	Normalized simulated acoustic waveforms recorded by the four transducers: Vantage Matrix Array Ultrasound Transducer, GE 9L-D Linear Array Ultrasound Transducer, Olympus V303 Immersion Transducer and Precision Acoustics ML4X50 Piston Hydrophone, when positioned at the locations displayed in Figure 34.	69
36	Frequency spectra of the acoustic signals recorded by the four transducers, shown in Figure 34, obtained by applying a FFT to the recorded waveforms.	73
37	Reconstructed pressure distribution, after eight iterations of the time-reversal algorithm, using the matrix array (a) and the linear array (b).	75
38	Reconstructed pressure distribution profiles along the x-(top), y-(middle) and z-(bottom) directions, using 8 iterations of the time-reversal algorithm.	76
39	Reconstructed pressure distribution, after eight iterations of the model-based minimization algorithm, using the matrix array (a) and the linear array (b).	78

40	Reconstructed pressure distribution profiles along the x-(top), y-(middle) and z-(bottom) directions, using 8 iterations of the model-based minimization algorithm.	79
41	Reconstructed pressure distribution using the back-projection algorithm, with the matrix array (a) and the linear array (b).	80
42	Ultrasound transmission loss experiment set-ups without (left) and with (right) a 50 μm Kapton foil and acoustic matching gel.	82
43	Matrix array's central element gated signal before (top) and after (bottom) up-sampling the number of data points by a factor of 4 using interpolation.	83
44	Cross-correlation function between an element of the matrix array and the central element. The red cross marks the peak of the cross-correlation function, indicating the time delay of the echoes.	84
45	Time delay of each matrix array transducer element relative to the central element, calculated using the cross-correlation function.	85
46	Signals from the elements in the central row of the matrix array, with the Kapton window in place, before (left) and after (right) time-alignment using the cross-correlation function.	86
47	Element-to-element coherence for one of the experimental datasets, calculated using Equation 5.1 [90].	87
48	Peak-to-peak amplitudes of the averaged signals for all datasets. Blue dots represent the results from Setup 1, while orange dots represent the results from Setup 2.	88

49	Experimental set-up of the fluorescent dye (Coumarin-120) experiment. Right: angled view showing the Chameleon3 CM3-U3-31S4M-CS camera, glass water tank, optical lens and UV LED source [100]. Left: side view, where the blue light corresponds to the UV light propagating through the Coumarin-water mixture.	92
50	Experimental set-up for measuring the linearity of the LED output. A beam splitter directs the beam into the Coumarin-water mixture while simultaneously sending a fraction of the light to the photodiode to measure the current.	93
51	Photodiode reading plotted against the input current from by the power supply, using the setup depicted in Figure 50.	94
52	Maximum pixel intensity of the background-corrected images obtained using the setup depicted in Figure 50, plotted against input current from the power supply.	94
53	Grayscale image of the UV light passing through the fluorescent dye (Coumarin-120)-water mixture, corrected for background noise, captured at an input current of 0.01 A. The light is incident from the top.	95
54	Image showing the four cuvettes prepared for measuring the absorbance of Ultima Gold XR and a 50-50 mixture with distilled water using a spectrophotometer. The cuvette containing air was used as a baseline for the measurements.	97
55	Optical absorption spectra of the liquid scintillator (blue) and a 50-50 mixture with distilled water (green), measured using a spectrophotometer. Baseline medium: air.	98

56	Computer-aided design model of the cuvette designed to contain the liquid scintillator (left) and images of the experimental set-up (middle and right) used to study the linearity of the liquid scintillator's response to absorbed dose and saturation behaviour. The experiment was conducted at the MC40 cyclotron in Birmingham [15].	99
57	Plot of PN diode current against the current measured at the MC40 cyclotron's Faraday cup, using the experimental set-up depicted in Figure 56 and a 26.65 MeV proton beam. A line of best fit is added to the data and a regression coefficient of 0.991 is calculated, indicating a strong linear correlation with no evidence of quenching in the liquid scintillator.	100
58	Image of the experimental set-up used to capture the scintillation light caused by the passage of the proton beam through the liquid scintillator inside the SmartPhantom.	101
59	Average pixel intensity of the images obtained using the experimental set-up shown in Figure 58, plotted against particle proton number at various proton energies.	102
60	Image captured with the experimental set-up depicted in Figure 58 when a 26.65 MeV proton beam of 95 million particles propagates through the liquid scintillator. The beam enters from the left, with the brightest region corresponding to the Bragg peak.	102
61	Colour map of the pixel intensities present in Figure 60. Deep purple corresponds to low-intensity pixels and bright yellow corresponds to the high-intensity pixels. The vertical and horizontal black lines indicate the transverse and longitudinal directions, respectively.	103

62	Energy deposition profiles of a 26.65 MeV proton beam with 95 million protons propagating through the liquid scintillator in the SmartPhantom. Top: longitudinal profile, obtained by averaging 60 pixels along the horizontal black line in Figure 61. Bottom: transverse profile, obtained from an average of 60 pixels along the vertical line.	104
63	Geant4 simulation of the SmartPhantom with four scintillating fibre planes (yellow) placed equidistant from the entrance window.	106
64	Energy deposited in each fibre of the two-dimensional scintillating fibre detectors, when the simulated LION beam consisting of 10^6 particles passes through them. Top: fibres oriented along the horizontal axis. Bottom: fibres oriented along the vertical axis. The different colours correspond to different detectors, with Plane 1 positioned closest to the entrance window and Plane 4 nearest the Bragg peak.	107
65	Two-dimensional energy distribution reconstructed using the simulated deposited energy in each scintillating fibre in the detector arrays, when the simulated LION beam consisting of 10^6 particles passes through them. Each subplot corresponds to a different detector, where Detector 1 is located nearest to the entrance window of the SmartPhantom and Detector 4 is closer to the Bragg peak. Each detector is 2 cm long.	108
66	Two-dimensional estimation of the scintillating fibre detectors' light output. The estimation is calculated from the energy depositions shown in Figure 65, the manufacturer's reported light yield of 8000 photons per deposited MeV and the stated fibre capture efficiency of 3.44% [109].	109

67	Reconstruction of the longitudinal energy deposition profile using the Bortfeld approximation (dashed line) as defined in Equations 7.1 - 7.3, fitted to the data from the scintillating fibre detectors (various shades of blue). The black points correspond to the the Geant4 simulation results for comparison.	112
68	Ion-acoustic signal generation and evolution within the SmartPhantom, simulated using k-Wave, including the scintillating fibre detectors.	113
69	Reconstructed pressure distribution, after eight iterations of the iterative time-reversal algorithm, using the matrix array (a) and the linear array (b), when the scintillating fibre detectors are included in the acoustic simulation. Voxel size: 0.1 mm.	115
70	Reconstructed pressure distribution profiles along the x-(top), y-(middle) and z-(bottom) directions, using 8 iterations of the time-reversal algorithm, when the scintillating fibre detectors are included in the acoustic simulation.	116
71	Geant4 simulation of the SmartPhantom, featuring the four scintillating fibre detectors (yellow) suspended in air, positioned equidistant from the end of the elongated entrance window.	117
72	Energy depositions in each scintillating fibre of the two-dimensional scintillating fibre detector when suspended in air, inside the SmartPhantom's volume.	118
73	Full Width Half Maximum (FWHM) calculation of the beam width using the energy deposited in the fibres in the scintillating fibres detectors suspended in air inside the SmartPhantom. Blue: horizontal plane. Green: vertical plane.	119

74	Annotated CAD design of the scintillating fibre frames, which form the foundation of the detectors positioned within the SmartPhantom to measure the incoming beam's cross-sectional area and divergence.	120
75	Annotated image of the winding jig used to manufacture the scintillating fibre detectors, showing two aluminium frames secured with screws on one of its sides.	121
76	Annotated image of the scintillating fibre planes mounted on the winding jig, showing the fibres wound around the aluminium frames and the cavities filled with resin to firmly secure them.	122
77	Image showing eight scintillating fibre planes, manufactured using the setup depicted in Figures 75 and 76, prepared for integration into the SmartPhantom.	123
78	Image showing four scintillating fibre detectors, composed of eight planes arranged perpendicularly, positioned inside the SmartPhantom. The planes are separated by approximately 2 mm and are mounted onto the entrance window, aligned on-axis with the incoming beam.	123
79	Experimental set-up showing the SmartPhantom, with the scintillating fibre detectors installed inside, positioned at the exit window of the MC40 cyclotron in Birmingham. An imaging system, comprising a Chameleon3 CM3-U3-31S4M-CS camera and several optical components, is mounted above to image the scintillation light from the top.	124
80	Averaged, background-corrected image captured using the setup depicted in Figure 79, and a 27.32 MeV proton beam of approximately 1.03×10^9 particles. The bright circles correspond to the polished ends of the fibres. The beam enters from the left.	125

81	Processed image captured with a 27.32 MeV proton beam and approximately 1.03×10^9 particles. The green circles correspond to the detected fibres using the Hough Circle Transform method. The fibre with the highest average intensity is shown in pink.	126
82	Plot of average central fibre intensity against particle number for 19.30 MeV (green) and 27.32 MeV (blue) proton energies. The black lines represent lines of best fit.	127
83	Average intensity of individual fibres as a function of particle number, with lines of best fit, when a 19.30 MeV proton beam passes through a scintillating fibre detector.	128
84	Average intensity of individual fibres as a function of particle number, with lines of best fit, when a 27.32 MeV proton beam passes through a scintillating fibre detector.	128
85	Average fibre intensity against fibre number from Figure 83, with a 19.32 MeV proton beam. The different colours correspond to different proton numbers in the beam. A third order polynomial fit was applied to the data.	129
86	Average fibre intensity against fibre number from Figure 84, with a 27.32 MeV proton beam. The different colours correspond to different proton numbers in the beam. A third order polynomial fit was applied to the data.	130
87	Third-order polynomial fits to the 19.30 MeV proton beam intensity profiles, before and after the data-driven fibre efficiency correction.	132
88	Third-order polynomial fits to the 27.32 MeV proton beam intensity profiles, before and after the data-driven fibre efficiency correction.	132

89	Schematic diagram of the Data Acquisition System (DAQ) to be used at the LION beamline for collecting synchronized optical and acoustic data, from two cameras and four ultrasound transducers, according to the photodiode-based laser trigger.	136
90	Interior of the SmartPhantom showing the scintillating fibre detectors attached onto the entrance window flange. Left: angled view. Right: on-axis view when the transducer window is removed.	137
91	Position of the SmartPhantom, containing the scintillating fibre detectors, relative to the LION beamline exit window. The imaging systems comprising of several optical components and cameras are attached. Side view: left. Top view: right.	137
92	Background-corrected images obtained at various proton energies at the LION beamline, showing partial imaging of the scintillating fibre detectors, captured using the setup shown in Figure 91 and the top-view camera (Camera 1).	139
93	Background-corrected images obtained at various proton energies at the LION beamline, showing partial imaging of the scintillating fibre detectors, captured using the setup shown in Figure 91 and the side-view camera (Camera 2).	140
94	Example images of the imaged scintillating fibre detectors when a proton beam with a modal energy 20 MeV passes through them. The green circles correspond to the fibres detected using the Hough Circle Transform method, with the fibre with the maximum average intensity indicated in pink. Top-view camera: (a). Side-view camera: (b)	141

95	Average fibre intensity against beam energy, calculated using the Hough Circle Transform method and the data from the top-view camera. Fibre 1 corresponds to the fibre at the top of the images, with the numbering ascending for fibres towards the bottom.	142
96	Average fibre intensity against beam energy, calculated using the Hough Circle Transform method and the data from the side-view camera. Fibre 1 corresponds to the fibre at the top of the images, with the numbering ascending for fibres towards the bottom.	142
97	Average fibre intensity, from the images obtained by the top-view camera, against position (measuring from top to bottom) for the various beam energies accelerated at the LION beamline. A Gaussian fit is applied to the data.	143
98	Average fibre intensity, from the images obtained by the side-view camera, against position (measuring from top to bottom) for the various beam energies accelerated at the LION beamline.	144
99	Full Width at Half Maximum (FWHM) of the beam profile in the direction imaged by the top-view camera, plotted against beam design energy. The values were extracted from the fitted Gaussian curves shown in Figure 97. .	145
100	3D-printed holder (orange) designed for securing stacks composing of eighteen layers of RadioChromic Films (RCF). The holder's position was adjusted vertically and horizontally using a motorized stage. Green alignment lasers were used to centre the square sections with the accelerator's exit window. .	146

101	Stack A (top) and Stack B (bottom) composing of eighteen layers of radiochromic films, after exposure to beams with various energies. In both stacks, the first two squares were non-irradiated.	147
102	Example scan of the RCF films from position 6 of Stack A, showing the deposition patterns caused by a 12 MeV beam passing through eighteen layers of Gafchromic TM EBT3 RCF films [118].	148
103	Depth-dose curves calculated by integrating the deposited energy within the irradiated sections across each layer of RCF Stack A.	149
104	Depth-dose curves calculated by integrating the deposited energy within the irradiated sections across each layer of RCF Stack B.	149
105	Experimental setup showing the SmartPhantom mounted on a motorized translation stage located at the accelerator’s exit window. The Piston hydrophone is aligned with the beam axis and the Olympus V303 transducer is positioned at the bottom.	150
106	Location of the collimators relative to the SmartPhantom and the accelerator’s exit window (left) and image of the collimators showing their respective diameters (right).	151
107	Averaged, background-corrected grayscale images captured using Camera 2 from the setup depicted in Figure 105, with no collimator placed at the front. The beam is incident from the left.	152
108	Averaged, background-corrected grayscale images captured using Camera 1 from the setup depicted in Figure 105, with no collimator was placed at the front. The beam is incident from the left.	153

109	Colourmaps of the pixel intensities from the images obtained using the setup depicted in Figure 105 when a 14 MeV proton beam passes through the liquid scintillator. Colourmap of the averaged image captured using the top camera:	
	(a). Colourmap of the averaged image captured using the side camera: (b).	154
110	Z-profile average of 60 pixels, defined by the horizontal line in Figure 109 (a), from images obtained at various LION proton energies transversing the liquid scintillator.	155
111	X-profile average of 60 pixels, defined by the vertical line in Figure 109 (a), from images obtained at various LION proton energies transversing the liquid scintillator.	156
112	Y-profile average of 60 pixels, defined by the vertical line in Figure 109 (b), from images obtained at various LION proton energies transversing the liquid scintillator.	156
113	Acoustic waveforms recorded by the Piston hydrophone, positioned on-axis with the beam, with various LION beam energies. No collimator was used in the setup.	158
114	Acoustic waveforms recorded by the Olympus V303 transducer, immersed at the bottom, with various LION beam energies. No collimator was used in the setup.	159
115	Averaged, background-corrected grayscale images obtained using Camera 2 from the setup shown in Figure 105. A 4 mm collimator was placed at the front.	160

116	Averaged, background-corrected grayscale images obtained using Camera 1 from the setup shown in Figure 105. A 4 mm collimator was placed at the front.	161
117	Colourmaps of pixel intensities from the images obtained using the top camera (a) and side camera (b) when a 14 MeV proton beam passes through the liquid scintillator. The setup included a 4 mm collimator in front of the SmartPhantom.	162
118	Z-profile average of 60 pixels from images obtained at various proton energies transversing the liquid scintillator, with 4 mm collimator at the front of the SmartPhantom.	162
119	X-profile average of 60 pixels from images obtained at various proton energies transversing the liquid scintillator, with 4 mm collimator at the front of the SmartPhantom.	163
120	Y-profile average of 60 pixels from images obtained at various proton energies transversing the liquid scintillator, with 4 mm collimator at the front of the SmartPhantom.	163
121	Acoustic waveform recorded by the Piston hydrophone, on-axis with the beam, with a 4 mm collimator placed in front of the SmartPhantom.	164
122	Acoustic waveform recorded by the Olympus V303 transducer, immersed from the bottom, with a 4 mm collimator placed in front of the SmartPhantom.	165
123	Averaged, background-corrected grayscale images obtained using Camera 1 from the setup shown in Figure 105. A 2 mm collimator was placed at the front.	166

124	Averaged, background-corrected grayscale images obtained using Camera 2 from the setup shown in Figure 105. A 2 mm collimator was placed at the front.	166
125	Colourmaps of pixel intensities from the images obtained with a 14 MeV proton beam. The setup included a 2 mm collimator in front of the SmartPhantom.	166
126	Z-profile average of 60 pixels from images obtained at various proton energies transversing the liquid scintillator, with 2 mm collimator at the front of the SmartPhantom.	167
127	X-profile average of 60 pixels from images obtained at various proton energies transversing the liquid scintillator, with 2 mm collimator at the front of the SmartPhantom.	167
128	Y-profile average of 60 pixels from images obtained at various proton energies transversing the liquid scintillator, with 2 mm collimator at the front of the SmartPhantom.	167
129	Acoustic waveform recorded by the Piston hydrophone, on-axis with the beam. It's position is shown in Figure 105. A 2 mm collimator was used in this configuration.	168
130	Acoustic waveform recorded by the Olympus V303 transducer, immersed from the bottom. It's position is shown in Figure 105. A 2 mm collimator was used in this configuration.	168

131	Optical simulation results developed in ZEMAX Optics Studio without (top) and with (bottom) the entrance window flange depicted in Figure 11 [125]. The simulation was performed using a 0.1 mm diameter beam emitting a uniform intensity in all directions.	170
132	Z-profile average of 60 pixels, without any collimator, corrected for the 0.5 mm shift observed due to the entrance window flange. The green dotted line marks the initial estimate of the entrance window, determined by the peak of the second derivative of the curves.	171
133	Z-profile average of 60 pixels, with a 4 mm collimator, corrected for the 0.5 mm shift observed due to the entrance window flange. The green dotted line marks the initial estimate of the entrance window, determined by the peak of the second derivative of the curves.	172
134	Z-profile average of 60 pixels, with a 2 mm collimator, corrected for the 0.5 mm shift observed due to the entrance window flange. The green dotted line marks the initial estimate of the entrance window, determined by the peak of the second derivative of the curves.	172
135	Acoustic waveforms recorded by the Piston hydrophone, without a collimator in the setup. The envelope is shown by the gray line, while the first and third peaks are marked by black dotted lines.	173
136	Acoustic waveforms recorded by the Piston hydrophone, with a 4 mm collimator in the setup. The envelope is shown by the gray line, while the first and third peaks are marked by black dotted lines.	174

137	Acoustic waveforms recorded by the Piston hydrophone, with a 2 mm collimator in the setup. The envelope is shown by the gray line, while the first and third peaks are marked by black dotted lines.	174
138	Effective range calculated using the peaks observed in the acoustic traces obtained by the Piston hydrophone positioned on axis with the beam. . . .	175
139	Mean beam energy calculated using the effective ranges shown in Figure 138 and the Bragg-Kleeman formula (Equation 2.4).	176
140	X-profile average of 60 pixels, from images obtained at various LION proton energies transversing the liquid scintillator. No collimator was used in the setup. A polynomial curve is fitted to the data for calculating the FWHM. .	177
141	X-profile average of 60 pixels, from images obtained at various LION proton energies transversing the liquid scintillator. A 4 mm collimator was used in the setup. A polynomial curve is fitted to the data for calculating the FWHM.	178
142	X-profile average of 60 pixels, from images obtained at various LION proton energies transversing the liquid scintillator. A 2 mm collimator was used in the setup. A polynomial curve is fitted to the data for calculating the FWHM.	178
143	Full Width Half Maximum (FWHM) calculation along the x-direction of the beam depositions at the various proton energies and collimator sizes used in the setup.	179
144	Y-profile average over 60 pixels from images obtained at various proton energies transversing the liquid scintillator, with a 4 mm collimator in the setup. A polynomial fit, shown by the dashed black line, is used to calculate the FWHM of the beam.	180

145	Y-profile average over 60 pixels from images obtained at various proton energies transversing the liquid scintillator, with a 2 mm collimator in the setup. A polynomial fit, shown by the dashed black line, is used to calculate the FWHM of the beam.	181
146	Acoustic waveforms recorded by the Olympus transducer, without a collimator in the setup. The compression and rarefaction peaks are indicated by vertical dashed lines and the time difference, dt , is marked by the horizontal line.	182
147	Acoustic waveforms recorded by the Olympus transducer, with a 4 mm collimator in the setup. The compression and rarefaction peaks are indicated by vertical dashed lines and the time difference, dt , is marked by the horizontal line.	183
148	Acoustic waveforms recorded by the Olympus transducer, with a 2 mm collimator in the setup. The compression and rarefaction peaks are indicated by vertical dashed lines and the time difference, dt , is marked by the horizontal line.	183
149	Full Width Half Maximum (FWHM) calculation along the y-direction of the beam depositions at the various proton energies and collimator sizes used in the setup.	184
150	Acoustic waveforms recorded by the Piston hydrophone, without a collimator in the setup. The amplitude of the peak originating from the entrance window that is directly proportional to the particle number in the bunch is marked by a black cross.	186

151	Acoustic waveforms recorded by the Piston hydrophone, with a 4 mm collimator in the setup. The amplitude of the peak originating from the entrance window that is directly proportional to the particle number in the bunch is marked by a black cross.	187
152	Acoustic waveforms recorded by the Piston hydrophone, with a 2 mm collimator in the setup. The amplitude of the peak originating from the entrance window that is directly proportional to the particle number in the bunch is marked by a black cross.	187
153	Comparison of the entrance window peak amplitude obtained from the Piston hydrophone waveforms (green) and the average pixel intensity from the images obtained during the same shot (blue). Both measurements are related to the particle number in the bunch.	188
154	Acoustic wave generation and propagation in the two-dimensional model of the SmartPhantom. The liquid scintillator, which forms the detector's volume, is enclosed by aluminium walls and the Olympus transducer is immersed inside 2.49 cm from the center.	201
155	Acoustic waveform recorded by an ideal point detector placed on axis with the beam for three different cases: liquid scintillator alone (green), liquid scintillator enclosed by aluminium walls (red) and liquid scintillator enclosed by aluminium walls with the Olympus transducer immersed (blue).	202

156	Frequency spectrum of the signals recorded by an ideal point detector placed on axis with the beam for three different cases: liquid scintillator alone (green), liquid scintillator enclosed by aluminium walls (red) and liquid scintillator enclosed by aluminium walls with the Olympus transducer immersed (blue).	203
157	Acoustic waveform recorded by an ideal detector placed on axis with the beam, with the SmartPhantom filled with the liquid scintillator enclosed by aluminium walls and the Olympus transducer immersed inside.	204
158	k-Wave simulation showing the designed hemispherical cup array transducer and its position relative to the beam energy depositions, indicated by the yellow region. The energy depositions depicted are generated by a proton beam exiting the LION beamline, optimized for a modal energy of 20 MeV, as it passes through the liquid scintillator.	206
159	Source pressure distribution (a) and reconstructed pressure distribution (b) after eight iterations of the iterative time-reversal algorithm, using the data acquired from the specified hemispherical cup array transducer.	206
160	Difference between reconstructed pressure distribution and source pressure distribution, using the data recorded by the hemispherical cup and the iterative time-reversal algorithm.	207
161	Reconstructed pressure distribution profiles along the x-(top), y-(middle) and z-(bottom) directions, using eight iterations of the iterative-time reversal algorithm and the specified hemispherical cup array transducer.	208

162	Deposited energy as a function of depth for a monoenergetic 100 MeV proton beam consisting of 10000 particles, propagating through various human body structures simulated in Topas [128].	210
163	Simulated acoustic waveforms, recorded by an ideal point detector capturing the ion-acoustic signals induced by a monoenergetic 100 MeV proton beam consisting of 10000 particles propagating through various human body structures. The ion-acoustic wave generation, propagation and detection were simulated using k-Wave.	211
164	Frequency spectra of the simulated signals, recorded by an ideal point detector capturing the ion-acoustic signals induced by a monoenergetic 100 MeV proton beam consisting of 10000 particles propagating through various human body structures. The ion-acoustic wave generation, propagation and detection were simulated using k-Wave.	212

List of Tables

1	Parameters present in Equation (2.1) that describes the maximum kinetic energy transferred between a particle and an electron in a head-on collision [25].	9
2	Parameters in the Bethe-Bloch Formula (2.2) [25].	10
3	Comparison of the cyclotron, synchrotron and fixed-field alternating gradient accelerator properties.	26
4	LhARA performance summary for protons, p^+ , and carbon ions, C^{6+} [4]. . .	29
5	Parameters present in the TNSA analytical Equations 4.1, 4.2, 4.3 and 4.4. . .	38
6	Table showing the ultrasound transducers that were to be used at the LION beamline experiment, along with key specifications [76] [77] [78] [80].	67
7	Ultima Gold XR chemical composition [93].	90
8	Third-order polynomial fit parameters to the 19.30 MeV proton beam intensity profiles, before and after the data-driven fibre efficiency correction. . . .	132
9	Third-order polynomial fit parameters to the 27.32 MeV proton beam intensity profiles, before and after the data-driven fibre efficiency correction. . . .	133

Abbreviations

2,6-DIPN 2,6-Diisopropylnaphthalene

ATLAS Advanced Titanium-Sapphire LAser

BDSIM Beam Delivery SIMulation software

BP Bragg Peak

CAD Computer-Aided Design

CALA Centre for Advanced Laser Applications

CSDA Continuous Slowing Down Approximation

DAQ Data Acquisition

dB Decibel

EMP ElectroMagnetic Pulse

FFA Fixed-Field Alternating gradient accelerator

FFT Fast Fourier Transform

FODO Focusing Optic Defocusing Optic

FWHM Full Width at Half Maximum

GPIO General Purpose Input/Output

ITRF Ion Therapy Research Facility

LET Linear Energy Transfer

LhARA Laser-hybrid Accelerator for Radiobiological Applications

LION Laser-driven Ion accelerator

Pa Pascal

PET Positron Emission Tomography

PMQ Permanent Magnet Quadrupole

PVDF Piezoelectric Polyvinylidifluoride

RCF RadioChromic Film

RF RadioFrequency

SNR Signal-to-Noise Ratio

SOBP Spread-Out Bragg Peak

SRIM Stopping Range of Ions in Matter

TIR Total Internal Reflection

TNSA Target Normal Sheath Acceleration

Chapter 1

Introduction

1.1 Context

Cancer is the second most common cause of death globally [1]. According to the World Health Organization, in 2022, approximately 20 million new cancer cases were diagnosed (of which 400000 were children) and around 9.7 million people died worldwide [2]. These numbers are estimated to rise in the next few years, highlighting the critical need for effective treatment to prevent the loss of life.

One of the most widely used treatment techniques is radiotherapy, treating approximately 50% of the cancer patients [3]. However, there are several limitations and drawbacks to this technique, underscoring the need for improvement. Novel, cost-effective and highly efficient treatment facilities need to be established that would be accessible to the wider population irrespective of socioeconomic status. These future facilities should incorporate more advanced techniques, surpassing current technologies, offering patients with more efficient therapies in both efficacy, accuracy, duration and comfort. This thesis introduces LhARA, the Laser hybrid Accelerator for Radiobiological Applications, a facility designed to fulfill this goal [4].

The LhARA collaboration aims to advance radiobiological research by exploring the therapeutic benefits and biological responses of different particle beam characteristics. Harnessing pulsed proton and light ion beam radiotherapy, the accelerator is designed to deliver a variety of different ions, beam widths, pulse durations and repetition rates, flexibly and precisely.

To reduce dose delivery uncertainties and facilitate more reliable, pulse-to-pulse adaptive treatment plans, the dose accumulation in the body needs to be monitored, on-the-fly, without disrupting the treatment. This work focuses on the development of a novel, real-time monitoring system of the three-dimensional dose accumulation in matter when using pulsed proton and light ion beams. The principle behind the system is the detection of acoustic waves emitted as a result of the transient increase in pressure caused by the passage of ions, delivered within a few nanoseconds, travelling through matter [5]. The detector, named the SmartPhantom, its conceptual development, construction and evaluation are presented.

The subject of this work is therefore the development, construction and evaluation of a real-time monitoring system of the three-dimensional dose accumulation in matter, during radiotherapy treatment using proton and light ion beams delivered in pulses of the order of a few nanoseconds.

1.2 Summary

The SmartPhantom detector is a hybrid system harnessing the detection of the induced acoustic waves along with a calibration mechanism using a commercially available liquid scintillator. The ultrasound waves carry comprehensive information about the spatial and temporal characteristics of the source that caused them [5]. Due to the high speed of ultrasound waves in matter, feedback of the dose accumulation can be provided in fractions of a second.

Ultrasound waves are typically detected using ultrasound transducers, however, their feedback provides a relative, and not an absolute, determination of the delivered dose [6]. To calibrate the acoustic response, a liquid scintillator serves as the propagating medium,

forming the inner volume of the SmartPhantom [7]. The scintillation light emitted during the ion beam propagation in the liquid scintillator, in combination with the known photon yield, can be used to infer the absolute three-dimensional dose distribution and calibrate the acoustic response.

In addition, this work explores the potential of using scintillating fibre detectors as an alternative to the liquid scintillator [8]. However, the acoustic wave distortion observed when used simultaneously with the acoustic measurements, restricts their use to serve only as a cross-sectional area and divergence measurement system.

A series of simulations were developed to design and integrate the optical and acoustic systems into the SmartPhantom. Initially, a suitable facility capable of delivering proton beam pulses short enough to allow the efficient generation of acoustic waves was identified to evaluate the detector. The selected facility was the Laser-driven ION (LION) accelerator located at the Centre for Advanced Laser Applications (CALA) in Munich [9].

To extract the characteristics of the emerging beam, the proton source at LION was parametrised using analytical equations and implemented in Python. This parametrised beam was then used as input in BDSIM, a particle tracking software, where the accelerator beamline was simulated and the particles were tracked [10][11].

The particle parameters at the accelerator's exit window were used as input for the next stage of the simulation pipeline, developed in Geant4, a software for simulating the passage of particles through matter [12]. In Geant4, the detector was modeled and the energy depositions of the beam within the detector's three-dimensional volume were extracted. The energy depositions were stored in a three-dimensional matrix file, which was then used as the source in k-Wave, a Matlab toolbox, for simulating the generation and propagation of the acoustic waves [13][14]. In k-Wave, four acoustic transducers were specified and

simulated, and their ability to reconstruct the pressure distribution was evaluated using multiple image reconstruction algorithms.

The SmartPhantom was manufactured with precise selection of dimensions, materials and coating colours, taking into account optical and acoustic reflections, imaging field of views and transducer focusing lengths. In addition, the mounting of the acoustic and optical systems was carefully designed to allow a variety of combinations and positioning options during experiments.

An initial evaluation of the SmartPhantom was conducted at the MC40 cyclotron in Birmingham [15]. However, testing the full hybrid system was not possible as the cyclotron could not produce beam pulses short enough to enable the generation of acoustic waves. As a result, the study focused exclusively on the optical system, where the properties of the liquid scintillator and scintillating fibre detectors were assessed.

The final evaluation of the SmartPhantom, including the acoustic system, was conducted at the LION beamline. The detector's performance was assessed as a function of beam energy and width by leveraging the accelerator's beam focusing properties. Using the obtained data, an analysis routine was developed to extract key information about the three-dimensional dose distribution, such as depth range, beam width and mean energy.

Finally, a comparison of optical and acoustic feedback was conducted to assess the extent of their correlation. The analysis of the results reveals a positive correlation between optical and acoustic measurements, with shot-to-shot values that match within the associated errors.

Chapter 2

Background Theory

Radiotherapy is a clinical therapy that uses ionizing radiation to treat tumours by killing malignant cells that proliferate [3]. Radiotherapy delivers a precise radiation dose to the patient, targeted at the tumour volume. The radiation is absorbed by the cancerous cells, causing DNA damage both directly and indirectly. A fraction of the DNA damage is caused by radiation striking the DNA, but more damage arises from free radicals created by reactive ion species upon radiation absorption [3]. This damage causes the excessive replication of the cell to stop, leading to cell death. By falsely irradiating the surrounding healthy tissue, there is a high risk of additional tumours being formed, called carcinogenesis, highlighting the importance of effective targeting.

Radiotherapy is used to treat over 50% of cancer patients [2], often in combination with chemotherapy and surgical removal. Despite the highly successful treatment, there are several drawbacks to this treatment modality, with the most important ones revolving around the effect of ionising radiation on healthy host cells surrounding the cancerous growths.

2.1 Particle Therapy

2.1.1 The Bragg Peak

Conventional radiotherapy uses x-rays, but, although photons are highly effective they don't deposit most of the dose in the tumour volume but along their entire path. As a result, protons and light ions are currently being incorporated in the development of new

cancer treatment facilities, due to the fact that the maximum dose is deposited in a small volume of tissue at the end of their range [16].

When ions interact with the tissue, they slow down and can deposit more energy in a shorter range and time. The maximum deposition is observed as a sharp peak, called the Bragg Peak (BP), and hence the effect on the healthy tissue surrounding the tumour is minimized [17]. A comparison of the dose delivery by the different species is illustrated in Figure 1.

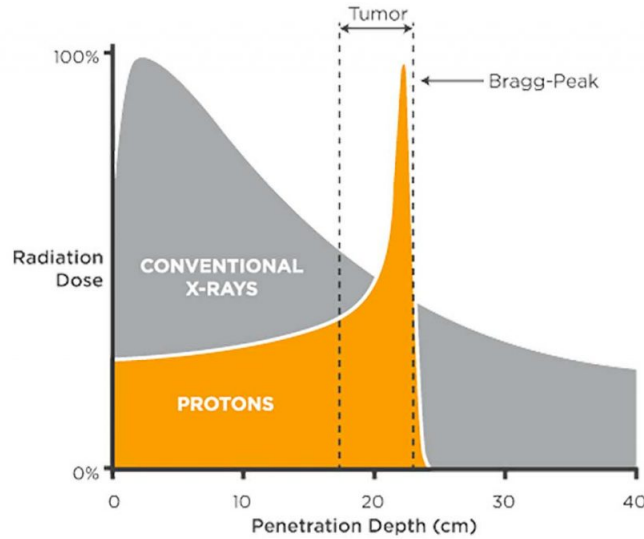


Figure 1: Relative depth-dose distribution for x-rays (photons) versus protons [17].

Figure 1 illustrates that there is an entrance dose. Such entry dose damages the healthy cells found at depths smaller than the tumour. This effect is reduced when using light-ion beams, compared to photons, however, there is the drawback of a fragmentation tail beyond the Bragg peak region that appears as a negative dose gradient [18]. This is mainly caused by the target nuclei fragmenting into lighter ion species as a result of inelastic scattering. These lighter ions can attain higher velocities, allowing them to travel further [19]. Such a fragmentation tail is undesirable, particularly in the case where vital organs are situated

behind the tumour, which can be severely damaged.

Furthermore, heavier ions, such as carbon and helium ions, exhibit a lower entrance dose and a sharper peak compared to protons. While these characteristics offer advantages over protons, accelerating these ions is more challenging due to their higher mass [20].

In general, the range of the Bragg peak is increased with increasing beam energy. Figure 2 compares the Bragg peak shapes for beams at various energies travelling through water. From the graph, it can be seen that the higher the energy, the longer the range of the particles, the lower the entrance dose and the broader the Bragg peak. Therefore, adjusting the beam's energy allows precise alignment of the Bragg peak to the desired depth, effectively targeting the tumour region.

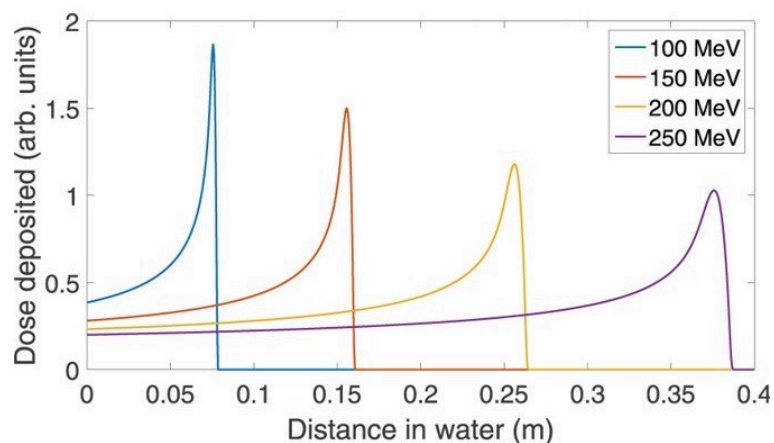


Figure 2: Comparison of the Bragg peak shapes resulting from proton beams at different energies travelling through water [21].

By treating patients with a combination of beams at different energies, it is possible to form a longitudinal profile and irradiate a larger volume. The beams can be delivered in pulses, each with its own energy and distinct Bragg peak. The delivered doses accumulate in the patient's body, resulting in a Spread-Out Bragg Peak (SOBP) that can cover the entire tumour volume, thereby increasing the efficiency of the treatment.

As of April 2022, 57 proton therapy centres are active worldwide and 37 centres are under construction [22]. The majority are located in high-income countries such as the USA, Japan and Germany. These centres vary in design, typically featuring fixed beams, one to three gantries (rotating machine that directs the radiation beam) and multiple treatment rooms. The number of proton therapy centres in clinical operation has been exponentially increasing over the years, with advances in technology enhancing the treatment efficiency. Furthermore, approximately 13 light-ion beam facilities are operating or are under construction, with the majority located in Japan (7). These facilities exclusively use carbon ions, with the highest energy, 800 MeV/u, achieved at the QST synchrotron in Chiba, Japan [23].

2.1.2 Energy Loss & Linear Energy Transfer

When charged particles transverse a medium, they lose energy. In the event of a head-on collision, the maximum kinetic energy transferred from a particle to an electron, W_{max} , is described by Equation 2.1 [24]. The parameters present in the equation are defined in Table 1. In general, the higher the energy of the particle, the greater the percentage of its total energy that is transferred.

$$W_{max} = \frac{2m_e c^2 \beta^2 \gamma^2}{1 + \frac{2\gamma m_e}{m_0} + (\frac{m_e}{m_0})^2} \quad (2.1)$$

In addition, the mean energy loss of a particle as it travels through a medium is described by the Bethe-Bloch formula, given in Equation 2.2 [25]. This formula provides the mass stopping power in $MeV g^{-1} cm^2$ and is valid for high-energy, relativistic particles. The variables present are defined in Table 2.

Table 1: Parameters present in Equation (2.1) that describes the maximum kinetic energy transferred between a particle and an electron in a head-on collision [25].

Parameter	Definition	Value	Unit
m_e	Electron mass	0.51099895	MeV/c^2
c	Speed of light in vacuum	1	-
β	Relative velocity	$\sqrt{1 - \frac{1}{\gamma^2}}$	-
γ	Lorentz factor	$(\frac{E}{m_0 c^2}) + 1$	-
E	Particle energy	<i>varies</i>	MeV
m_0	Incident particle mass	<i>particle dependent</i>	MeV/c^2

$$-\langle \frac{dE}{dx} \rangle = K z^2 \frac{Z}{A} \frac{1}{\beta^2} \left[\frac{1}{2} \ln \left(\frac{2m_e c^2 \beta^2 \gamma^2 W_{max}}{I^2} \right) - \beta^2 - \frac{\delta(\beta\gamma)}{2} \right] \quad (2.2)$$

According to the formula, the stopping power is directly proportional to the square of the particle's charge. Therefore, higher charged particles experience greater stopping power (caused by stronger electromagnetic interactions with the atomic electrons of the material), resulting in faster energy loss. In addition, as particles decelerate, dE/dx increases and hence gives rise to the characteristic shape of the depth-dose distribution and the rising slope of the Bragg peak.

The energy lost by the particles is mostly deposited in the medium. This is commonly referred to as Linear Energy Transfer (LET), which is the average energy transferred per unit length [26]. Different particles have varying LET values; photon and proton beams typically have a low LET, while heavy ions exhibit a high LET, particularly around the Bragg peak region. High LET values offer several biological advantages, including greater

DNA damage and the suppression of radiation repair [26].

Table 2: Parameters in the Bethe-Bloch Formula (2.2) [25].

Parameter	Definition	Value	Unit
E	Energy	<i>varies</i>	MeV
x	Depth	<i>varies</i>	cm
K	Coefficient	0.307075	MeV $mol^{-1}cm^2$
z	Charge number	<i>particle dependent</i>	-
Z	Atomic number of medium	<i>medium dependent</i>	-
A	Mass number of medium	<i>medium dependent</i>	-
β	Relative velocity	$\sqrt{1 - \frac{1}{\gamma^2}}$	-
γ	Lorentz factor	$(\frac{E}{m_0c^2}) + 1$	-
m_e	Electron mass	0.51099895	MeV/ c^2
c	Speed of light	1	-
W_{max}	Maximum energy transfer	2.1	MeV
I	Ionisation energy	13.6	MeV
$\delta(\beta\gamma)$	Density effect correction	$ln(\frac{\hbar\omega}{I_e}) + ln(\beta\gamma) - \frac{1}{2}$	MeV
I_e	Mean excitation energy	0.000075	MeV
$\hbar\omega$	Plasma energy	$\sqrt{\rho < \frac{Z}{A} > \frac{28.816}{1000000}}$	MeV
ρ	Medium density	<i>medium dependent</i>	g/cm ³

The range of a particle in a medium is the distance travelled before it comes to rest. During its trajectory, the particle interacts with the medium, losing a fraction of its energy with each interaction. Since this energy loss depends on the number of collisions, the range and energy values fluctuate. This statistical variation is referred to as range or energy straggling [27].

The average range of a particle in a medium can be approximated using the Continuous Slowing Down Approximation (CSDA) [28]. This is the integral of the inverse of the stopping power, dE/dx , divided by the medium density, ρ . The relation is described in Equation 2.3, where E_0 is the initial kinetic energy of the propagating particle.

$$R = \int_0^{E_0} \left[\frac{dE}{dx} \right]^{-1} \frac{dE}{\rho} \quad (2.3)$$

In addition, the range and energy of highly energetic protons are related by the Bragg-Kleeman formula, as shown in Equation 2.4 [29]. In this formula, a and p are parameters dependent on the material and energy, respectively. Specifically, a is proportional to the square root of the absorbing medium's atomic mass (equal to 0.0022 for water) and p is equal to 1.77 for proton energies in the range of 10-250 MeV [30].

$$R^{proton} = aE_0^p \quad (2.4)$$

2.1.3 FLASH Dose Rates & Minibeams

FLASH radiotherapy is a technique where doses are delivered at ultra-high dose rates, typically within fractions of a second [31]. The rapid delivery of the dose reduces toxicity and better preserves the healthy tissue. As a result, the overall treatment time is reduced, offering a more comfortable experience to the patients. In addition, current studies show fewer side effects and indicate that the efficacy results from the ultra-high dose rates altering cell oxygenation levels and biological responses [32]. Furthermore, dose rates within the FLASH regimen can exceed 40 Gy/s, where 1 Gray is the absorption of 1 joule of radiation energy per kilogram of matter (i.e. $1 \text{ Gy} = 1 \text{ J/Kg}$) [33]. Such high dose rates make FLASH radiotherapy with proton and light ions very challenging using conventional accelerators.

Radiotherapy using minibeam and microbeam offers significant advantages compared to larger diameter beams [34]. A minibeam is defined as a beam where the Full Width at Half Maximum (FWHM) of its transversal profile is between 0.1 and 1 mm, where a microbeam has a FWHM equal to or is less than 1 μm [35]. Their sub-cellular size allows for precise introduction of intra- and inter-cellular damage at specific locations. Combining spatially fractionated radiation with light ion narrow beamlets can maximize tumour damage while sparing healthy tissue. Pre-clinical biological experiments using proton microbeam irradiation have demonstrated this enhanced sparing effect [36].

2.2 Dosimetry

The effectiveness of radiation treatment is determined by the dose, which defines the energy deposited by radiation per unit of target mass. For an infinitesimal cylinder with cross-sectional area dA , thickness dx and dN particles passing through, the dose, D , can be related to the stopping power, dE/dx , and medium density, ρ , using Equation 2.5 [37].

$$D = \frac{\text{energy}}{\text{mass}} = \frac{-(\frac{dE}{dx}) \times dx \times dN}{\rho \times dx \times dA} \quad (2.5)$$

Dosimetry refers to the measurement of the radiation doses absorbed by materials. A precise dose measurement is crucial to ensure that the appropriate amount of radiation is delivered accurately and safely. Dose can be measured using several different methods.

Radiochromic Film

Dosimetry with radiochromic films involves using specialized films that change colour, in a process induced by polymerization, in response to ionizing radiation exposure [38]. These films, known as radiochromic films or radiochromic dosimeters, typically change to

a deep blue colour, with the intensity directly proportional to the amount of radiation absorbed. This method, therefore, enables dose mapping measurements of protons and heavy ions. However, its accuracy is limited due to inconsistencies in radiation detection, leading to reduced precision. Unlike traditional film dosimetry, which requires chemical development after exposure, radiochromic films provide real-time or near-real-time feedback on the radiation dose distribution without chemical processing.

Calorimeters

Calorimeters measure the temperature change caused by deposited energy. The absorbed dose is calculated by multiplying this change by the specific heat capacity of the medium and applying correction factors [39]. Calorimeters must be well-insulated to minimize heat exchange with the surroundings. However, achieving perfect thermal isolation is challenging, leading to some degree of heat loss or gain. This can introduce errors in the measurements and reduce the accuracy of the results.

Ionization Chambers

Ionisation chambers are cavities filled with gas that become ionized as an ion passes through. The resulting current is measured using electrodes. The dose within the cavity can be calculated and then translated into the dose delivered to the medium using appropriate calibration techniques [40]. Unfortunately, using ionization chambers for high dose rates presents challenges due to saturation effects.

Faraday Cups

Faraday cups are conductive metals that trap charged particles. The number of particles per unit area, called fluence, can be obtained by measuring the electric current. Correction factors can then be applied to this value to obtain the dose [41]. Detector ar-

rays, composed of a series of diodes or ionization chambers, can be used to measure the dose. However, a drawback of this method is that the size of the detector and its distance from the source limits the resolution.

Positron Emission Tomography

Positron Emission Tomography (PET) can be used to infer the dose delivered when a patient is treated with proton or light-ion beams [42]. During irradiation, nuclear activation and fragmentation reactions occur, generating positron-emitting isotopes such as ^{15}O , ^{13}N and ^{11}C . The activity of these isotopes can be measured using a PET scan machine. However, this method is limited by scattering which reduces the spatial resolution of the reconstructed images. In addition, this method faces challenges such as long acquisition times due to low activity, limited sensitivity, poor counting statistics, restricted post-treatment assessment, and the need for complex, expensive, and bulky instrumentation. Moreover, this nuclear interaction-based technique provides only indirect information about the Bragg peak and does not offer anatomical details of the patient. Lastly, the decaying nature of the produced isotopes prevents real-time imaging.

Prompt Gamma Imaging

Prompt gamma imaging is based on the detection of gamma rays emitted from the annihilation of nuclear fragmentation products as ions slow down in a medium [43]. Since fragmentation occurs along the entire beam path, the longitudinal beam range can be related to the observed emissions. Unfortunately, this method suffers from high background radiation that arises from gamma rays caused by ion scattering. While prompt gamma imaging is fast enough to offer real-time monitoring, it has several limitations such as the short-lived nature of the emitted radioisotopes and the need for expensive equipment.

2.3 Ion-Acoustic Imaging

Ion-acoustic imaging is a non-invasive technique that utilizes ultrasound (pressure) waves induced by the passage of ions [5]. As the ion beam transverses a medium, it interacts via Coulomb scatterings, transferring its kinetic energy to the atoms in the form of heat. If the ion pulse duration is significantly shorter than the medium's stress relaxation time, the energy remains confined within the system. This condition, commonly referred to as the stress-confinement criterion, leads to a rapid increase in temperature [44]. Assuming that the temperature rise is short enough to neglect thermal diffusion, the energy is converted into mechanical stress in the form of an acoustic wave. Figure 3 illustrates the ion-acoustic wave generation and detection.

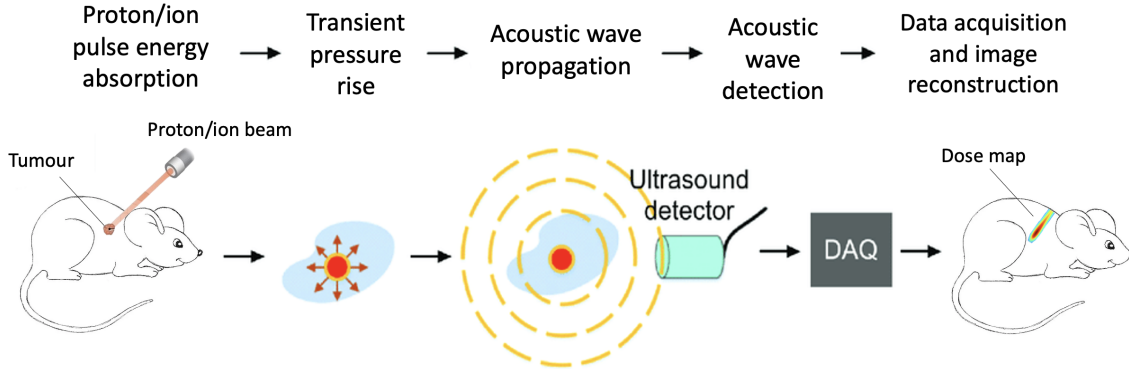


Figure 3: Schematic diagram of the ion-acoustic wave generation and detection.

The source pressure distribution at location \mathbf{r} and temperature T , denoted as $p_0(\mathbf{r}, T)$, can be calculated from the energy deposition distribution, $E(\mathbf{r}, T)$, using Equation 2.6 [45]. In this equation, $\Gamma(\mathbf{r}, T)$ is the dimensionless Grüneisen coefficient, which gives a measure of the efficiency of converting absorbed heat energy to induced pressure. The Grüneisen coefficient is calculated using Equation 2.7, where v_s is the speed of sound in the medium, β

is the thermal expansion coefficient and C_p is the pressure-specific heat capacity. At room temperature, the Grüneisen coefficient is approximately 0.11 for water, around 0.8 for fat, and ranges from 0.25 to 0.28 for soft tissue [45].

$$p_0(\mathbf{r}, T) = \Gamma(\mathbf{r}, T) \times E(\mathbf{r}, T) \quad (2.6)$$

$$\Gamma(\mathbf{r}, T) = \frac{v_s^2 \beta}{C_p} \quad (2.7)$$

The time evolution of the generated pressure is described by Equation 2.8, where v_s represents the speed of sound in the medium, t denotes time and $\rho(\mathbf{r}, T)$ is the target mass density [46]. The solution to the equation is given in Equation 2.9, which gives the pressure amplitude of the wave at position \mathbf{r} . These equations suggest that the relative dose can be computed by reconstructing the initial pressure and using the known properties of the medium.

$$\nabla^2 p(\mathbf{r}, t) - \frac{1}{v_s^2} \frac{\partial^2}{\partial t^2} p(\mathbf{r}, t) = -\frac{\Gamma}{v_s^2} \frac{\partial}{\partial t} E(\mathbf{r}, t) \rho(\mathbf{r}) \quad (2.8)$$

$$p(\mathbf{r}, t) = \frac{1}{4\pi} \frac{\Gamma}{v_s^2} \int_V \frac{dV'}{|\mathbf{r} - \mathbf{r}'|} \frac{\partial^2}{\partial t^2} E(\mathbf{r}', t - \frac{|\mathbf{r} - \mathbf{r}'|}{v_s}) \rho(\mathbf{r}) \quad (2.9)$$

Ultrasound waves can be detected by ultrasound transducers, providing time-series data that enable the reconstruction of the spatial and temporal distribution of the source causing them. Due to the high speed of ultrasound in various media, signals are detected almost instantaneously [47]. While this rapid detection theoretically allows for real-time ion-acoustic imaging, the actual imaging speed is primarily limited by the processing time.

For accelerators operating at high repetition rates, such as 10 Hz, even faster processing is necessary.

Ion-acoustic imaging provides a direct measurement of the dose distribution, unlike nuclear-based techniques. While its application is limited to body areas suitable for acoustic access and free from obstructions like bone or gas, it offers several advantages. These include high spatial resolution, large penetration depth and *in-vivo* applicability. In addition, ion-acoustic imaging enables the co-registration of ultrasound images, providing information about both dose and anatomy. This integration allows the measured profile to be aligned with the underlying tissue anatomy and morphology while simultaneously enabling tissue motion tracking. This capability could enhance the precise delivery of the dose to the tumour region.

2.4 Scintillators

Scintillators are materials commonly used in radiation detection and measurement applications due to their ability to emit visible light or other detectable photons when exposed to ionizing radiation [48]. When radiation interacts with a scintillator, it transfers energy to the atoms within the material, exciting them to higher energy states. As these excited atoms return to their ground state, they release the excess energy in the form of photons, where the number of photons is proportional to energy deposited. These can be detected and measured to quantify the intensity and nature of the incident radiation. Scintillators are available in various forms, including solids and liquids, and come in both organic and inorganic varieties.

2.4.1 Scintillating Fibres

Scintillating fibres are thin, flexible optical fibres [8]. They are composed of a core material that scintillates when it interacts with high-energy particles and a cladding material that guides and protects the scintillation light. The emitted photons within the scintillating fibre core are transmitted along the fibre through Total Internal Reflection (TIR), due to the higher refractive index of the core compared to the cladding.

2.4.2 Liquid Scintillators

Liquid scintillators play an important role in large-scale neutrino experiments due to their high efficiency in converting kinetic energy into detectable light with a high yield [7]. These liquids typically consist of three components: a solvent and two fluors. One fluor acts as a light absorber and the other one serves as a wavelength shifter to maximise the fraction of emissions that fall within the detector's sensitivity range.

The fluorescent intensity, I , decays exponentially over time, t , as shown in Equation 2.10. In this equation, I_0 represents the maximum intensity and τ is the fluorescent decay time [49].

$$I = I_0 e^{-\frac{t}{\tau}} \quad (2.10)$$

The density-normalised scintillation photon yield, L , per unit path length, x , of an ion moving through a scintillating material, is described by Equation 2.11. In this equation, S is the conversion factor between energy deposition and light production (called scintillation efficiency), kB is the Birks constant (a material-specific quenching parameter), dE/dx is the stopping power and C a second-order quenching term [50]. By knowing the stopping power, the total photon yield can be determined through numerical integration. The light

yield of the scintillator can be assessed using photomultiplier tubes or a camera, facilitating a direct connection between the measured and the incident radiation.

$$\frac{dL}{dx} = \frac{S \frac{dE}{dx}}{1 + kB \frac{dE}{dx} + C \left(\frac{dE}{dx} \right)^2} \quad (2.11)$$

Care must be taken when using liquid scintillators due to quenching effects, which can reduce the scintillation light output [51]. Quenching occurs due to a phenomenon called "non-radiative energy transfer". When a proton deposits energy in the scintillator medium, there is a possibility that the excitation energy is transferred to neighbouring molecules without the emission of scintillation light. This transfer reduces the overall light output. The extent of quenching depends on various factors, such as the energy and intensity of the proton beam, the composition and properties of the liquid scintillator, and the specific interactions between the protons and the scintillator molecules.

Chapter 3

LhARA

3.1 Facility

LhARA, the Laser-hybrid Accelerator for Radiobiological Applications, is designed to advance technologies that can enhance the clinical application of radiotherapy [4]. It will use proton and light ion beams to study radiobiological effects and the impact of ionising radiation on tissue, enabling particle-beam therapy to be delivered in new regimens.

The LhARA facility will be significantly smaller, more cost-effective, and more flexible than current facilities, with an extended range of beam characteristics. Its triggerable source and highly automated accelerator design would enable patient-specific treatment to be feasible. LhARA is currently being developed to serve the Ion Therapy Research Facility (ITRF) [52].

The beam will be generated using a thin foil target and a powerful pulsed laser. The laser-driven particles will be captured and focused into a large flux using Gabor (electron plasma) lenses [53]. This setup allows for a wide variety of time structures, spectral distributions, and spatial configurations, enabling the delivery of instantaneous dose rates (≥ 40 Gy/s) and ions in the mini- and micro- beam range [54]. These high dose rates can potentially offer more effective therapy and treatment duration, the therapeutic effect of which can be studied.

The LhARA accelerator will have three end stations. The first, low-energy end station (Stage 1) will deliver proton beams at 10–15 MeV for *in vitro* radiobiological studies. Post-acceleration will be achieved using fixed-field alternating-gradient acceleration, with the

beam reaching the *in vitro* and *in vivo* high-energy end stations (Stage 2) at proton energies up to 127 MeV or ions up to 33 MeV per nucleon. A schematic diagram of the LhARA beamlines is shown in Figure 4.

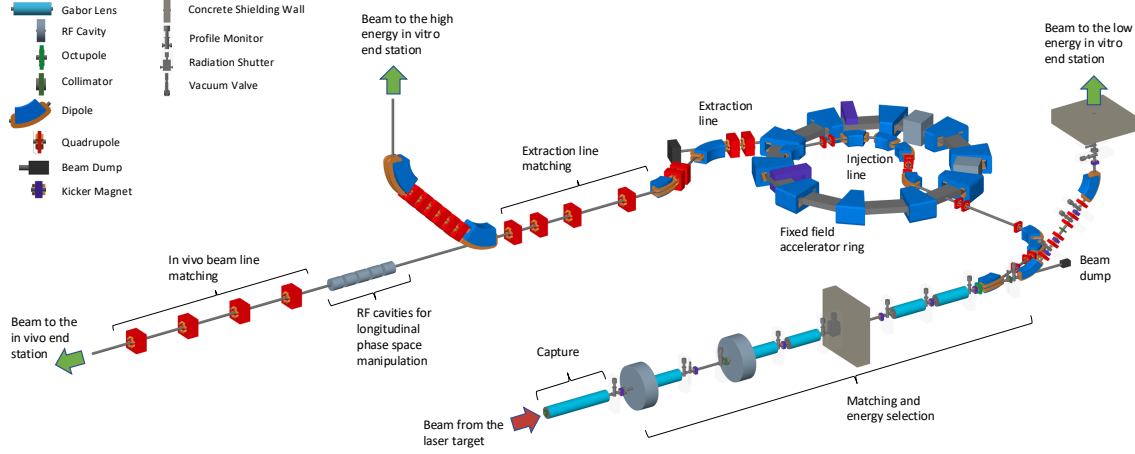


Figure 4: Schematic diagram of the LhARA beamlines [4].

3.2 Stage 1

3.2.1 Laser-Driven Source

LhARA will generate and accelerate particles by irradiating a thin foil target with a short laser pulse. The acceleration of the particles occurs through a process known as Target Normal Sheath Acceleration, or TNSA [55]. TNSA can achieve high acceleration gradients over short distances, enabling a huge number of particles to be produced [56].

Due to the high laser intensity ($>10^{18} \text{ W/cm}^2$), the particles at the front surface of the foil become ionized, creating a pre-plasma with a steep density gradient. This process, part of the Target Normal Sheath Acceleration (TNSA) mechanism [55], involves the interaction between the laser pulse and the plasma, which generates electrons that make it to the foil's rear (non-irradiated) surface due to the Lorentz force. Because of the large nucleon-

to-electron mass ratio, the electrons are moving much faster than the ions. The highly energetic electrons can escape the foil, creating a potential difference perpendicular to the target surface which traps the remaining electrons. This leaves a positive charge on the rear surface, resulting in a charge separation field. This field causes further ionization of atoms, which mainly come from water vapour, hydrocarbon and oxide contaminants on the target's surface [57]. The ions are then accelerated to high speeds and exit the foil in a direction normal to the target due to the direction of the charge separation field. The TNSA process is illustrated in Figure 5.

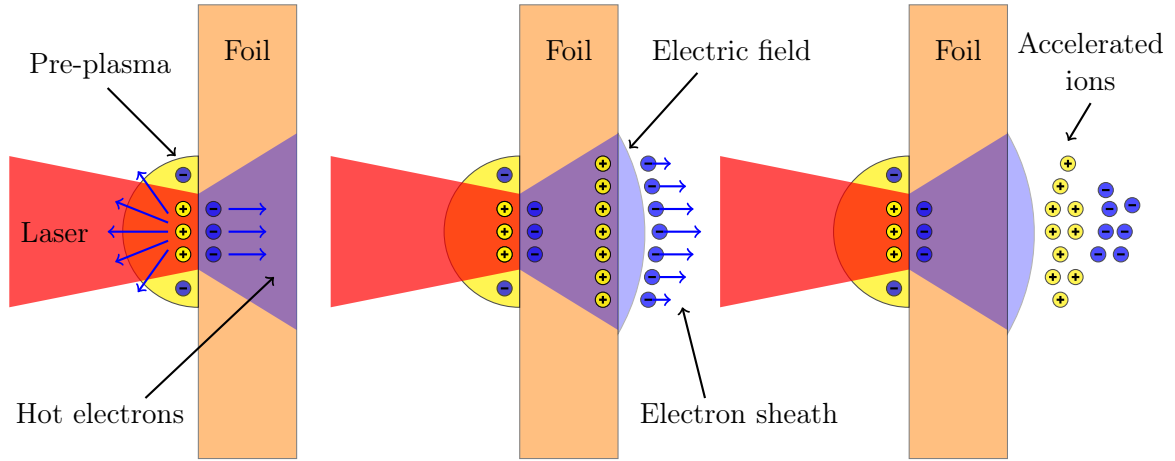


Figure 5: Schematic diagram illustrating the Target Normal Sheath Acceleration mechanism.

TNSA can produce and accelerate ions up to 40 MeV/u [58]. The number of particles can reach up to 10^{13} per pulse, with energies ranging from a few MeV to tens of MeV. The beam energy can be adjusted by varying the laser intensity and target thickness, while different ion species can be accelerated by changing the target material and particle-capture optics. Protons are predominantly accelerated by this process due to their high charge-to-mass ratio.

Beams accelerated by this mechanism offer several advantages over those accelerated by conventional methods, such as lower transverse emittance and shorter pulse duration. In general, using thinner foil targets increases the accelerated ions' maximum energy and the efficiency of converting laser energy into ion energy [57]. However, if the foil is too thin ($\leq 8 \mu\text{m}$), the shock wave reaches the rear surface of the target before the electron sheath is formed, preventing the ions from being accelerated to very high energies [57].

LhARA will use a commercially available laser with 2.5 J energy and 25 fs pulse length, at a repetition rate of 10 Hz to irradiate an aluminium or steel target foil [4]. Such a combination can produce protons up to 10-15 MeV that can be captured, collimated and accelerated to higher energies.

3.2.2 Ion Capture

Laser-driven beams are highly divergent ($> 10^\circ$ emission cone) and have a large energy spread, therefore, a strong capture and focusing system are required [59]. Gabor lenses have been proposed in the LhARA design to focus the ions strongly and form them into a narrow beam.

A Gabor lens is a plasma lens consisting of solenoid coils that contain an electron cloud and cylindrical anodes, as depicted in Figure 6 [53]. These lenses offer significant advantages over high-field solenoids: in principle, they are much cheaper, have simpler construction and require a significantly lower magnetic field (and thus less power) to achieve the same focusing effect. In addition, plasma lenses can generate magnetic fields that are orders of magnitude stronger, enabling a more effective beam focusing.

The radial focusing force, F_{gabor} , exerted on an ion beam with mass m_i is given by Equation 3.1. In this equation, n_e is the electron density, e is the electron charge, ϵ_0 is the

permittivity of free space and r is the radial position [60].

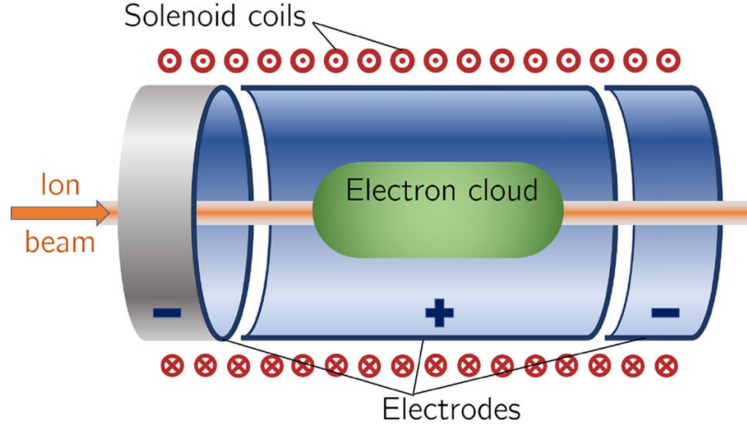


Figure 6: Schematic diagram of the Gabor lens to be used in LhARA. The orange arrow shows the direction of the beam, the red circles indicate the direction of the current within the coils, and the green represents the electron cloud [53].

$$F_{gabor} = \frac{n_e e^2}{2\epsilon_0} r \quad (3.1)$$

The focal point, f , of a Gabor lens is given by Equation 3.2, where l is the length of the lens and U the kinetic energy of the beam. According to the equation, the focusing strength of the lens can be adjusted by varying the electron density within it [53].

$$\frac{1}{f} = \frac{e^2 n_e}{4e_0 U} l \quad (3.2)$$

3.2.3 Beam Transport

A beam transport system has been designed to minimize beam losses and maximize the energy delivered per shot. A schematic diagram of the LhARA low-energy Stage 1 beamline is shown in Figure 7 [4].

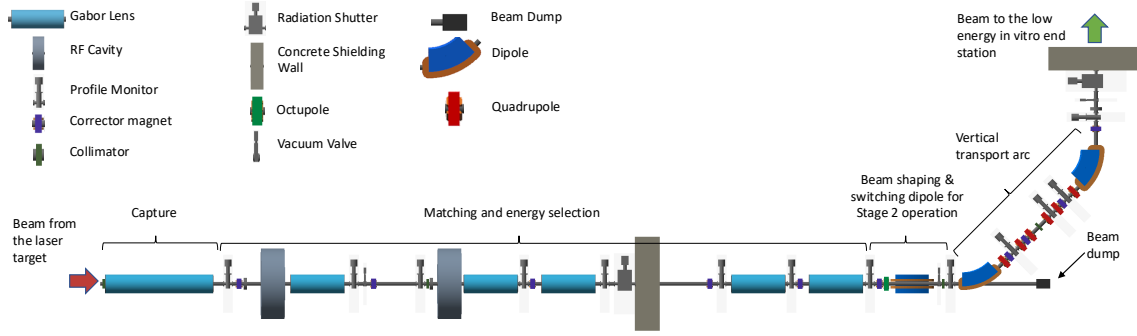


Figure 7: Schematic diagram of the LhARA Stage 1 beamline [4].

Two Gabor lenses in a single device capture the divergent ion beam, reduce transverse momentum and minimize particle loss. The first radiofrequency (RF) cavity manipulates the phase space of the particles and controls the bunch length. The third Gabor lens focuses the bunch, while the second RF cavity allows for further phase-space manipulation. The four subsequent Gabor lenses ensure the beam remains parallel and transport the beam to the transfer lines. The octupole magnets provide additional third-order focusing, while the collimators ensure that the beam's circular aperture meets the end station requirements. Due to the focusing properties of Gabor lenses, which focus different energies at different focal lengths, this set-up combination ensures that only particles within a specific energy range, selected from the broad energy spectrum produced by the laser-driven source, are transmitted. This selection enhances beam stability and allows for reproducible measurements.

3.2.4 Transfer Line

In the low-energy transfer line, six quadrupole magnets and a collimator are used to enhance beam uniformity and correct dispersion. They enable precise momentum selection, provide the final beam focusing and reduce the spot size to approximately 1 to 3 cm in diameter. Two dipole magnets direct the beam upwards, bending it by 90° . The 2-meter

drift section ensures that the beam passes through the concrete shielding and is directed towards the end station. In addition, if the first dipole is not energized, the beam is directed towards the abort line, which consists of a drift section followed by a beam dump. Furthermore, if the beam is required to be accelerated further, the first dipole before the arc can be activated to divert the beam towards Stage 2.

3.3 Stage 2

3.3.1 Post-Acceleration

To increase the energy of the beam and deliver variable energies at the high-energy end-stations, the LhARA design has a Fixed-Field Alternating (FFA) gradient accelerator. The FFA accelerator combines features of both cyclotrons and synchrotrons: it has a fixed magnetic field, like a cyclotron, and alternating gradient, like a synchrotron [61]. A comparison between a cyclotron, a synchrotron and an FFA is shown in Table 3.

Table 3: Comparison of the cyclotron, synchrotron and fixed-field alternating gradient accelerator properties.

	Cyclotron	Synchrotron	FFA
Revolution time	Constant	Variable	Variable
Orbit radius	Variable	Constant	Variable
Transverse focusing	Variable	Constant	Variable

The fixed magnetic field causes the beam to bend and change radius as it accelerates. Unlike a cyclotron, the alternating gradient approach in an FFA allows the beam to be tightly focused to very small sizes. This strong focusing capability enables the FFA to achieve high output energies with a more compact and cost-effective machine, as well as

enabling the acceleration of multiple species. In addition, this rapid acceleration scheme can handle beams from pulsed sources at a high repetition rate.

The LhARA FFA ring consists of 10 spiral magnet cells configured in a circular arrangement, as illustrated in Figure 8. The number of cells was chosen to accommodate the injection and extraction systems, and to fit the size of the orbit. To operate at 10 Hz, a voltage of 0.5 kV is required for the RF cavities, with a frequency range between 2.89 and 6.48 MHz [4]. Various beam energies and repetition rates can be achieved by adjusting the magnetic field settings. This post-acceleration scheme enables energies up to 127 MeV for protons and up to 33.4 MeV/u for carbon ions.

3.3.2 Beam Transport

After post-acceleration, two dipole magnets ensure that the beam is aligned parallel to the high-energy *in-vitro* and *in-vivo* extraction line. The subsequent four quadrupoles focus the beam to different sizes and transport it to the vertical arcs: to the *in-vitro* station if the third dipole is energized or to the *in-vivo* station if the third dipole remains de-energized. If the beam needs to be aborted, the first dipole is de-activated, directing the particles towards the beam dump via the second abortion line.

3.3.3 Extraction Line

In the high energy *in-vitro* end station, six quadrupole magnets provide further beam focusing. The subsequent and final dipole magnet diverts the beam upwards by 90° towards the end station. For the high energy *in-vivo* station, the design incorporates additional RF cavities for longitudinal phase-space manipulation and four quadrupole magnets for final focusing. The selected number of quadrupole magnets allows for the delivery of beams with diameters ranging from 1 to 3 cm [4].

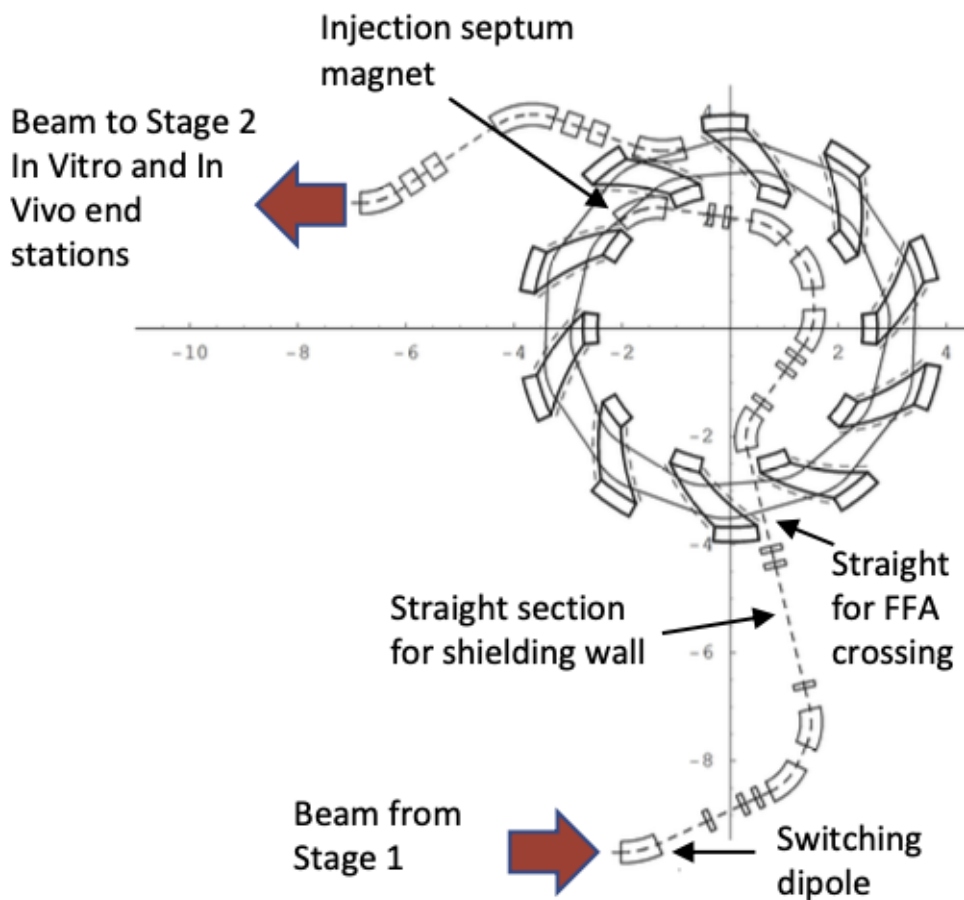


Figure 8: Fixed-field alternating (FFA) gradient acceleration scheme to be used in LhARA, with parts of the injection and extraction lines shown at the bottom and top left, respectively [4].

With the current LhARA baseline specifications, 10^9 particles per shot can be achieved, with proton dose rates reaching up to 156 Gy/s and carbon ion dose rates up to 730 Gy/s. A summary of LhARA's performance is provided in Table 4 [4].

3.4 Dosimetry System

For LhARA, the development of an on-the-fly, non-invasive, dose-deposition mapping system is essential. This system should provide a quantitative three-dimensional dose distri-

Table 4: LhARA performance summary for protons, p^+ , and carbon ions, C^{6+} [4].

	12 MeV p^+	15 MeV p^+	127 MeV p^+	33.4 MeV/u C^{6+}
Dose per pulse	7.1 Gy	12.8 Gy	15.6 Gy	73.0 Gy
Instantaneous dose rate	1.0×10^9 Gy/s	1.8×10^9 Gy/s	3.8×10^8 Gy/s	9.7×10^8 Gy/s
Average dose rate	71 Gy/s	128 Gy/s	156 Gy/s	730 Gy/s

bution and accurately localize the Bragg peak. The real-time acquisition and quantification of the radiation dose will reduce delivery uncertainties and facilitate a more reliable, real-time pulse-to-pulse adaptive treatment plan.

This work focuses on the design, development, construction and calibration of a detector to serve this scope. The proposed instrumentation, called the SmarPhantom, is a proof-of-principle device that employs a hybrid approach, integrating various dosimetry methods to achieve a real-time absolute dose distribution rather than relative dose measurements of the deposited dose. The ultimate goal is to develop trust in the acoustic measurement that will lead to a reliable dose-determination system.

Acoustic Transducers

The very short pulses delivered by LhARA (10-40 ns) satisfy the stress-confinement criterion, enabling the generation of ion-acoustic waves. Given the high speed of ultrasound in tissue, ion-acoustic imaging is deemed the most suitable method for real-time monitoring, as it enables the system designed around it to deliver rapid feedback.

Acoustic signals are detected using ultrasound transducers which are usually made of piezoelectric materials that convert pressure variations into voltage in the front end.

Acoustic signals induced by ion beams at clinically relevant energies (60-200 MeV) are typically of the order of a few kHz, making their detection very challenging. Conversely, ion beam energies in the pre-clinical range (< 60 MeV) are favourable for ion-acoustic measurements as they produce a shorter Bragg peak, with acoustic signals reaching a few MHz. These higher frequencies are more favourable for ion-acoustic experiments because they fall within the detection range of current transducer technologies.

However, acoustic signals often suffer from a high signal-to-noise ratio (SNR), a significant limitation for clinical applications where high accuracy is essential. This issue can be mitigated by using multichannel acoustic sensors to average in the spatial domain, in addition to the time domain (multiple beam pulses) [62]. The signals received by each element are processed and combined, reducing random noise and maximizing the total signal amplitude.

Multichannel piezoelectric transducers are therefore used for detecting the ion-induced acoustic signals in the proposed dosimetry system. The transducers are placed on the three orthogonal planes to achieve a 3D reconstruction of the deposited dose with minimal SNR. The chosen transducers have a centre frequency and bandwidth that match the frequency spectrum of the signal produced to maximize signal detection and eliminate low-frequency noise. In addition, appropriate pre-amplifier boards are necessary to amplify the signal. The choice of transducers and amplifiers is discussed later in Section 5.2. However, the acoustic signals can be used to infer a relative, and not an absolute dose distribution, therefore calibration is essential.

Liquid Scintillator Detector

Liquid scintillators have been considered ideal for pulse-to-pulse acoustic calibration due

to their ability to emit scintillation light that can be imaged in real-time. If the scintillation yield is known, the absolute dose distribution can be inferred from the light distribution. Therefore, a liquid scintillator is used to fill the inner volume of the SmartPhantom and act as the propagating medium, allowing simultaneous measurements of both scintillation light and acoustic signals.

Liquid scintillators offer significant advantages, such as forming a uniform solution, which minimises the attenuation (reflection or diffraction) of the acoustic signal. A detailed discussion of the imaging system is presented later in Section 6. To facilitate the reconstruction of a three-dimensional light distribution, two identical systems are placed perpendicular to each other.

Scintillating Fibre Detectors

To reconstruct the cross-sectional area of the beam, scintillating fibre detectors are used because they have high spatial and temporal resolution. As with the liquid scintillator, real-time acquisition is possible and the scintillation light is imaged by an optimised optical system. The fibres' known scintillation yield is used to convert the recorded intensity into energy and subsequently to dose.

To obtain a two-dimensional reconstruction of the beam's profile, scintillating fibres are placed parallel to each other to form a plane. The chosen fibres have a $250\ \mu\text{m}$ diameter and in the fibre detector design, they are arranged with a $300\ \mu\text{m}$ centre-to-centre distance. The scintillating fibre detectors are made of two planes placed perpendicular to each other to form a 2D fibre array. An effective area of $20 \times 20\ \text{mm}$ has been regarded as sufficient to capture the cross-sectional area of the beam. By employing multiple detectors positioned along the beam axis, the three-dimensional dose profile can be reconstructed by fitting an-

alytical approximations. A detailed discussion of the simulation, design and manufacturing process is discussed in Section 7.

3.5 The SmartPhantom

The CAD design of the SmartPhantom is illustrated in Figure 9. The SmartPhantom has a cuboid structure and is made of 5 mm thick aluminium walls, with the inner volume measuring 100 mm on each side. The interior is filled with a commercially available liquid scintillator (discussed in Section 6) that acts as a beam energy absorber and propagating medium. The beam enters through an air-filled 15 mm diameter cylindrical entrance window that is sealed with a 50 μm Kapton® (polyimide) foil. The foil has a dual role; it acts as both a boundary to avoid spillage of the liquid as well as cuts protons with energies less than 2.1 MeV.

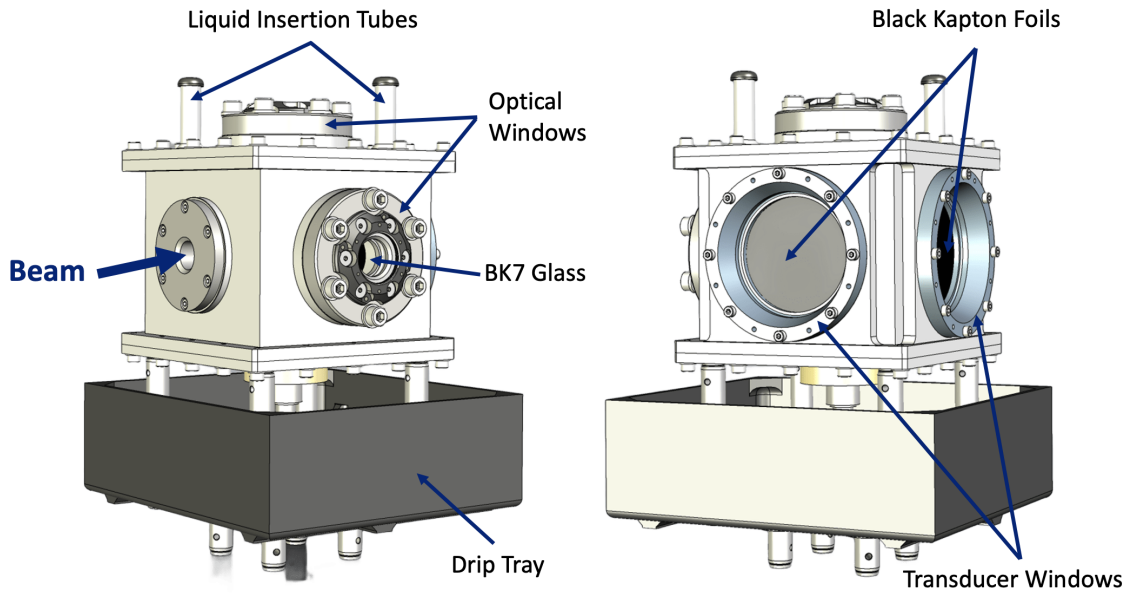


Figure 9: Computer-Aided Design of the final version of the SmartPhantom, evaluated at the LION beamline, featuring four windows for mounting the optical and acoustic systems. Left: front view. Right: near view.

Several acoustic and optical windows are incorporated into the design to allow the detection of various types of signals. The design features four windows: two for mounting optical systems and two for mounting acoustic transducers. Each optical window consists of a 5 mm thick BK7 glass window and a flange to secure the optical components [63].

The optical windows are positioned perpendicular to one another, for imaging at two different angles, with one capturing the scintillation light from the top and the other from the side. The two transducer windows are also positioned orthogonally, on two of the remaining sides: one directly opposite to the entrance window and the other one opposite to the side glass window. Notably, the transducer windows are significantly larger than those designed for the optical systems due to the large surface area of the transducers to be mounted. The choice of transducers is discussed later in Chapter 5. In addition, the transducer windows are sealed with black Kapton foils to minimize any internal reflections of scintillation light, and for the same reason, the entire detector was anodised black.

A drip tray was incorporated into the design to collect any liquid that might drip from the detector—a possible scenario as the transducers would push hard against the Kapton foil. The capacity of the tray was over 1 liter to ensure that all the liquid could be collected in case of a major leak. Lastly, the top lid features two vertical tubes that enable the liquid scintillator to be inserted into the detector. These tubes enable the entire volume to be completely filled, preventing any air gaps between the liquid scintillator and the glass window, which could introduce reflections or refraction issues.

In addition, custom-designed transducer housings were 3D-printed to hold and secure the transducers perpendicularly to their respective windows. Two separate housings were made, one for each transducer, with their inner surface shaped to match the transducers' contours, obtained from 3D-scans. The external mounting of the transducers enables in-

terchangeable use, simply by swapping and mounting them onto a different window. In addition, the screws within the housings allow the transducers to be fixed firmly in all degrees of freedom, ensuring precise fit. This would minimize transducer movement thereby reducing the risk of damage. Lastly, a hole was introduced at the bottom of the SmartPhantom to mount one of the transducers (Olympus V303), allowing it to be immersed into the liquid scintillator. Figure 10 shows the CAD model of the SmartPhantom, with the integrated optical systems, transducer housings and immersion transducer.

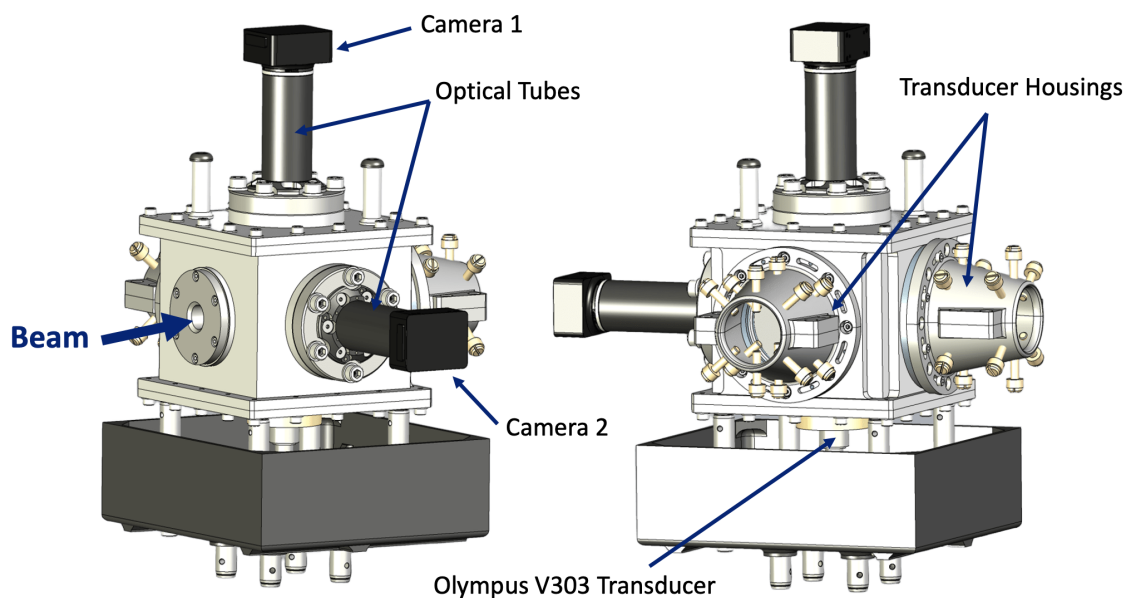


Figure 10: Computer-Aided Design of the final version of the SmartPhantom, featuring the optical systems and the transducer housings attached onto the designated windows, along with the Olympus V303 transducer secured at the bottom.

Lastly, the interior of the SmartPhantom is displayed in Figure 11. The left and middle sections of the figure show the entrance window, which extends to approximately the center of the SmartPhantom, where the scintillating fibre detectors are mounted. The right hand side of the figure displays the entrance window with the scintillating fibre detectors

removed, showing only their attachment flange and revealing the configuration used when the SmartPhantom volume is filled with the liquid scintillator.

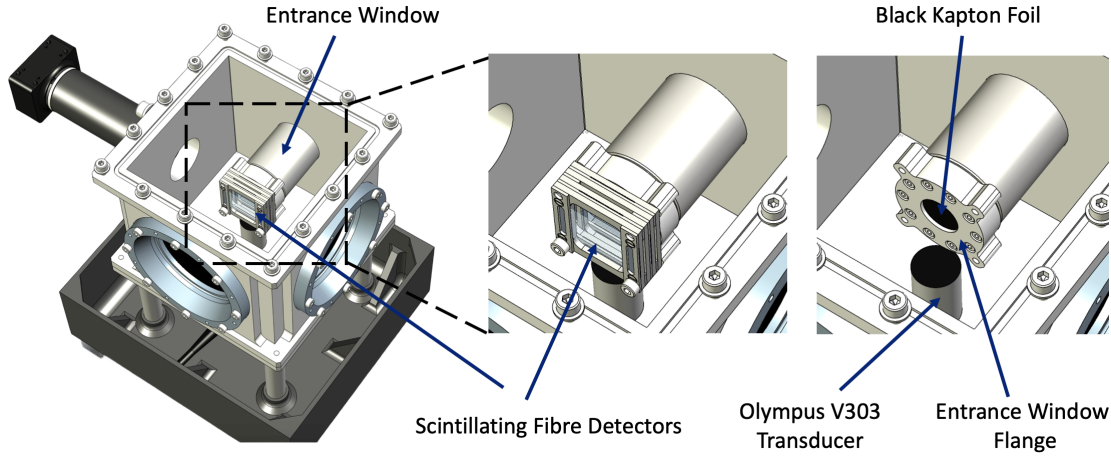


Figure 11: Computer-Aided Design of the interior of the SmartPhantom. Left and middle: entrance window with the scintillating fibre detectors attached. Right: entrance window without the scintillating fibre detectors, featuring only the attachment flange.

Detector Evaluation

An ion accelerator is required to test and evaluate the proposed detector. The ideal accelerator should share similar characteristics to LhARA, such as accelerating a bunch of protons via the TNSA mechanism, with comparable pulse length and repetition rate. In addition, the accelerator should offer pulse durations that enable the generation of acoustic signals. For these reasons, the Laser-driven Ion (LION) accelerator at the Centre for Advanced Laser Applications (CALA) has been selected [9].

Chapter 4

LION Beamline

The LION accelerator was simulated using the Beam Delivery Simulation (BDSIM) software [9] [11]. The software tracks particles through the various beamline elements, extracting valuable information about the beam's properties. This information is useful for determining the beam characteristics of particles reaching the detector, understanding the expected energy depositions in the scintillating fibre detectors and the liquid scintillator, and characterizing the generated acoustic signal. Exploring this information through simulation can help design and optimize the acoustic and optical detection systems. In addition, BDSIM accounts for the materials in the accelerator. This capability enables the production and tracking of secondary particles, which can be used to investigate background radiation and potential damage to the accelerator's elements, electronics or the detector.

4.1 Particle Source

The LION facility generates a bunch of protons using the TNSA mechanism. The particle source is powered by a high-intensity 2.5 PW Ti:Sa ATLAS 3000 (Advanced Titanium-Sapphire Laser) laser, operating at a maximum repetition rate of 1 Hz [64]. This laser can deliver pulses up to 25 fs in duration and 60 J of energy. Several analytical equations have been used to simulate the particle distribution at the source, incorporating the laser and foil target specifications. The energy spectrum and angular distribution of the proton bunch have been parameterized separately.

4.1.1 Source Energy Spectrum

As explained in Section 3.1, when a laser with focal spot r_0 irradiates a thin foil target with thickness d , the electrons inside the foil are accelerated and spread within the foil at a divergence angle θ . When the electrons reach the rear side of the foil, they occupy a circular area of radius B and mean density n_{e0} . An electric field is therefore set up which ionizes and accelerates the particles on the rear side normal to the foil.

To parametrize the energy spectrum of the particles emerging from the laser-target interaction, an analytical equation, based on existing isothermal, time-limited fluid models, has been used. The analytical approximation is defined in Equation 4.1, where N is the number of ions per unit solid angle and ϵ is the ion kinetic energy. All the variables present, with associated units, are listed in Table 5 [57].

$$\frac{dN}{d\epsilon} = \frac{n_{e0} c_s t_{laser} S_{sheath}}{\sqrt{2\epsilon T_e}} \exp\left(-\sqrt{\frac{2\epsilon}{T_e}}\right) \quad (4.1)$$

The ions which are accelerated by this mechanism have a cut-off energy due to the limited laser intensity, pulse duration, limited electric field strength and laser-plasma instabilities [65]. The parametrisation above assumes unlimited (electron) acceleration and hence a different model should be used for the cut-off energy. For this, the Schreiber model has been used, which assumes that only some of the electrons are heated up to the hot electron temperature, T_e , and not the entire target. According to this model, the cut-off energy, ϵ_{max} , can be calculated using Equation 4.2, where $\epsilon_{i,\infty}$ is the maximum energy and X is obtained by solving Equation 4.3 [65].

$$\epsilon_{max} = X^2 \epsilon_{i,\infty} \quad (4.2)$$

$$\frac{t_{laser}}{t_0} = X(1 + \frac{1}{2} \frac{1}{1 - X^2}) + \frac{1}{4} \ln \frac{1 + X}{1 - X} \quad (4.3)$$

A third-order Taylor expansion is used to calculate X , with the result shown in Equation 4.4. All parameters present in Equations 4.1, 4.2, 4.3 and 4.4, with associated units, are listed in Table 5, and are based on the laser and foil target specifications of the LION beamline. Using these specifications, the cut-off energy is calculated to be 26.38 MeV.

$$X = \tanh \frac{t_{laser}}{t_0} \quad (4.4)$$

Table 5: Parameters present in the TNSA analytical Equations 4.1, 4.2, 4.3 and 4.4.

Parameter	Definition	Value	Unit
N	Ion number	-	-
ε	Ion energy	-	J
n_{e0}	Hot electron density	$\frac{N_E}{ct_{laser} S_{sheath}}$	pp/m^3
N_e	Accelerated electron number	$\frac{f E_{laser}}{T_e}$	-
E_{laser}	Laser energy	70	J
f	Energy conversion efficiency	$1.2 \times 10^{-15} I^{0.75}$, max=0.5	-
I	Laser intensity	4×10^{20}	W/cm^2
T_e	Hot electron temperature	$m_e c^2 [\sqrt{1 + \frac{I \lambda^2}{1.37 \times 10^{18}}} - 1]$	keV
m_e	Electron mass	9.11×10^{-31}	Kg
c	Speed of light	3×10^8	m/s
λ	Laser wavelength	0.8	μm

t_{laser}	Laser pulse duration	28×10^{-15}	s
B	Radius of electron bunch	$B = r_0 + d \tan(\theta)$	m
S_{sheath}	Electron acceleration area	πB^2	m^2
r_0	Laser spot radius	$\sqrt{\frac{P_{laser}}{I\pi}}$, I in W/m^2	m
d	Target thickness (plastic foil)	$400 - 600 \times 10^{-9}$	m
θ	Electron half angle divergence	0.436	rad
P_{laser}	Laser power	2.5×10^{15} , $P_{laser} = \frac{E_{laser}}{t_{laser}}$	W
c_s	Ion-acoustic velocity	$(\frac{Zk_B T_e}{m_i})^{\frac{1}{2}}$	m/s
Z	Ion charge number	1	-
k_B	Boltzmann constant	1.380649×10^{-23}	$m^2 kg s^{-2} K^{-1}$
m_i	Proton mass	1.67×10^{-27}	Kg
P_R	Relativistic power unit	$\frac{m_e c^2}{r_e} = 8.71 \times 10^9$	W
r_e	Electron radius	2.82×10^{-15}	m
$\varepsilon_{i,\infty}$	Maximum ion energy	$2Zm_e c^2 \sqrt{\frac{f P_{laser}}{P_R}}$	MeV
t_0	Ballistic time	$\frac{B}{v(\infty)}$	s
$v(\infty)$	Ballistic velocity	$\sqrt{\frac{2\varepsilon_{i,\infty}}{m_i}}$	m/s

A Monte Carlo algorithm was written in Python [10] to generate particles whose energy distribution follows the equations outlined above, using the 'accept-reject', or, Von Neumann method [66]. A random number y is generated between zero and the maximum value given by Equation 4.1 and another number x is generated between 0 and ε_{max} . If y is less than or equal to $p(x)$, where p is the function defined by Equation 4.1, the value is accepted. This process is repeated until a distribution with enough particles is formed. Figure 12 shows a plot of the theoretical equation and the energies generated by the algorithm.

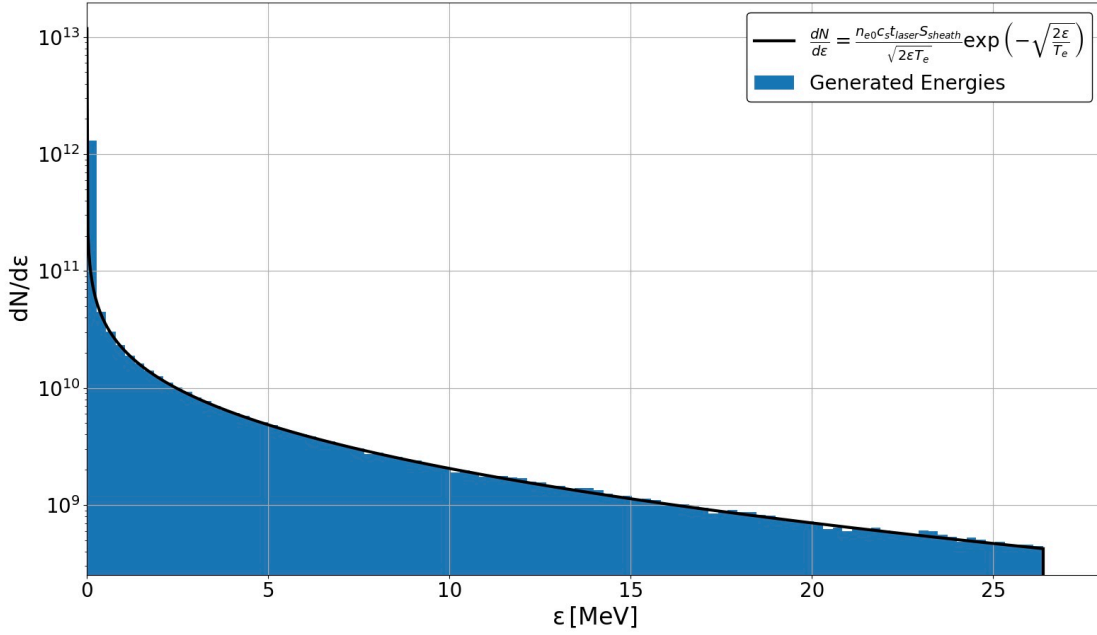


Figure 12: Parametrised energy distribution of the laser-driven protons generated at the LION beamline source, based on the specific laser and foil target parameters listed in Table 5. The solid black line represents Equation 4.1 and the blue area is a histogram of the generated spectrum.

The energy distribution of the particles follows an exponential shape, which can be explained by the electric field established during the process. Due to the thermal distribution of the accelerated electrons, discussed later in Section 4.1.2, the resulting electric field also follows the same distribution. Consequently, the electron sheath decays exponentially with distance from the target, leading to the accelerated ions gaining energies following the exponential spectrum. In addition, the broadness of the distribution can be understood by the variations of the electric field in the radial and longitudinal directions. Ions found at different depths experience different ionization and acceleration strengths.

4.1.2 Source Angular Distribution

The source angular distribution of the ions is approximated by a Gaussian distribution, with ions emitted in a cone centred normal to the target surface. Research suggests that the opening angle of the cone is energy-dependent, starting from a higher value for low ion energies, decreasing almost linearly to a smaller value at the cut-off energy [38]. This implies that higher-energy particles are less divergent than lower-energy particles.

For the simulation, a maximum divergence angle of 20 degrees is assumed for the low-energy ions, which linearly decreases to 5 degrees at the cut-off energy [38]. Thus, to generate the Gaussian distribution, the standard deviation, σ , is calculated using Equation 4.5.

$$\sigma = 15 \times (20 - (\epsilon_{max} - \epsilon)) \quad (4.5)$$

The maximum divergence angle for each particle is determined based on the energy provided by the parametrized energy distribution described in Section 4.1.1. Figure 13 shows the generated envelope divergence angles used for the parametrization, with the generated data compared to the theoretical Equation 4.5. A Gaussian distribution with a width corresponding to that angle is used to generate a random divergence (polar) angle, θ , for each particle. In addition, the azimuthal angle, ϕ , is randomly generated from a uniform distribution between 0 and 2π . The process is repeated for all particles in the beam to create the spectrum. Figure 14 shows the histograms of the spherical polar coordinate angles used to generate the parametrised beam distribution.

The spatial distributions along the x and y dimensions are assumed to be independent. A FWHM diameter of 10 μm was selected, consistent with values reported in the literature

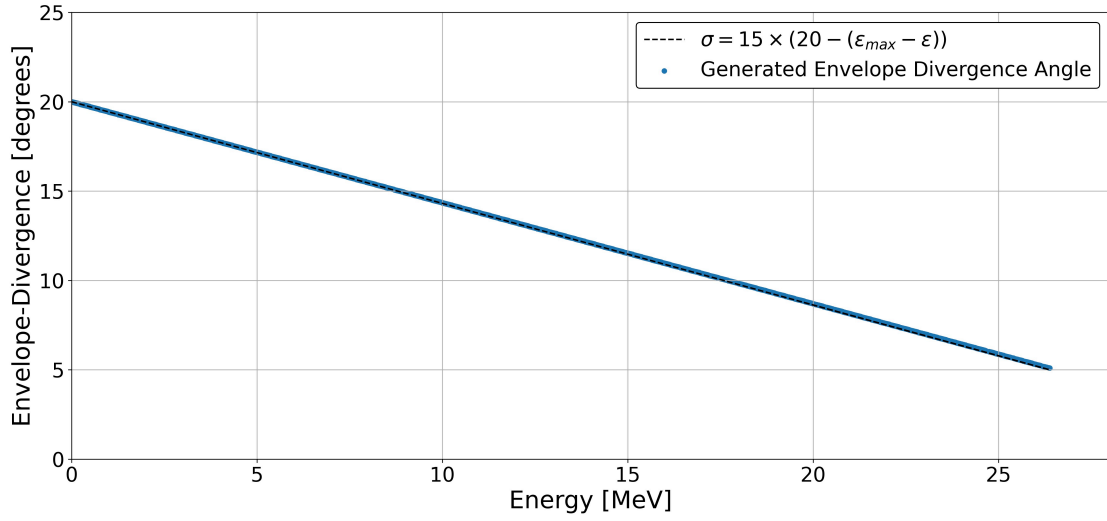


Figure 13: Comparison of the generated envelope divergence angles for the parameterized angular distribution of the LION beamline source (blue) with the theoretical linear relationship described in Equation 4.5 (black).

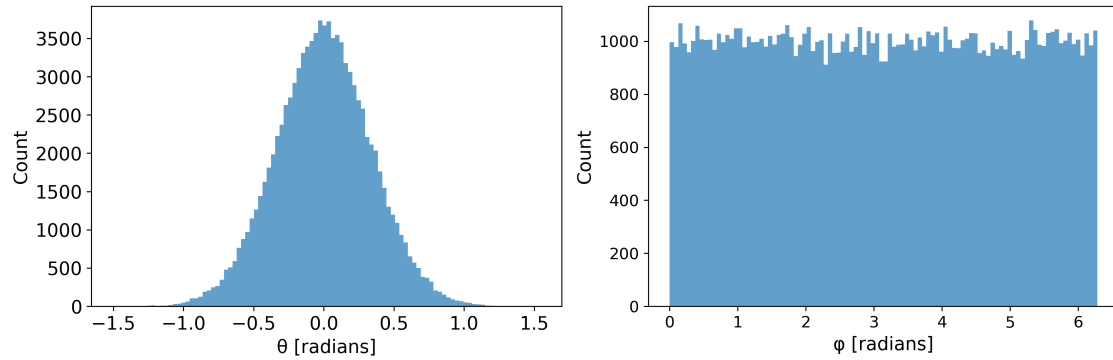


Figure 14: Histograms of the divergence angle (left), generated from a Gaussian distribution, and the azimuthal angle (right), uniformly distributed between 0 and 2π , representing the parametrized angular distribution of 100000 particles at the LION beamline source.

[59]. The two-dimensional cross-section of the parametrised beam is shown in Figure 15.

The absolute momentum of each particle is calculated using Equation 4.6, where E is the energy given by the energy distribution function and m is the rest mass of the particle. Subsequently, the momentum components along each axis are calculated in spherical polar

coordinates using Equations 4.7 - 4.9.

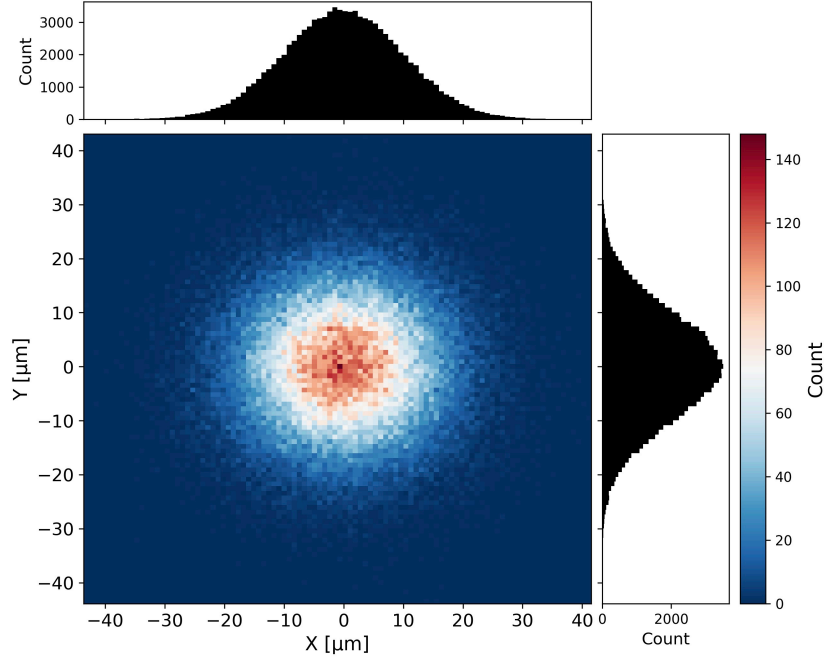


Figure 15: Two-dimensional cross-section of the LION beamline parametrised beam consisting of 1 million particles. The simulated distribution is symmetric, with a Gaussian profile that has a FWHM diameter of 10 μm .

$$E = \frac{\mathbf{p}^2}{2m} \text{ [MeV/c]} \quad (4.6)$$

$$p_x = \mathbf{p} \sin(\theta) \cos(\phi) \quad (4.7)$$

$$p_y = \mathbf{p} \sin(\theta) \sin(\phi) \quad (4.8)$$

$$p_z = \mathbf{p} \cos(\theta) \quad (4.9)$$

4.2 Quadrupole Doublet

The LION beamline primarily consists of a quadrupole doublet made up of two Permanent Magnet Quadrupoles (PMQs). When a particle with charge e moves through a

magnetic field $\mathbf{B} = (B_x, B_y, 0)$ propagating in the z -direction with velocity $\mathbf{v} = (v_x, v_y, v_z)$, it experiences the Lorentz force $F_x = -ev_z B_y(x, y, z)$ in the horizontal plane and the Lorentz force $F_y = -ev_z B_x(x, y, z)$ in the vertical plane. In addition, it experiences the centrifugal force, $F = \gamma m v_z^2 / R(x, y, z)$, where γ is the Lorentz factor and $R(x, y, z)$ is the radius of curvature [67]. For a stable orbit, these Lorentz forces must be in equilibrium, leading to Equation 4.10, where p is the particle's momentum.

$$\frac{1}{R(x, y, z)} = \frac{e}{p} B_{x,y}(x, y, z) \quad (4.10)$$

A Taylor expansion of this formula in the x -direction, shown in Equation 4.11, reveals the various magnetic field components that contribute to the particle's trajectory. In this equation, k_1 corresponds to the dipole magnetic field strength and k_2 corresponds to the quadrupole magnetic field strength.

$$\frac{e}{p} B_y(x) = \frac{e}{p} B_y + \frac{e}{p} \frac{dB_y}{dx} x + \frac{e}{p} \frac{1}{2} \frac{d^2 B_y}{dx^2} x^2 + \dots = \frac{1}{R} + k_1 x + \frac{1}{2} k_2 x^2 + \dots \quad (4.11)$$

$$k_1 = \frac{e}{p} \frac{dB_y}{dx} [m^{-2}] \quad (4.12)$$

$$k_2 = \frac{e}{p} \frac{1}{2} \frac{d^2 B_y}{dx^2} [m^{-2}] \quad (4.13)$$

Examining the magnetic field lines of a typical quadrupole, shown in Figure 16, it is evident that the Lorentz force causes focusing in one plane and defocusing in the other [68]. Therefore, to achieve a net focusing of the beam, two quadrupoles must be placed perpendicular to each other. Such system is usually referred to as a Focusing Optic Defocusing Optic (FODO) cell [69].

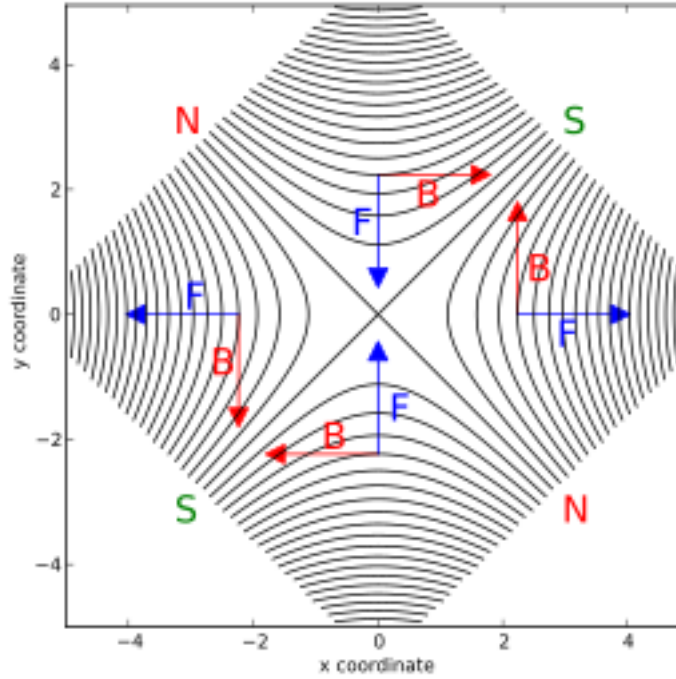


Figure 16: Sketch of the magnetic field lines within a quadrupole magnet. The blue arrows illustrate the Lorentz force, indicating a focusing effect in the x-plane and a defocusing effect in the y-plane [68].

In the LION beamline, two PQMs are arranged orthogonally to form a quadrupole doublet and magnetically focus the beam into a small spot size. The first quadrupole has a length of 40 mm and an effective gradient of 332 T/m, while the second quadrupole has a length of 20 mm and an effective gradient of 318.5 T/m. Both magnets have a 10 mm bore diameter and an overall diameter of 50 mm [70]. Due to the energy dependence in the Equations 4.11 - 4.13, particles with varying kinetic energies are focused at different focal points, giving rise to chromatic effects.

4.3 Configuration

The LION beamline configuration is optimized to increase the particle fluence and transport more particles in a high-intensity pulse. To focus a specific beam energy downstream, the quadrupole drifts are adjusted using motorized stages.

To achieve a proton beam with a modal energy of 20 MeV, the drift lengths have been determined as follows: 60.34 mm from the source to the first quadrupole, 55.77 mm between the two quadrupoles, and 1728.59 mm from the last quadrupole to the focus. This combination of drift lengths ensures the focal spot occurs inside the SmartPhantom, a pre-clinically relevant energy at which a significant Bragg peak can be obtained.

Due to the limited aperture of the quadrupoles, not all particles generated at the source are able to pass through and be transported along the beamline. Particles that reach the bore of the magnets can cause severe damage. To prevent this, an elliptical aluminium shielding plate is introduced at the front, with several apertures available in various dimensions. The appropriate plate is selected, based on the modal energy to be focused, ensuring that most particles can pass through both quadrupoles and provide radiation protection. The selected collimator, with indicated dimensions, is shown in Figure 17.

The beamline, extending from the source to the exit window, operates in vacuum. After the exit window, the particles travel through air towards the detector. The LION beamline exit window consists of a 50 μm Kapton foil. Since Kapton is partially transparent, an additional 12 μm aluminium foil is placed behind it to stop any unwanted electromagnetic radiation coming from source-generated electrons and bremsstrahlung, discussed later in Section 4.5 [71]. This combination of foils effectively stops protons up to 2.1 MeV.

To decrease the phase space, a collimator is placed after the exit window and before

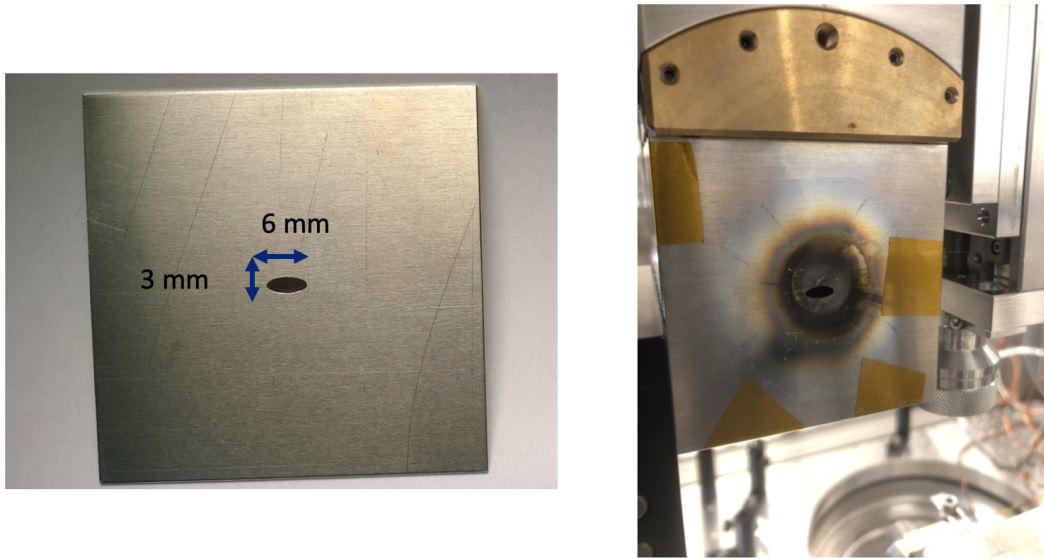


Figure 17: Elliptical aluminium collimator used for shielding to ensure radiation protection for the quadrupole magnets. The specific aperture size is selected for focusing a proton beam with a nominal energy of approximately 20 MeV.

the SmartPhantom. For the simulations, an aluminium collimator with a 3 mm circular aperture was chosen that is 5 mm thick. The collimator not only cuts the width of the beam but also eliminates the lower and higher energy particles that are not focused at the center on the focal spot. The BDSIM simulation of the LION beamline is shown in Figure 18. The simulation has been split in two: the vacuum section and the air section.

Figure 19 illustrates the particle depletion as a function of distance travelled in the vacuum section (top) and the air section (bottom) of the accelerator. As can be seen from the graph, out of the initial 1 million protons generated at the source, only around 35 thousand reach the SmartPhantom. A significant number of particles are lost at the first collimator due to the enforced physical acceptance. Additional losses occur as particles transverse the first and second quadrupoles. This is because particles with different momenta have different focal lengths in the transverse plane and therefore are lost inside the chamber

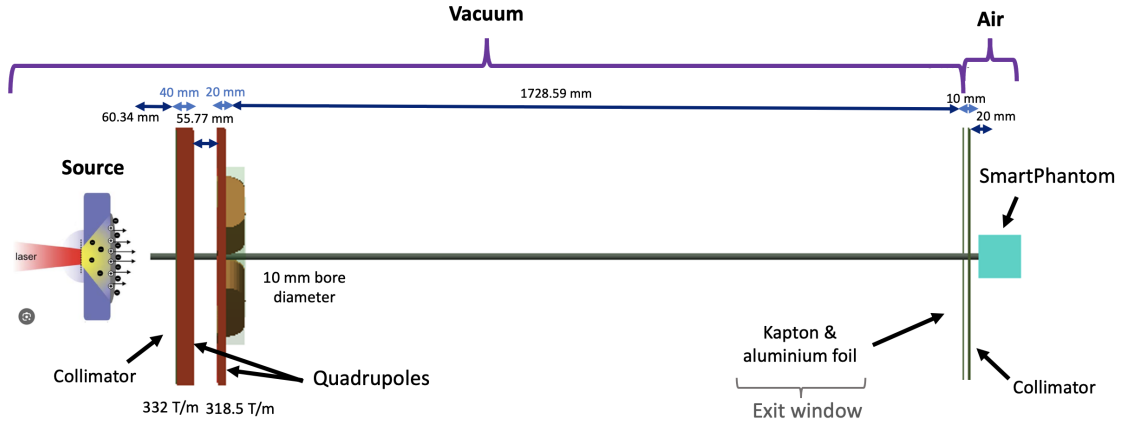


Figure 18: Annotated diagram of the LION beamline simulated in BDSIM, showing the accelerator elements and their drifts designed to focus a beam with a modal energy of approximately 20 MeV.

before reaching the SmartPhantom. Furthermore, many particles are lost at the second collimator, located after the exit window, because of the physical acceptance that reduces the phase space and eliminates low-energy particles found at the beam's outer radius.

4.4 PMQ Focus

The BDSIM simulation was run multiple times to ensure that around 1 million protons enter the SmartPhantom. The energy spectrum of the particles, after transversing all the accelerator elements, is shown in Figure 20. As can be seen from the plot, the beam entering the SmartPhantom has a modal energy of 20.43 MeV and an energy spread of around 1.52 MeV.

Figure 21 shows a two-dimensional histogram of the spatial distribution of the particles, with the colour bar indicating the particle count in each bin. As shown in the figure, there is a higher particle concentration in the central region which decreases towards the edges, as expected for a quadrupole doublet-focused beam. In addition, the shape of the beam

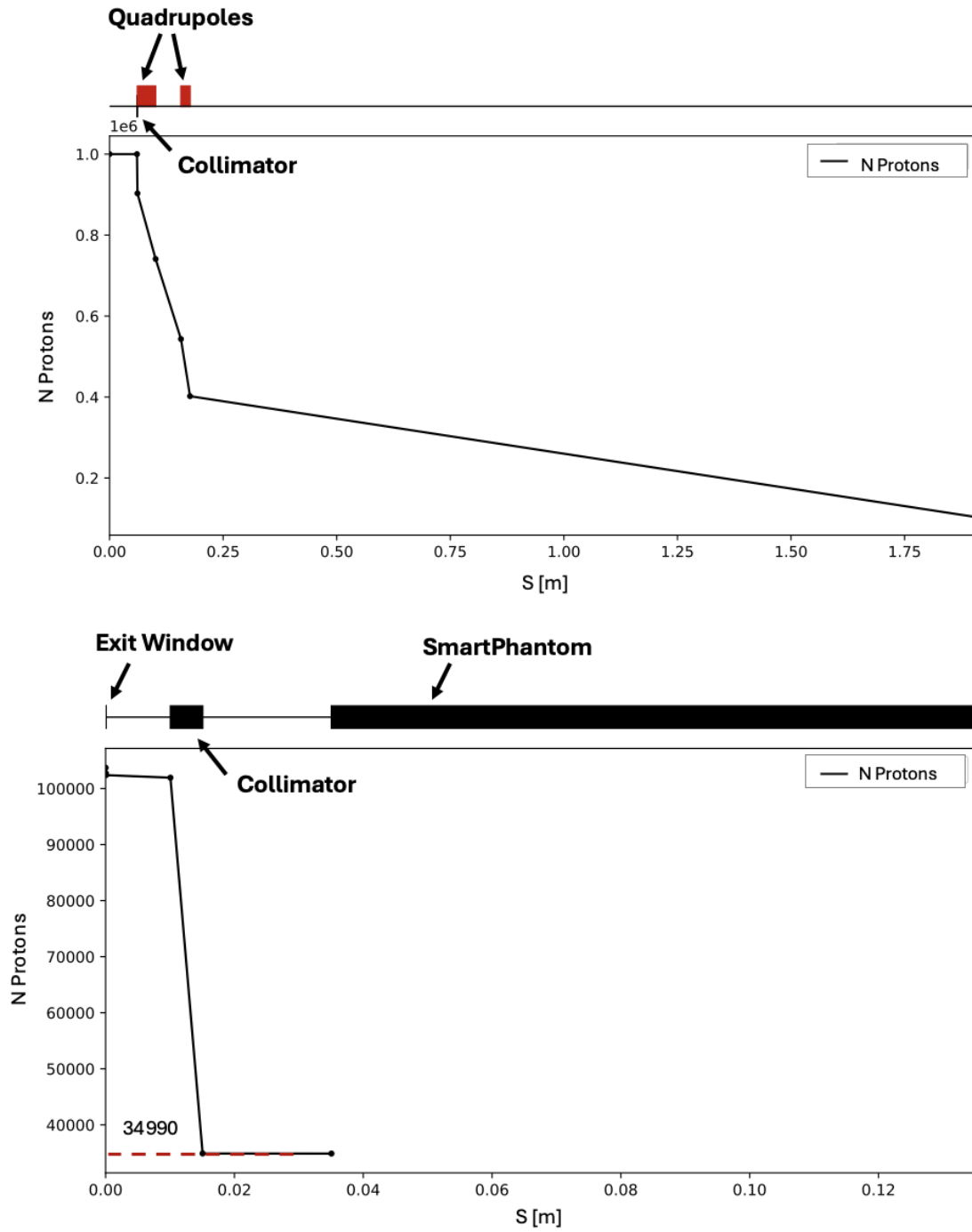


Figure 19: Proton depletion as a function of distance when the parametrised particles at the laser-driven source of the LION beamline propagate through the beamline elements. Vacuum section (top) and air section (bottom).

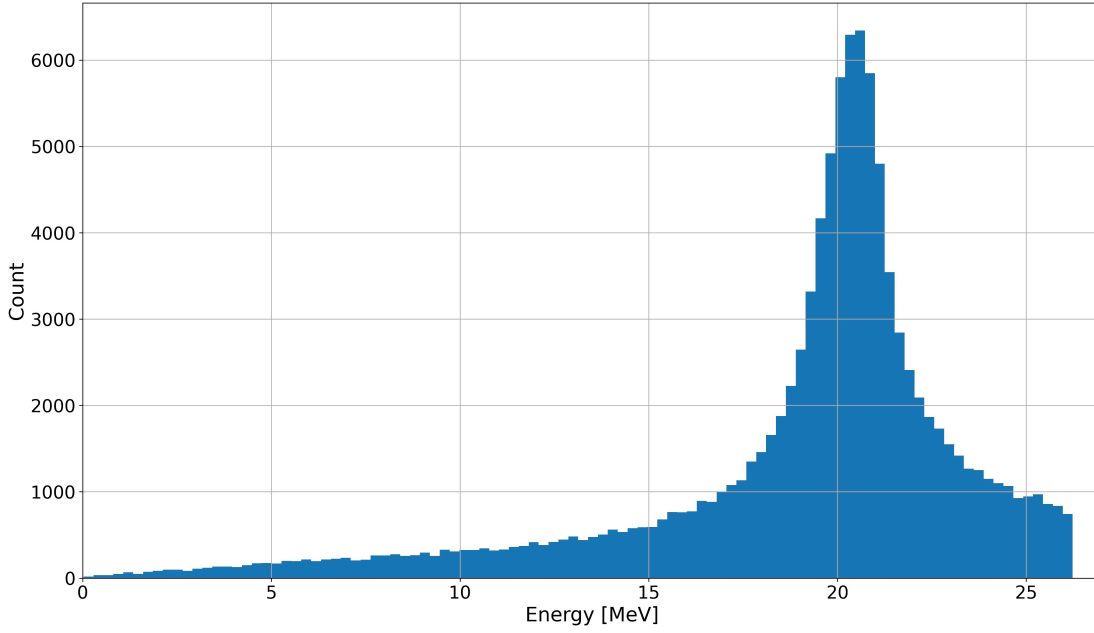


Figure 20: Histogram of the final energy spectrum of the particles after passing through all accelerator elements in the LION beamline and focused onto the SmartPhantom. The peak energy is approximately 20.43 MeV.

appears elliptical, with a FWHM of 0.77 mm and 0.39 mm along each axis and a total diameter of around 2 mm.

4.5 Electron Background

The interactions between the plasma formed when a high-intensity laser strikes a solid target and subsequent laser pulses can lead to the generation of "hot" electrons [72]. These electrons contribute to radiation noise, disrupting or damaging nearby devices. To understand this noise and take radiation protection measures, the energy and angular distribution of these electrons was parametrised using analytical equations, following a similar approach to the proton spectra described above. Their propagation through the LION beamline and subsequent energy depositions in the SmartPhantom were simulated.

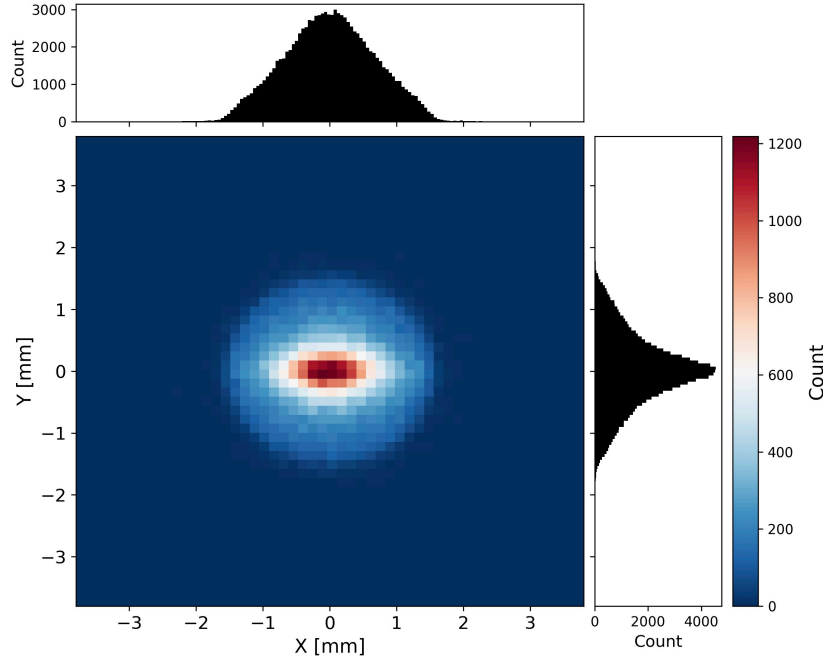


Figure 21: Two-dimensional histogram of the spatial distribution of particles at the LION beamline focus for a nominal beam energy of 20.43 MeV. The focused beam has a FWHM of 0.77 mm and 0.39 mm along each axis and a total diameter of approximately 2 mm.

The energy distribution of "hot" electrons can be described by a Maxwellian distribution, shown in Equation 4.14. In this equation, E is the electron energy and T_h is the hot electron temperature that is calculated using Equation 4.15, where I is the laser intensity [72]. Based on the intensity of the laser used at the LION facility, displayed in Table 5, the hot electron temperature is calculated to be around 6.53 MeV. The parametrised energy distribution of 100000 hot electrons produced at the source of the LION beamline, is shown in Figure 22. The modal energy of the electrons is around 3.24 MeV.

$$f(E) \sim E^{1/2} \exp\left[\frac{-E}{T_h}\right] \quad (4.14)$$

$$T_h = 1.05 \times 10^{-10} I^{0.514} \quad (4.15)$$

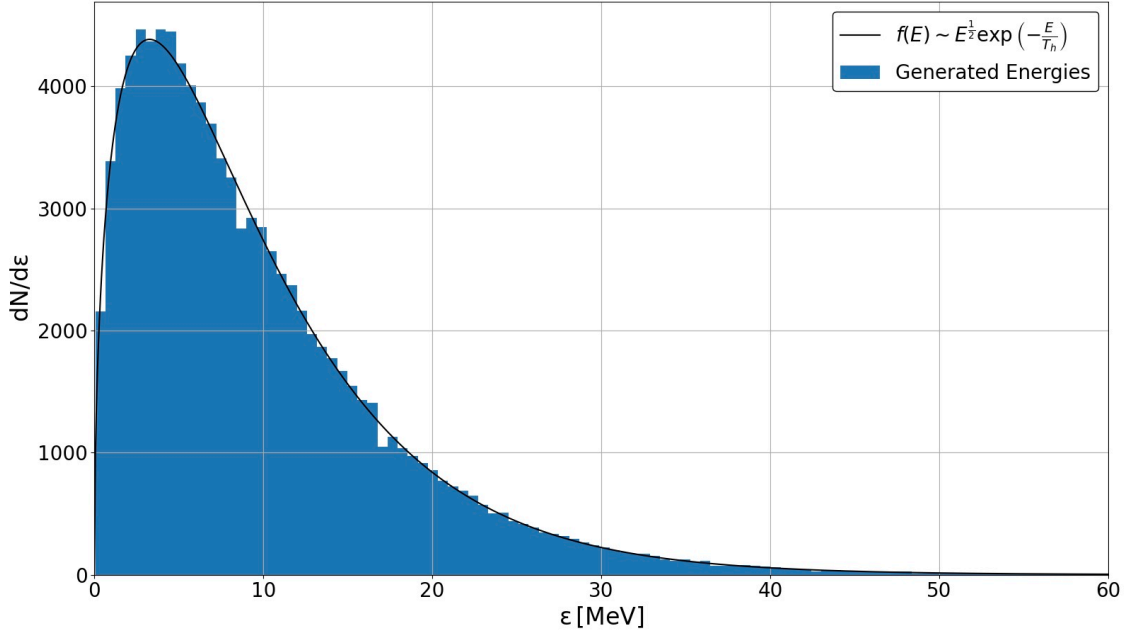


Figure 22: Parametrised energy distribution of the laser-driven electrons generated at the LION beamline source. The solid black line represents Equation 4.14 and the blue area is a histogram of the generated spectrum of 100000 electrons.

The angular distribution of "hot" electrons is parametrised by a Gaussian shape, following Equation 4.16 [72]. A standard deviation, σ , of 45 degrees is used and the emission angle, θ , is determined using Equation 4.17, where γ is the Lorentz factor [72]. Figure 23 shows the parametrised angular distribution of 100000 electrons at the LION beamline source. The azimuthal angle has been uniformly distributed between 0 and 2π .

$$f(\theta) \sim \exp\left[-\frac{\theta^2}{2\sigma^2}\right] \quad (4.16)$$

$$\theta = \tan^{-1} \sqrt{\frac{2}{\gamma - 1}} \quad (4.17)$$

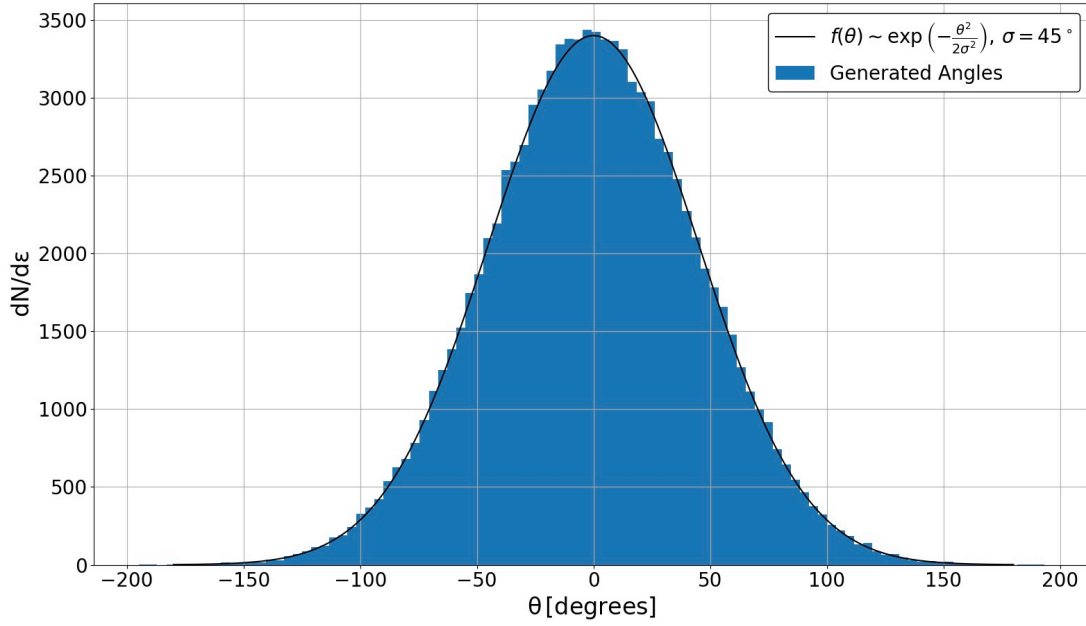


Figure 23: Histogram of the electron divergence angle distribution generated using Equation 4.16, showing 100 thousand electrons at the LION beamline source.

For the simulation, it is assumed that one electron is produced per proton in the TNSA interaction. However, the proportion of electrons emitted in the forward direction is determined using Equation 4.18, with the value calculated to be around 98.2% [72]. Therefore, the BDSIM simulation was run with 928000 electrons at the source. The simulation indicated that 21.5% of those could enter the SmartPhantom, with a modal energy of approximately 2.73 MeV.

$$r(I) = 2.8 \times 10^{-9} I^{0.49} \quad (4.18)$$

Taking into account the percentage yield of protons and electrons through the beamline, the 1:1 production ratio at the source and the proportion of electrons emitted in the forward direction, the number of electrons entering the SmartPhantom is calculated to be

approximately 650000. These electrons deposit energy in the detector, potentially contributing to noise or the generation of weak acoustic and optical signals. The time-of-flight plot, shown in Figure 24, reveals that electrons reach the detector earlier than protons. Therefore, care should be taken in the experimental data analysis to eliminate their effect.

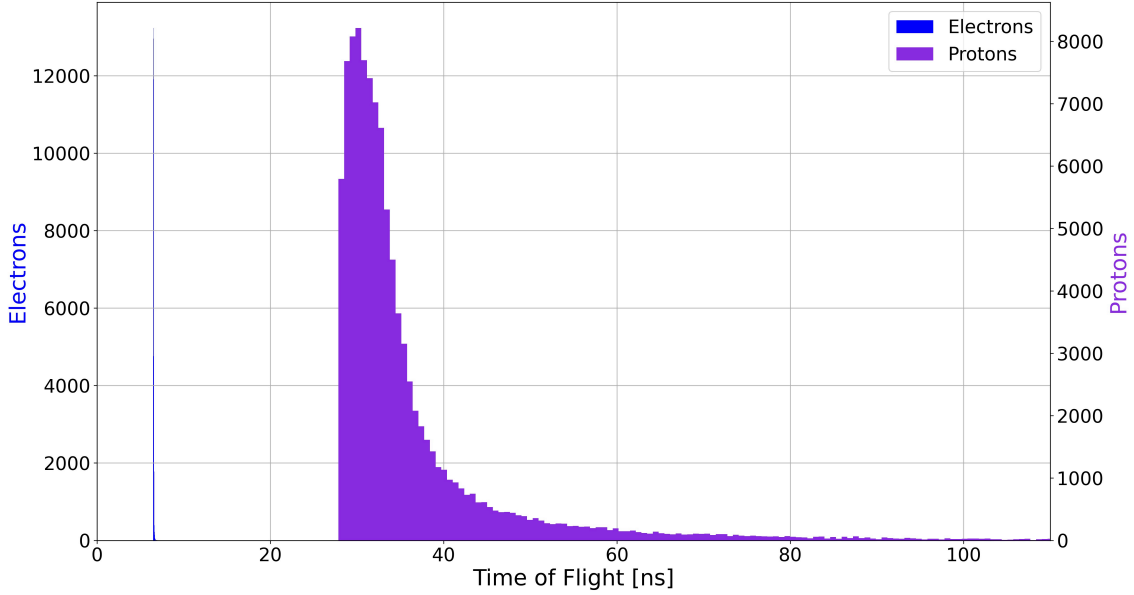


Figure 24: Time-of-flight distributions for source-generated protons (purple) and electrons (blue) as they propagate through the LION beamline.

4.6 Electromagnetic Pulse & Bremsstrahlung

In addition to the noise arising from the electrons produced by TNSA, there is another form of electromagnetic radiation known as electromagnetic pulse (EMP) [72]. EMP is a burst of electromagnetic energy that is typical for laser-driven accelerators. EMP can originate from various sources, including cables or electrons being ejected from the target, which then create changing currents and charge separations. This type of radiation is hazardous and can potentially disrupt or damage electronic devices. Unfortunately, EMP is challenging to define precisely and is an area of active research.

Another type of radiation emitted by this acceleration mechanism is bremsstrahlung [71]. Bremsstrahlung radiation occurs when particles interact with atomic nuclei or electrons in a solid, causing changes in their velocity. The energy lost during the acceleration or deceleration is emitted as electromagnetic radiation in the form of photons (x-rays). The energy spectrum of bremsstrahlung x-rays is continuous and spans a wide range of energies. The intensity of this radiation typically scales with the number of laser shots and the laser intensity. Given that the SmartPhantom is located approximately 2 meters away from the second quadrupole and that the entrance window has a small diameter, any x-rays entering will be extremely weak and of low flux.

Chapter 5

Ion-Acoustic Signal

The energy depositions caused by the passage of the particles in the SmartPhantom have been simulated. Multiple acoustic transducers, positioned at various locations, have been modelled and the characteristics of the acoustic signal have been determined. The signals obtained were used to reconstruct the (relative) three-dimensional dose distribution, accounting for the sensors' geometry, electronic noise and frequency response.

5.1 SmartPhantom

To understand the energy depositions of the incoming particles inside the SmartPhantom, a detailed simulation has been developed in Geant4, a software that uses stochastic Monte Carlo techniques to simulate the passage of particles through matter [12]. The annotated diagram of the Geant4 simulation of the SmartPhantom is shown in Figure 25. The SmartPhantom is a cuboid with an internal volume of 10 cm x 10 cm x 10 cm enclosed by 5 mm thick aluminium walls. It features an elongated air-filled entrance window sealed with a Kapton (polyamide) foil, with multiple windows around the aluminium frame to allow optical and acoustic measurements. The detailed design is discussed later in Section 8.

5.1.1 Energy Depositions

To examine the impact of the liquid scintillator on the energy depositions, three simulations were run: the entire volume filled with water, a 50-50 mixture of water and liquid scintillator and 100% liquid scintillator. The choice of the scintillating liquid is discussed later in Chapter 6. Given the complexity of organic molecules, the dominant compound, 2,6-

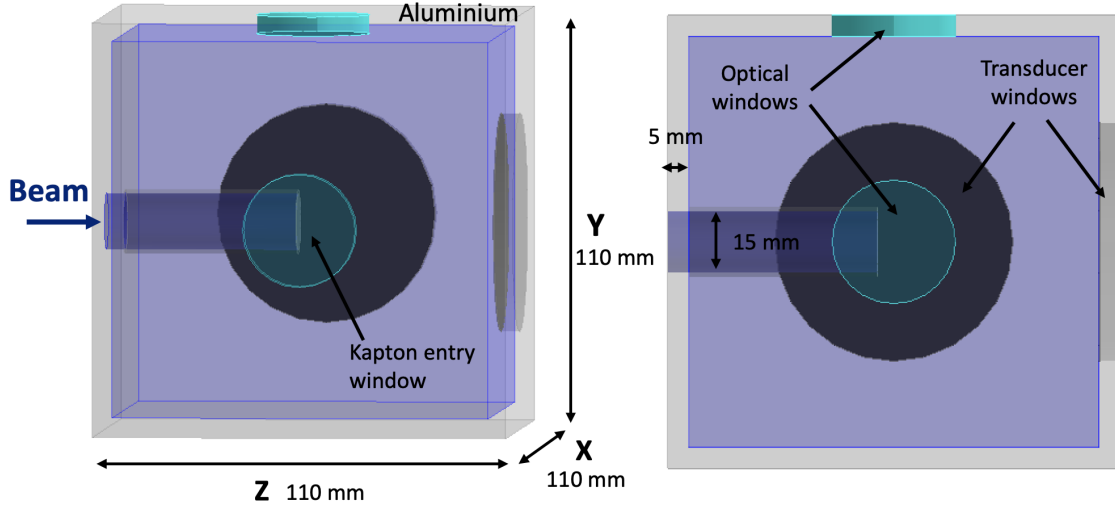


Figure 25: Geant4 simulation of the SmartPhantom. Angled view (left), cross-section view (right). The beam, given by the BDSIM simulation, is incident from the left.

Diisopropylnaphthalene (2,6-DIPN), has been used for the simulation, which corresponds to a material with stoichiometry $C_{16}H_{20}$.

The Geant4 simulation has been split into 0.1 mm cubic voxels and the energy depositions of the particles have been written in a three-dimensional matrix. The size of the voxels has been chosen so that the grid spacing is at least 4 grid points per shortest acoustic wavelength for a reasonable reconstruction accuracy. Figure 26 shows a comparison of the energy depositions caused by 1 million protons along the three orthogonal axes for each liquid. From the graph, it can be seen that there is minimal impact on the deposited-energy distribution, with only around 1.5% variation in the range between water and the liquid scintillator. Due to this, and light scattering observed when a water-scintillator mixture is used (discussed in Section 6.4), 100% liquid scintillator has been chosen to fill the entire volume of the SmartPhantom.

Figure 27 shows the energy depositions in each plane caused by the passage of the proton

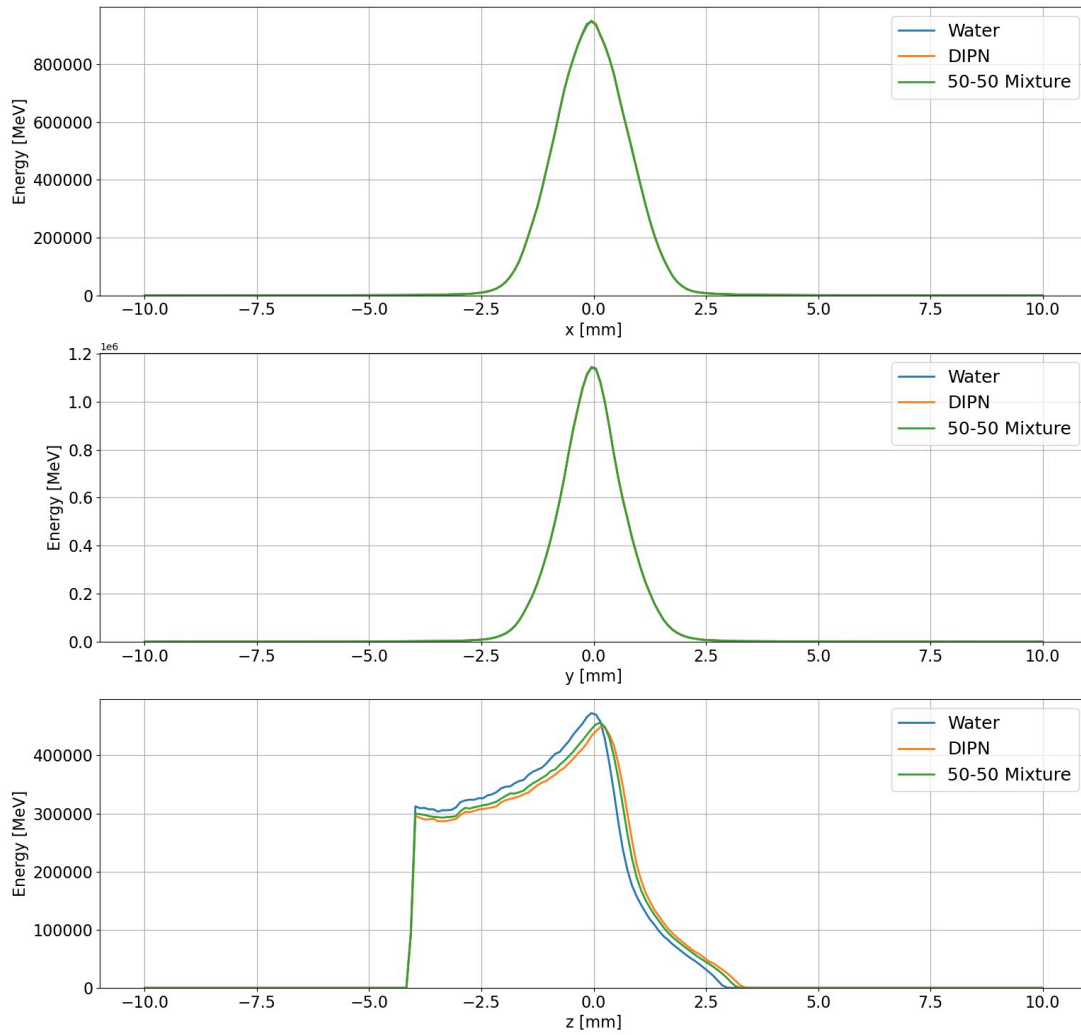


Figure 26: Energy depositions, along the three orthogonal axes, caused by particles emerging from the LION beamline and entering the SmartPhantom, for three cases: the entire volume filled with water, a 50-50 mixture of water and liquid scintillator and 100% liquid scintillator.

beam emerging from the LION beamline transversing the liquid scintillator. Similarly, the energy depositions caused by source-generated electrons are shown in Figure 28. In both figures, the beam travels from left to right, along the z-axis. The colour scale represents the energy deposited in MeV, with higher energy depositions shown in pink and black, and lower energy depositions shown in grey.

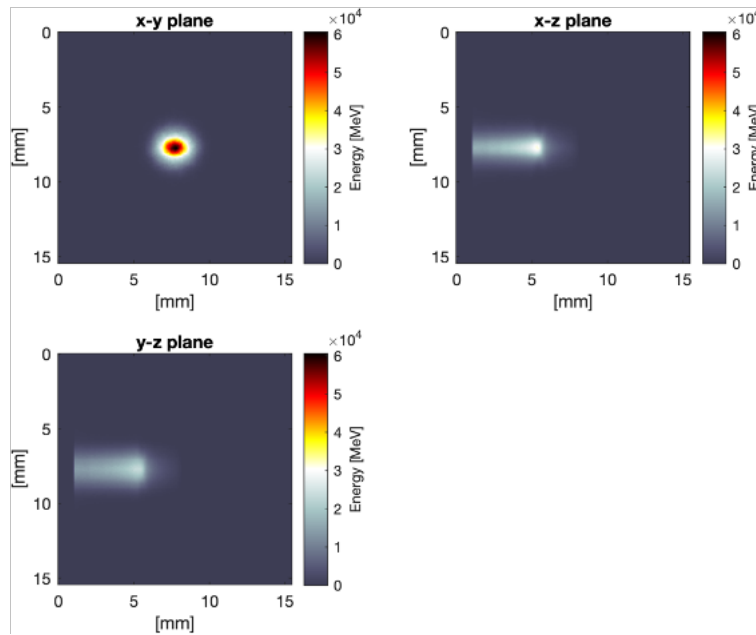


Figure 27: Energy depositions in the liquid scintillator inside the SmartPhantom, caused by the passage of protons emerging from the LION beamline. Voxel size: 0.1 mm.

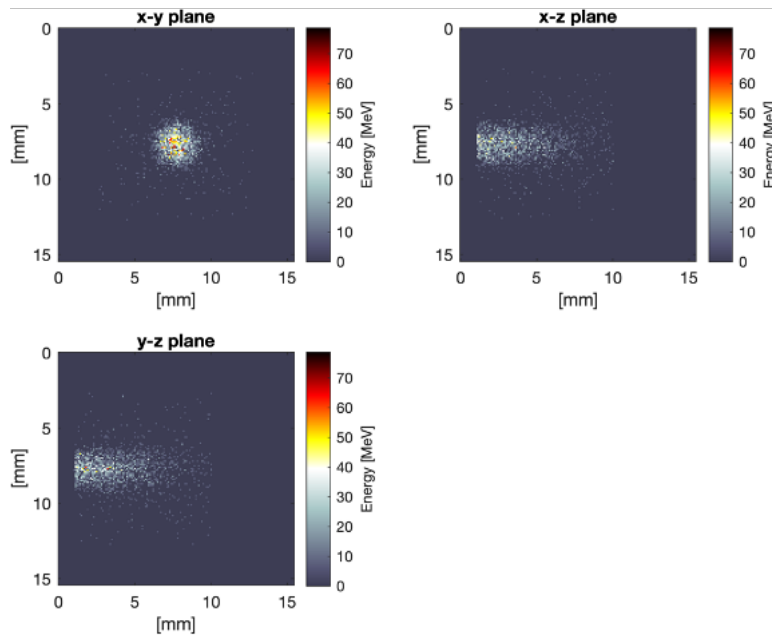


Figure 28: Energy depositions in the liquid scintillator inside the SmartPhantom, caused by the passage of source-generated electrons emerging from the LION beamline. Voxel size: 0.1 mm.

When the proton beam propagates through the liquid, secondary particles are produced from the interactions. Figure 29 shows all the secondary particles produced, as predicted by the Geant4 simulation. The corresponding three-dimensional energy deposition plots are shown in Figure 30.

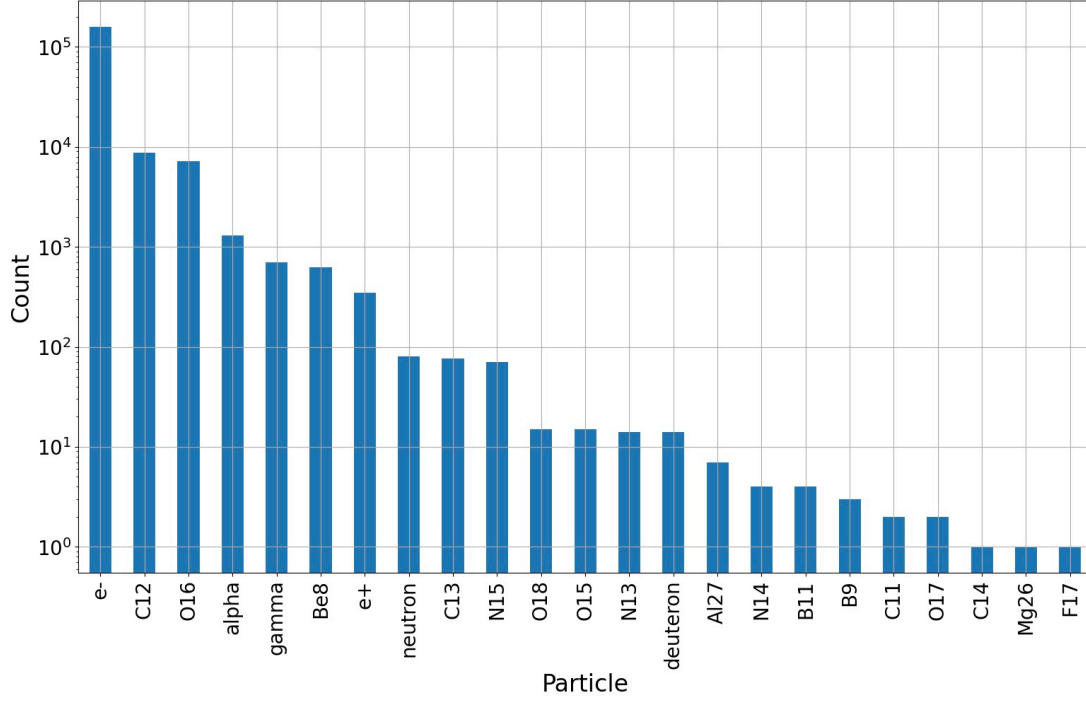


Figure 29: Secondary particles produced from the interactions between the incoming beam and the solution in the inner volume of the SmartPhantom.

5.1.2 Pressure Distribution

The three-dimensional energy matrix from Geant4 was used as the source input into k-Wave, to simulate the ion-energy transfer to the medium, the generation of the acoustic waves and their propagation in the three-dimensional space. k-Wave is an open-source MATLAB toolbox designed for simulating the propagation of linear and non-linear acoustic waves [14] [13]. It operates in the time domain and can simulate signals in both homogeneous

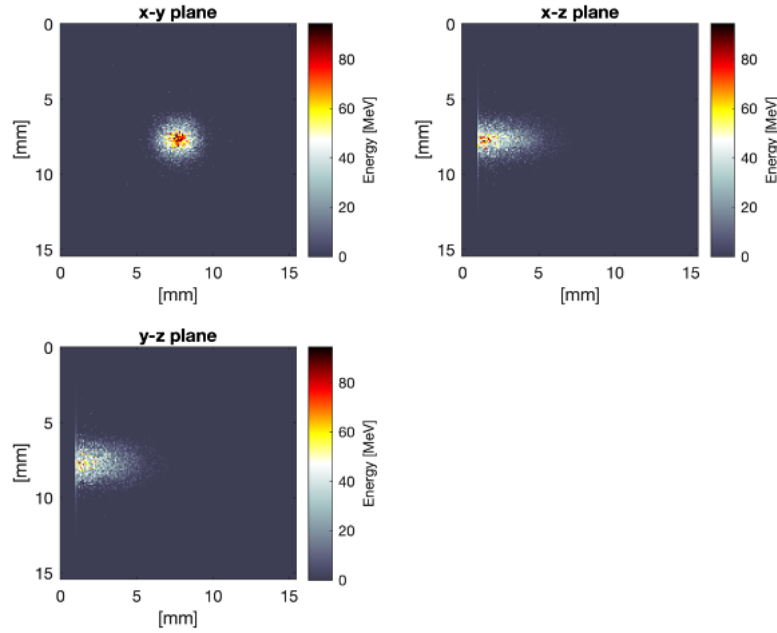


Figure 30: Energy depositions in the liquid scintillator caused by secondary particles produced in the SmartPhantom. Voxel size: 0.1 mm.

and heterogeneous media, accounting for attenuation and reflections.

The pressure value at each voxel is calculated based on the energy using Equation 2.6. The resulting pressure distribution, in the three orthogonal planes, caused by the passage of the beam in the SmartPhantom is shown in Figure 31. The colour scale represents the pressure in Pascals (Pa), with higher energy depositions shown in red and black, and lower energy depositions shown in grey.

The pressure distribution determines the characteristics of the acoustic signals induced, which have been generated and propagated through space. To ensure that the signals are properly sampled and prevent artefacts in the reconstructed images, a sampling frequency of 90 MHz was selected as a compromise between accuracy and computational speed.

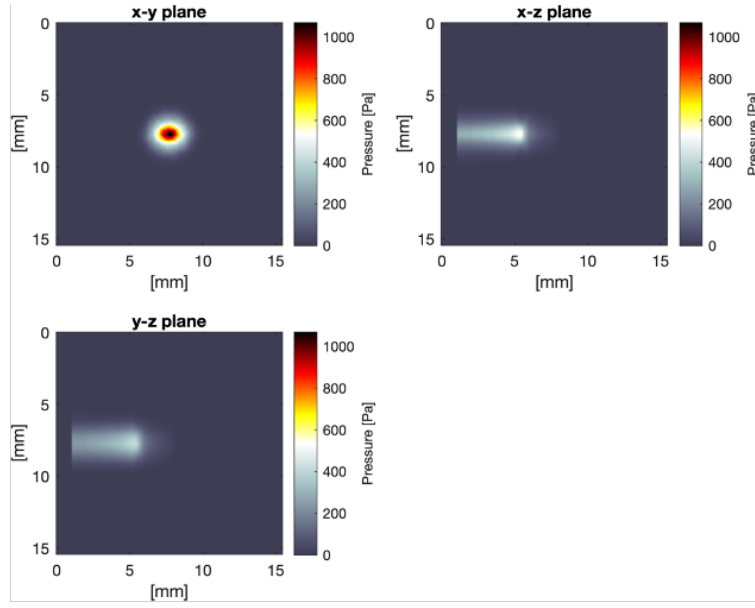


Figure 31: Total pressure distribution of particles depositing energy as they propagate through the SmartPhantom, shown in three orthogonal planes. Voxel size: 0.1 mm.

Acoustic measurements of the liquid scintillator indicated a speed of sound of approximately 1474 m/s, a 0.5% reduction compared to pure water [74]. Therefore this value has been used for the simulation. The generation and evolution of the ion-acoustic waves within the SmartPhantom is illustrated in Figure 32. The figure shows two pressure waves propagating along the z-axis being generated: one arising from the BP due to the steep pressure gradient and one created at the entrance window, where the boundary between the liquid and air is located, due to the rapid change in the deposited energy density.

Both waves propagate outwards from the heated regions, with a portion of the acoustic wave originating from the BP travelling towards the Kapton foil. The Kapton-liquid boundary acts as an interface discontinuity due to the difference in acoustic impedance between the two media [112]. Since there is an acoustic mismatch, with the acoustic impedance of air being much lower than that of the liquid, a larger fraction of the wave is reflected. Consequently, three distinct waves are detected by the transducers, explaining the peaks in

the acoustic traces discussed below.

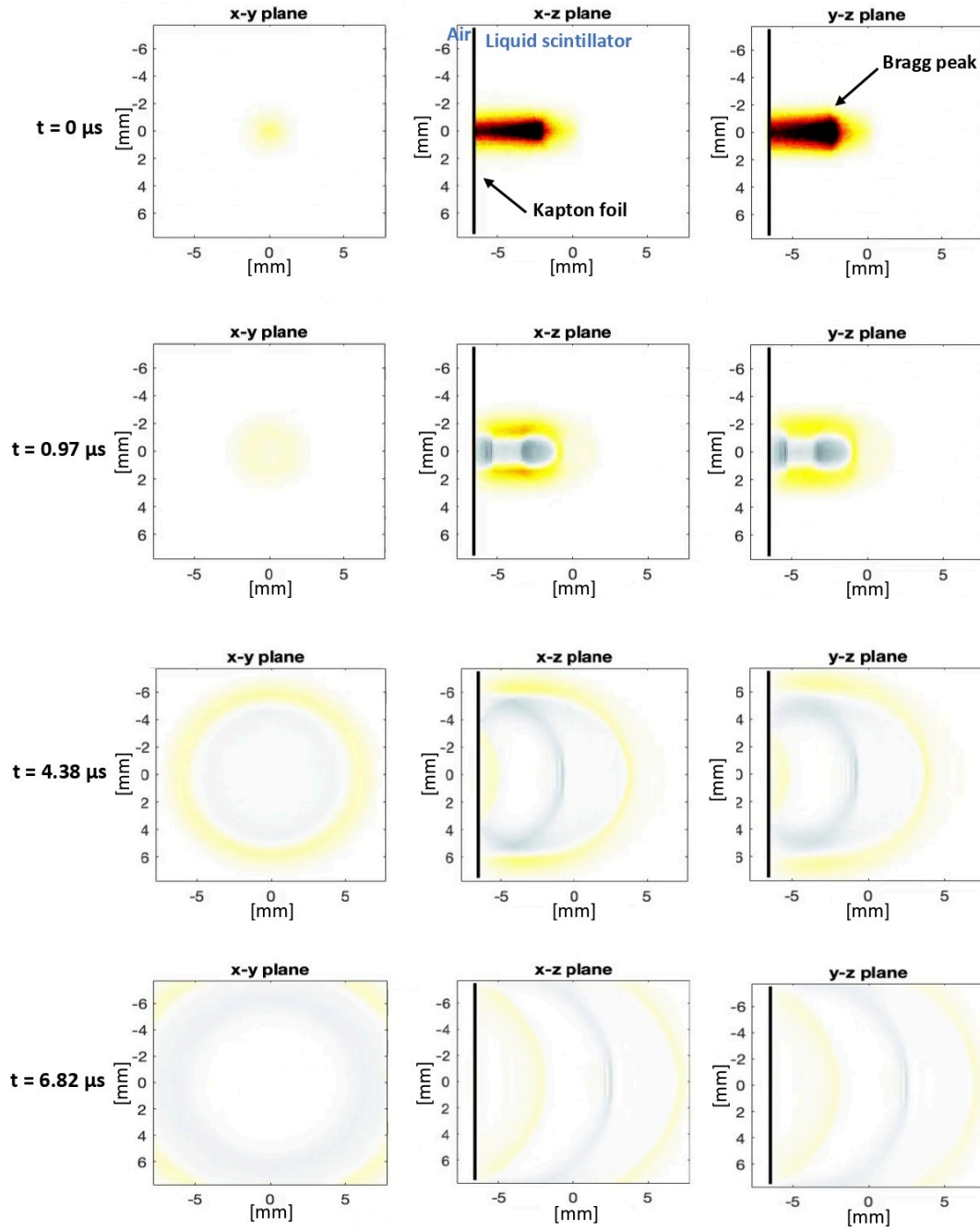


Figure 32: Ion-acoustic signal generation and evolution within the SmartPhantom, simulated using k-Wave. Two pressure waves are generated at $t = 0$ originating from the Bragg peak and the entrance window. Both waves propagate outwards, with the second one reflected off the liquid-air interface at the Kapton foil due to acoustic impedance mismatch.

As illustrated in Figure 32, two different shapes of pressure waves are emitted: the α -wave, a cylindrical wave emitted perpendicular to the beam axis before the BP, and the γ -wave, a spherical wave emitted from the BP in all directions. The two waves are highlighted in Figure 33.

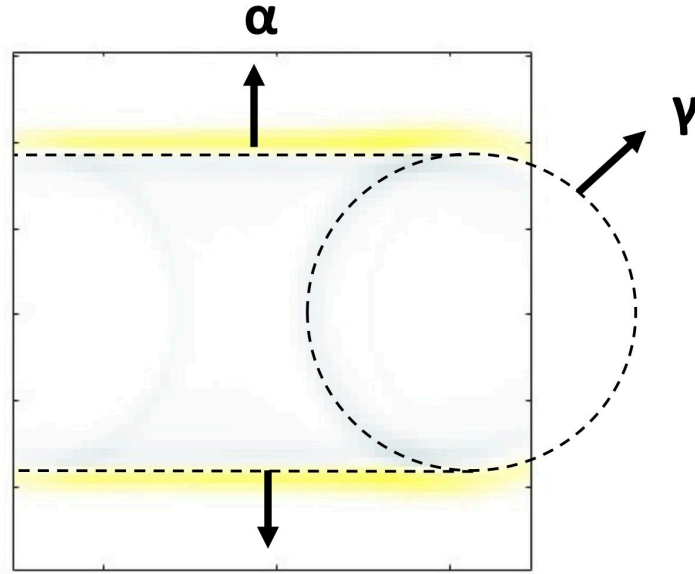


Figure 33: An illustration of the two distinct waves emitted as the beam propagates through the SmartPhantom. The α -wave is emitted laterally in the pre- BP region and the γ -wave is emitted at the BP in all directions. The particles travel from left to right.

5.2 Acoustic Transducers

As discussed in Section 3.4, spatial averaging in addition to temporal averaging usually improves the SNR. For this reason, multichannel sensors are incorporated into the design of the SmartPhantom to record the acoustic signals. Ideally, the selected transducers should have a wide bandwidth to capture the full frequency range of the signals and minimize distortion. The choice of transducers is discussed below.

Vantage Matrix Array Ultrasound Transducer

To capture signals and reconstruct the pressure distribution in both the axial and radial directions, a Vantage matrix array ultrasound transducer is used that has a centre frequency of 3.5 MHz and a frequency bandwidth of 60% [76]. The array consists of 1024 elements arranged in 32×32 configuration. For efficient data acquisition, the array is divided into 4 banks, each with a 32×8 configuration, forming smaller 256-element arrays. The division enables 4:1 multiplexing, allowing the 256 channels of the Vantage system to acquire data from all 1024 elements by switching to different subsets of elements across the banks. Synchronised, real-time three-dimensional ultrasound data acquisition from all elements can be achieved through this multiplexing scheme in combination with the Vantage system software. Due to the two-dimensional shape of the array, three-dimensional data can be acquired (two spatial and one temporal) and therefore the transducer is placed on-axis with the beam to reconstruct the pressure distribution in all three dimensions.

GE 9L-D Linear Array Ultrasound Transducer

The GE 9L-D linear array transducer is an array of 192 elements, with a centre-to-centre pitch of 0.23 mm [77]. Each element measures 5 mm in length and 0.205 mm in width. The transducer has a field of view of 43.0 mm, making it able to capture ultrasound waves across a wide area. In addition, this transducer has a centre frequency of 5.3 MHz and a frequency bandwidth of 75%. The broadband feature is advantageous as it enables a wide range of frequencies to be recorded. The linear array is placed parallel to the beam axis to reconstruct the plateau region of the energy distribution by capturing the lateral (α -) waves. However, the radial dimensions may be more challenging to reconstruct due to its limited cross-section.

Olympus V303 Immersion Transducer

The Olympus V303 immersion transducer is a narrow-band piezoelectric ceramic transducer that can be immersed in water [78]. It consists of a single flat circular element, approximately 13 mm in diameter with an acoustic matching layer for maximum ultrasound transmission. The transducer has a centre frequency of 1 MHz and a frequency bandwidth of 60%, making it suitable for detecting the low-frequency spectrum of the signals. The housing is made of stainless steel and the transducer's flat surface is placed 2.49 cm from the centre of the SmartPhantom's inner volume, positioned perpendicular to the beam axis. Due to the single-element configuration, this transducer cannot be used to reconstruct an image because there is a single time-series. Moreover, the element size is very large compared to the signal wavelengths, therefore, it is only sensitive to waves arriving close to normal incidence [79].

Precision Acoustics ML4X50 Piston Hydrophone

The Precision Acoustics ML4X50 piston hydrophone is a high-sensitivity, broadband single-element transducer that has a circular aperture 23 mm in diameter [80]. The hydrophone is a piezoelectric polyvinylidene difluoride (PVDF) foil with gold electrodes, offering a broad and flat frequency response from 100 kHz to 10 MHz, a feature that minimizes signal distortion. Due to its ability to detect the low-frequency spectrum of the acoustic signals, this transducer can be used downstream of the BP, looking up the beam axis, as an alternative to the matrix array but with the expectation of detecting signal from parts of the plateau region. Furthermore, the ML4X50 piston hydrophone is calibrated, enabling the conversion of voltage to pressure as a function of frequency. This feature makes it ideal for precise dose mapping.

A comparison of the specifications for the Vantage matrix array, GE 9L-D linear array, Olympus V303 transducer and Precision Acoustics ML4X50 piston hydrophone is tabulated in Table 6. The specifications include the transducers' centre frequency, bandwidth, number of elements and element-to-element pitch.

Table 6: Table showing the ultrasound transducers that were to be used at the LION beamline experiment, along with key specifications [76] [77] [78] [80].





Parameter	Matrix Array	Linear Array	Olympus Transducer	Piston Hydrophone
				
Centre Frequency	3.5 MHz	5.3 MHz	1 MHz	0.1 - 1 MHz
Bandwidth	60%	75%	80%	n/a
Elements	1024 (32x32)	192 (192x1)	1	1
Pitch	0.3 mm	0.23 mm	-	-

Figure 34 illustrates the four transducers and their planned locations relative to the energy depositions of the beam, indicated by the yellow region. The Vantage matrix array transducer, shown in the top left, is placed on-axis with the beam and the Olympus V303 transducer, shown in the top middle, is aligned axially at the bottom of the SmartPhantom. Similarly, the GE 9L-D linear array transducer, displayed in the top right, is placed axially but oriented parallel to the beam axis and the Precision Acoustics ML4X50 piston hydrophone is used interchangeably with the matrix array, positioned along the beam axis.

All transducers are oriented to face the centre of the SmartPhantom, ensuring that the waves strike their surfaces perpendicularly. In the simulations, the transducers' limited bandwidth has been implemented by applying a Gaussian filter, the centre frequency and

bandwidth of which correspond to the transducers' specifications displayed in Table 6.

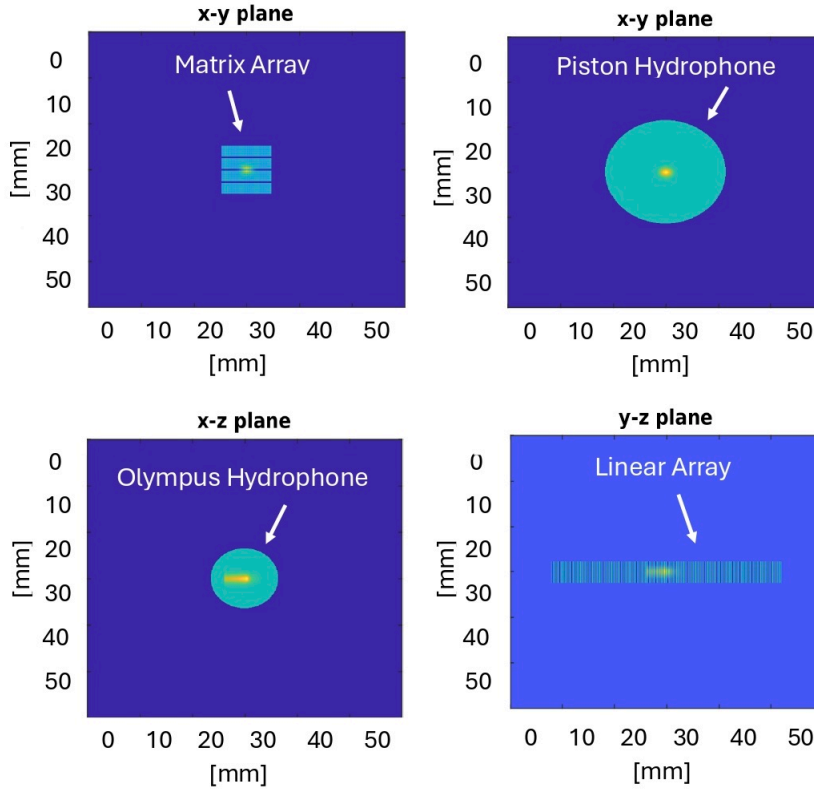


Figure 34: k-Wave simulation illustrating the acoustic transducers and their location relative to the beam energy depositions, indicated by the yellow region. The energy depositions depicted are generated by a beam exiting the LION beamline, optimized for a modal energy of 20 MeV, as it passes through the liquid scintillator.

5.3 Signal Evaluation

Waveforms

The normalized simulated acoustic waveforms that would be recorded by each transducer, according to the k-Wave simulation, are shown in Figure 35. For the matrix and linear arrays, the average of all the elements is presented. The shape of the traces is influenced by the incoming beam's radius, pulse duration, deposited dose, as well as the transducers' orientation and depth of detection.

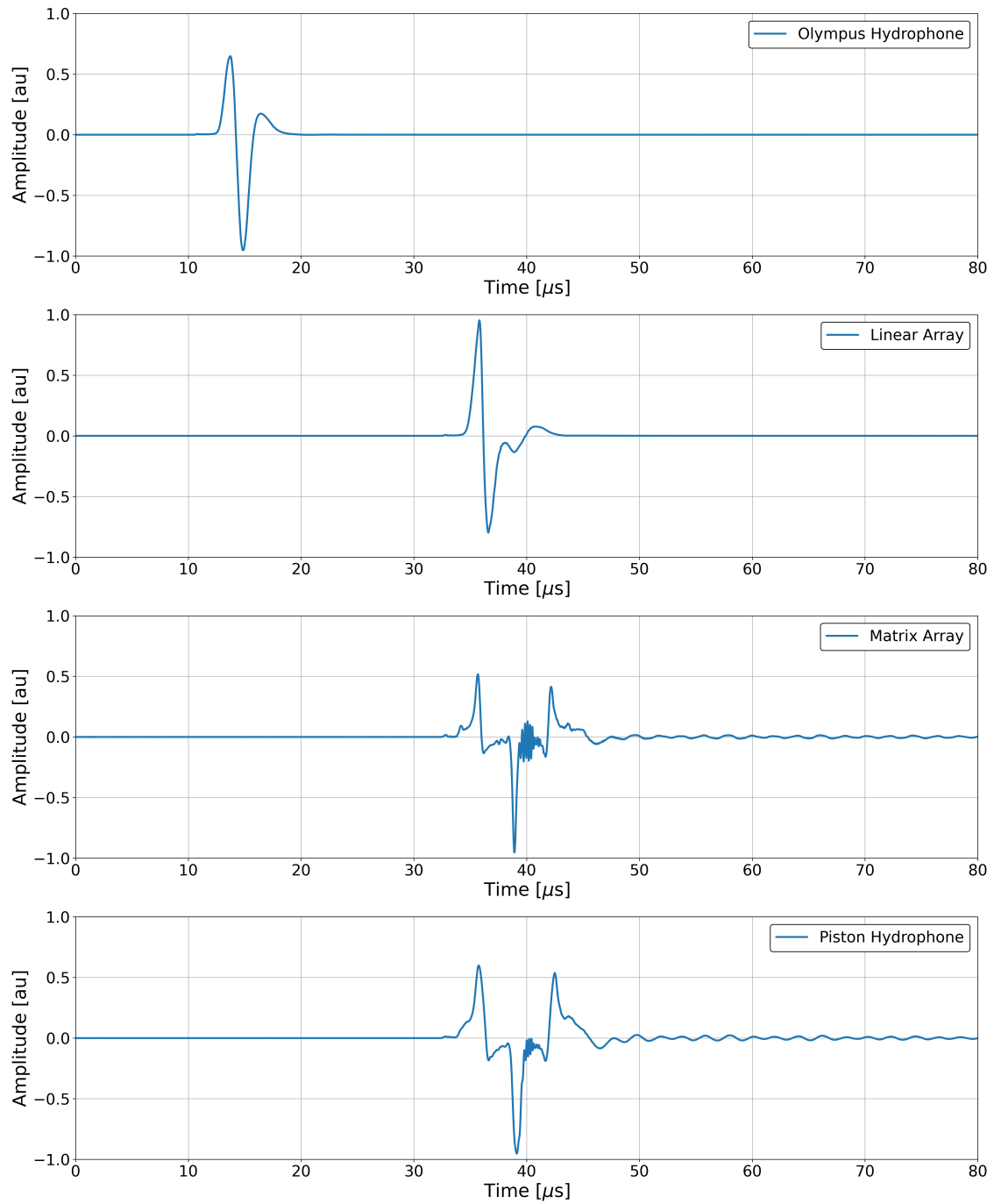


Figure 35: Normalized simulated acoustic waveforms recorded by the four transducers: Vantage Matrix Array Ultrasound Transducer, GE 9L-D Linear Array Ultrasound Transducer, Olympus V303 Immersion Transducer and Precision Acoustics ML4X50 Piston Hydrophone, when positioned at the locations displayed in Figure 34.

Figure 35 shows the Olympus V303 transducer recording a signal that starts at approximately $16.6 \mu\text{s}$. This delay corresponds to the time required for the ultrasound wave to travel approximately 2.49 cm (the distance between the transducer's surface and the BP) at a speed of 1474 m/s. The recorded signal shows a high-pressure positive peak, followed by a sudden negative pressure and a plateau. This pattern results from the ionacoustic effect: the rapid increase in temperature and pressure generates a compression wave, followed by rarefaction as the wave is released, leading to equilibrium. In addition, the transducer's relatively large cross-sectional area compared to the wavelength of the emitted wave makes it highly directional. This results in a distinct signal originating from the Bragg peak being recorded, with reduced sensitivity to the parts of the signal originating from the off-axis directions. The directional effect and position of the transducer relative to the beam depositions also explain the absence of any oscillations after the dominant peaks.

A similar acoustic time trace is recorded by the linear array, with the signal arriving at approximately 36.7 microseconds. This corresponds to the time required for the ultrasound wave to travel approximately 5.5 cm at a speed of 1474 m/s. The greater number of elements, compared to the Olympus transducer, enhances the spatial resolution, while the smaller element size eliminates the directionality effect. This improves the detection efficiency of the off-axis signals, resulting in additional compression-rarefaction patterns being observed after the dominant peaks. Furthermore, the improved spatial resolution sharpens the peaks, enabling the array to detect finer variations in the acoustic field. Lastly, unlike the Olympus transducer, the positive signal amplitude is more pronounced than the negative, due to the array's greater sensitivity.

The third subplot of Figure 35 presents the signal recorded by the matrix array, with the waveform displaying more intricate characteristics. Unlike the linear array, the two-

dimensional configuration of the matrix array elements enables efficient detection of radially propagating signals. This results in enhanced resolution, evident from the finer peaks observed in the signal trace. In addition, the on-axis positioning of the array relative to the beam enables the detection of signals reflected off the entrance window. In the acoustic waveform, this is observed as a spatially inverted signal following the dominant signal from the Bragg peak, attributed to the phase inversion caused by the reflection. Furthermore, the subsequent oscillations arise from waves arriving at various angles and distances, giving rise to intricate patterns in the signal.

Lastly, a similar time trace is recorded by the piston hydrophone, albeit with slightly poorer resolution due to its single-element configuration. This results in the waveform appearing smoother, as the acoustic pressure is averaged across the hydrophone's surface.

Range, Energy and Beam Width

The acoustic time-series of the signals can be used to extract information about the range, width and modal energy of the incoming beam. The beam range, defined as the distance between the entrance window and the BP, can be calculated based on the time difference between the first and the third peaks observed in the waveforms of a transducer aligned with the beam axis. The first peak corresponds to the signal emitted at the BP travelling towards the transducer, while the third peak results from the same signal after being reflected at the entrance window. This time difference multiplied by the speed of sound in the liquid scintillator corresponds to twice the beam range.

Using the piston hydrophone's waveform as an example, the time between the first peak ($35.4 \mu\text{s}$) and the third peak ($42.25 \mu\text{s}$) is calculated to be $6.85 \mu\text{s}$. Using the speed of sound in the liquid scintillator, equal to approximately 1474 m/s , the range is determined

as 4.97 ± 0.03 mm. Moreover, the mean energy, E , of the beam can be calculated using this range and Equation 2.4. For this example, the mean energy is determined to be 21.39 ± 0.08 MeV, which aligns with the modal energy obtained from the BDSIM simulation (20.43 MeV) when the energy spread is considered.

In addition, the FWHM of the beam, w , can be determined by analysing the signal recorded by a transducer on axis with the beam. The time difference between the two peaks multiplied by the speed of sound gives the beam's FWHM in the radial direction. Using the Olympus V303 transducer as an example, this value is calculated to be 1.62 ± 0.02 mm, which agrees with the value observed in the Geant4 simulations (1.45 ± 0.2 mm).

Frequency Spectra

The frequencies present in the signal are identified by translating it from the time domain to the frequency domain using a Fast Fourier Transform (FFT) [81]. Figure 36 shows the frequency spectra of the signals from each transducer. The frequency spectrum of the signals from the Olympus transducer appears as a smooth curve with a single broad peak at around 0.3 MHz, indicating a greater sensitivity to the lower-frequency components.

The frequency spectrum of the signal from the linear array shows an increased number of peaks implying an improved resolution. This can be attributed to the increased number of elements and the smaller element size. In addition, the curve extends to higher frequencies indicating a broader range of sensitivity.

The matrix array frequency spectrum exhibits multiple, sharper, peaks indicating greater resolution, as expected from its small element two-dimensional array configuration. This design allows the array to detect and distinguish signals that arrive at various angles, offering finer resolution. In comparison, the frequency spectrum of the piston hy-

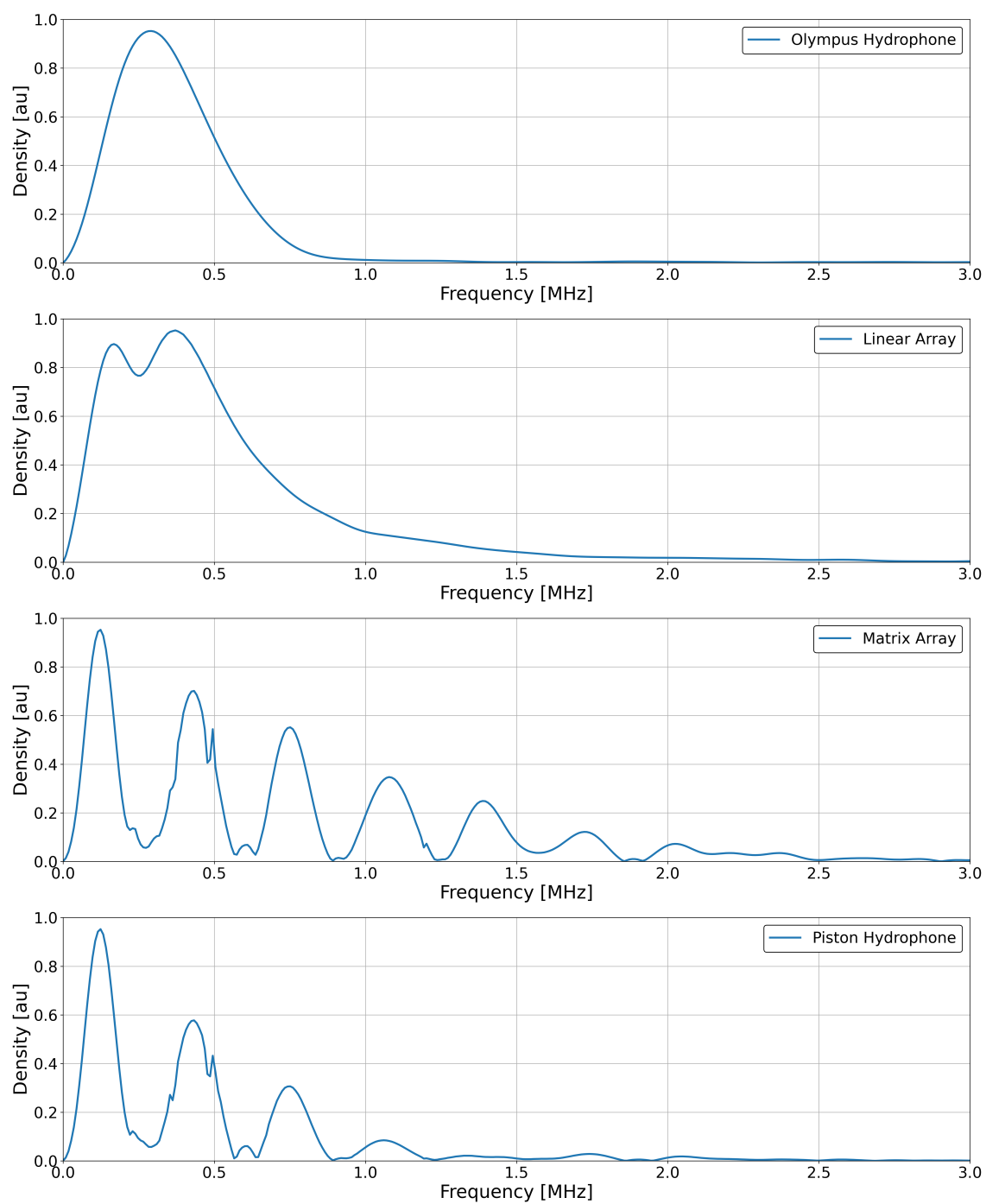


Figure 36: Frequency spectra of the acoustic signals recorded by the four transducers, shown in Figure 34, obtained by applying a FFT to the recorded waveforms.

drophone shows a similar pattern but with a smoother curve and less pronounced peaks. The transducer's large element size results in reduced resolution and finer details are lost.

Furthermore, random variations are introduced to the data in the post-processing to simulate the effect of electrical noise. This noise can arise from various sources, including thermal energy caused by the motion of electrons in the cables or electromagnetic interference from nearby devices [82]. In the simulation, these variations are drawn from a Gaussian distribution with a standard deviation set to 10% of the maximum amplitude. The noise is scaled for each element accordingly, and the value is added to the signal.

5.4 Image Reconstruction

The acoustic waveforms received at each transducer element are used to reconstruct the source pressure distribution. Three different reconstruction algorithms have been written in Matlab: iterative time-reversal, model-based minimization and back-projection. These algorithms have been evaluated to determine their ability to reconstruct the pressure distribution caused by the passage of the particles in the SmartPhantom.

5.4.1 Iterative Time-Reversal Reconstruction

Time-reversal reconstruction is performed in several steps. First, the time-varying acoustic field generated by the source pressure is recorded by the transducer. Next, the recorded signals at each transducer element are propagated backwards in time, with each transducer element treated as an emitting source. These emitted signals travel back to the original pressure source where they interfere constructively and an image is formed [83]. To improve the reconstruction, the time-reversal algorithm can be iterated. This is done by using the initial reconstructed image as a new emitting source and then subtracting the

newly formed image from the previous one to calculate a residual. The residual is then used to create another image, which is added to the former to yield an improved estimate.

The time-reversal algorithm has been iterated until no noticeable improvement was observed. The reconstructed pressure distributions, along each plane, after eight iterations are shown in Figure 37. The reconstruction obtained using the matrix array is shown on the left, while the reconstruction using the linear array is shown on the right. Furthermore, the reconstructed pressure profiles along each axis, compared to the source pressure depicted in Figure 31, are shown in Figure 38.

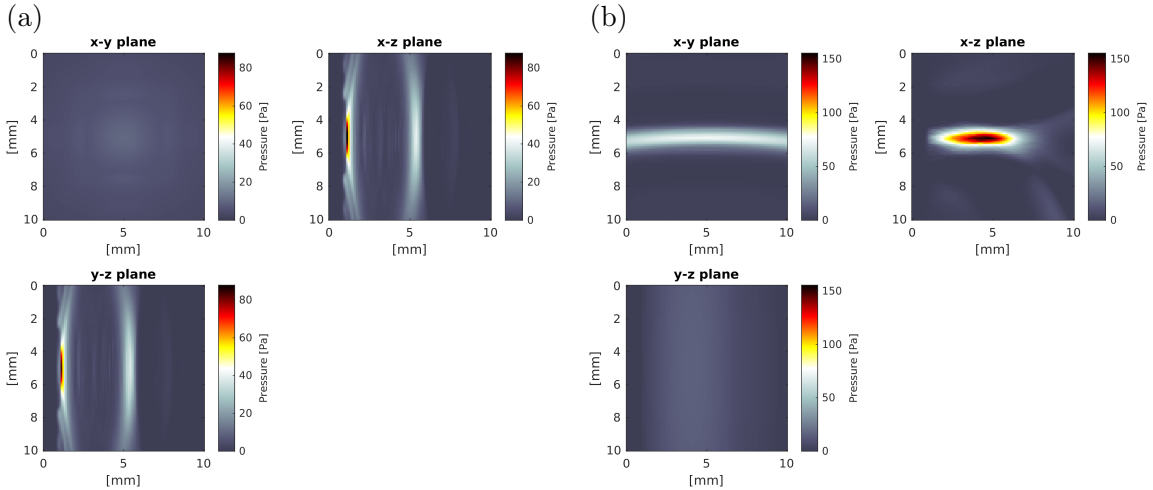


Figure 37: Reconstructed pressure distribution, after eight iterations of the time-reversal algorithm, using the matrix array (a) and the linear array (b).

The figures demonstrate that both array transducers perform poorly in reconstructing the x and y profiles of the beam. This indicates inefficiency in capturing waves emitted radially (α -waves) that are typically weak and may fall outside the angular coverage of the transducers. Although the linear array is placed parallel to the beam axis and is expected to capture lateral waves more efficiently, its limited cross-section provides insufficient lateral coverage, limiting its ability to provide good reconstruction in those directions. This

constraint results in the reconstructions looking smeared.

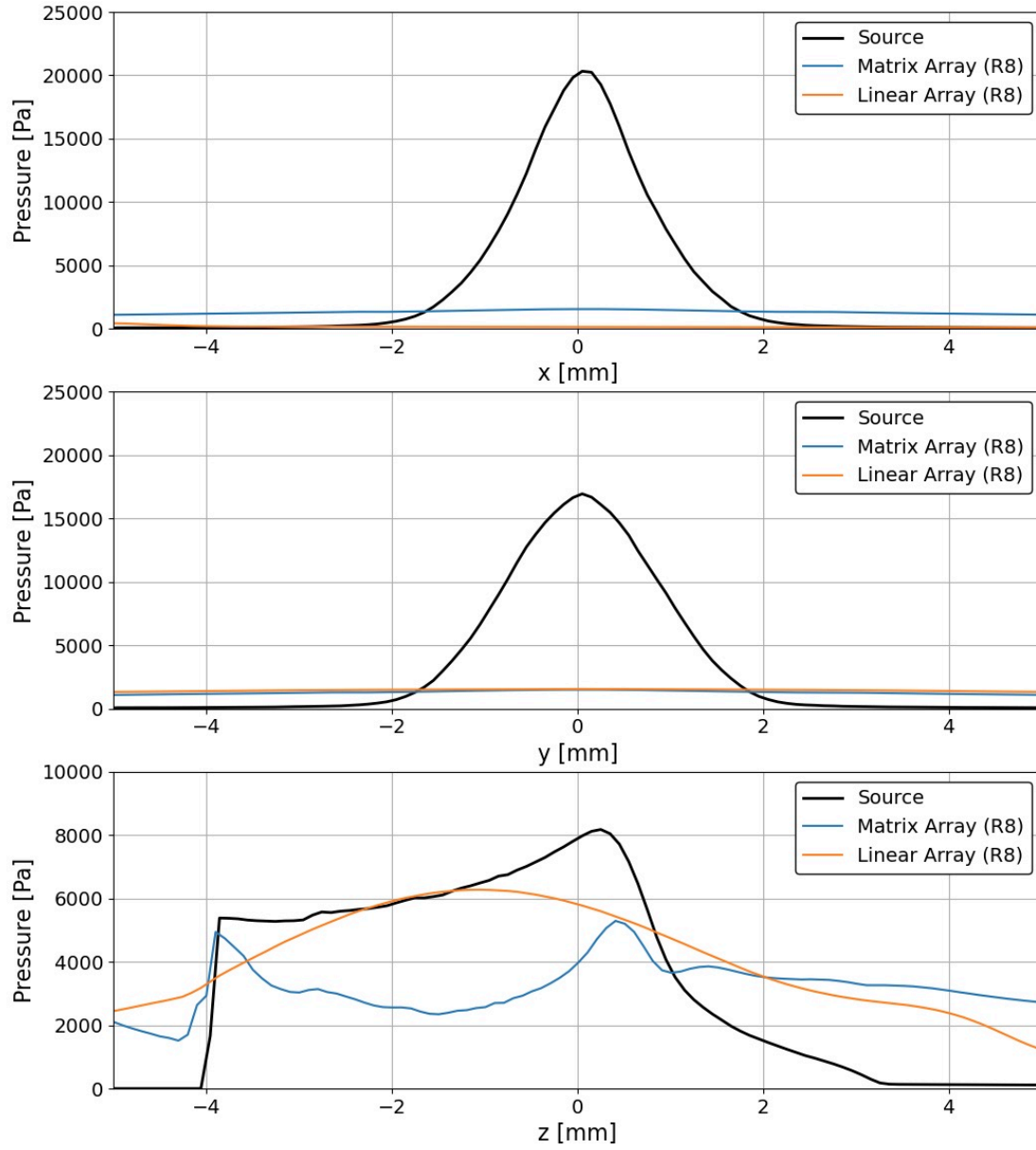


Figure 38: Reconstructed pressure distribution profiles along the x-(top), y-(middle) and z-(bottom) directions, using 8 iterations of the time-reversal algorithm.

The z-profile of the pressure distribution is more closely reconstructed by both arrays. For the matrix array, this can be attributed to the sharp pressure gradients along the

beam axis, particularly at the BP and entrance window. These gradients generate axial (γ -) waves with higher frequency components that are more likely to fall within the bandwidth of this transducer, resulting in improved reconstruction. Elsewhere, such as in the upstream plateau region, the low frequency waves emitted generate weak signals because they fall below this transducer's bandwidth. In contrast, the linear array performs better at reconstructing the rising edge of the BP. Its parallel alignment with the beam axis enhances its ability to detect the waves emitted radially, offering improved sensitivity in that region.

5.4.2 Model-Based Minimization Reconstruction

The model-based minimisation reconstruction technique combines the time-reversal and gradient-descent optimization methods [84]. To perform this reconstruction, the difference (residual) between the measured and the simulated time-series is calculated. The residual is then used as an adjoint source that is propagated backwards in time to produce a residual reconstructed source pressure distribution. This residual distribution indicates how much the reconstructed pressure distribution needs to be adjusted to reduce the error. Next, the error is minimized through the gradient descent method, with the updated field added to the previous estimate. Multiple iterations can be performed until convergence is reached. The results of the reconstruction after eight iterations of the model-based minimization are shown in Figure 39 and Figure 40.

From these figures, similar trends are observed in the reconstructed images, however, the overall accuracy is lower compared to the iterative time-reversal method for the same number of iterations. The x and y profiles remain poorly reconstructed due to the shape and strategic location of the transducers that limit their ability to capture lateral waves. In the z-profile, the reconstruction using the matrix array shows reduced accuracy, with the

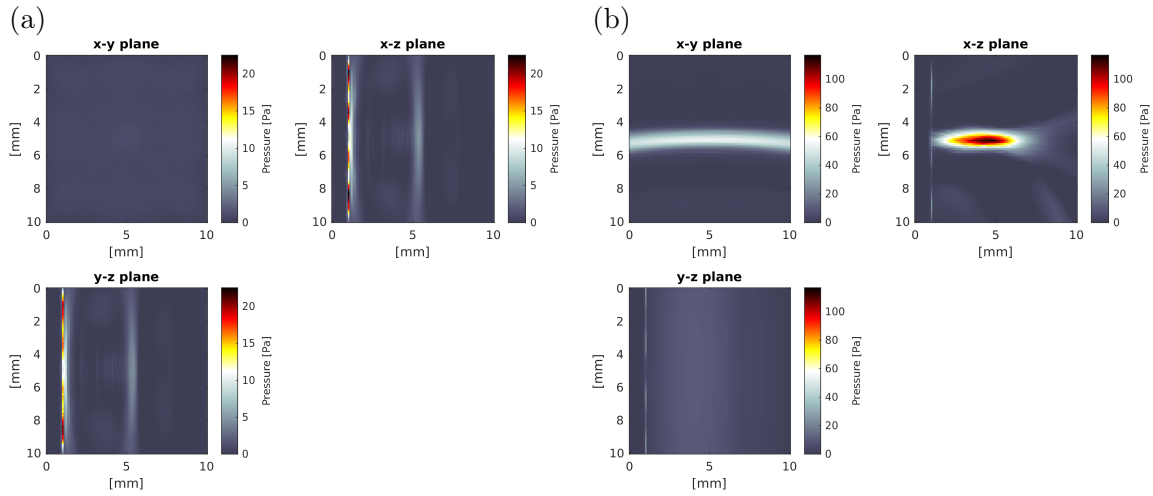


Figure 39: Reconstructed pressure distribution, after eight iterations of the model-based minimization algorithm, using the matrix array (a) and the linear array (b).

gradient appearing less steep and the edges less well-defined. The BP appears more smeared and loses its sharp features. Interestingly, the linear array shows improved reconstruction of the entrance window edge compared to the iterative time-reversal technique, possibly due to sufficient adjustment of the pressure field during the minimization algorithm.

The discrepancies observed with the time-reversal technique might arise due to additional steps involved in the model-based minimization algorithm. For instance, steps such as gradient descent and loss minimization require careful tuning, otherwise, suppression of detail might occur. Moreover, if the residuals calculated from the backwards propagated signals contain artefacts, major errors and incorrect adjustments might be introduced in the updated field, degrading the overall reconstruction accuracy.

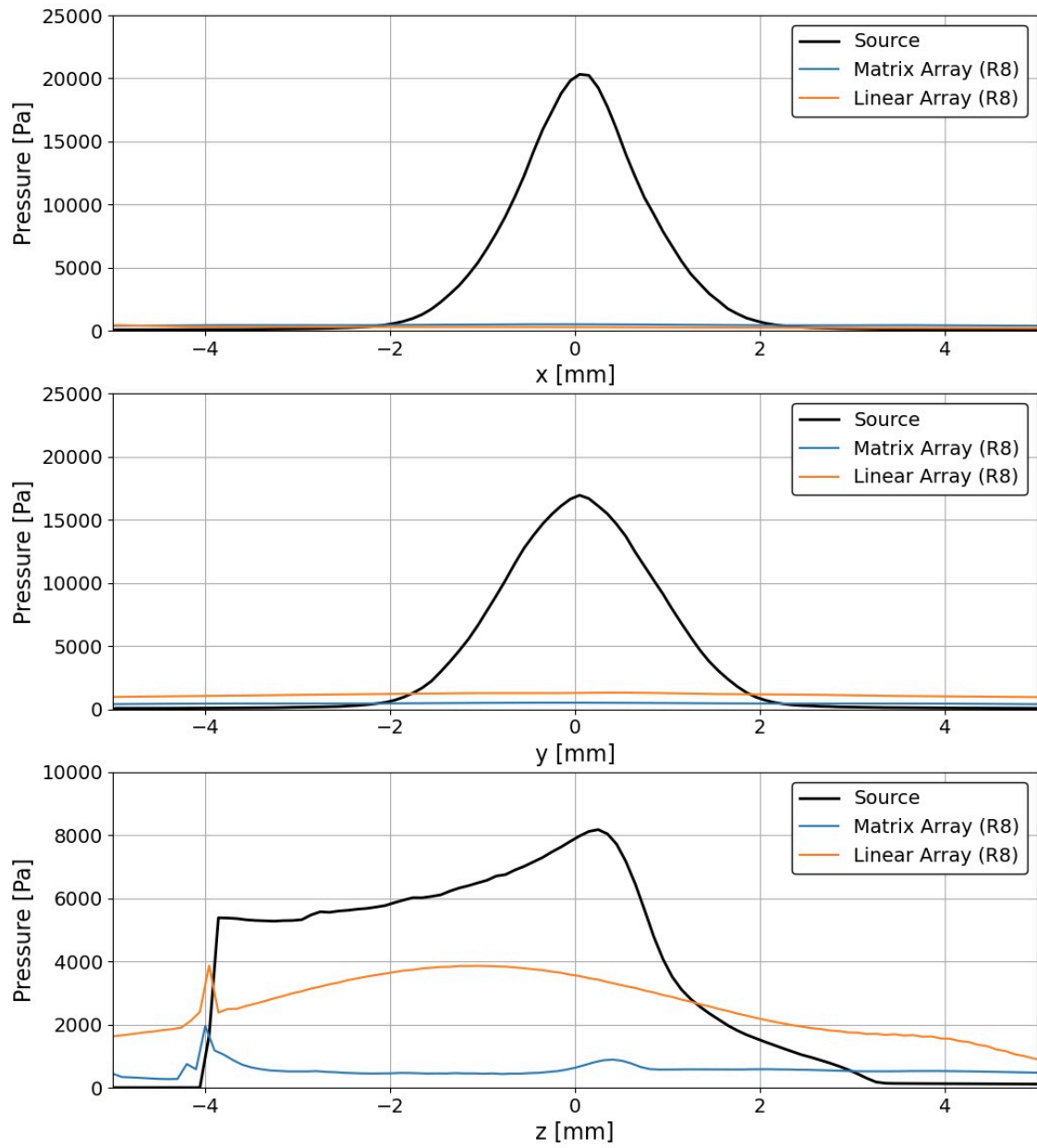


Figure 40: Reconstructed pressure distribution profiles along the x-(top), y-(middle) and z-(bottom) directions, using 8 iterations of the model-based minimization algorithm.

5.4.3 Back-Projection Reconstruction

In the back-projection reconstruction technique, the measured signals are projected back to their source points, travelling along their original propagation paths, with each transducer

element acting as a single projection point [85]. These back-projected signals are then summed in the imaging domain and the spatial distribution of the source is reconstructed. In general, the more projection angles the better the quality of the reconstructed image. Areas corresponding to angles where there is no transducer element will appear blurred. Furthermore, back-projection is significantly faster than the time-reversal and model-based minimization techniques because no complex wave equations have to be solved and no multiple forward and backwards propagations of the pressure field are needed. The back-projected reconstructed images of the pressure distribution using the matrix and linear array are shown in Figure 41.

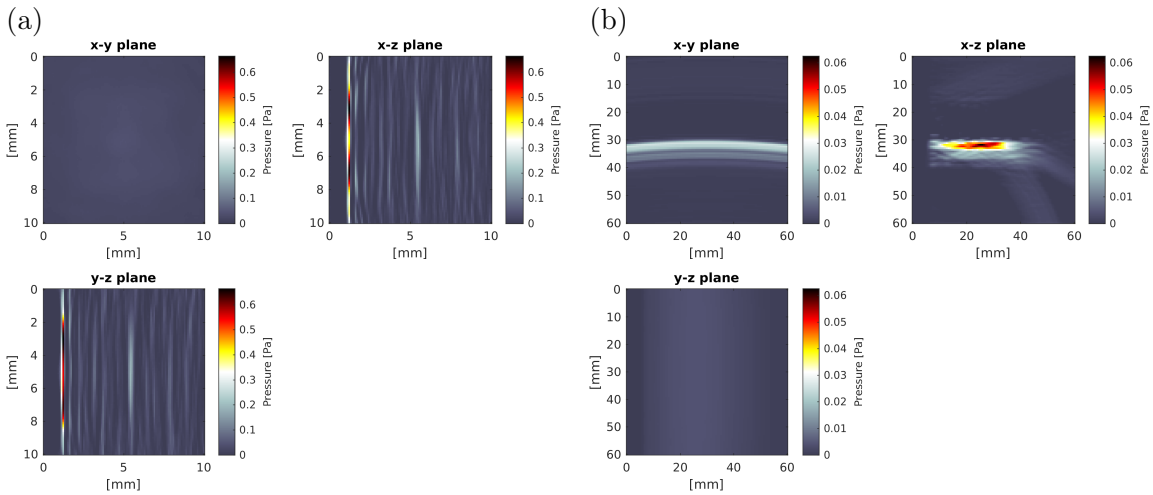


Figure 41: Reconstructed pressure distribution using the back-projection algorithm, with the matrix array (a) and the linear array (b).

The reconstructed images are heavily dominated by artefacts, with noise occluding meaningful information. Neither the BP, the window edge or the rising slope can be resolved. Although the reconstruction with the linear array appears cleaner, it fails to provide any valuable features of the pressure distribution. The sparse transducer placement, limited angular coverage and small element sizes make this reconstruction technique unsuitable.

5.5 Kapton Transmission Loss

In the SmartPhantom design, the matrix and linear array transducers are coupled to the liquid scintillator with a Kapton foil and acoustic coupling gel. It was hypothesised, that since the foil is only $50\text{ }\mu\text{m}$ thick, the waves would incur no significant loss or delay due to transmission through it. An experiment has been performed to quantify the signal loss and test the hypothesis. The experiment took place at the Institute of Cancer Research in Sutton, London [86].

A Perspex tank was filled with water to act as the propagating medium for the ultrasound waves. To eliminate the possibility of bubbles being trapped, which could affect the acoustic signals, the tank was filled with warm water the day before to allow for de-gassing. A specially designed tripod held a transducer window, identical to the ones used in the SmartPhantom, parallel to the water surface. In addition, a golf tee was designed to hold a 2.5 cm diameter bronze ball bearing below the window within the water volume.

For the experiment, the matrix array transducer operating in pulse-echo mode was used. The transducer emitted plane ultrasound waves, which reflected off the ball bearing and were then received by all 1024 elements of the array. The ball bearing was chosen for its uniform and smooth curved surface, ensuring consistent reflections from one experiment to another. The experiment was performed with and without the Kapton window in place. In both set-ups, the matrix array was placed vertically, with its flat surface aligned on-axis with the ball bearing. The alignment was achieved by looking at live ultrasound images. With the Kapton window in place, ultrasound coupling gel was applied on the top surface of the Kapton foil and the transducer pressed down on it, mimicking the procedure that would be used when coupling the transducer to the SmartPhantom. The two experimental

arrangements are shown in Figure 42.

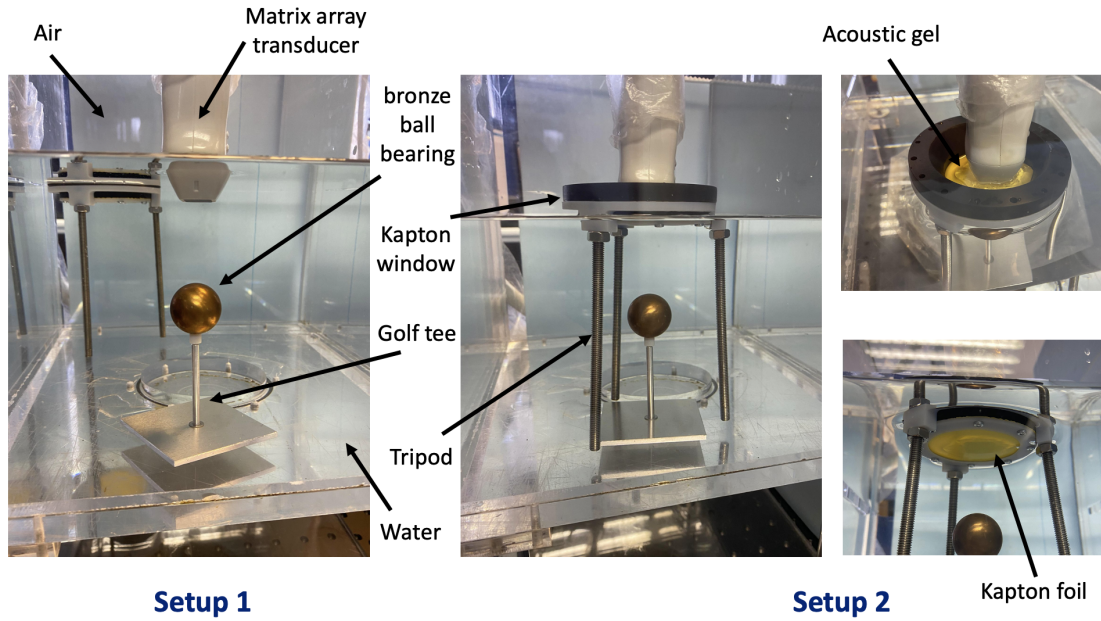


Figure 42: Ultrasound transmission loss experiment set-ups without (left) and with (right) a $50\ \mu\text{m}$ Kapton foil and acoustic matching gel.

A sampling rate of 15 Hz was set and the signals received were amplified using a Verasonics Vantage 256 ultrasound amplifier [87]. The experiment was repeated three times for each set-up and the raw data were analyzed in Matlab. The attenuation caused by the water-Kapton-gel interface was determined by assessing changes in the signal amplitude.

The datasets were loaded in Matlab and reshaped into 3D arrays representing the x dimension, y dimension and time. For the matrix array transducer, this resulted in 1024 individual 1D arrays, which were then averaged across the depth dimension to produce a single voltage-time waveform for each array element. The signals have then been gated to isolate the part of the signal that corresponds to the first arriving echo [88].

To enhance the resolution, the number of points in each signal was increased through linear interpolation. A factor of 4 was chosen as a compromise between improved sampling and computational efficiency. Figure 43 shows the gated signal received by the central element of the matrix array, before and after interpolation, for one of the experimental datasets.

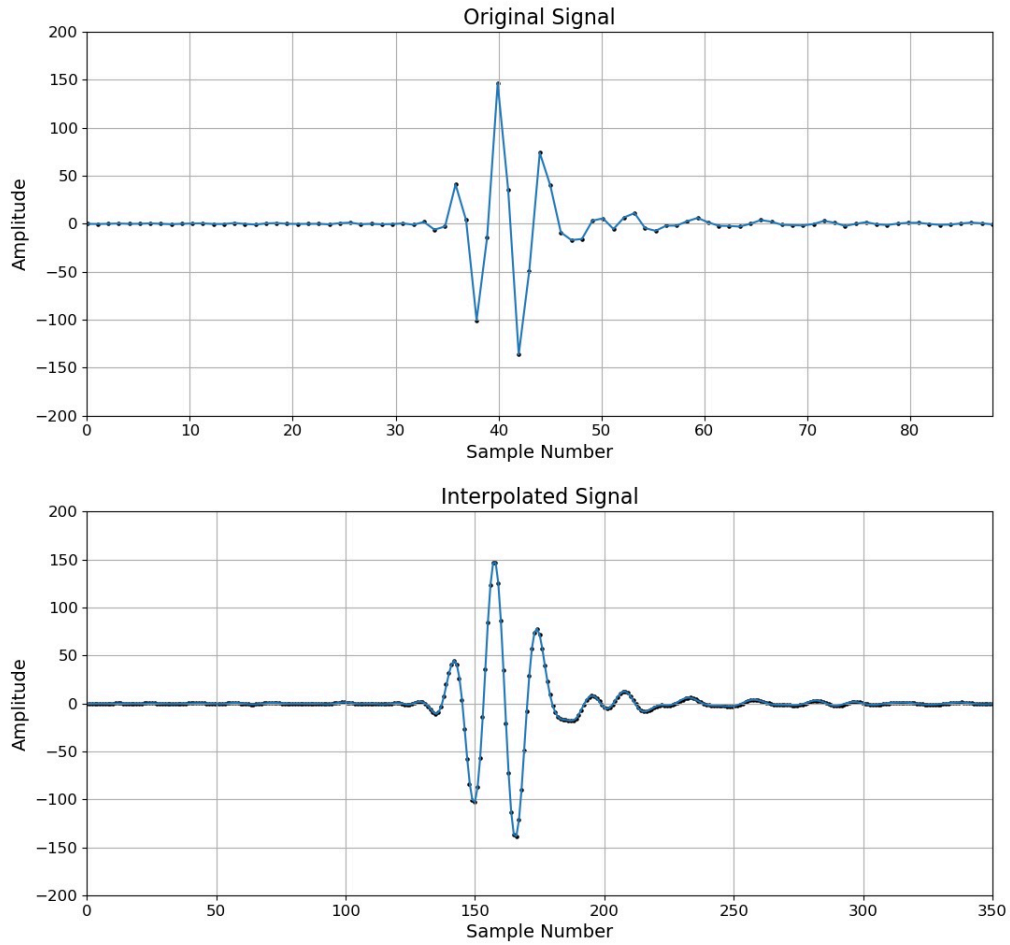


Figure 43: Matrix array's central element gated signal before (top) and after (bottom) up-sampling the number of data points by a factor of 4 using interpolation.

Due to the spherical shape of the reflecting object, the waves emitted and received by each element have different arrival times. To compute an average signal for each experi-

mental run, the relative times of arrival of the echoes for each element were determined and the signals were time-aligned. For time-alignment, the central element has been chosen as the reference signal.

The cross-correlation function between the gated section and the entire signal from each element was calculated. This function measures the similarity between two signals over time, with the peak indicating the difference in the time of arrival between the two elements [89]. Figure 44 shows the cross-correlation function of one element compared to the central, with the peak representing the time delay marked by a red cross.

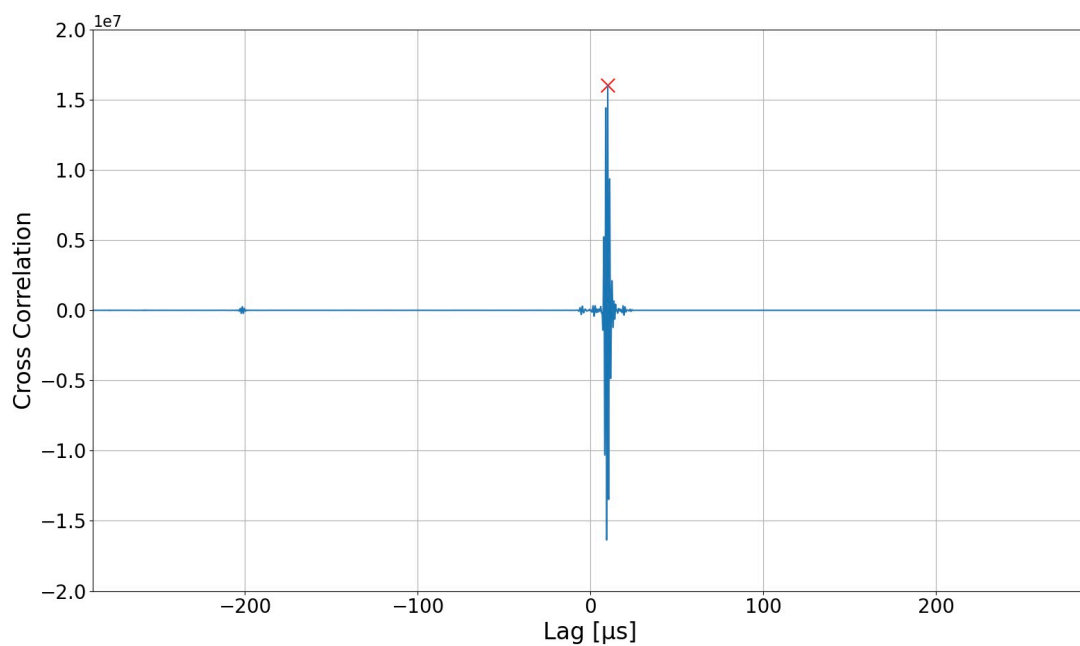


Figure 44: Cross-correlation function between an element of the matrix array and the central element. The red cross marks the peak of the cross-correlation function, indicating the time delay of the echoes.

The calculated time delays for one of the datasets are shown in Figure 45. The results indicate a larger time delay for the elements located on the outer radius of the array, which

is expected due to the curved surface of the ball bearing.

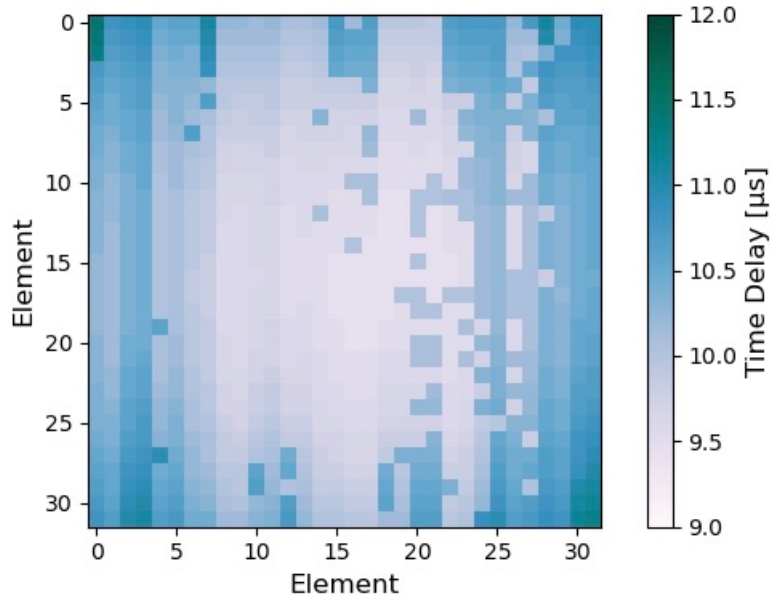


Figure 45: Time delay of each matrix array transducer element relative to the central element, calculated using the cross-correlation function.

The signals were time-aligned by shifting them according to the lag of the peak determined from the cross-correlation function. The process is applied to all signals that require alignment to the reference. The signals from the central row of the matrix array before and after time-alignment are shown in Figure 46.

The element-to-element coherence was evaluated by computing the correlation coefficient, $R(i, j)$, using Equation 5.1 [90]. In this equation, $A(i, j, t)$ represents the signal on each element, $A(16, 16, t)$ denotes the signal on the reference (central) element and $\bar{A}(16, 16, t)$ is the mean of the reference element over time. The calculated 2D spatial coherence for one of the experimental datasets is shown in Figure 47.

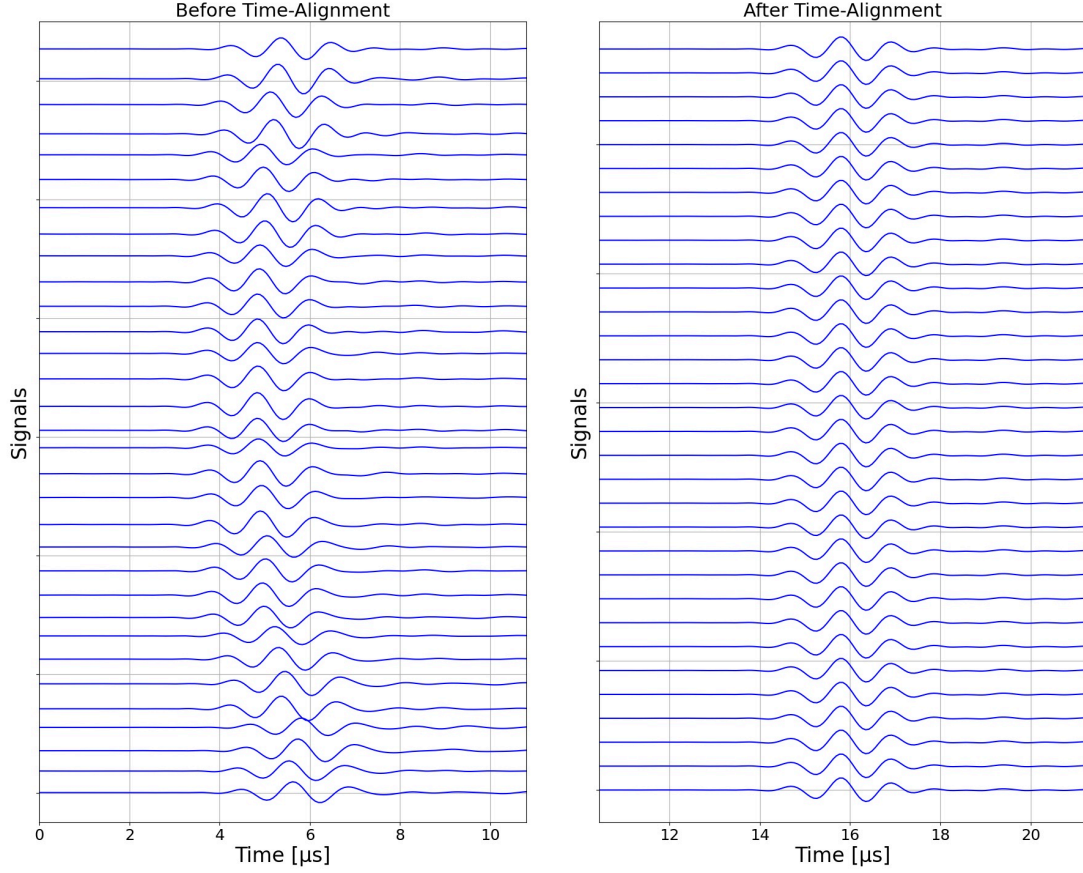


Figure 46: Signals from the elements in the central row of the matrix array, with the Kapton window in place, before (left) and after (right) time-alignment using the cross-correlation function.

$$R(i, j) = \frac{\sum (A(i, j, t) - \text{mean}(A(i, j, t))) (A(16, 16, t) - \bar{A}(16, 16, t))}{\sqrt{\sum (A(i, j, t) - \text{mean}(A(i, j, t)))^2} \sqrt{\sum (A(16, 16, t) - \bar{A}(16, 16, t))^2}} \quad (5.1)$$

The coherence matrix provides a quantitative measure of the correlation between the signals from each element compared to the reference. From Figure 47, it can be seen that the coherence values appear relatively uniform across the array, with the Kapton window in place, indicating consistent time-alignment. Variations in the values can be attributed

to noise or acoustic reflections caused by the container or tripod legs.

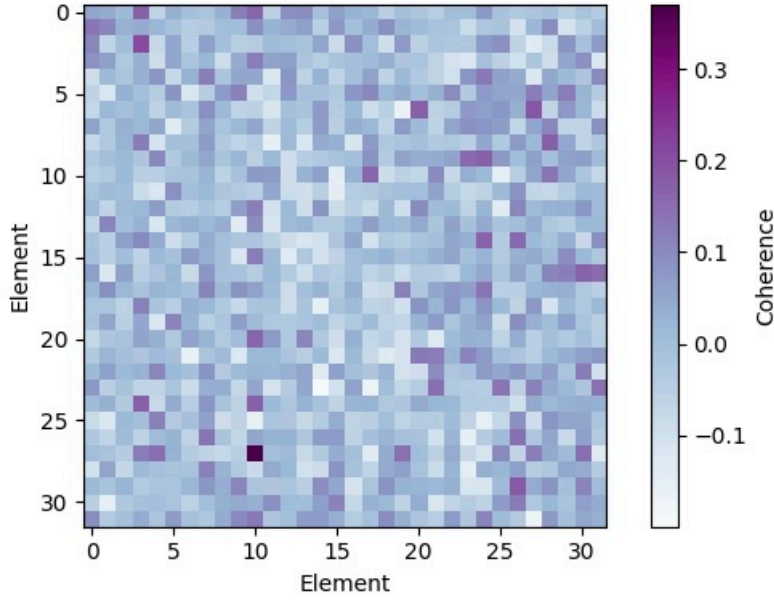


Figure 47: Element-to-element coherence for one of the experimental datasets, calculated using Equation 5.1 [90].

After time-aligning and coherence checks, the 1024 signals were averaged to form an average signal for each experimental run. This averaging process across all matrix elements enhances the signal-to-noise ratio. To evaluate the impact of the Kapton foil and the acoustic gel, the peak-to-peak amplitude of each averaged signal was calculated. The results, shown in Figure 48, reveal a statistically significant and hence measurable decrease in amplitude between signals coupled with the Kapton foil and the gel, compared to those received by the transducer when immersed in water. A similar effect is expected when using the liquid scintillator, given the similarity in mass density and speed of sound.

The three experimental repetitions, with and without the Kapton window, were averaged to obtain a single signal for each configuration. The signal loss, L_{dB} , was then determined and quantified in decibels (dB) using Equation 5.2, where \bar{K} represents the

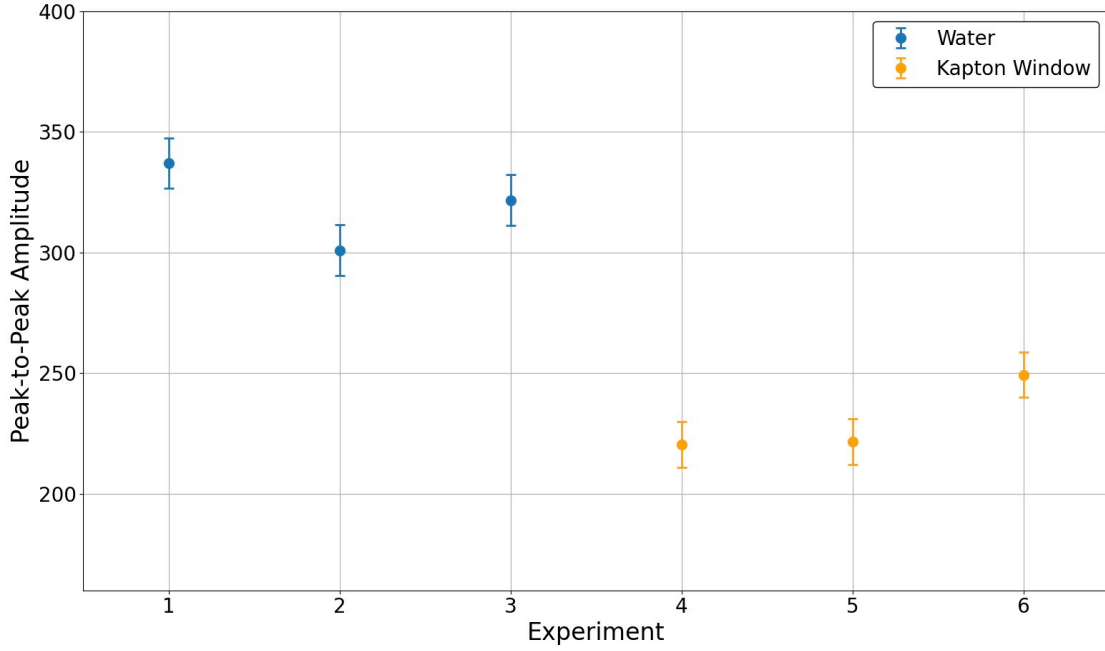


Figure 48: Peak-to-peak amplitudes of the averaged signals for all datasets. Blue dots represent the results from Setup 1, while orange dots represent the results from Setup 2.

average signal of the Kapton measurements and \bar{W} represents the average signal for the water-only measurements [91].

$$L_{dB} = 20 \log_{10} \left(\frac{\bar{K}}{\bar{W}} \right) \quad (5.2)$$

To account for the ultrasound waves passing through the Kapton interface twice, the value obtained was divided by 2. The calculated signal loss is 1.43 ± 0.23 dB. This result suggests that although the signal loss is measurable, it would not be expected to render the ionacoustic signal undetectable. Consequently, the SmartPhantom was constructed with Kapton windows for coupling the ultrasound transducers.

Chapter 6

Liquid Scintillator

6.1 Scintillating Liquid

The liquid scintillator was carefully selected to have a density close to that of water (1.005 g/cm^3) while exhibiting similar acoustic properties, such as sound speed and signal attenuation. For these reasons, the **Ultima Gold XR** cocktail was chosen to fill the SmartPhantom volume [92]. The solution has a high flash point ($\sim 150^\circ \text{ C}$) and low toxicity and corrosiveness, making it well-suited for the intended use. In addition, it is highly dilutable, designed for up to 50/50 mixing with water.

Table 7 provides the chemical composition of the cocktail [93], showing that it primarily consists of di-isopropyl naphthalene (DIPN). The scintillator has a refractive index of around 1.54 (15 % greater than water), a peak emission wavelength of 427 nm and a light yield of approximately 11200 photons per MeV [94] [95].

6.2 Scintillation Correction

Imaging scintillation light from the liquid scintillator in the SmartPhantom is expected to encounter various optical artefacts [96]. These include stray radiation, camera noise, Rayleigh scattering and blurring due to lens distortion and refraction. Correcting or preventing these artefacts is crucial, as they can distort the shape and size of the object to be imaged, leading to inaccurate conclusions.

Stray radiation refers to the radiation that arises from sources other than the proton beam. This can be in the form of secondary particles that are produced from interactions

Table 7: Ultima Gold XR chemical composition [93].

Name	Solvent	Scintillator	Composition [%]
Di-isopropyl naphthalene	✓		40 - 60
Ethoxylated alkylphenol	✓		20 - 40
Bis(2-ethylhexyl) hydrogen phosphate	✓		2.5 - 10
Triethyl phosphate	✓		2.5 - 10
Sodium di-octylsulphosuccinate	✓		2.5 - 10
3,6-dimethyl-4octyne-3,6-diol	✓		1.0 - 2.5
2,5 diphenyloxazole		✓	0 - 1.0
1,4-bis (2-methylstyryl)-benzene		✓	0 - 1.0

with the scintillating liquid or from external sources that make it to the liquid volume. To correct this effect, a spatial median filter can be applied to the images by replacing each pixel with the median value of the neighbouring pixels within a defined window [96]. The median value and not the mean is chosen to reduce the impact of outliers as the median is less sensitive to extreme values.

Camera noise refers to random spots of brightness in an image that are not caused by the scintillating object. These are caused by the current in the camera chip that is influenced by several factors, such as temperature variations. Such noise is typically observed as "hot" pixels in the image. To correct this, multiple images of a dark background (or with the lens covered) can be captured, averaged, and then subtracted from the image of the scintillating object [96].

Rayleigh scattering can arise from interactions between the generated photons and the particles in the liquid scintillator, as well as from optical reflections caused by the walls of

the SmartPhantom [97]. This scattering could cause the captured image to appear blurred. When imaging scintillation light from particle beams, the blurring is more pronounced around the Bragg peak, where there is a steep energy gradient, and can cause it to appear broader and shorter than it is. This effect can be reduced by shielding the apparatus in a dark box or by making the walls less reflective, such as by making them black. This measure has been implemented in the design of the SmartPhantom, with the core structure anodised black to reduce optical reflectivity.

Lastly, the boundaries between the liquid scintillator, the glass window, the focusing lens and the air in the delivery tube, can introduce significant distortion of the light rays due to refraction. This distortion can lead to errors by shifting the object's position as well as by changing its size and light intensity. This effect can be minimized by ensuring that the refractive index of the liquid scintillator and the glass window match. Additional reflections can be prevented by making sure that the liquid level is above the camera's field of view. Furthermore, a change in the object size can also result from an increasing distance between the source and the imaging lens, also referred to as "perspective". This can be corrected by scaling the imaged object according to the total magnification of the imaging system.

6.3 Fluorescent Dye and UV Source

Prior to handling the Ultima Gold XR solution and to gain experience with cameras and imaging systems, a preliminary experiment was performed using a fluorescent dye. The dye named Coumarin-120 (also known as Coumarin-440 or 7-Amino-4-methylcoumarin) was selected for its water solubility and its peak emission wavelength (440 nm), which closely matches that of the liquid scintillator [98]. Due to the molecular weight of Coumarin-120

being 175.18 g/mol, 0.02 grams were used to form a weak solution with 1.5 litres of water.

A UV light source was generated using a commercially available UV LED operating in the 365-525 nm range. The emitted light passed through the Coumarin-water mixture enclosed in a 7 cm \times 16 cm \times 14 cm glass water tank, followed by an air gap before the front surface of an imaging lens [99]. In addition, a Chameleon3 CM3-U3-31S4M-CS camera, externally connected to a PC, was securely mounted using an optical construction rail and an adjustable clamp [100]. The experimental set-up has been placed inside a dark box to eliminate background light and is shown in Figure 49.

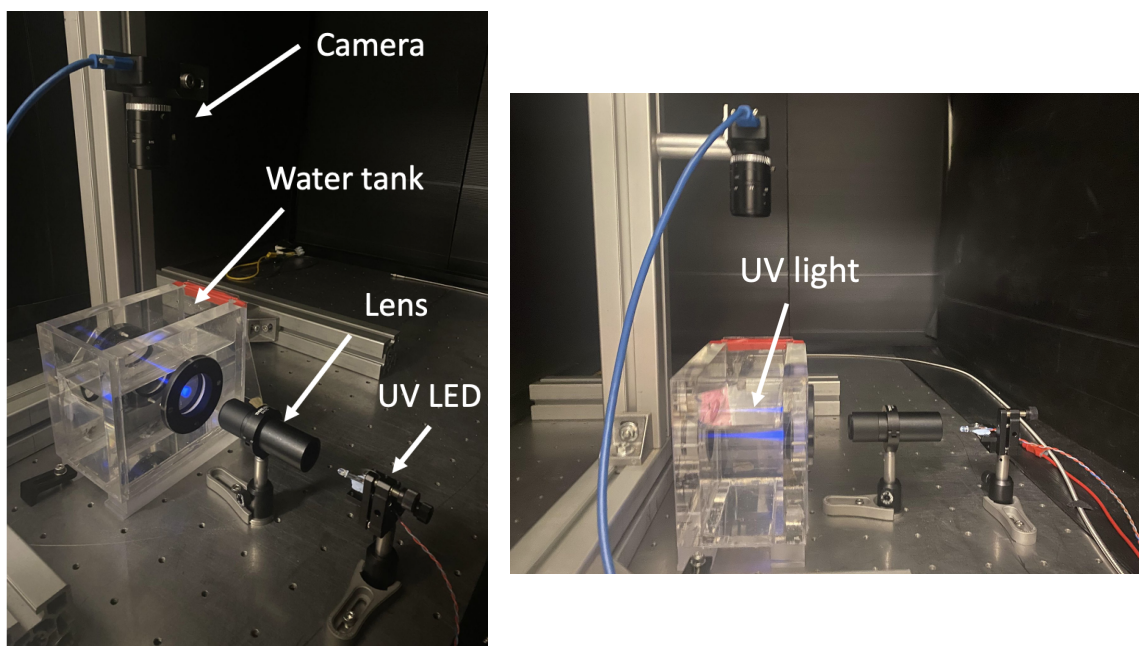


Figure 49: Experimental set-up of the fluorescent dye (Coumarin-120) experiment. Right: angled view showing the Chameleon3 CM3-U3-31S4M-CS camera, glass water tank, optical lens and UV LED source [100]. Left: side view, where the blue light corresponds to the UV light propagating through the Coumarin-water mixture.

Initially, the linearity of the LED was investigated. A beam splitter (90°) was inserted between the LED and the lens, to split the beam and allow real-time calibration without

re-assembling the mechanically stable set-up. The input current at the LED was varied using a power supply and the output current was detected by a photodiode placed at 90° to it and measured with a multimeter [101]. Simultaneously, images were captured using the camera. Figure 50 shows the experimental set-up for the linearity test.

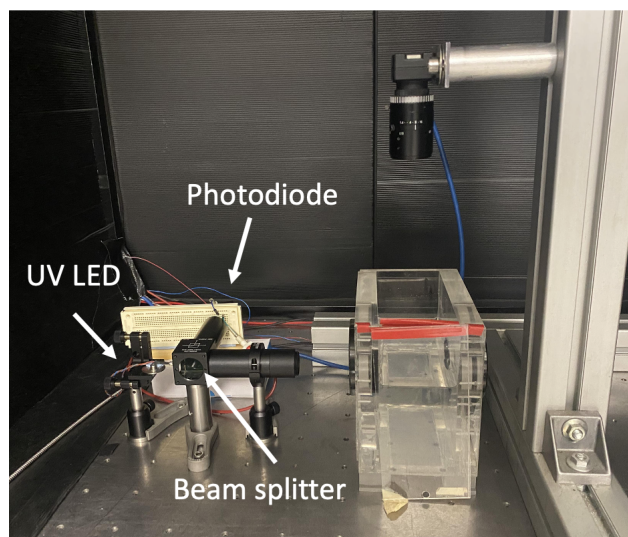


Figure 50: Experimental set-up for measuring the linearity of the LED output. A beam splitter directs the beam into the Coumarin-water mixture while simultaneously sending a fraction of the light to the photodiode to measure the current.

Figure 51 displays the relationship between the input current (from the power supply) and the output current (photodiode reading). The error bars are calculated based on the precision of the power supply and the current fluctuations observed on the multimeter. The graph shows a linear relationship up to 0.035 A, beyond which an equivalent increase in input current results in a smaller increase in photodiode reading. This behaviour might result from series resistance and heating effects at higher currents.

Image saturation was evaluated by analyzing the images obtained simultaneously with the photodiode measurement. The camera captures up to 55 frames per second and has a resolution of 2048×1536 pixels. To reduce random noise and remove 'hot' pixels, the

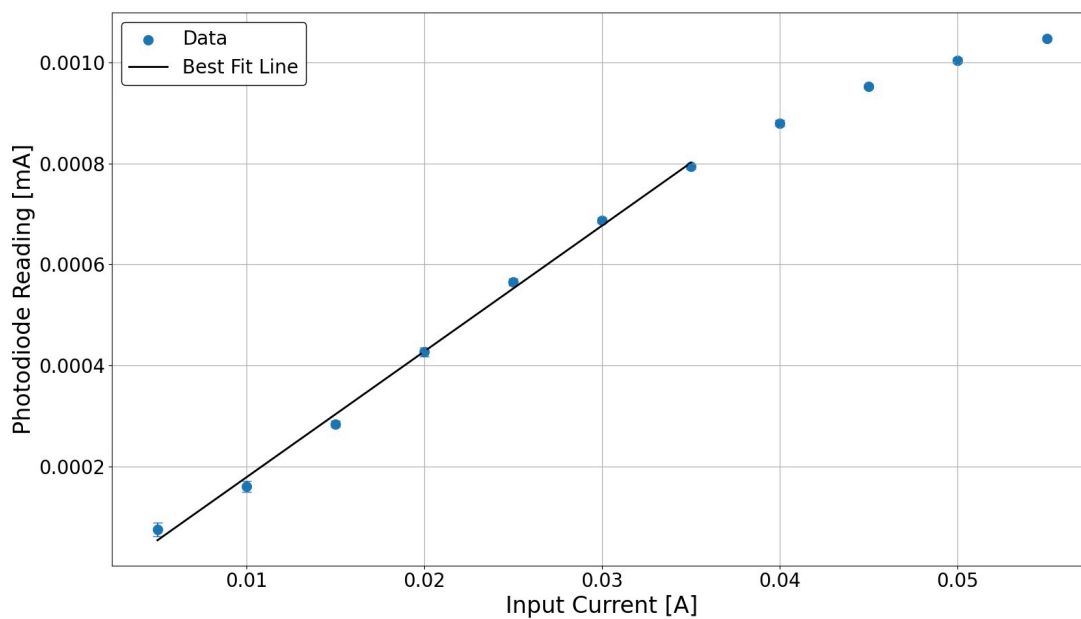


Figure 51: Photodiode reading plotted against the input current from by the power supply, using the setup depicted in Figure 50.

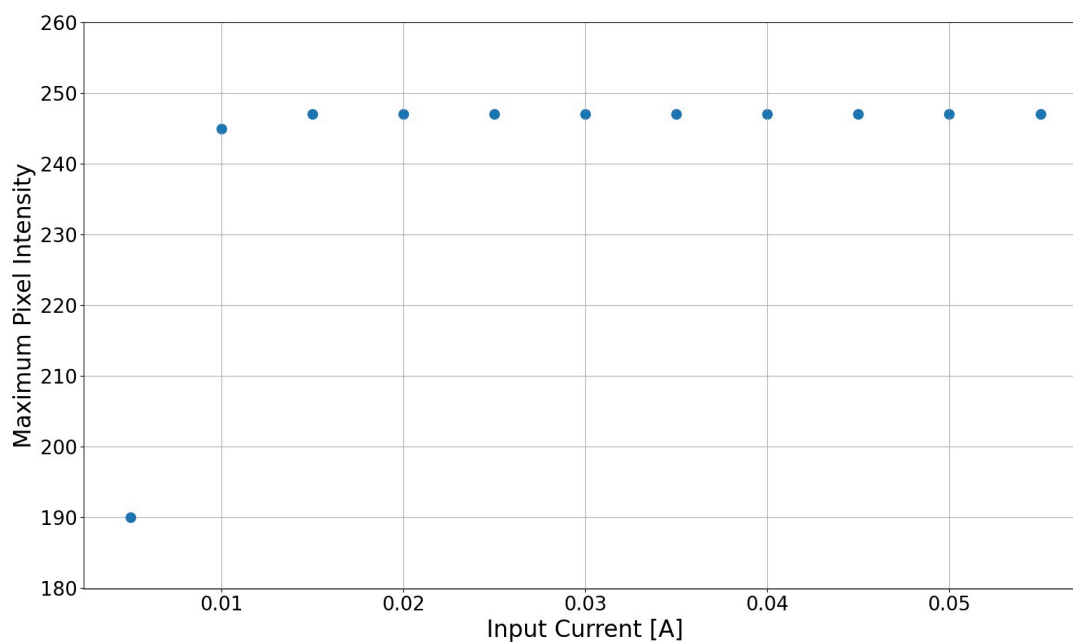


Figure 52: Maximum pixel intensity of the background-corrected images obtained using the setup depicted in Figure 50, plotted against input current from the power supply.

obtained images were corrected by subtracting an average background image composed of 10 frames before powering the LED. Figure 52 presents the maximum pixel intensity of the corrected images at various input currents. The graph reveals that input currents up to 0.015 A produce unsaturated images. An input current of 0.01 A was selected, as it gives a maximum pixel intensity of 245—approximately 95% of the 8-bit maximum intensity value of 255—and remains within the linearity range of the LED. The background-corrected image, converted to grayscale, is shown in Figure 53.

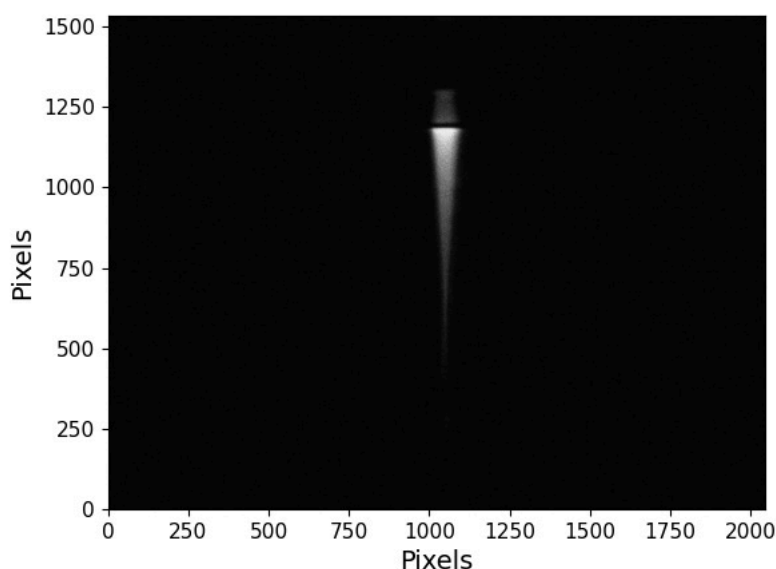


Figure 53: Grayscale image of the UV light passing through the fluorescent dye (Coumarin-120)-water mixture, corrected for background noise, captured at an input current of 0.01 A. The light is incident from the top.

6.4 Optical Absorption

The optical absorption properties of UltimaGold XR were studied to understand the efficiency at which light is absorbed as it travels through the solution. This property was quantified by measuring the attenuation length, which is the distance over which the intensity of light decreases to approximately $1/e$ (about 36.8%) of its initial value [102].

The optical absorption is typically measured using a spectrophotometer. A light source is used to generate wavelengths within the visible spectrum, which are captured and focused into a prism or grating. These components act as monochromators, dispersing light into different wavelengths. A slit is used to select a specific wavelength, which passes through the sample contained in a cuvette. The transmittance, T , is calculated by dividing the measured intensity of the transmitted light, I_t , by the intensity of the light before it passes through the sample, I_0 . The absorbance, A , is then calculated using Equation 6.1 [103].

$$A = -\log\left(\frac{I_t}{I_0}\right) = -\log(T) \quad (6.1)$$

Given that the absorbance is related to the absorption coefficient, ϵ , the concentration of the sample, c , and the path length, l , using Equation 6.2 (known as the Beer-Lambert Law), the attenuation length, L_{att} , is calculated using Equation 6.3 [104].

$$A = \epsilon cl \quad (6.2)$$

$$L_{att} = \frac{1}{\epsilon c} = \frac{l}{A} \quad (6.3)$$

For the optical absorption measurement, two samples were prepared and evaluated as potential candidates for filling the inner volume of the SmartPhantom: a cuvette containing the Ultima Gold XR cocktail and another containing a 50-50 mixture with distilled water. The optical absorption of these solutions was measured using a SHIMADZU UV-3600 spectrophotometer, with an air-filled cuvette serving as baseline [105]. The cuvettes, each 10 mm wide, were sealed with 3D-printed lids and double-sealed with tape to prevent any spillage. The prepared solutions are shown in Figure 54.

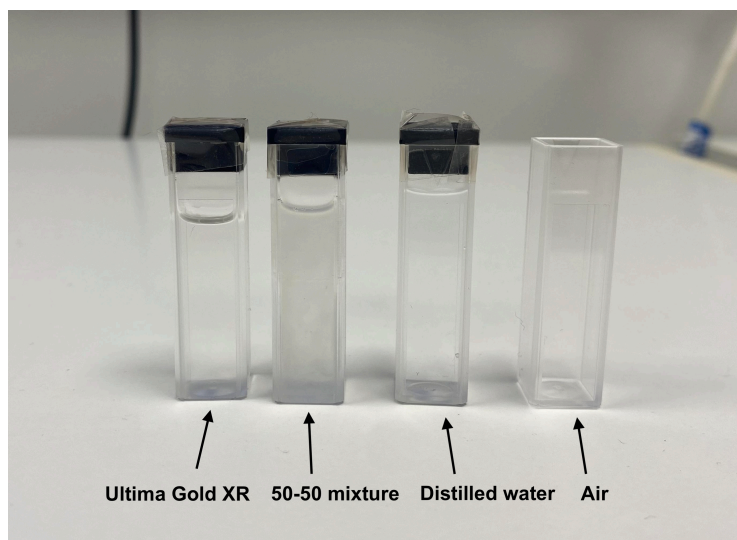


Figure 54: Image showing the four cuvettes prepared for measuring the absorbance of Ultima Gold XR and a 50-50 mixture with distilled water using a spectrophotometer. The cuvette containing air was used as a baseline for the measurements.

A 1 nm slit was used and the absorption measurement was performed across the 400 to 550 nm wavelength range at a scanning speed of 0.1 nm/s. Figure 55 shows the absorbance as a function of wavelength for the 2 different samples.

Both solutions show high absorbance at short wavelengths, towards the UV range, which falls rapidly as the wavelength increases. In addition, the absorbance of the Ultima Gold XR cocktail drops to zero at approximately 430 nm. In contrast, the 50-50 mixture exhibits relatively high absorbance beyond 430 nm, extending in the visible spectrum. This behaviour suggests significant light scattering in the presence of water. Such scattering can interfere with the light emitted due to the energy depositions of the incoming beam and can potentially lead to distorted images. To prevent this, a pure (100%) Ultima Gold XR cocktail is chosen to fill the SmartPhantom. In addition, at 400 nm, the attenuation length is calculated to be 2.96 mm, meaning that the intensity of the light will be reduced by 36.8% after travelling 2.96 mm in the liquid scintillator. In contrast, the attenuation

length at wavelengths greater than 430 nm is infinite, suggesting that light emitted at these wavelengths will not be absorbed or scattered.

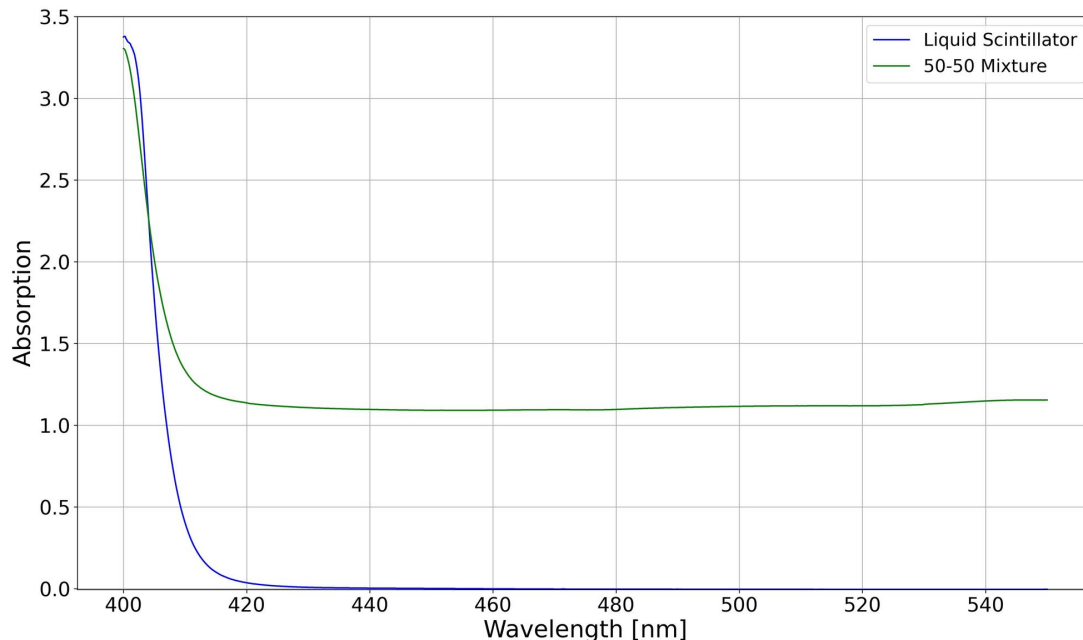


Figure 55: Optical absorption spectra of the liquid scintillator (blue) and a 50-50 mixture with distilled water (green), measured using a spectrophotometer. Baseline medium: air.

6.5 Response and Saturation

The linearity of the response and the saturation behaviour of the liquid scintillator were investigated through a series of experiments conducted at the MC40 cyclotron in Birmingham [15]. Firstly, a small quantity of the Ultima Gold XR cocktail was inserted in a custom-designed 3D-printed cuvette, which was positioned at the cyclotron's exit window. An optical system, comprising an achromatic lens followed by a 1 mm aperture, was used to collimate the scintillation light and focus it onto a PN diode, which generated a photocurrent that was measured using a multimeter. The cuvette, associated optics and photodiode readout system were provided by Professor Peter Hobson, School of Physical and Chemical

Sciences, Queen Mary University of London. The Computer-Aided Design (CAD) model of the cuvette and images of the experimental set-up are shown in Figure 56.

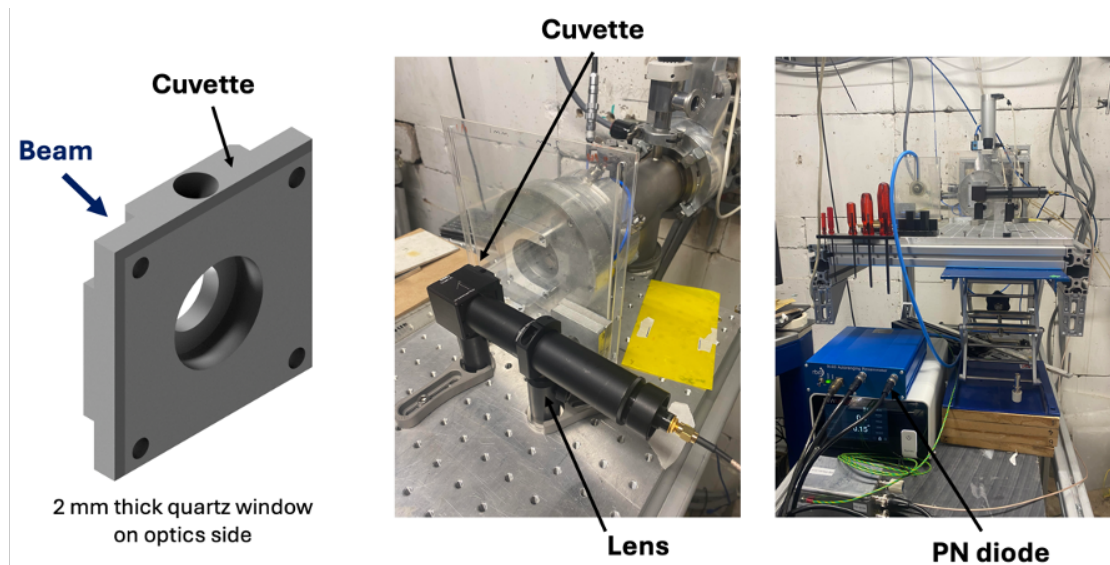


Figure 56: Computer-aided design model of the cuvette designed to contain the liquid scintillator (left) and images of the experimental set-up (middle and right) used to study the linearity of the liquid scintillator’s response to absorbed dose and saturation behaviour. The experiment was conducted at the MC40 cyclotron in Birmingham [15].

Figure 57 shows the measured PN diode current against the current at the Faraday cup for a design proton energy of 26.65 MeV. A line of best fit was applied to the data and the Pearson correlation coefficient, R^2 , was calculated to be 0.991, indicating a strong linear correlation [108]. The results demonstrate a linear response up to 1600 nA, suggesting that the liquid scintillator remains unsaturated at this level, with no evidence of quenching.

A second experiment was conducted in which an imaging system, comprising an achromatic lens (25.4 mm diameter, 50.8 mm focal length) and a Chameleon3 CM3-U3-31S4M-CS camera, was mounted on the side of the SmartPhantom through a glass window [106]. To create a narrow beam resembling the one expected at the LION beamline, a 2 mm circular collimator was placed at the entrance window of the SmartPhantom. Moreover, the cam-

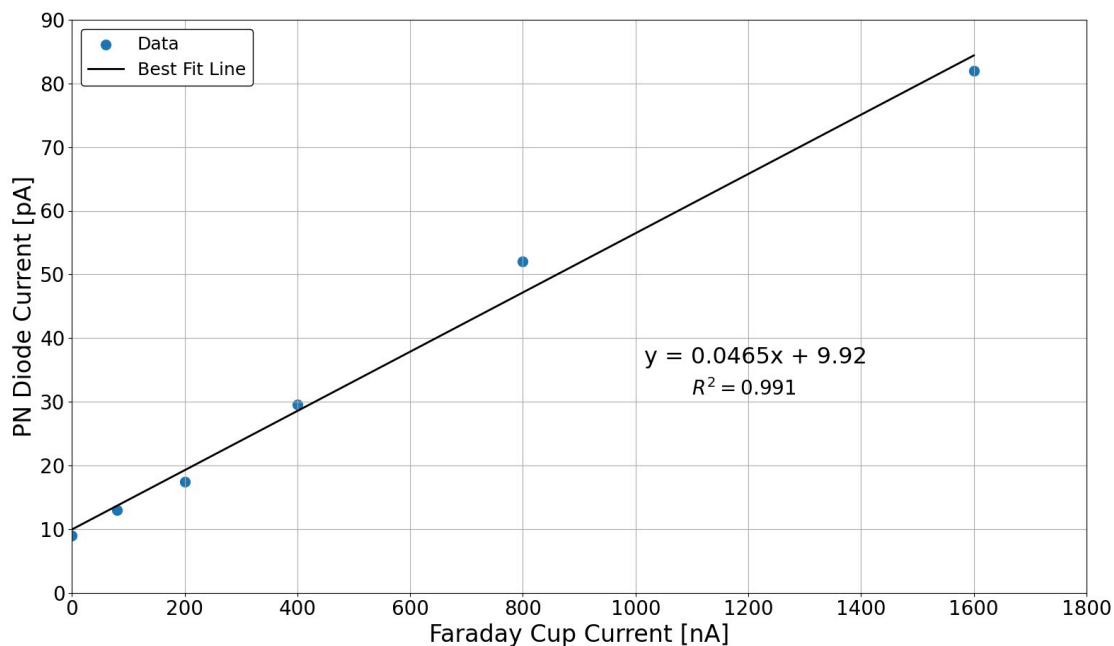


Figure 57: Plot of PN diode current against the current measured at the MC40 cyclotron’s Faraday cup, using the experimental set-up depicted in Figure 56 and a 26.65 MeV proton beam. A line of best fit is added to the data and a regression coefficient of 0.991 is calculated, indicating a strong linear correlation with no evidence of quenching in the liquid scintillator.

era was connected to a laptop operated remotely outside the concrete chamber, enabling real-time light acquisition. An image of the experimental set-up is shown in Figure 58.

The proton beam current in the cyclotron, and hence the number of particles in the beam, was varied up to 1050 nA, corresponding to approximately 96 million protons. To study different proton energies, the energy of the particles was degraded from an initial energy of 26.65 MeV by placing Perspex sheets of varying thicknesses at the cyclotron’s exit window. Specifically, 1, 2 and 3 mm Perspex sheets were used, resulting in proton beam energies of 23.66, 21.25 and 18.59 MeV, respectively.

The camera orientation was adjusted until a clear image of the proton beam depositions in the liquid scintillator was obtained. The average pixel intensity of the images was

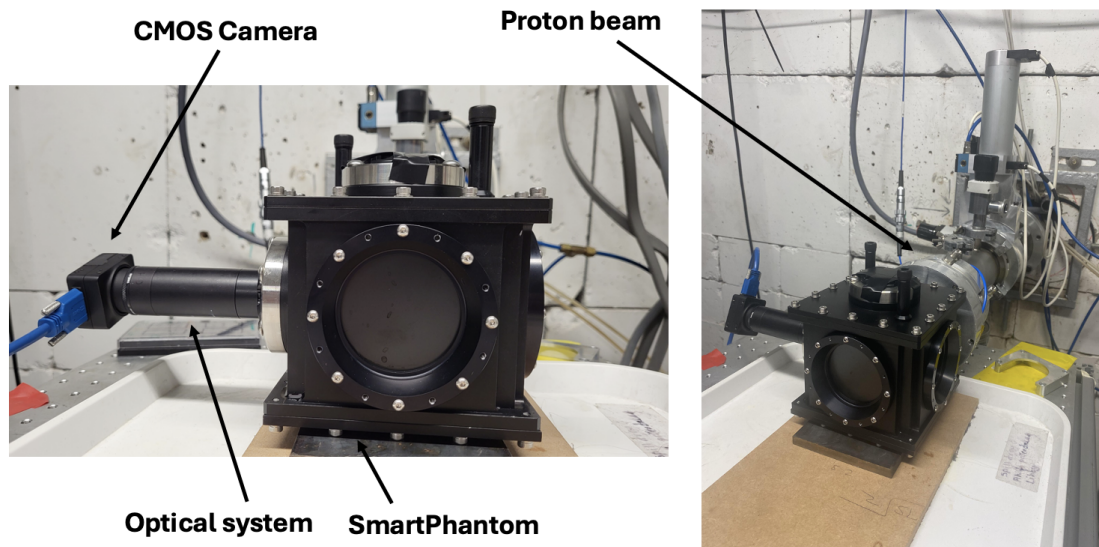


Figure 58: Image of the experimental set-up used to capture the scintillation light caused by the passage of the proton beam through the liquid scintillator inside the SmartPhantom.

calculated, with the results displayed in Figure 59. The background noise was kept constant by maintaining a consistent camera exposure time of 0.2 seconds across all runs. Lines of best fit were added to the data to assess the linearity in the liquid scintillator's response. The results demonstrate that the liquid scintillator exhibits a linear response to the absorbed dose across the investigated energies and particle numbers.

Figure 60 shows the image obtained with a 26.65 MeV proton beam and 96 million protons, corrected for the background and converted to grayscale. The beam enters from the left. From the image, it can be concluded that the SmartPhantom's entrance window is located at approximately the 850th pixel on the x-axis due to the sudden increase in brightness observed at that point. The pixel brightness appears low and uniform, gradually increasing towards the right, consistent with the energy deposition curve expected for a proton beam. The brightest region in the image corresponds to the Bragg peak, beyond which the brightness gradually drops to zero.

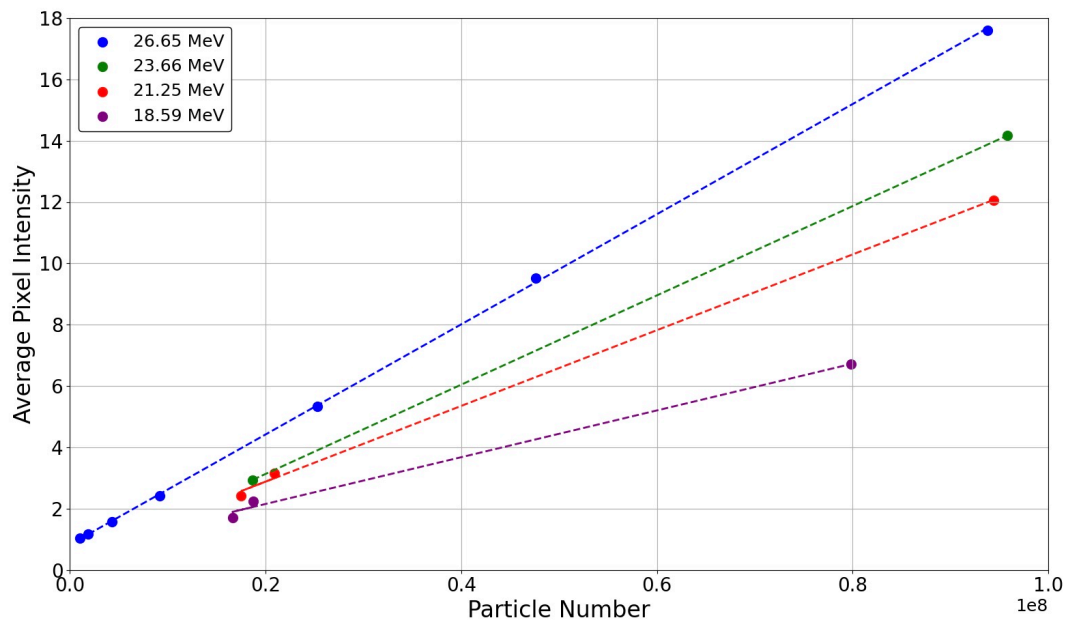


Figure 59: Average pixel intensity of the images obtained using the experimental set-up shown in Figure 58, plotted against particle proton number at various proton energies.

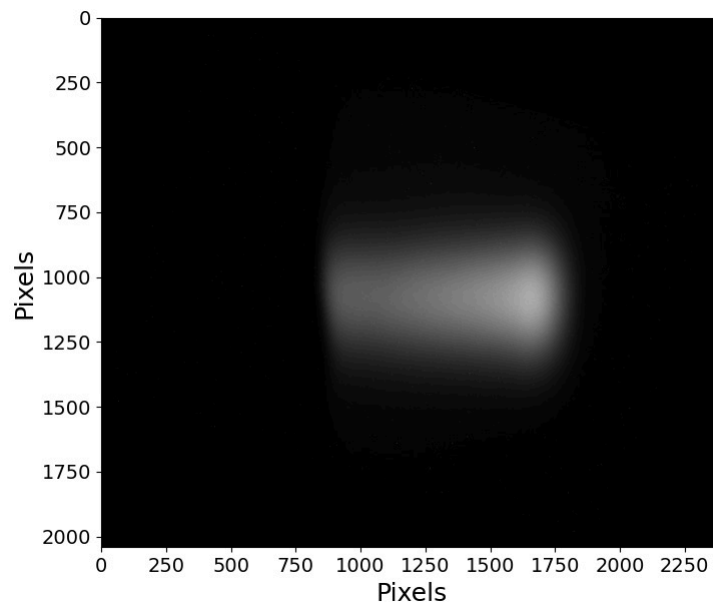


Figure 60: Image captured with the experimental set-up depicted in Figure 58 when a 26.65 MeV proton beam of 95 million particles propagates through the liquid scintillator. The beam enters from the left, with the brightest region corresponding to the Bragg peak.

Figure 61 displays a colour map of the pixel intensities in the image shown in Figure 60. The deep purple colour corresponds to low-intensity pixels and bright yellow corresponds to high-intensity pixels. The colour scale on the right-hand side of the plot indicates a maximum pixel intensity of approximately 250, suggesting that the image is unsaturated at the given proton beam energy and particle count. In addition, a vertical and a horizontal black line are overlaid on the image to indicate the transverse and longitudinal directions, respectively.

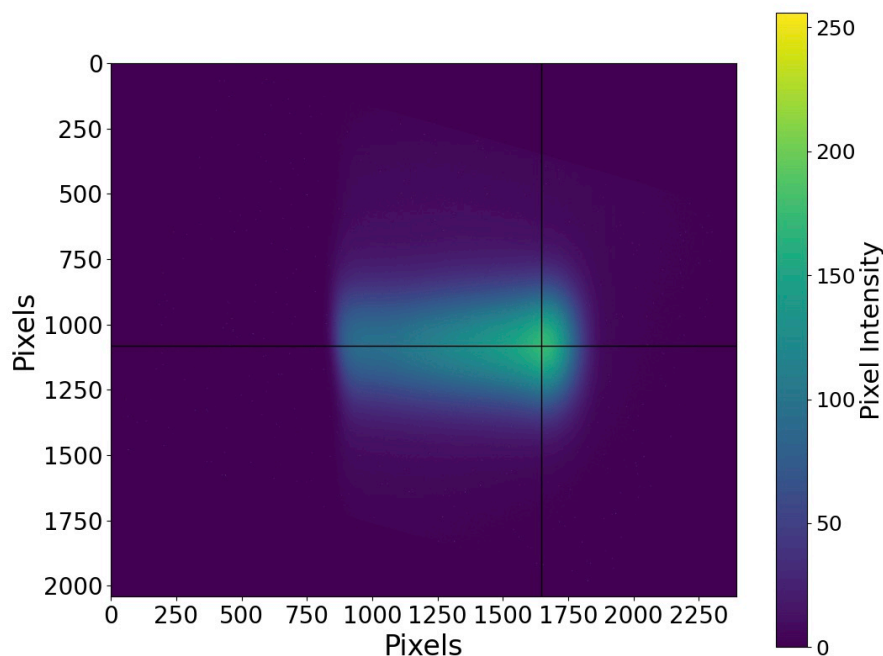


Figure 61: Colour map of the pixel intensities present in Figure 60. Deep purple corresponds to low-intensity pixels and bright yellow corresponds to the high-intensity pixels. The vertical and horizontal black lines indicate the transverse and longitudinal directions, respectively.

The energy deposition profiles in the z-direction, that is the beam propagation axis, and the x-direction were plotted by averaging 60 pixels along the respective black lines. These profiles are displayed in Figure 62, with the height corresponding to the average

pixel intensity. The top plot shows the beam profile along the direction of beam propagation, revealing a shape resembling the Bragg peak curve, while the bottom plot shows the transverse profile, revealing a highly symmetrical circular proton beam. The ability to extract these profiles from the images obtained suggests that positioning an additional camera orthogonal to the existing setup could provide the y-profile, enabling a three-dimensional reconstruction of the beam's energy depositions within the SmartPhantom.

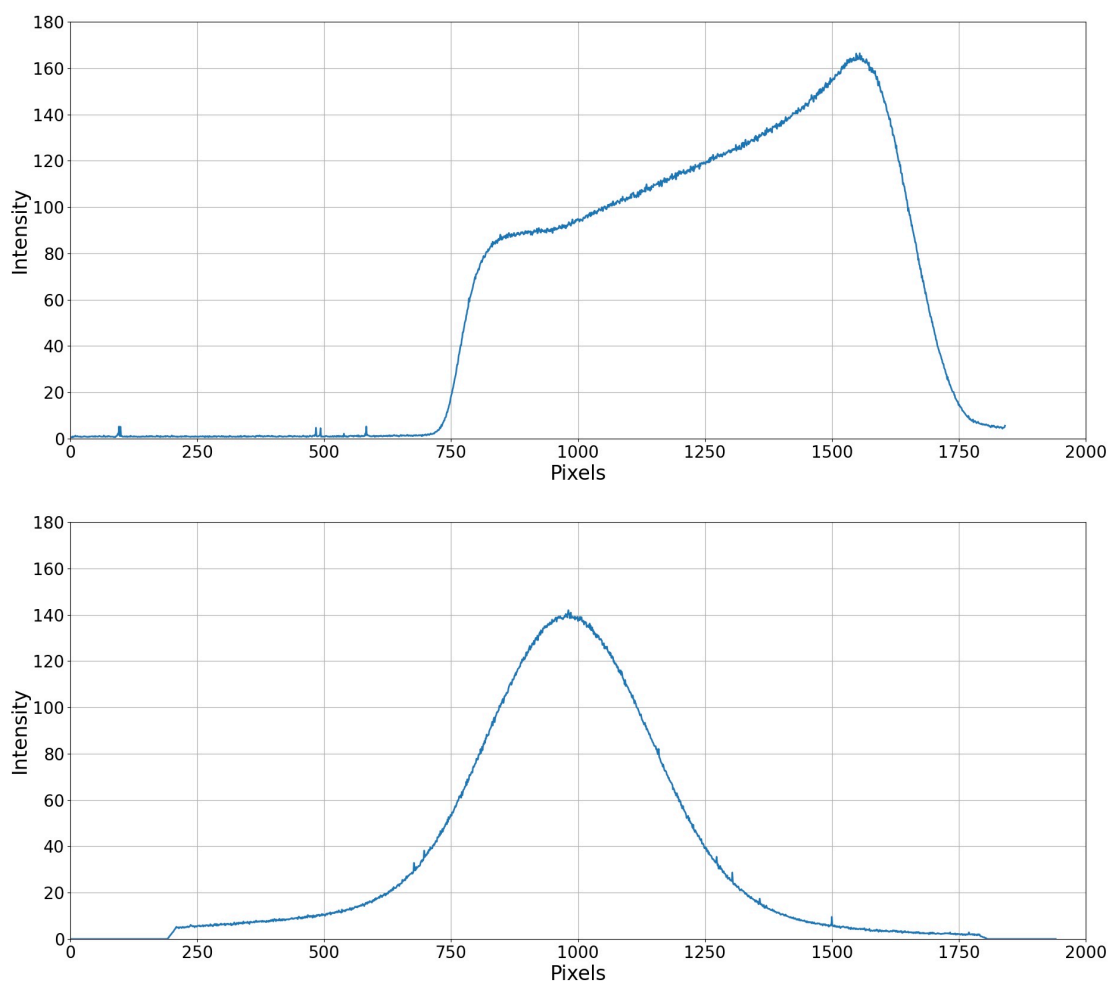


Figure 62: Energy deposition profiles of a 26.65 MeV proton beam with 95 million protons propagating through the liquid scintillator in the SmartPhantom. Top: longitudinal profile, obtained by averaging 60 pixels along the horizontal black line in Figure 61. Bottom: transverse profile, obtained from an average of 60 pixels along the vertical line.

Chapter 7

Scintillating Fibre Detectors

The scintillating fibre detectors are composed of multiple scintillating fibres arranged in a two-dimensional array. The fibres are secured on aluminium frames using epoxy resin as an adhesive. BCF-20 plastic scintillating fibres have been chosen, which are $250\text{ }\mu\text{m}$ in diameter, produce approximately 8000 photons per MeV and have a decay time of approximately 2.7 ns [109].

An array of 66 fibres in each direction was deemed sufficient to cover the effective area of the beam. This design led to the development of 20 mm square scintillating fibre detectors, with a centre-to-centre pitch of $305\text{ }\mu\text{m}$ to facilitate construction. In addition, multiple scintillating fibre detectors can be arranged in parallel. Strategic placement of the detectors along the rising edge of the energy deposition curve could provide three-dimensional information about the energy depositions of the beam inside the SmartPhantom.

7.1 Simulation

The scintillating fibre detectors were simulated in Geant4. For simplicity, the fibres have been modelled as polystyrene cylinders, without a scintillating doped core or cladding coating. The detectors were uniformly spaced and placed near the entrance window of the SmartPhantom. For the configuration where the scintillating fibre detectors are used, water is chosen as the propagating medium to avoid interference with the scintillation light produced by the liquid scintillator. Figure 63 provides a schematic diagram of the Geant4 simulation, illustrating the arrangement of the scintillating fibre detectors.

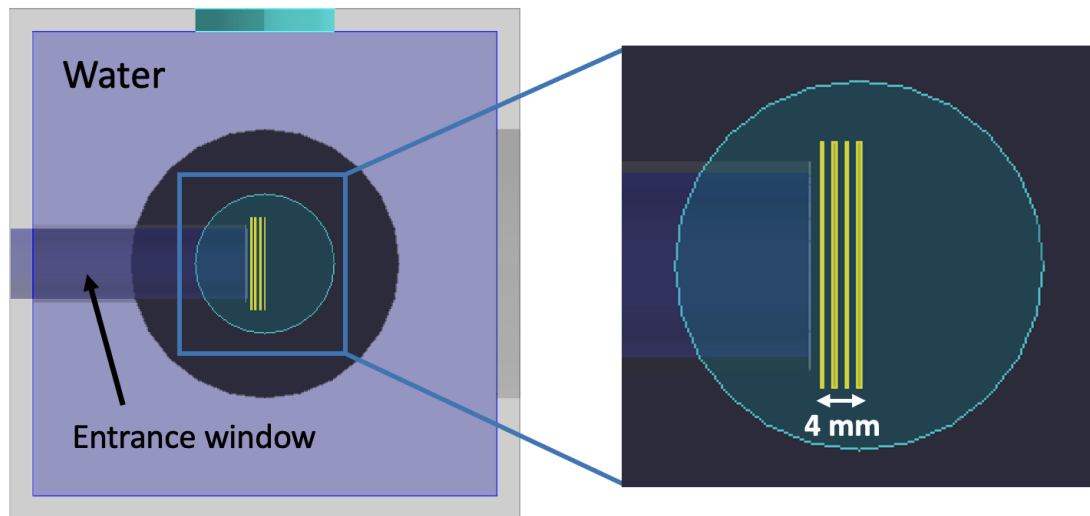


Figure 63: Geant4 simulation of the SmartPhantom with four scintillating fibre planes (yellow) placed equidistant from the entrance window.

7.1.1 Two-Dimensional Reconstruction

The energy deposited in each individual fibre as the simulated LION beam consisting of 10^6 particles passes through the detectors, along the vertical plane (top) and horizontal plane (bottom), is shown in Figure 64. The plots reveal a peak energy deposited in the middle fibre, as it is directly aligned with the axis of the beam. Neighbouring fibres exhibit lower energies, with the values decreasing symmetrically towards zero at the detector's edges. Both distributions exhibit a Gaussian-like shape, with the horizontal plane appearing broader due to the elliptical shape of the incoming beam.

Figure 65 displays the two-dimensional distribution of the energy depositions at the various depth, plotted by combining the data from the horizontal and vertical fibre planes. Detector 1 is positioned closest to the entrance window and Detector 4 nearest to the Bragg peak. The energy deposited, in MeV, is presented by the colourbar on the right, with red corresponding to the highest energy depositions and dark blue the lowest.

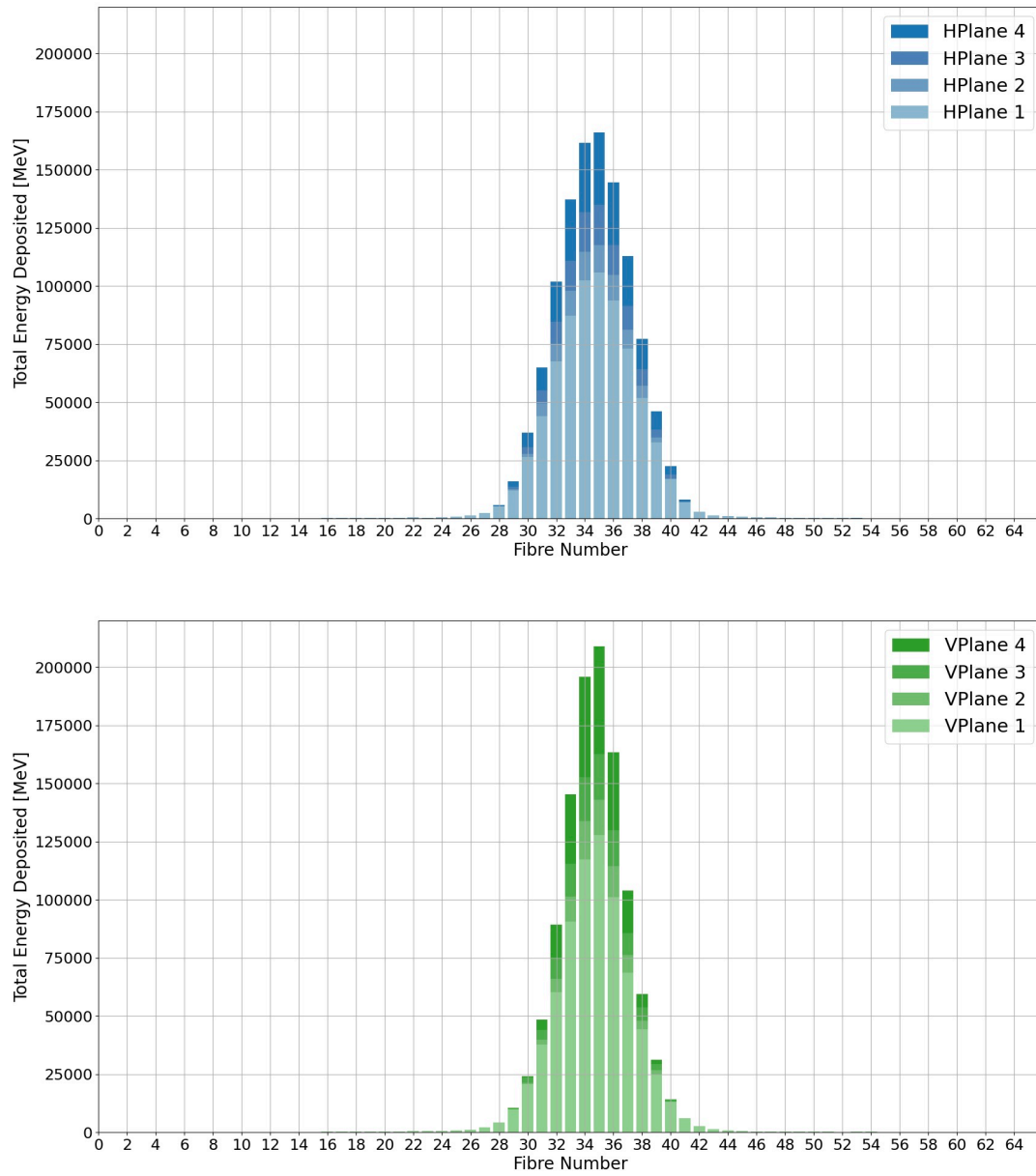


Figure 64: Energy deposited in each fibre of the two-dimensional scintillating fibre detectors, when the simulated LION beam consisting of 10^6 particles passes through them. Top: fibres oriented along the horizontal axis. Bottom: fibres oriented along the vertical axis. The different colours correspond to different detectors, with Plane 1 positioned closest to the entrance window and Plane 4 nearest the Bragg peak.

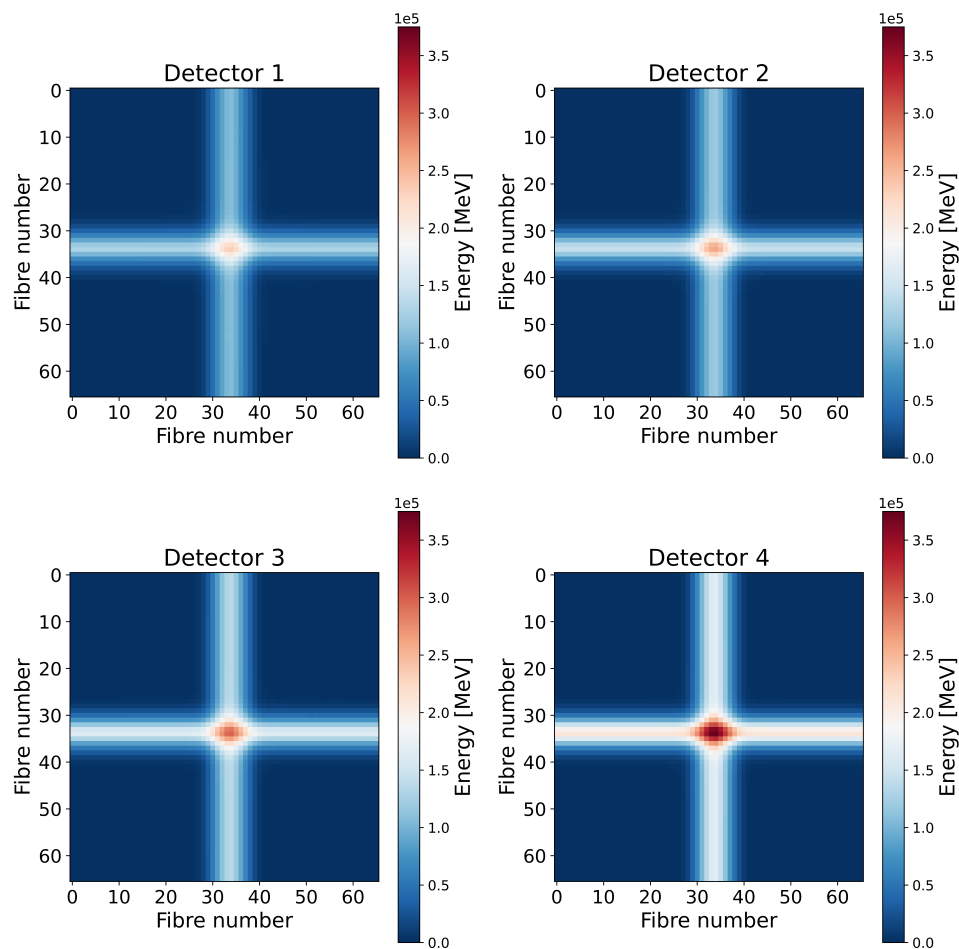


Figure 65: Two-dimensional energy distribution reconstructed using the simulated deposited energy in each scintillating fibre in the detector arrays, when the simulated LION beam consisting of 10^6 particles passes through them. Each subplot corresponds to a different detector, where Detector 1 is located nearest to the entrance window of the SmartPhantom and Detector 4 is closer to the Bragg peak. Each detector is 2 cm long.

Figure 65 demonstrates a gradual increase in the energy deposited as the beam propagates deeper into the SmartPhantom. This behaviour arises from the fact that beam slows down as it penetrates the medium, depositing more and more energy until it comes to a stop—a characteristic of the energy deposition curve. In addition, an increasing radius is observed, which can be explained by Coulomb scatterings that cause the beam to diverge.

Moreover, the energy can be converted into light output using the manufacturer's reported light yield of 8000 photons per MeV deposited in the fibres. In addition, the capture efficiency is specified to be 3.44% [109]. Based on these values, the two-dimensional photon light yield in the detectors was estimated and presented in Figure 66.

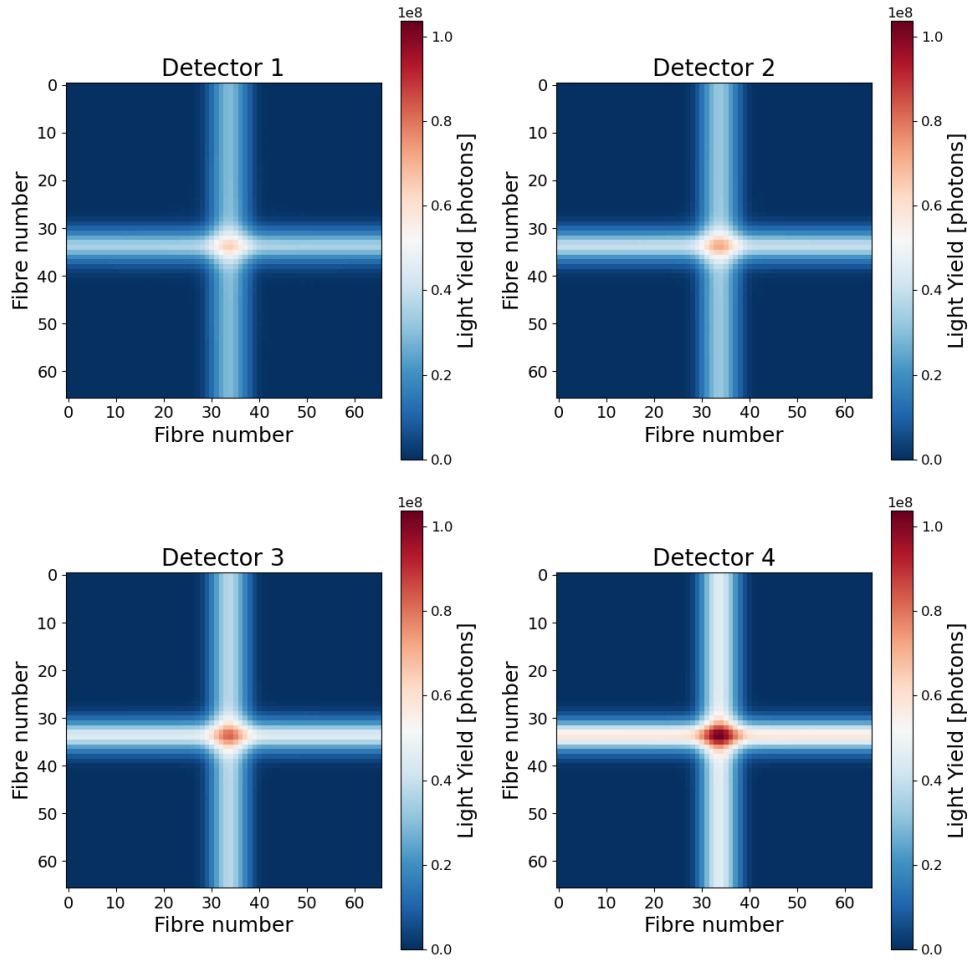


Figure 66: Two-dimensional estimation of the scintillating fibre detectors' light output. The estimation is calculated from the energy depositions shown in Figure 65, the manufacturer's reported light yield of 8000 photons per deposited MeV and the stated fibre capture efficiency of 3.44% [109].

7.1.2 Bragg Peak Reconstruction

The energy deposited in each scintillating fibre was used to calculate the total energy deposited in each detector. By fitting the data to an analytical approximation of the Bragg peak curve, the longitudinal energy profile can be reconstructed. This analytical approximation, known as the Bortfeld approximation, is defined by Equations 7.1, 7.2 and 7.3 [30]. In these equations, z represents the longitudinal position, R_0 denotes the particle range, σ is the standard deviation, Φ_0 is the particle fluence (the number of particles per unit area), ϵ is the fraction of the fluence contributing to the 'tail' of the energy spectrum and \mathfrak{D} refers to the parabolic cylinder function. These equations are valid for proton beams with energies ranging between 10 and 200 MeV, travelling through water [30].

$$D(z) \approx \begin{cases} \hat{D}(z) & \text{for } z < R_0 - 10\sigma \\ D(z) & \text{for } R_0 - 10\sigma \leq z \leq R_0 + 5\sigma \\ 0 & \text{otherwise.} \end{cases} \quad (7.1)$$

$$\begin{aligned} \hat{D}_{H_2O}(z) = \frac{\Phi_0}{1 + 0.012R_0} & \left[17.93(R_0 - z)^{-0.435} \right. \\ & \left. + (0.444 + 31.7\epsilon/R_0)(R_0 - z)^{0.565} \right] \end{aligned} \quad (7.2)$$

$$\begin{aligned} D_{H_2O}(z) = \Phi_0 \frac{e^{\frac{-(R_0-z)^2}{4\sigma^2}} \sigma^{0.565}}{1 + 0.012R_0} & \times \left[11.26\sigma^{-1} \mathfrak{D}_{-0.565}\left(-\frac{R_0 - z}{\sigma}\right) \right. \\ & \left. + (0.157 + 11.26\epsilon/R_0) \mathfrak{D}_{-1.565}\left(-\frac{R_0 - z}{\sigma}\right) \right] \end{aligned} \quad (7.3)$$

For the fit, the beam range in water, R_0 , was calculated using Equation 2.4, while Φ_0 and σ were determined using Equations 7.4 - 7.7. In these equations, σ_{mono} and σ_{E_0} are the width of the Gaussian range straggling and the width of the Gaussian energy spectrum, respectively [30]. In addition, the parameter ϵ was set to 10% and the parabolic cylinder function, \mathfrak{D} , was implemented using a special function available in Python.

$$\Phi_0 = \frac{N_{\text{protons}}}{\pi r_{\text{beam}}^2} \quad (7.4)$$

$$\sigma_{\text{mono}} = 0.012 \times R_0^{0.935} \quad (7.5)$$

$$\sigma_{E_0} = 0.01 \times E_0 \quad (7.6)$$

$$\sigma = \sqrt{\sigma_{\text{mono}}^2 + \left(\sigma_{E_0} \times \alpha \times p \times E_0^{p-1} \right)^2} \quad (7.7)$$

Figure 67 illustrated the reconstructed Bragg peak curve using the Bortfeld approximation, fitted to the data from the scintillating fibre detectors. The data points with different shades of blue represent the total energy deposited in each detector, calculated by summing the energy in each individual fibre in the arrays. The blue dashed line corresponds to the Bortfeld fit. For comparison, the black points present the energy depositions extracted from Geant4, where the simulation was divided into 0.5 mm voxels to match the detectors' width, ensuring a fair comparison of the plot heights.

Figure 67 demonstrates that the Bortfeld fit provides a good estimate of the rising edge of the energy deposition curve, however, it significantly overestimates the range. The peak of the curve occurs at approximately 4.4 mm, compared to the expected range of approximately 4.05 mm. The discrepancy is expected to improve with further optimization of the detector positions [110]. In addition, both curves seem to reach zero at a depth approx-

imately 6 mm from the SmartPhantom's entrance window. Lastly, the small deviations between the detector energy measurements and the Geant4 data along the rising edge can be attributed to the different voxel sizes used for each.

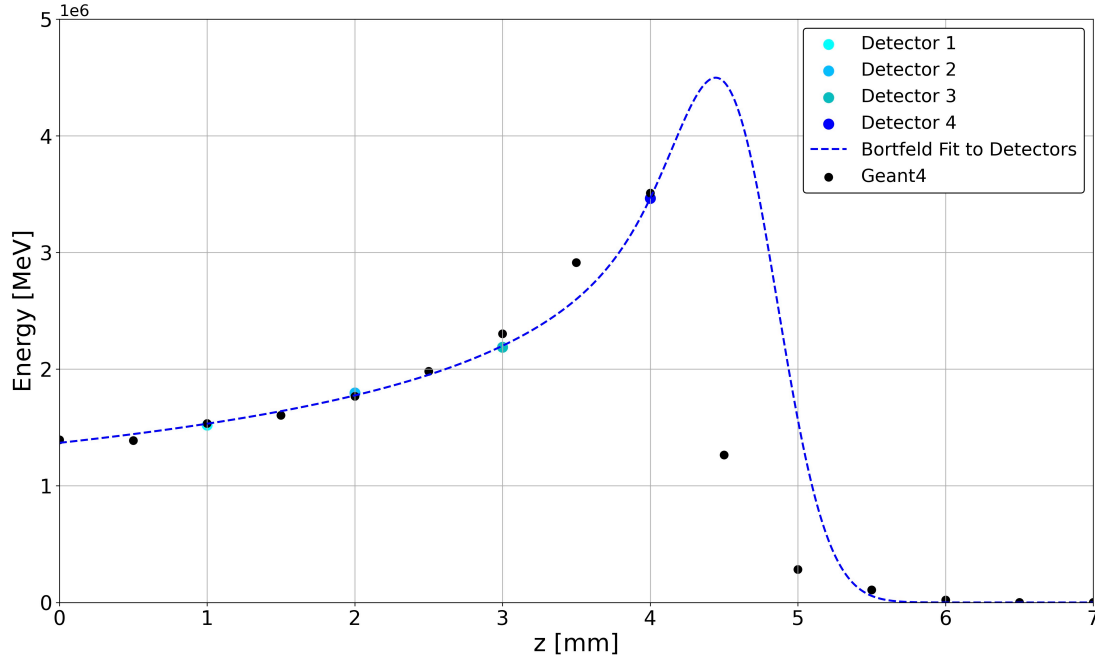


Figure 67: Reconstruction of the longitudinal energy deposition profile using the Bortfeld approximation (dashed line) as defined in Equations 7.1 - 7.3, fitted to the data from the scintillating fibre detectors (various shades of blue). The black points correspond to the the Geant4 simulation results for comparison.

7.1.3 Acoustic Wave Distortion

The scintillating fibre detectors were simulated in k-Wave to investigate their influence on the acoustic signals. For simplicity, the detectors were simulated as cuboid objects with the same speed of sound and density as the fibres. Figure 68 displays the acoustic wave generation and propagation within the three-dimensional space when the scintillating fibre detectors are positioned at the same locations as the Geant4 simulation.

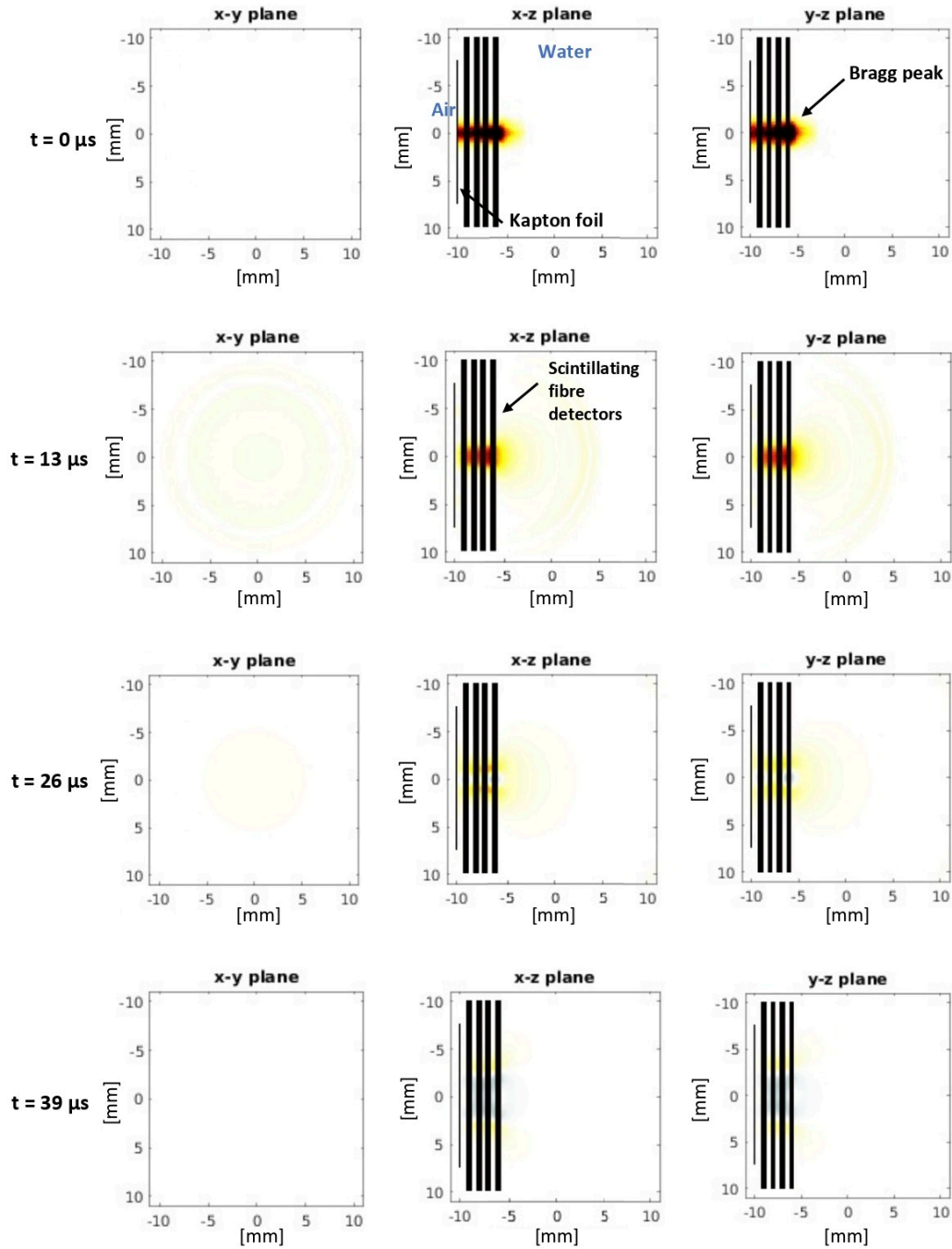


Figure 68: Ion-acoustic signal generation and evolution within the SmartPhantom, simulated using k-Wave, including the scintillating fibre detectors.

Figure 68 shows that the acoustic waves reflect off the detector surfaces when present, in contrast to their smooth propagation in their absence, seen in Figure 32. The waves interact with the scintillating fibre detectors, with the disturbance of the acoustic field being anisotropic. This effect is likely due to the acoustic impedance mismatch.

At room temperature, water has a sound speed of 1500 m/s and a density of 997 kg/m³. Using the acoustic impedance formula, $Z = \rho c$, the acoustic impedance for water, Z_{water} , is calculated to be $1.496 \times 10^6 \text{ Pa} \cdot \text{s/m}$ [112]. Similarly, the acoustic impedance for the scintillating fibre detectors, Z_{SciFi} , is found to be $1.92 \times 10^6 \text{ Pa} \cdot \text{s/m}$, based on the density of 1050 Kg/m³ and the sound speed of 1825 m/s. The reflection and transmission coefficients between the two media are then calculated using Equations 7.8 and 7.9 and are found to be equal to 0.0154 and 0.9846, respectively [112].

$$R = \frac{Z_{SciFi} - Z_{water}}{Z_{SciFi} + Z_{water}} \quad (7.8)$$

$$T = \frac{2Z_{SciFi}}{Z_{SciFi} + Z_{water}} \quad (7.9)$$

These values indicate the proportion of energy reflected or transmitted when an acoustic wave travels from one medium towards another. The values obtained therefore imply that approximately 1.54% of the acoustic wave is reflected off the scintillating fibre detectors, with that energy remaining confined between them. Approximately 98.46% is transmitted and reaches the ultrasound transducers.

Furthermore, Figure 69 displays the reconstructed images, generated after eight iterations of the iterative time-reversal algorithm, along the three orthogonal planes, with the scintillating fibre detectors included in the acoustic simulation. The reconstruction using the signals obtain by the matrix array is shown on the left, while the reconstruction using

the data from the linear array is shown on the right. For comparison, the three-dimensional source pressure is shown in Figure 31. In addition, the reconstructed profiles along each plane, compared to the source pressure, are displayed in Figure 70.

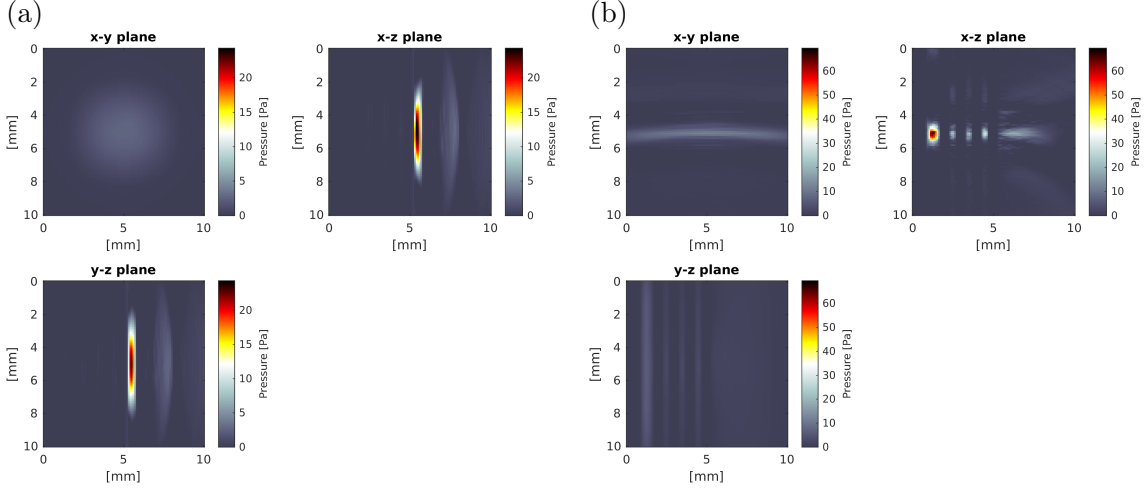


Figure 69: Reconstructed pressure distribution, after eight iterations of the iterative time-reversal algorithm, using the matrix array (a) and the linear array (b), when the scintillating fibre detectors are included in the acoustic simulation. Voxel size: 0.1 mm.

From the figures, it is evident that the regions covered by the scintillating fibre detectors are poorly reconstructed. These limitations can be attributed to the fact that only a small fraction of the acoustic waves are transmitted through, leading to a significant absence of acoustic information in the corresponding regions. As a result, the reconstruction algorithm is unable to retrieve the necessary signals, preventing it from recovering the corresponding pressure field.

As with the case without the detectors immersed in the SmartPhantom, discussed in Section 5.4, the matrix array performs better at reconstructing the Bragg peak due to its alignment with the beam axis and acoustic frequency bandwidth. However, the relatively high pressure values reconstructed at depths beyond the Bragg peak, can be due

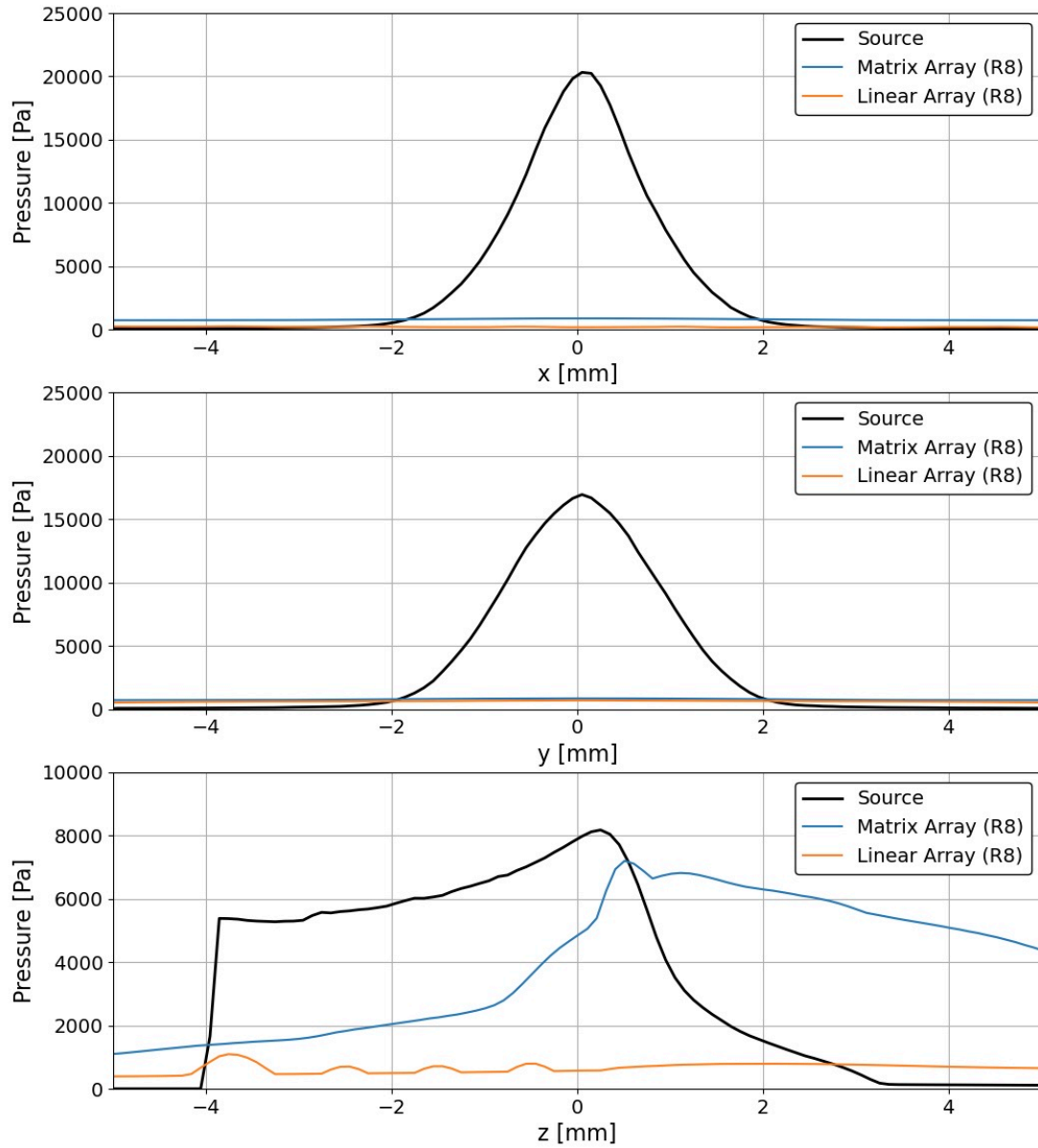


Figure 70: Reconstructed pressure distribution profiles along the x-(top), y-(middle) and z-(bottom) directions, using 8 iterations of the time-reversal algorithm, when the scintillating fibre detectors are included in the acoustic simulation.

to artefacts arising from multiple acoustic reflections off the detector surfaces or scattering of the acoustic waves. In addition, the linear array performs better at reconstructing the rising edge of the beam. However, it is still unable to provide an accurate reconstruction

in the regions occupied by the scintillating fibre detectors. This is observed as a dip in pressure, shown by the orange line in the third subplot of Figure 70.

7.1.4 Beam Divergence

Due to the acoustic wave distortion observed in the reconstructed pressure distributions, it was decided not to perform simultaneous acoustic and optical measurements with the scintillating fibre detectors. Instead, it was decided to suspend the scintillating fibre detectors in air and take measurements before filling the interior volume of the SmartPhantom. As the detectors do not need to be spaced by 1 mm and to ease the mechanical alignment, the detectors are now spaced over a total length of 9 mm. This arrangement enables the divergence of the beam emerging from the accelerator's exit window to be determined. The new Geant4 simulation is shown in Figure 71.

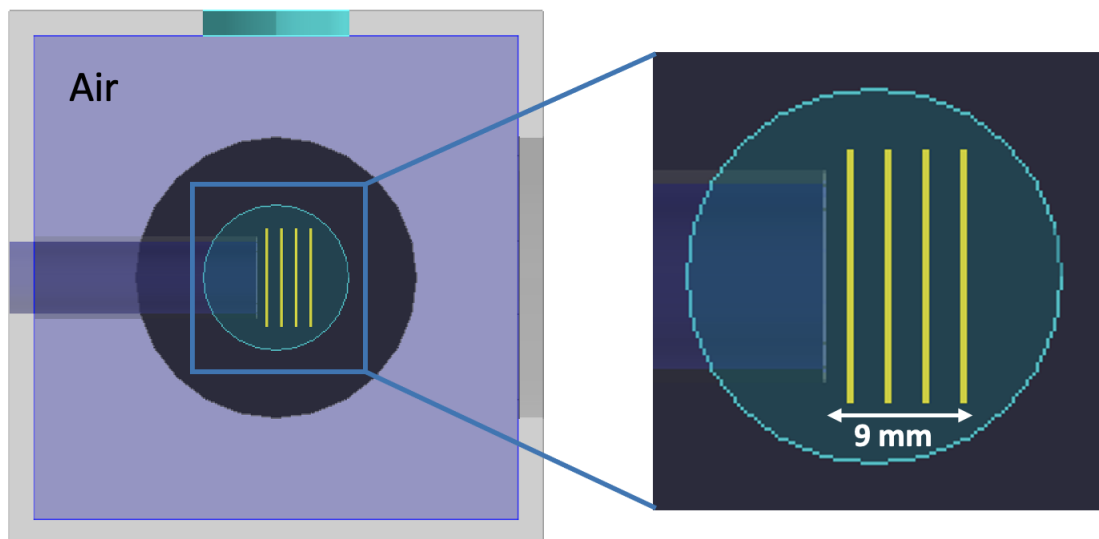


Figure 71: Geant4 simulation of the SmartPhantom, featuring the four scintillating fibre detectors (yellow) suspended in air, positioned equidistant from the end of the elongated entrance window.

The energy deposited in each fibre, when a 20 MeV proton beam passes through the detectors, in the horizontal and vertical fibre orientations are shown in Figure 72. The plots show minimal differences between each detector, suggesting little beam divergence. To quantify this, the FWHM of the beam along each axis was calculated by fitting Gaussian curves to the data, shown by the black dashed lines.

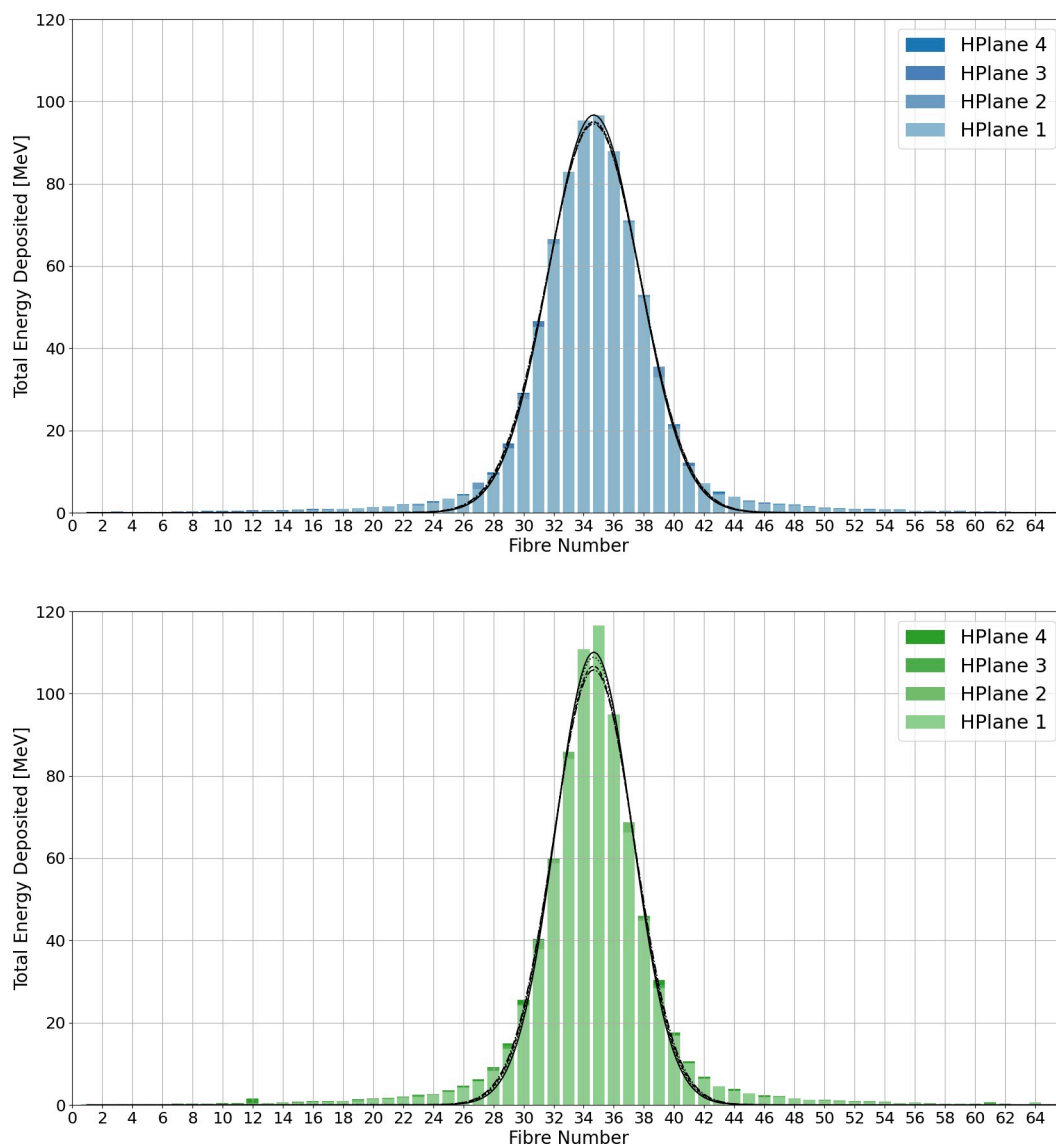


Figure 72: Energy depositions in each scintillating fibre of the two-dimensional scintillating fibre detector when suspended in air, inside the SmartPhantom's volume.

Figure 73 shows the FWHM values calculated from the fitted curves, in the horizontal direction (blue) and the vertical direction (green). From these plots, it is more noticeable that there is divergence of the beam as it travels in air. This divergence was quantified by calculating the tangent of each line, yielding a horizontal beam divergence of 0.0131 radians and a vertical beam divergence of 0.0236 radians over a travel distance of 9 mm in air.

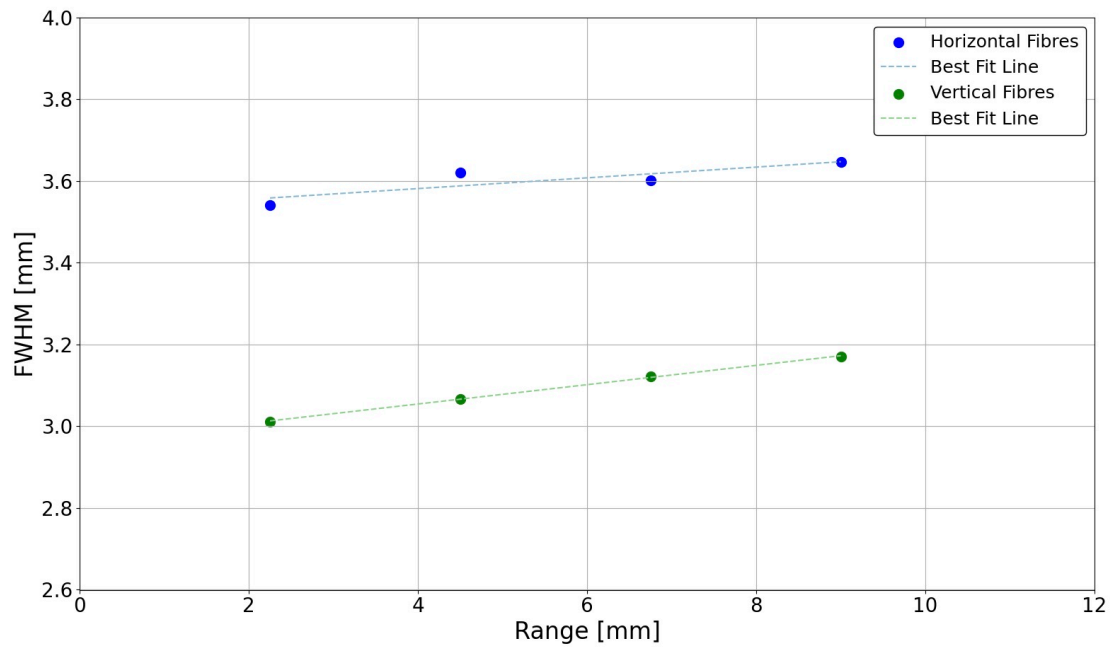


Figure 73: Full Width Half Maximum (FWHM) calculation of the beam width using the energy deposited in the fibres in the scintillating fibres detectors suspended in air inside the SmartPhantom. Blue: horizontal plane. Green: vertical plane.

7.2 Construction

Eight aluminium frames were designed and manufactured to serve as the foundation of the scintillating fibre detectors. Each frame is square measuring 32 mm on each side, with fibres arranged parallel to each other. To facilitate alignment and secure the fibres in place, multiple grooves, matching the diameter of the fibres, have been machined along the edges of the frames. The pre-cut grooves aid the production of detectors with consistent and uniform pitch.

In addition, sixteen aluminium clamps were designed to secure the scintillating fibres to the aluminium frames. Two clamps are placed on top of the fibres on each side, pressing them down. Each clamp features a central cavity that provides space for the application of epoxy resin, which acts as an adhesive. Moreover, multiple screw holes have been incorporated into the design to secure the assembly. To minimize reflections of the scintillation light from the silver aluminium surfaces, the frames have been anodised in black. An annotated CAD design of the scintillating fibre frames is shown in Figure 74.

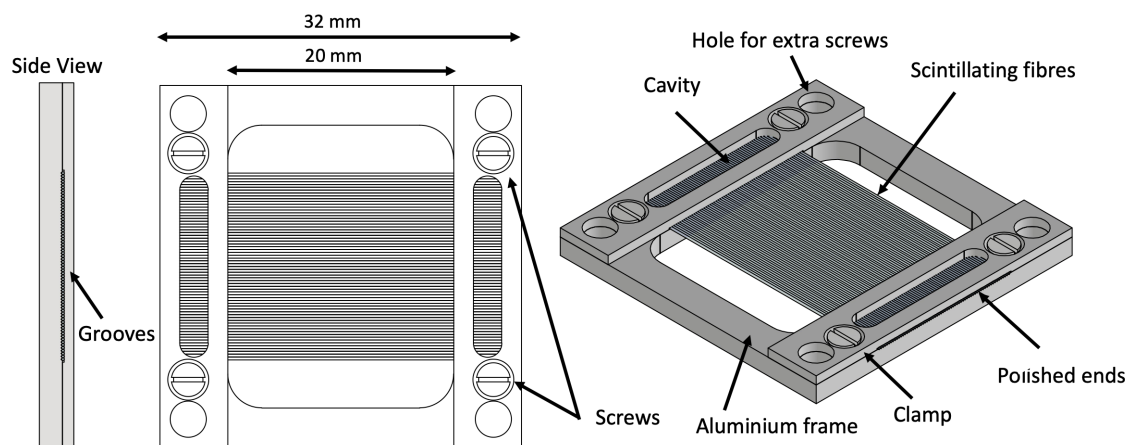


Figure 74: Annotated CAD design of the scintillating fibre frames, which form the foundation of the detectors positioned within the SmartPhantom to measure the incoming beam's cross-sectional area and divergence.

A winding jig has been fabricated to assist in the manufacturing of the scintillating fibre detectors. Two frames are mounted on each side of the jig, which is then rotated to wind the fibres around the jig, aligning them in the pre-cut grooves with each rotation. The use of a winding jig ensures constant and uniform tension between the fibres, while enabling the production of four scintillating fibre planes in each attempt. Figure 75 shows the winding jig, with two frames securely screwed onto one of its sides.

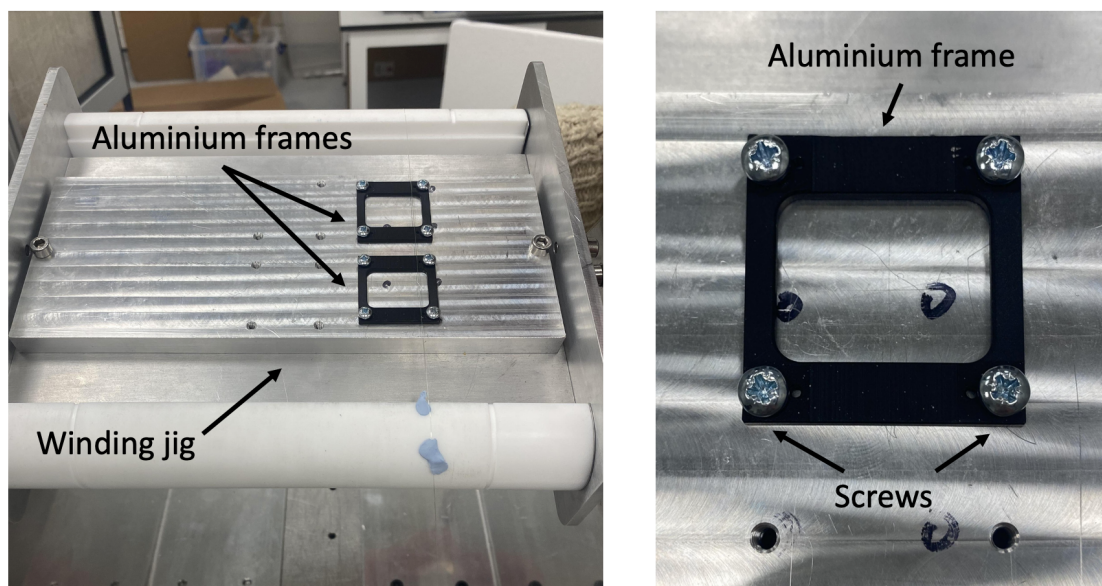


Figure 75: Annotated image of the winding jig used to manufacture the scintillating fibre detectors, showing two aluminium frames secured with screws on one of its sides.

Once the fibres were wound and aligned, the aluminium clamps were positioned to push the fibres down. A small amount of IN2 epoxy resin was mixed with AT30 slow hardener in a beaker at a 2:1 ratio [111] [113]. The ratio was chosen to ensure the mixture was neither too runny to spill into the detectors' activate area nor too hard to set immediately. After mixing, a pipette was used to apply gently a small portion of the solution into each frame's cavity. The resin was distributed evenly to ensure all the fibres were glued securely. The

setup was then covered with a light-proof black sheet to protect it from external light and left overnight to allow the resin to dry completely. Figure 76 shows the fibre planes on the winding jig after the scintillating fibres have been wound and the resin applied.

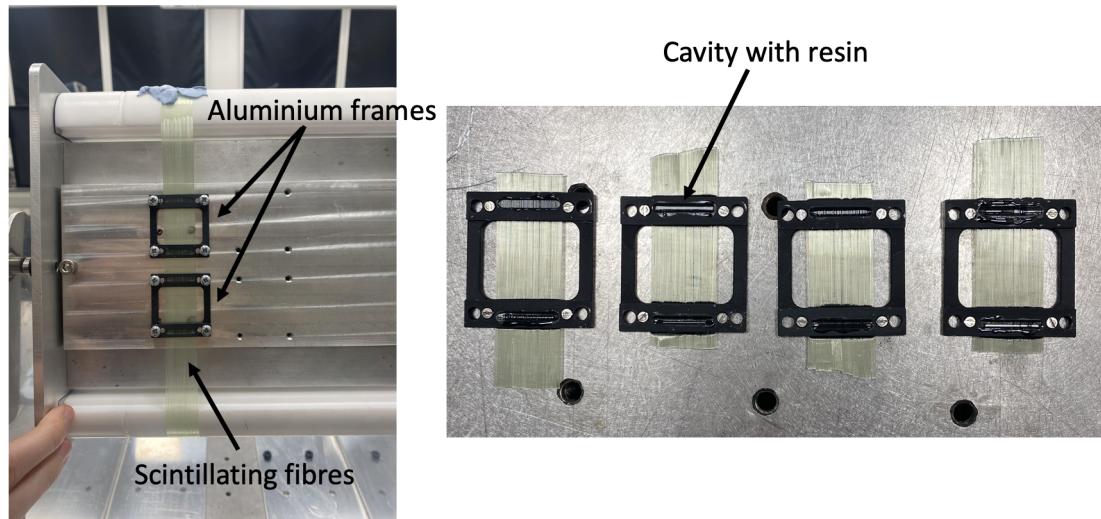


Figure 76: Annotated image of the scintillating fibre planes mounted on the winding jig, showing the fibres wound around the aluminium frames and the cavities filled with resin to firmly secure them.

The following day, the planes were separated by cutting sections of the fibres with a scalpel. Afterwards, the ends of the fibres were machined and polished to obtain a smooth, flat surface. Figure 77 displays the final result, showing eight scintillating fibre planes. These were paired and arranged perpendicularly to form two-dimensional fibre arrays. This configuration resulted in four detectors, which were then positioned side by side and mounted onto the elongated entrance window inside the SmartPhantom, as shown in Figure 78. To capture the scintillation light passing through them, the polished circular ends are imaged.

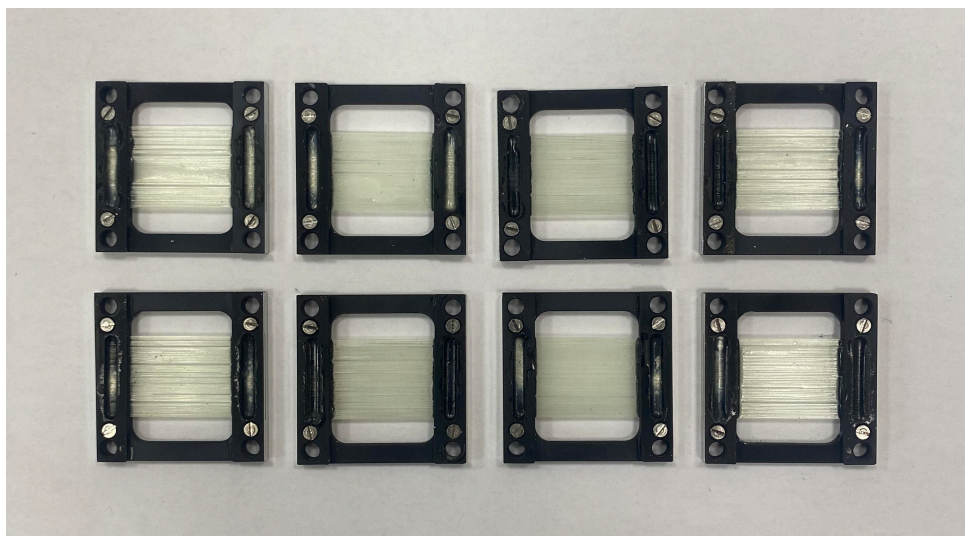


Figure 77: Image showing eight scintillating fibre planes, manufactured using the setup depicted in Figures 75 and 76, prepared for integration into the SmartPhantom.

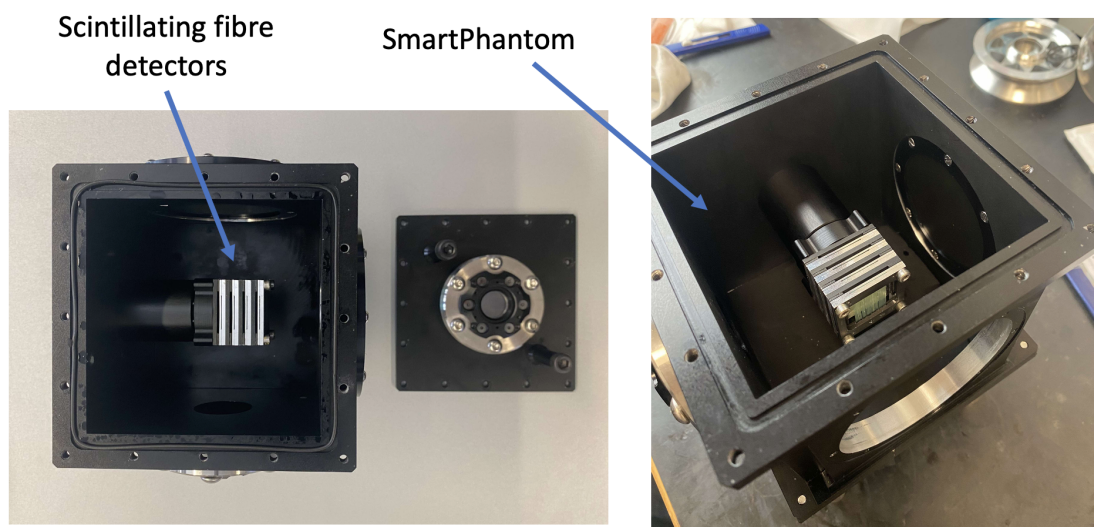


Figure 78: Image showing four scintillating fibre detectors, composed of eight planes arranged perpendicularly, positioned inside the SmartPhantom. The planes are separated by approximately 2 mm and are mounted onto the entrance window, aligned on-axis with the incoming beam.

7.3 Response

The performance of the scintillating fibre detectors was assessed at the MC40 cyclotron in Birmingham [15]. Two key aspects were investigated: saturation and the linearity of the response as a function of energy and particle number. For these measurements, the SmartPhantom was positioned at the cyclotron's exit window, with a collimator featuring a 2 cm diameter circular aperture placed in front. An imaging system identical to the one discussed in Section 6.5 was on the top to capture the scintillation light emitted by the fibres as the beam passed through. In this configuration, the detectors were suspended in air. An image of the experimental set-up is shown in Figure 79.

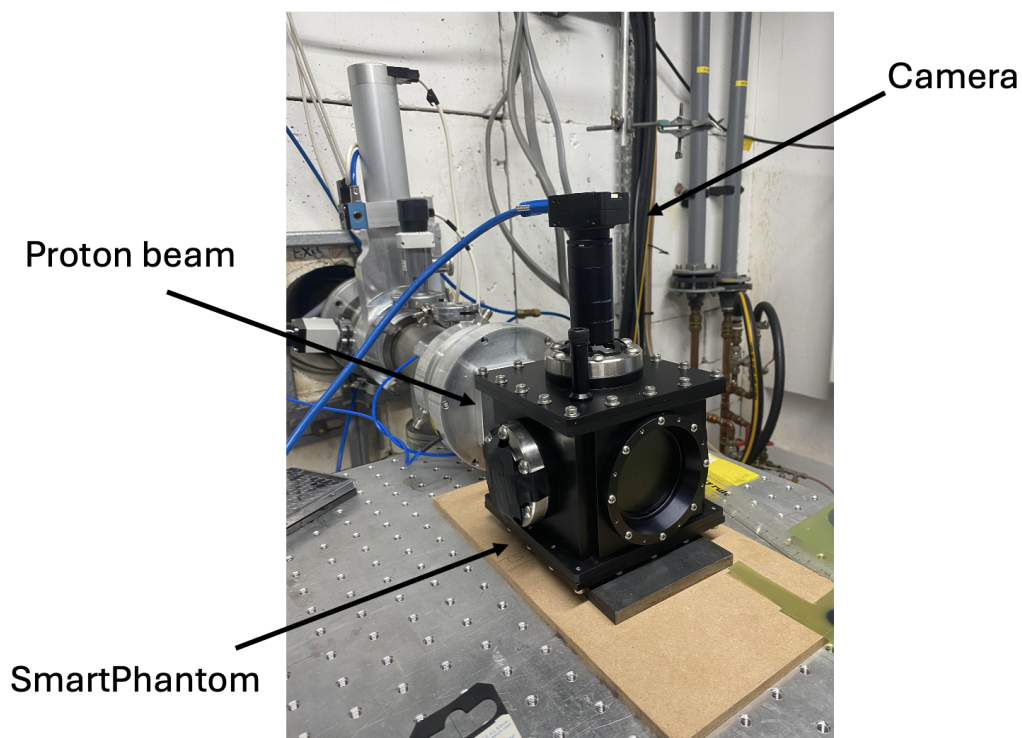


Figure 79: Experimental set-up showing the SmartPhantom, with the scintillating fibre detectors installed inside, positioned at the exit window of the MC40 cyclotron in Birmingham. An imaging system, comprising a Chameleon3 CM3-U3-31S4M-CS camera and several optical components, is mounted above to image the scintillation light from the top.

Twenty background images were captured and averaged to create a single image of the background. The cyclotron was then operated, with the current in the ionisation chamber varied to generate particle numbers of up to approximately 1×10^9 at two proton energies: 19.30 MeV and 27.32 MeV. During each run, 60 frames per second were recorded over a period of 60 seconds. The background image was subtracted from each frame and the corrected frames were averaged to produce the final image.

The averaged, background-corrected image, captured at 27.32 MeV with approximately 1.03×10^9 particles is shown in Figure 80. In this image, the bright circles correspond to the polished ends of the fibres, with the beam entering from the left. The gaps observed are a result of deficiencies in the gluing technique, where the resin shifted some the fibres during the setting process. It is important to note that at this stage, the optical system was optimised solely for the liquid scintillator, resulting in partial imaging of the scintillating fibre detectors due to the restricted field.

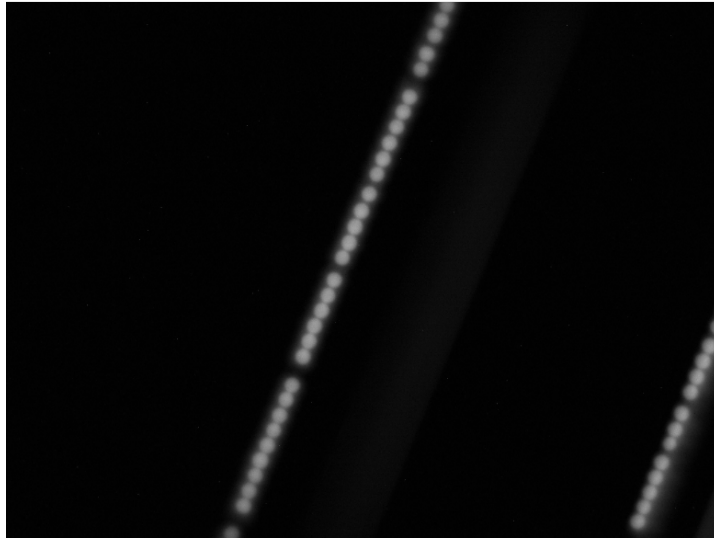


Figure 80: Averaged, background-corrected image captured using the setup depicted in Figure 79, and a 27.32 MeV proton beam of approximately 1.03×10^9 particles. The bright circles correspond to the polished ends of the fibres. The beam enters from the left.

An algorithm was developed in Python to detect and analyze the fibres in the images obtained using the Hough Circle Transform [114]. The algorithm works by identifying circular patterns. The center of each circle is detected and a radius is determined through edge detection. Subsequently, a circumference is drawn for each circle, with each one corresponding to the polished end of a scintillating fibre. The average intensity within each circle is calculated to assess the fibre's response.

Figure 81 displays the processed image captured with a 27.32 MeV proton beam and approximately 1.03×10^9 particles. In this image, the green circles correspond to the detected fibres using the Hough Circle Transform method, while the fibre with the highest average intensity is highlighted in red. This fibre, expected to be aligned with the beam axis, consistently exhibited the highest average intensity across all investigated energies and particle counts.

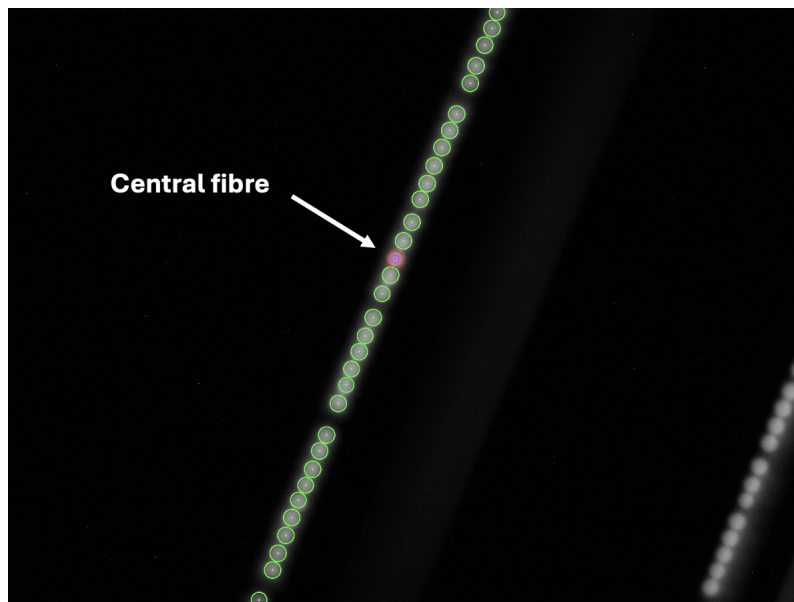


Figure 81: Processed image captured with a 27.32 MeV proton beam and approximately 1.03×10^9 particles. The green circles correspond to the detected fibres using the Hough Circle Transform method. The fibre with the highest average intensity is shown in pink.

The Hough Circle Transform image analysis was performed for all images captured across the energies and particle numbers investigated. Figure 82 presents the average central fibre intensity as a function of particle number for 19.30 MeV (green points) and 27.32 MeV (blue points) proton beams. Lines of best fit were added to assess the linearity of the scintillating fibres' response. The figure demonstrates that the scintillating fibres exhibit a linear response to increasing particle number, with no saturation observed within the range tested. In addition, the higher light intensities observed at 19.30 MeV for the same particle count can be attributed to the greater stopping power.

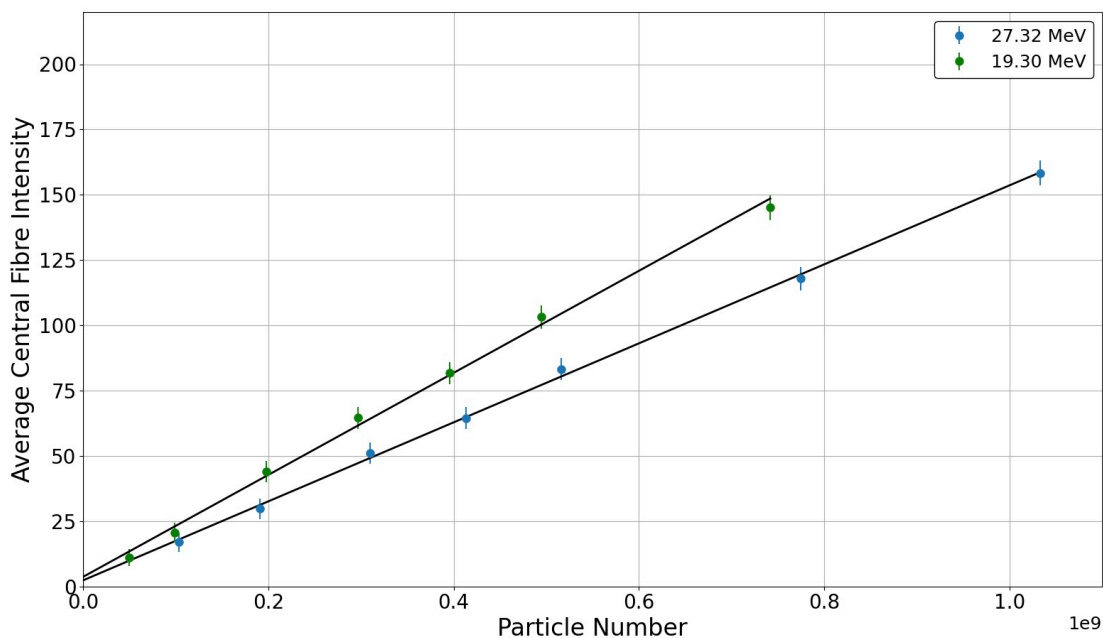


Figure 82: Plot of average central fibre intensity against particle number for 19.30 MeV (green) and 27.32 MeV (blue) proton energies. The black lines represent lines of best fit.

The procedure was repeated for all fibres across the obtained images. The results are presented in Figures 83 and 84, corresponding to data from 19.30 MeV and 27.32 MeV proton beams, respectively. In these plots, Fibre 1 corresponds to the circle at the top-right of the image (as illustrated in Figure 81), while Fibre 32 is the one at the bottom-left.

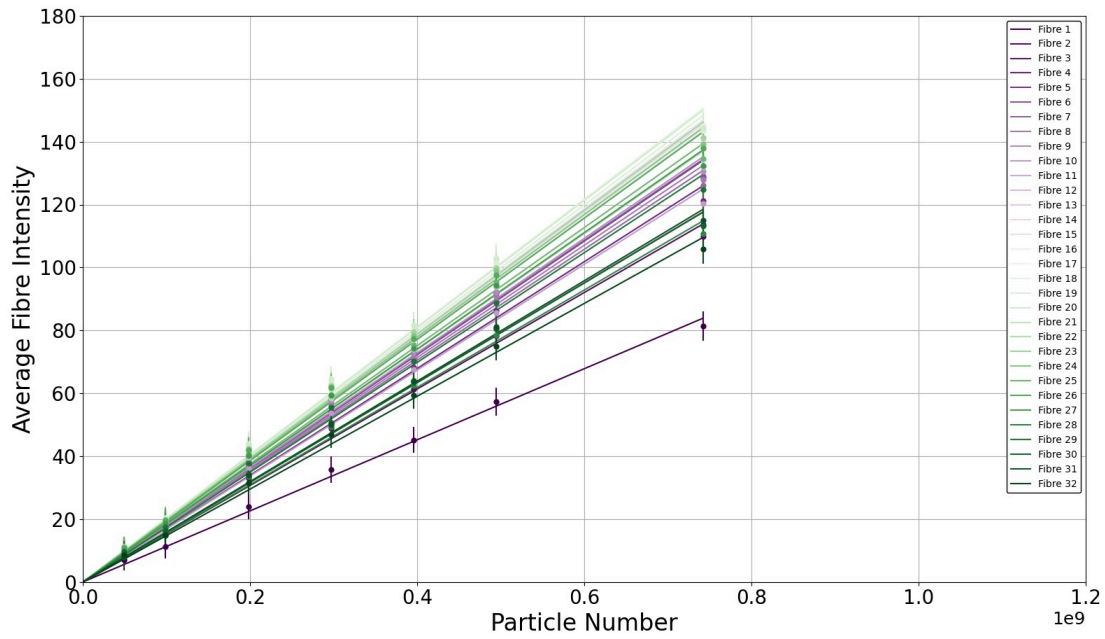


Figure 83: Average intensity of individual fibres as a function of particle number, with lines of best fit, when a 19.30 MeV proton beam passes through a scintillating fibre detector.

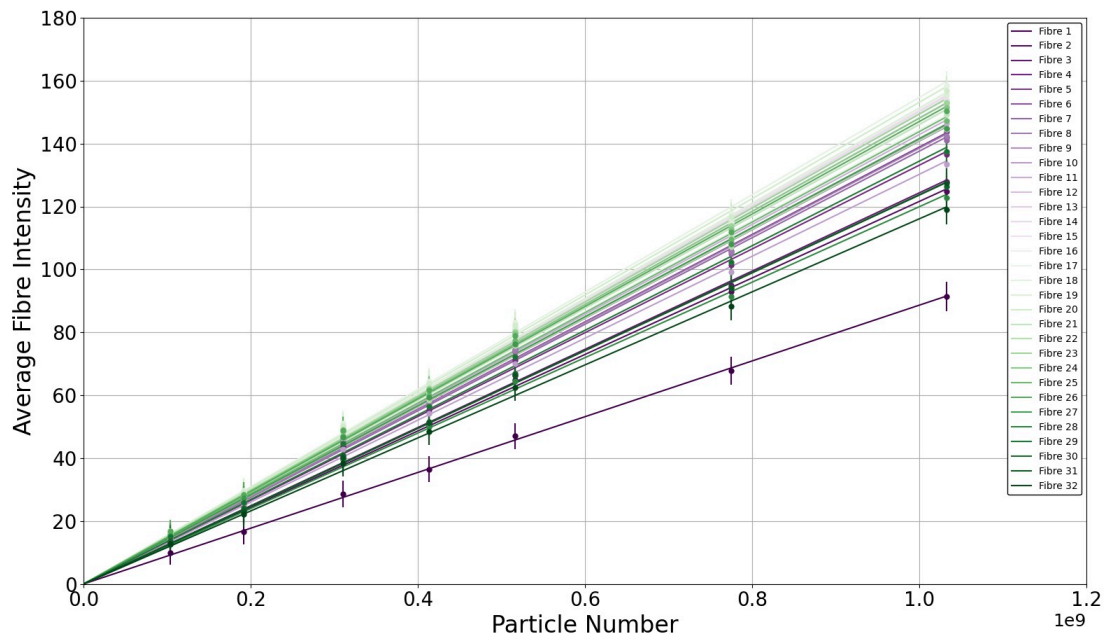


Figure 84: Average intensity of individual fibres as a function of particle number, with lines of best fit, when a 27.32 MeV proton beam passes through a scintillating fibre detector.

The plots reveal that the central fibres exhibit higher pixel intensities. This is probably a result of the increased particles density in that region, as they are aligned with the beam axis. Moreover, the plots reveal that the average pixel intensity in each fibre does not exceed 165, remaining below the 8-bit camera's maximum of 256. This suggests that the fibres do not reach saturation even at 1.03×10^9 particles.

The pitch between the fibres was initially calculated in pixels based on the detected circle centers and subsequently converted to millimetres using the known physical pixel width. The corrected average intensities for each fibre, combined with the calculated fibre pitch, were then used to reconstruct the beam profile. The resulting profiles for incoming proton beam energies of 19.30 MeV and 27.32 MeV are presented in Figures 85 and 86. To analyze the beam profile, a third order polynomial fit was applied to the data.

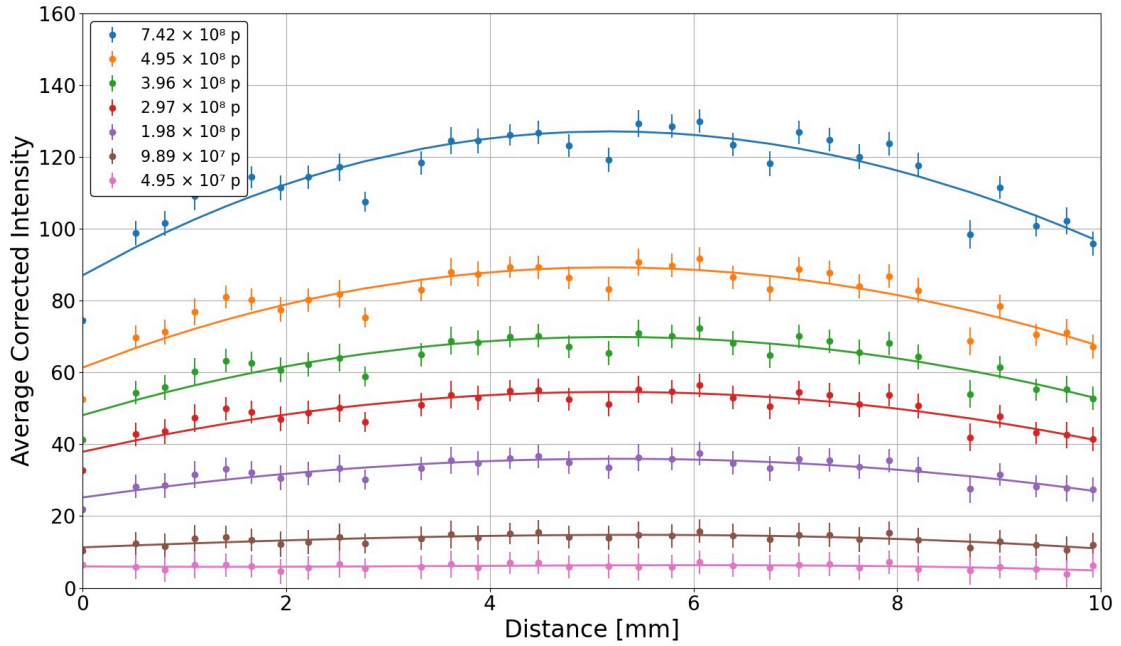


Figure 85: Average fibre intensity against fibre number from Figure 83, with a 19.32 MeV proton beam. The different colours correspond to different proton numbers in the beam. A third order polynomial fit was applied to the data.

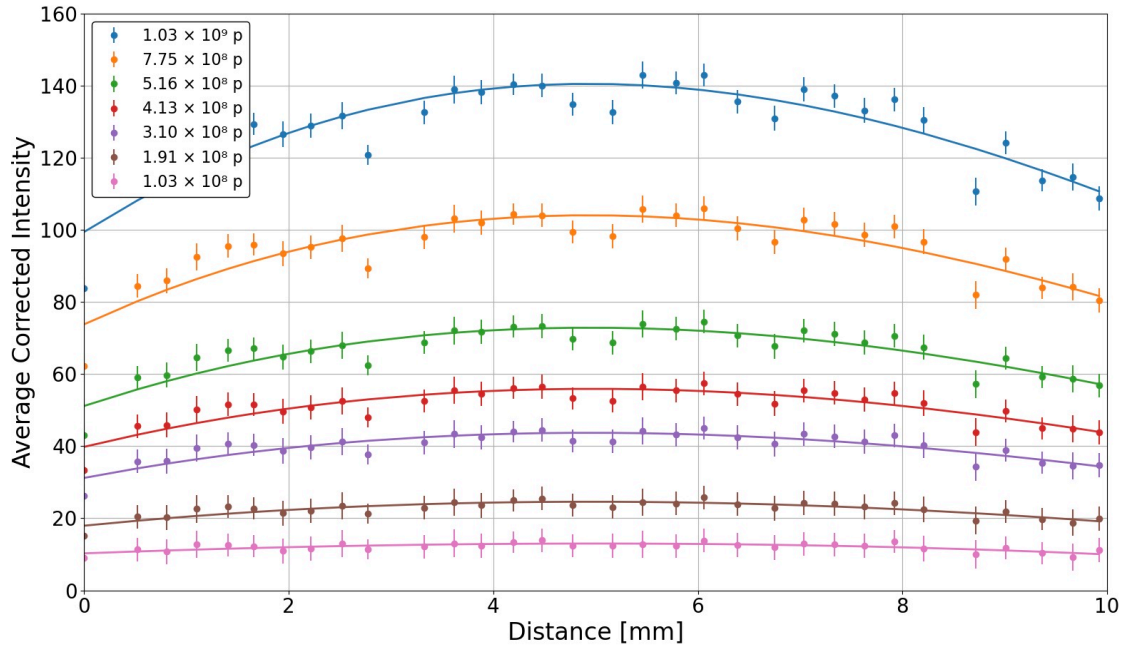


Figure 86: Average fibre intensity against fibre number from Figure 84, with a 27.32 MeV proton beam. The different colours correspond to different proton numbers in the beam. A third order polynomial fit was applied to the data.

The plots show that as the number of particles in the beam increases, the average intensity in the fibres also increases. In addition, the shape of the polynomial fits reveals that higher particle counts result in a greater proportion of the particles being concentrated at the beam's center, relative to the outer radius. This is also visible in the data from the lowest particle numbers, represented by the pink curves, which display a more uniform intensity distribution across the irradiated area.

Although the current version of scintillating fibre detectors is able to provide a general estimate of the beam profile, the non-uniform pitch introduces significant errors. To address this issue, a new gluing mechanism must be developed, either by adjusting the epoxy resin-to-hardener ratio or by introducing an additional support structure to secure the fibres

firmer prior gluing. In addition, the machined holes in the aluminium frames can be made slightly deeper to ensure the fibres fit more precisely into the designated positions, thereby prompting a more uniform and accurate pitch.

Moreover, the persistent features observed in Figures 85 and 86 suggest variations in fibre signal efficiency, particularly at positions 2.8, 5, 6.4, and 8.4 mm, where the signal intensities deviate significantly below the expected trend. This is likely due to inconsistencies arising from the manual cutting and polishing of the fibres. This issue can be mitigated by employing automated cutting and polishing techniques, which would ensure greater uniformity and improve the consistency of signal transmission across all fibres.

To address this issue using the current data, the signal efficiency of each fibre was adjusted using a data-driven correction. This was done by averaging the response of each fibre across all beam intensities and normalizing them to the central fibre (assuming that it is aligned with the beam axis and exhibits the highest and most consistent signal). This provided a correction factor which was subsequently used to scale the intensities values of each fibre to "flat-field" the detector response.

Figures 87 and 88 display the beam profiles and third-order polynomial fits before and after correction for the 19.30 MeV and 27.32 MeV data, respectively. In addition, the polynomial fit parameters are quantified in Tables 8 and 9. The parameters reveal that the correction method significantly improves the uniformity of the beam profile, as after adjustment, the resulting fit coefficients have lower χ^2 values in all particle counts and beam energies investigated. This confirms that the correction process improves the fidelity of the beam shape.

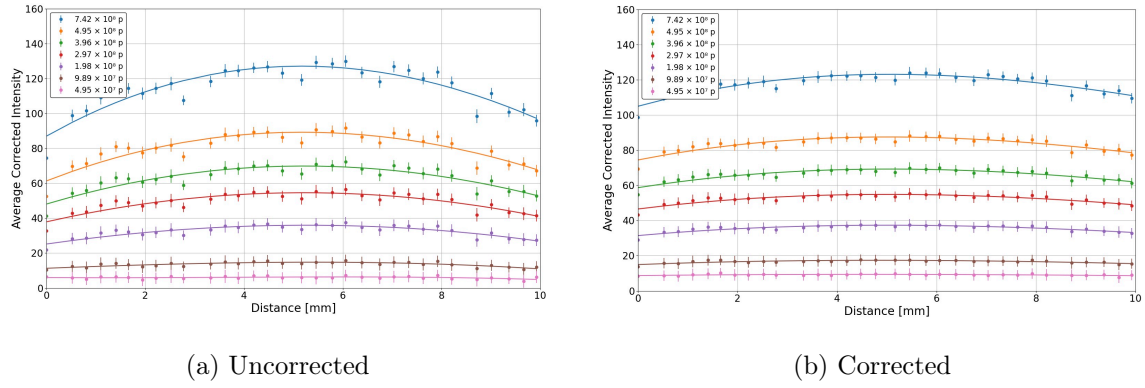


Figure 87: Third-order polynomial fits to the 19.30 MeV proton beam intensity profiles, before and after the data-driven fibre efficiency correction.

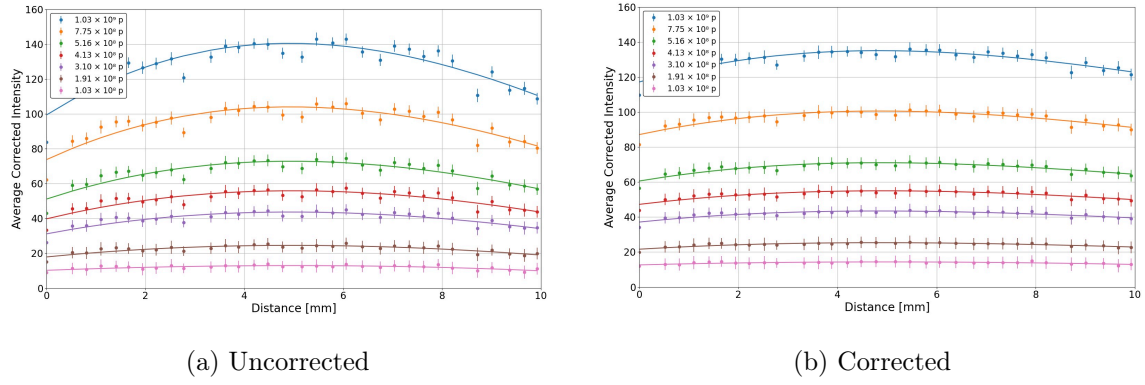


Figure 88: Third-order polynomial fits to the 27.32 MeV proton beam intensity profiles, before and after the data-driven fibre efficiency correction.

Table 8: Third-order polynomial fit parameters to the 19.30 MeV proton beam intensity profiles, before and after the data-driven fibre efficiency correction.

Particle number	Uncorrected					Corrected				
	A_0	A_1	A_2	A_3	χ^2	A_0	A_1	A_2	A_3	χ^2/ndf
7.42×10^8	0.02	-1.69	16.00	99.50	3.36	0.02	-0.92	7.72	104.99	0.73
4.95×10^8	0.01	-1.14	11.04	61.37	2.12	0.01	-0.67	5.58	74.44	0.43
3.96×10^8	0.00	-0.85	8.48	8.11	1.32	0.01	-0.53	4.46	58.68	0.26
2.97×10^8	0.00	-0.63	6.45	37.91	0.84	0.01	-0.42	3.55	46.55	0.17
1.98×10^8	0.00	-0.37	4.04	25.19	0.42	0.01	-0.30	2.53	31.43	0.10
9.89×10^7	-0.01	-0.05	1.09	11.29	0.11	0.00	-0.13	1.08	14.93	0.04
4.95×10^7	-0.01	0.09	-0.19	5.97	0.04	0.00	-0.04	0.33	8.66	0.02

Table 9: Third-order polynomial fit parameters to the 27.32 MeV proton beam intensity profiles, before and after the data-driven fibre efficiency correction.

Particle number	Uncorrected					Corrected				
	A_0	A_1	A_2	A_3	χ^2	A_0	A_1	A_2	A_3	χ^2/ndf
1.03×10^9	0.05	-2.19	17.9	99.50	4.71	0.03	-1.06	8.13	117.2	0.89
7.75×10^8	0.03	-1.59	13.1	73.80	2.67	0.02	-0.78	6.06	87.12	0.51
5.16×10^8	0.03	-1.15	9.42	51.15	1.31	0.02	-0.63	4.77	60.50	0.26
4.13×10^8	0.02	-0.81	6.87	39.81	0.84	0.01	-0.44	3.45	47.24	0.18
3.10×10^8	0.01	-0.65	5.40	31.19	0.54	0.01	-0.39	2.91	37.13	0.12
1.91×10^8	0.01	-0.32	2.81	17.93	0.18	0.01	-0.20	1.69	21.61	0.05
1.03×10^8	0.00	-0.09	1.05	10.25	0.07	0.00	-0.08	0.72	12.64	0.03

In conclusion, the scintillating fibres detectors are able provide the necessary information to reconstruct the energy deposition profile of a propagating beam in water along the beam's propagation axis. However, the simulations revealed that the scintillating fibre detectors disrupt the acoustic wave propagation, making simultaneous optical and acoustic measurements impossible due to artefacts appearing in reconstructed images. Furthermore, the results from the Birmingham experiments demonstrated that the cross-sectional area of the beam can be reconstructed successfully using the proposed detectors and imaging system, with no image saturation expected up to 10^9 protons in the beam. In addition, the scintillating fibre's response as a function of particle number was observed to be linear. Based on these observations, in Munich, the scintillating fibre detectors will be suspended in air to measure the beam's cross-sectional area and divergence, rather than reconstructing the energy deposition profile in water.

Chapter 8

SmartPhantom Evaluation

Following the initial experiments at the MC40 cyclotron in Birmingham, the SmartPhantom was evaluated at the LION beamline at the Center for Advance Laser Applications in Munich [9]. With this accelerator, the generation of ionacoustic signals is possible because of the very short laser pulses and hence simultaneous optical and acoustic measurements could be obtained.

8.1 Synchronized Data Acquisition

To enable synchronous data collection within the very short duration of the pulse, on the order of a few nanoseconds, a Data Acquisition (DAQ) system was designed. The system uses an existing trigger box, which receives the laser signal detected by a photodiode. The trigger box then distributes the trigger to various devices, ensuring synchronized operation. Due to the high performance of the trigger box, the process happens without delay.

To capture simultaneous images from the cameras, two trigger signals are sent to each camera through General Purpose Input/Output (GPIO) connectors. The camera shutters open and close during the trigger window, ensuring that the images capture the emitted scintillation light within the timeframe in which the beam transverses the SmartPhantom. The images obtained are saved with timestamps and sent to a central computer that is operated remotely.

The Olympus V303 transducer and the Piston hydrophone are connected to a multi-channel picoscope (Picoscope 6404D), which records and digitizes the acoustic signals [115]. One trigger signal is sent from the trigger box to the picoscope, which activates the two transducers simultaneously. In addition, amplifiers are placed between the picoscope and each of the transducers to enhance the signal strength. The acoustic signal recording occurs only within the designated trigger window, after which the picoscope transmits the recorded data to the central PC, where they are saved along with the corresponding timestamp.

The matrix and linear array transducers are operated using the Verasonics system, as discussed in Section 5.2. A fourth trigger signal is therefore designed to be sent to the Verasonics system, which subsequently triggers the two transducer arrays. The recorded signals are saved with timestamps within the system, which has its own monitor interface and operating unit. Given the low experimental operation rate of approximately 1 Hz, clock-synchronization between the timestamped data from the central PC and the Verasonics system can be achieved. A schematic diagram of the complete DAQ system is shown in Figure 89. Unfortunately, the Verasonics system could not be transported to Munich. As a result, the matrix and linear array transducers, which rely on the Verasonics for operation, were not used in the experiment at the LION beamline.

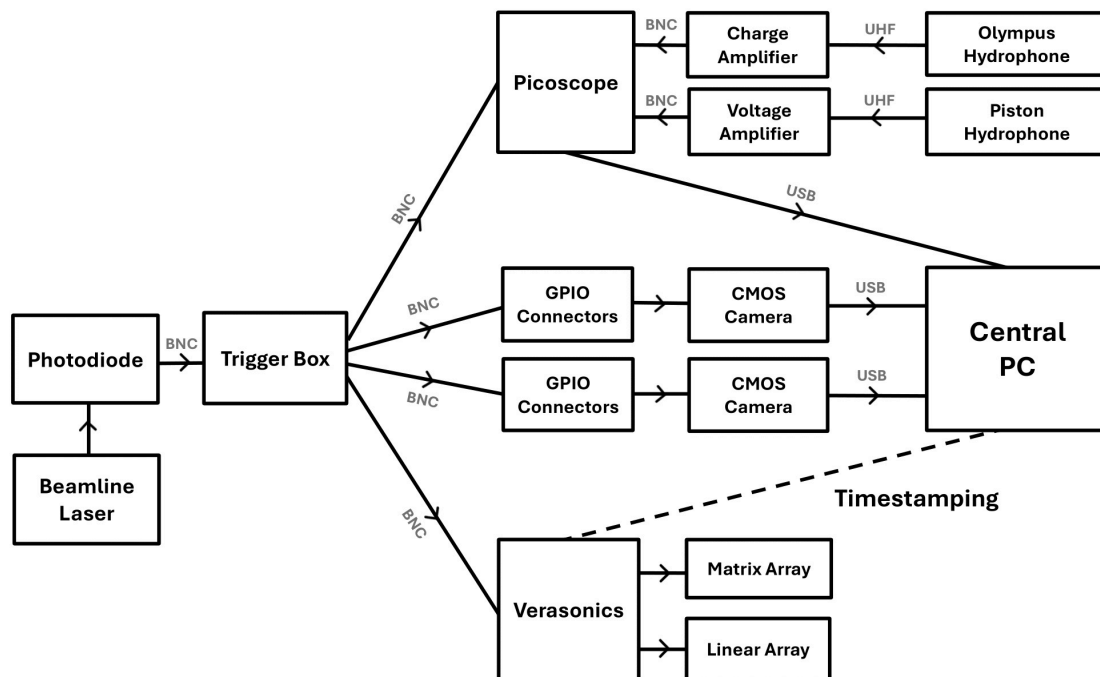


Figure 89: Schematic diagram of the Data Acquisition System (DAQ) to be used at the LION beamline for collecting synchronized optical and acoustic data, from two cameras and four ultrasound transducers, according to the photodiode-based laser trigger.

8.2 Scintillating Fibre Detectors

Initially, the scintillating fibre detectors were evaluated. The detectors were mounted onto the entrance window of the SmartPhantom and suspended in air, as shown in Figure 90. The SmartPhantom was securely fixed onto a motorized stage that could be controlled remotely and was positioned close to the LION beamline’s exit window to reduce beam divergence. In addition, two imaging systems were mounted orthogonally to image the scintillating light emerging from the polished ends of the fibres. Figure 91 shows an image of the experimental set-up. To evaluate the scintillating fibre detectors, proton beams of varying energies were generated by adjusting the quadrupole drifts.

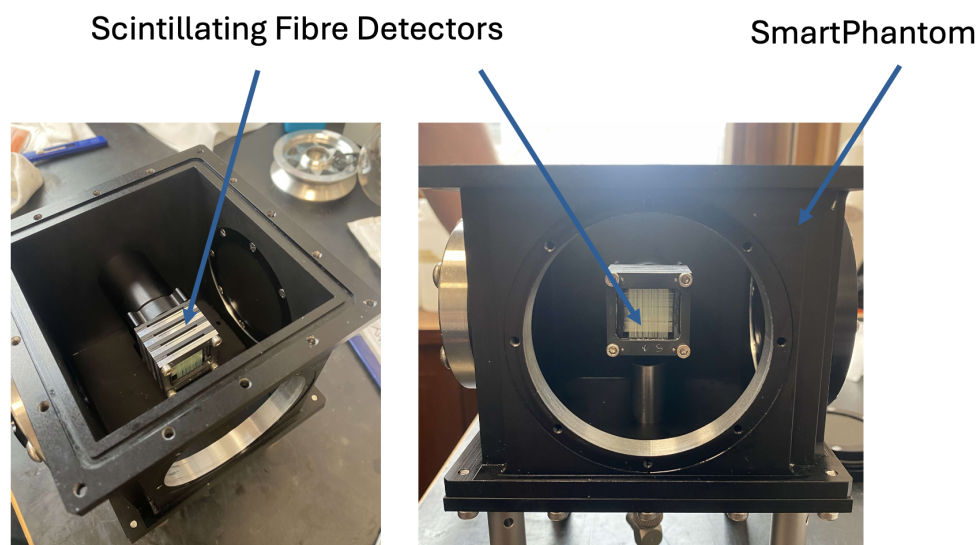


Figure 90: Interior of the SmartPhantom showing the scintillating fibre detectors attached onto the entrance window flange. Left: angled view. Right: on-axis view when the transducer window is removed.

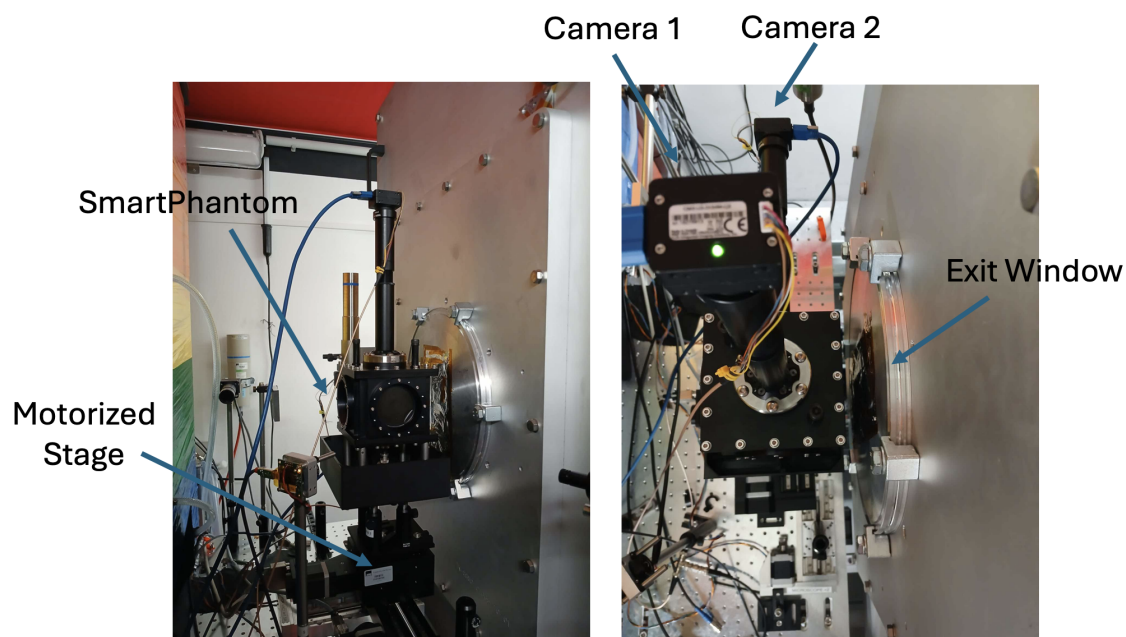


Figure 91: Position of the SmartPhantom, containing the scintillating fibre detectors, relative to the LION beamline exit window. The imaging systems comprising of several optical components and cameras are attached. Side view: left. Top view: right.

8.2.1 Energy Response

The proton beam energies studied were 12, 14, 16, 18, 20 and 24 MeV. Due to time constraints, a single image was captured for each proton energy as the beam passed through the detectors. To correct for background noise, an average background image, composed of 20 images taken with the laser turned off, was subtracted from each one. The background-corrected images captured using the top-view and side-view cameras, at each investigated energy, are shown in Figures 92 and 93, respectively. In these images, the beam enters from the left, with the scintillating fibres' polished ends identified as the bright circular regions. Notably, at the time of the experiment, the imaging system was not optimized, resulting in only partial imaging of the detectors.

Moreover, at low proton energies (12, 13 and 16 MeV), some fibres display extremely bright intensities, suggesting potential saturation. This phenomenon can be attributed to the increased number of particles passing through the detector at lower energies, as a result of the quadrupole doublet focusing mechanism. Furthermore, bright pixels are also observed on the sides of the imaged detectors, resulting from light reflections off the silver-polished surfaces of the detector frames.

Figure 92 reveals that the central fibres are brighter than the outer ones, as expected for a beam where the particles are focused at the center. In contrast, Figure 93 reveals a uniform particle distribution, suggesting weak particle focusing in that direction. This could be possibly due to quadrupole misalignment errors.

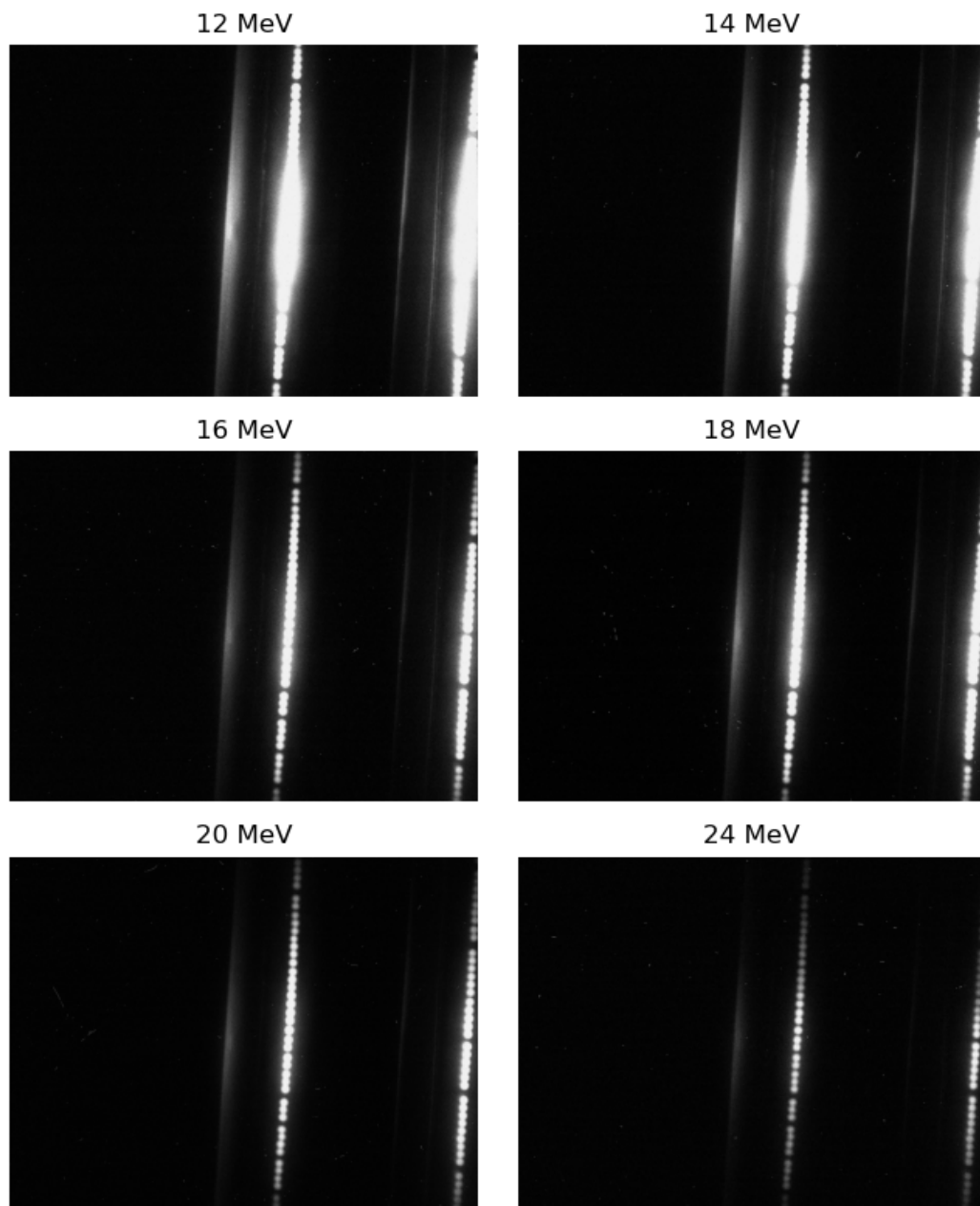


Figure 92: Background-corrected images obtained at various proton energies at the LION beamline, showing partial imaging of the scintillating fibre detectors, captured using the setup shown in Figure 91 and the top-view camera (Camera 1).

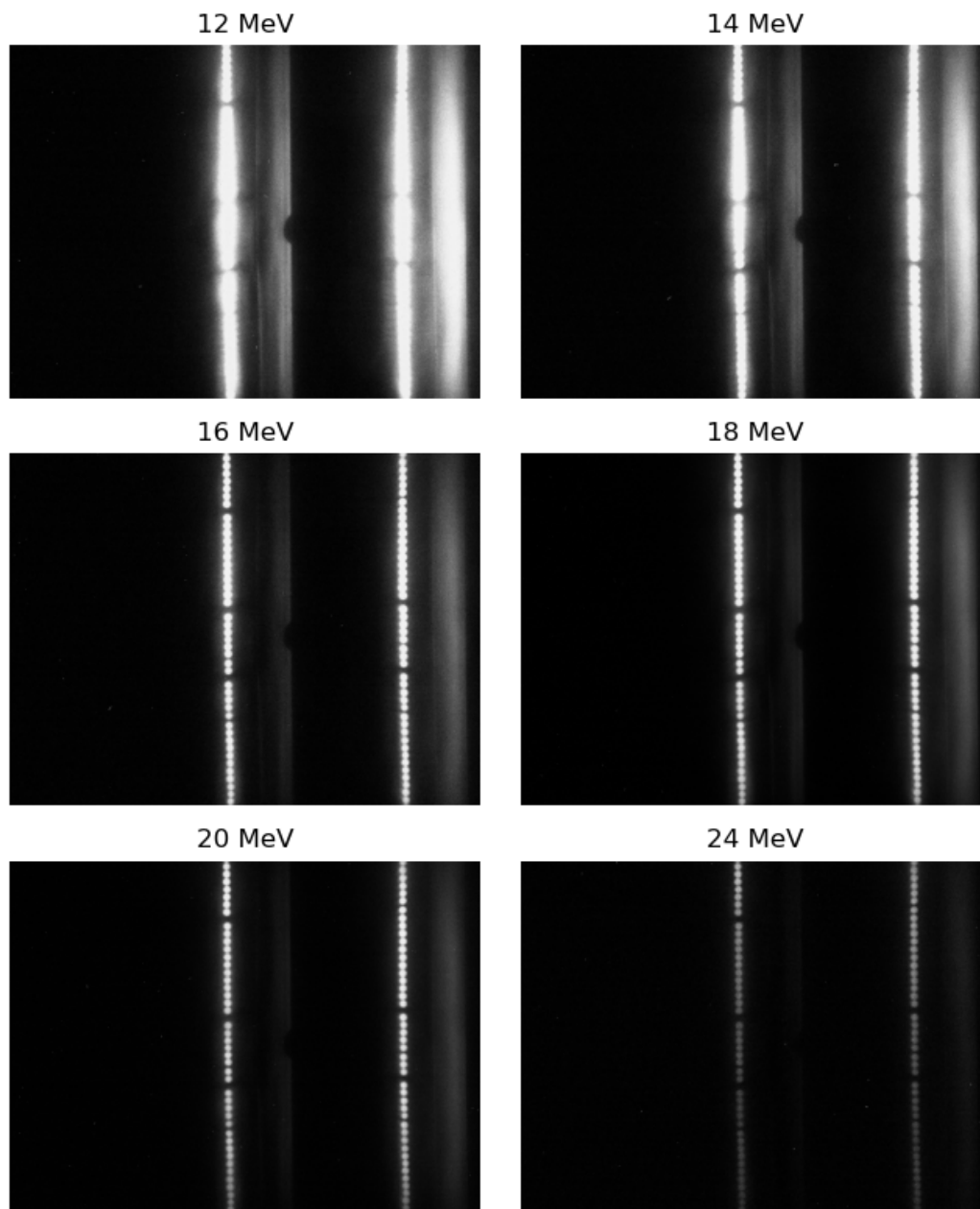


Figure 93: Background-corrected images obtained at various proton energies at the LION beamline, showing partial imaging of the scintillating fibre detectors, captured using the setup shown in Figure 91 and the side-view camera (Camera 2).

The Hough Circle Transform image analysis was applied to the background-corrected images, following the same approach used for the data obtained in Birmingham (discussed in Section 7.3). Figure 94 shows the results using the 20 MeV beam, with green circles marking the detected fibres and pink circles indicating the fibre with the highest intensity.

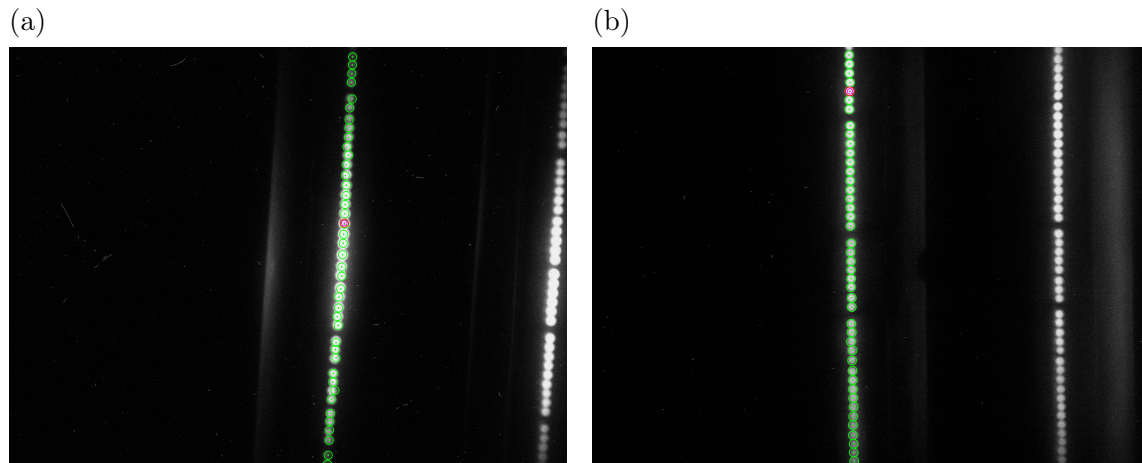


Figure 94: Example images of the imaged scintillating fibre detectors when a proton beam with a modal energy 20 MeV passes through them. The green circles correspond to the fibres detected using the Hough Circle Transform method, with the fibre with the maximum average intensity indicated in pink. Top-view camera: (a). Side-view camera: (b)

The average pixel intensity within each circle was calculated across all obtained images. Figures 95 and 96 present the average fibre intensity, calculated from the images captured by the top-view. In the plots, Fibre 1 corresponds to the fibre found at the top of the images, with the numbering ascending for fibres towards the bottom.

The plots reveal that the overall average fibre intensity decreases as the beam energy increases, as expected due to the lower particle count. In addition, it is observed that the fibre intensities recorded by the top-view camera exhibit a wider spread, as the highly focused beam in that direction has a greater concentration of particles at the center, with the count gradually decreasing towards the edges.

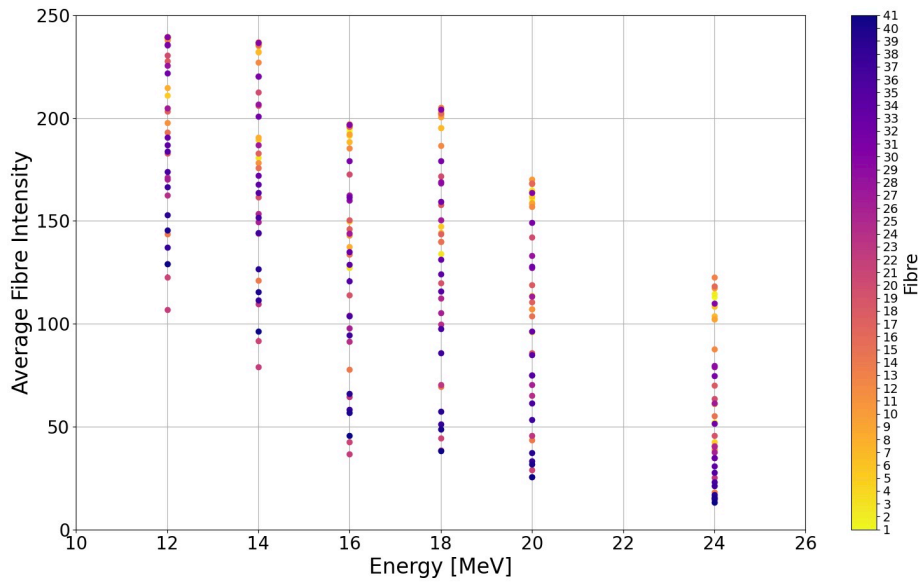


Figure 95: Average fibre intensity against beam energy, calculated using the Hough Circle Tranform method and the data from the top-view camera. Fibre 1 corresponds to the fibre at the top of the images, with the numbering ascending for fibres towards the bottom.

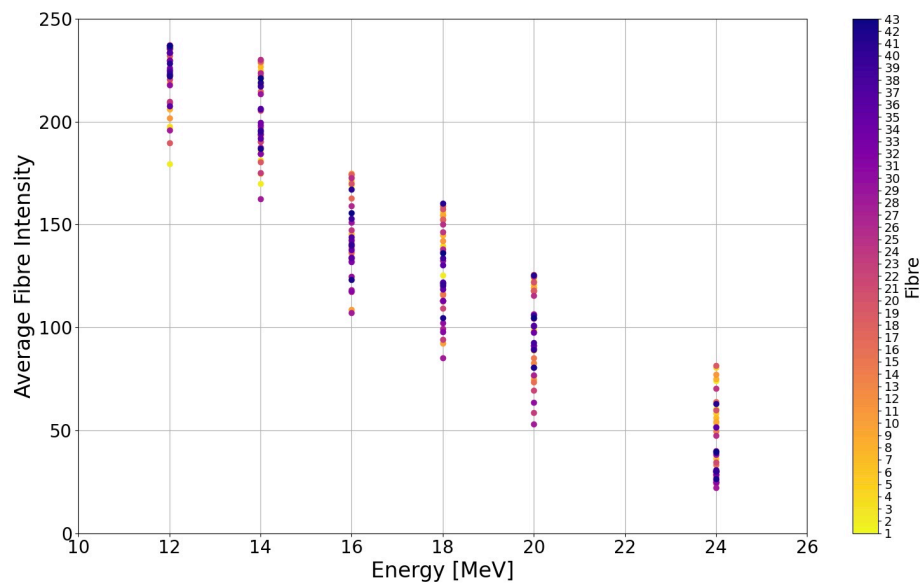


Figure 96: Average fibre intensity against beam energy, calculated using the Hough Circle Tranform method and the data from the side-view camera. Fibre 1 corresponds to the fibre at the top of the images, with the numbering ascending for fibres towards the bottom.

8.2.2 Beam Profile

The data from the individual fibres were used to reconstruct the beam profile in each direction, for each design energy. Figures 97 and 98 present the average fibre intensity against position in millimeters, determined using the known fibre pitch, from the data using the top-view and side-view cameras, respectively. In addition, a Gaussian fit was applied to top-view camera data. This was omitted for the side-view camera data due to the weak focusing in that direction.

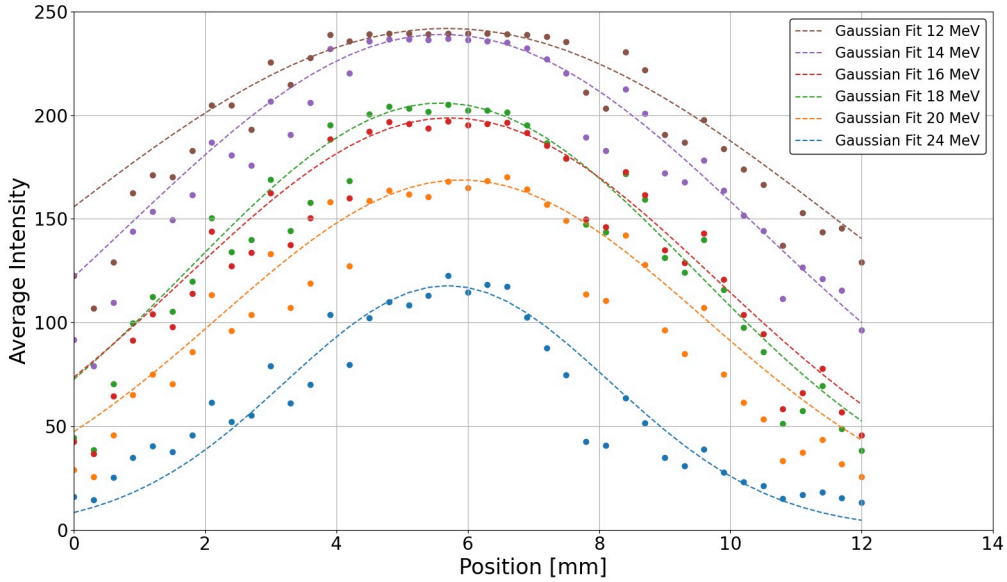


Figure 97: Average fibre intensity, from the images obtained by the top-view camera, against position (measuring from top to bottom) for the various beam energies accelerated at the LION beamline. A Gaussian fit is applied to the data.

From Figure 97 it is evident that as the beam energy increases, the average fibre intensity decreases, due to fewer particles. In addition, a peak in intensity appears at the center of the detectors' imaged region, that is consistent across all energies. This suggests strong particle focus in that direction and good alignment of the detector's center with the beam axis. In contrast, Figure 98 displays a flat, uniform intensity distribution across the

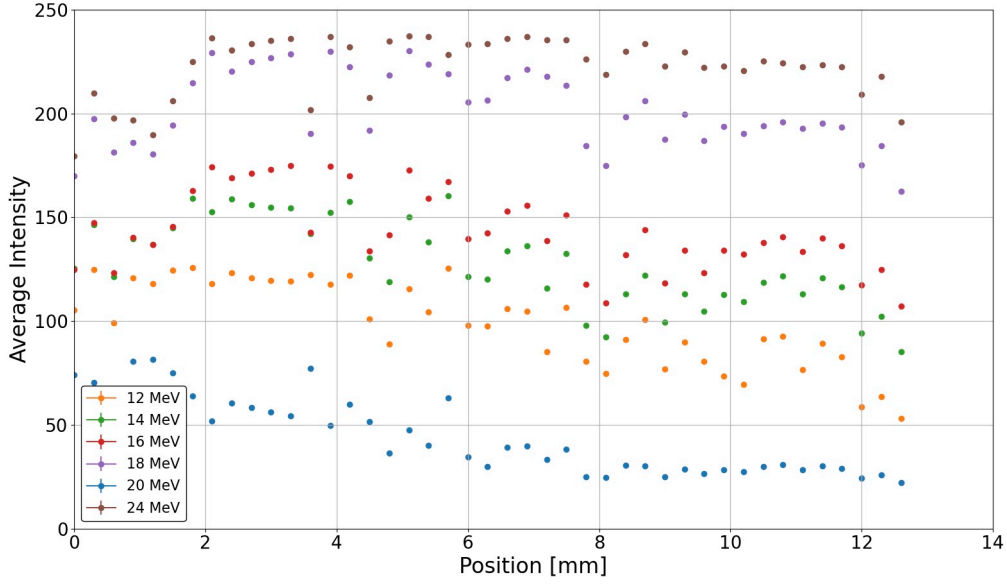


Figure 98: Average fibre intensity, from the images obtained by the side-view camera, against position (measuring from top to bottom) for the various beam energies accelerated at the LION beamline.

fibres, indicating poor focusing in that direction and an even particle distribution.

Lastly, the FWHM of the beam profile in the direction imaged by the top-view camera was calculated from the Gaussian fit, with the results presented in Figure 99. The plot reveals that as the beam energy increases, the beam width decreases. This trend can be explained by the focusing properties of the accelerator, as higher-energy particles are more tightly focused by the quadrupoles' electromagnetic fields.

8.3 Radiochromic Films

The cross-sectional area and depth range of the particles in the proton bunch were determined by using RadioChromic Films (RCFs) [117]. Specifically, the GafchromicTM EBT3 RCF films were used, which are 28 μm thick [118]. Two RCF stacks were prepared, containing 18 film layers each. The stacks, labelled as "Stack A" and "Stack B", were

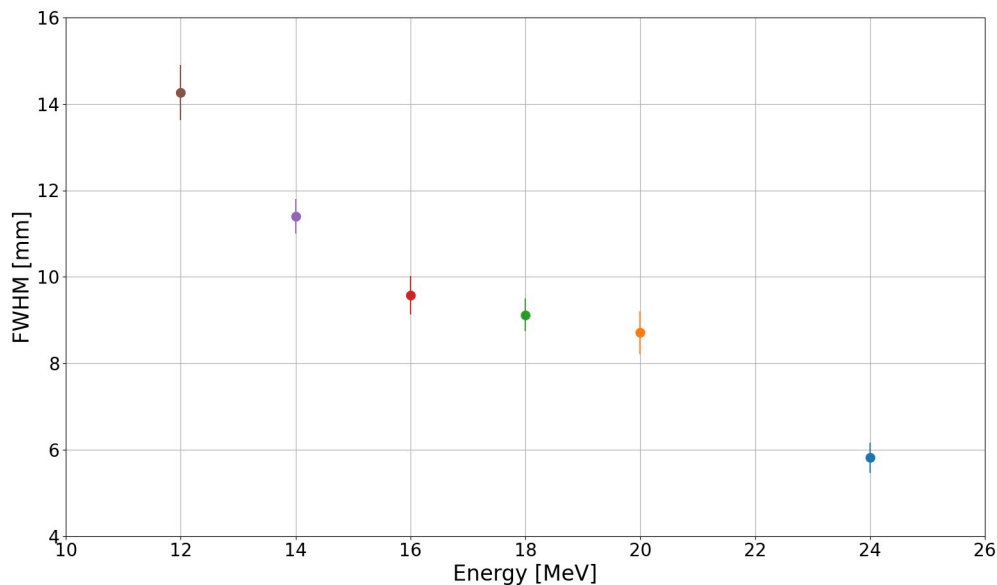


Figure 99: Full Width at Half Maximum (FWHM) of the beam profile in the direction imaged by the top-view camera, plotted against beam design energy. The values were extracted from the fitted Gaussian curves shown in Figure 97.

irradiated on two different days: Stack A on the day the scintillating fibre detectors were evaluated and Stack B when the liquid scintillator and acoustic transducers were tested.

Each stack was placed on a 3D-printed holder, shown in orange in Figure 100, which divided the area into six distinct 3×3 cm squares. The position of the holder was adjusted using the motorised translation stage, which was moved horizontally to irradiate different sections of the stack after adjusting the beam energy. Lastly, green alignment lasers were used to centre the square sections with the accelerator’s exit window.

The beam energy was varied by adjusting the quadrupole drift lengths and subsequently, the RCF stacks were irradiated. Figure 101 shows RCF Stack A (top) and Stack B (bottom) after irradiation, where the forefront film layers were oriented to face the accelerator’s exit window. In both stacks, the first two sections, labeled 1 and 2, were not irradiated. For Stack A, positions labelled 3-6 were exposed to beam irradiation with design

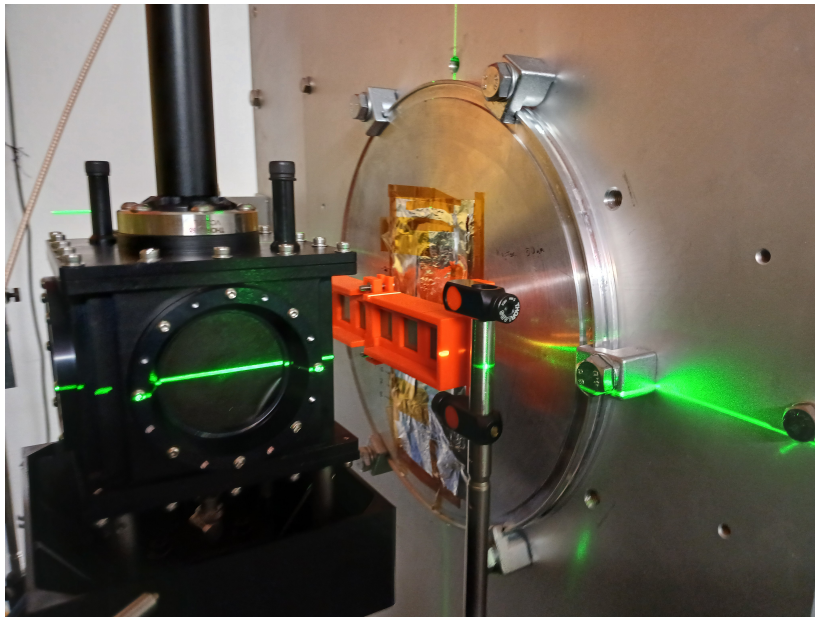


Figure 100: 3D-printed holder (orange) designed for securing stacks composing of eighteen layers of RadioChromic Films (RCF). The holder's position was adjusted vertically and horizontally using a motorized stage. Green alignment lasers were used to centre the square sections with the accelerator's exit window.

energies of 20 MeV, 20 MeV (repeat), 16 MeV and 12 MeV, respectively. In the corresponding positions, Stack B was irradiated with design energies of 18 MeV, 14 MeV, 10 MeV and 10 MeV (repeat).

The RCF films were scanned using an EPSON Expression 11000 XL Pro scanner at 36 hours post-irradiation for Stack A and 12 hours for Stack B [119]. Figure 102 displays an example scan of the RCF films from position 6 of Stack A, which shows the deposition patterns from a 12 MeV beam. For calibration purposes, the RCF films were taken from the same batch as in [120], where they were calibrated by exposure to known radiation doses in an x-ray medical accelerator at LMU Klinikum in Munich [121]. The scanning settings were identical and the optical density from the scans was converted into dose (and then energy) using the known properties of the films.

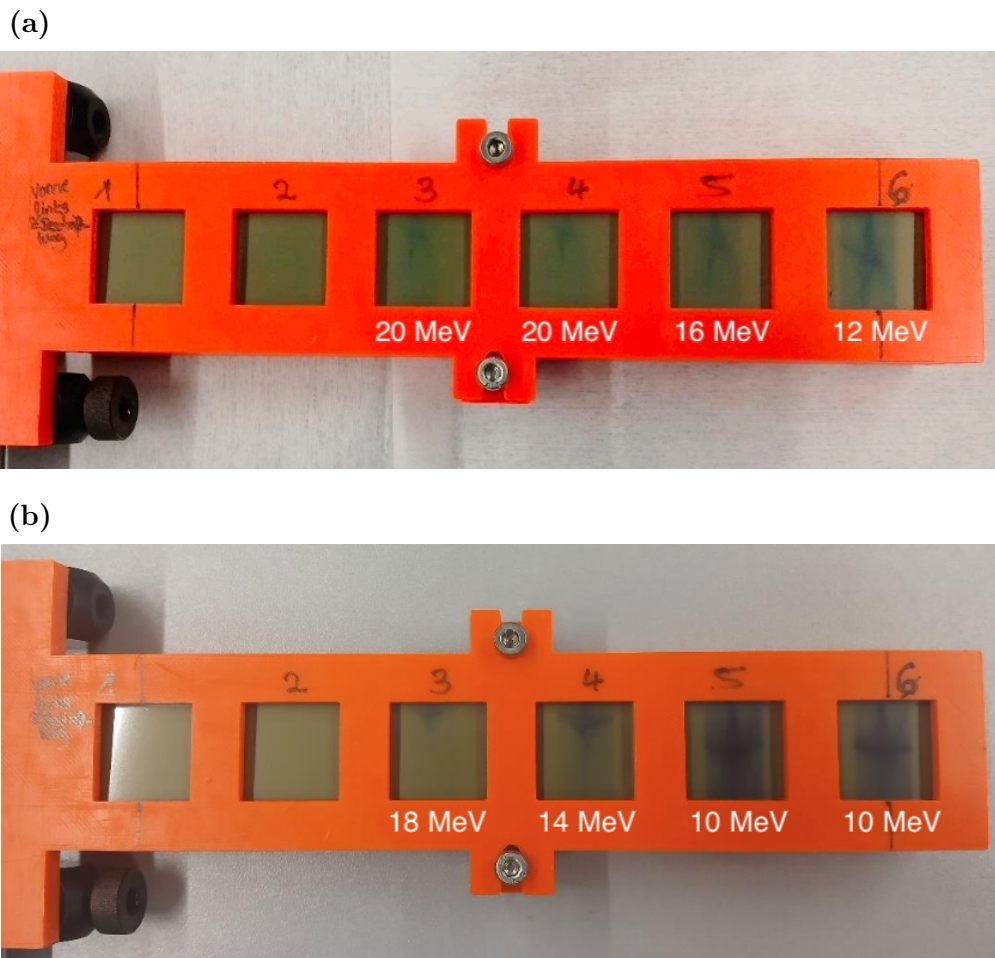


Figure 101: Stack A (top) and Stack B (bottom) composing of eighteen layers of radiochromic films, after exposure to beams with various energies. In both stacks, the first two squares were non-irradiated.

The integrated energy deposited within each square section in each layer of the RCF stacks was calculated and plotted against depth. The results for Holder A and Holder B are displayed in Figures 103 and 104, respectively. The plots reveal that beams with higher design energies penetrate deeper into the stack, as expected due to their lower stopping power, which enables them to travel further before coming to rest.

In addition, the plots show that the deposited energy decreases as the proton beams penetrate deeper into the RCF layers. However, the curves do not resemble the charac-

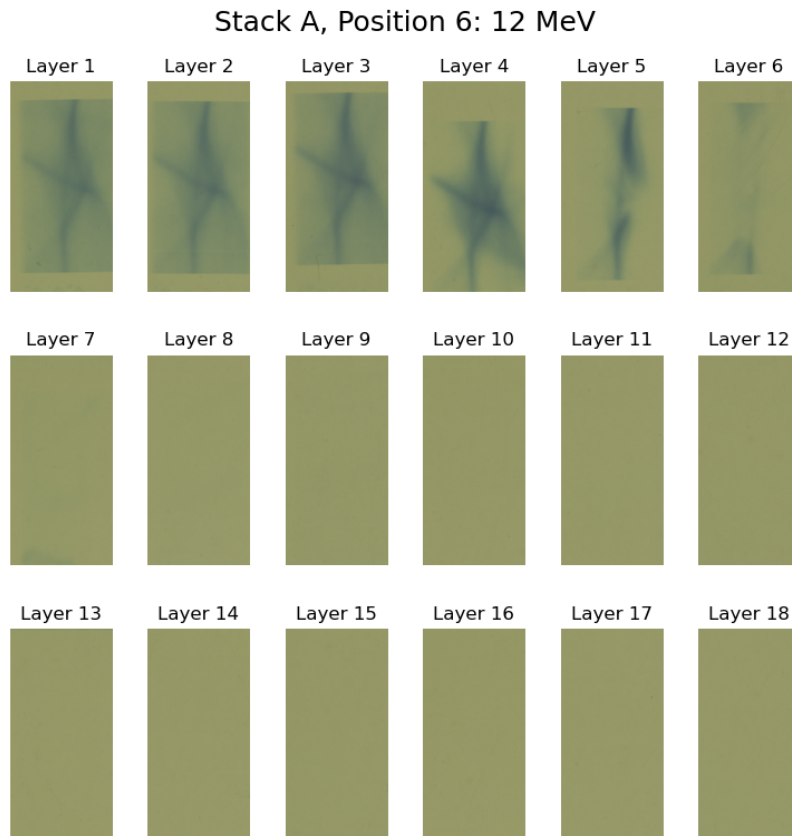


Figure 102: Example scan of the RCF films from position 6 of Stack A, showing the deposition patterns caused by a 12 MeV beam passing through eighteen layers of Gafchromic™ EBT3 RCF films [118].

teristic Bragg peak shape, where the deposited energy is lower at the entry point, steadily increasing to a peak and then sharply falls off. The observed patterns suggest that each beam is composed of particles with a wide range of energies, where each one gives its own distinct peak, resulting in a more complex overall shape. Lastly, beams with the same energies, such as those in the bottom plots in Figure 104, exhibit slightly different depth-dose curve shapes and energy intensities, due to the large shot-to-shot beam variations.

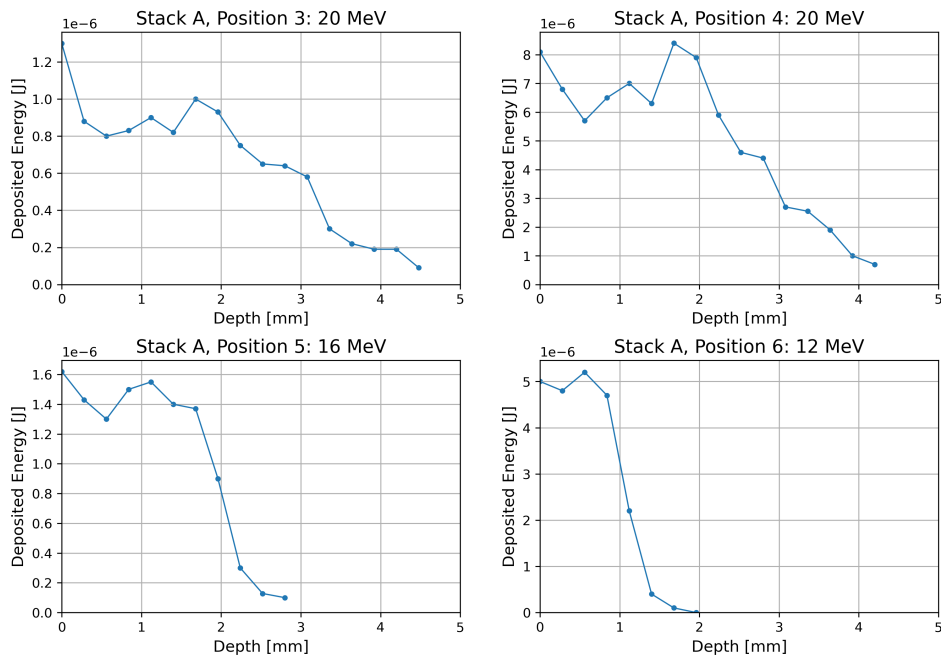


Figure 103: Depth-dose curves calculated by integrating the deposited energy within the irradiated sections across each layer of RCF Stack A.

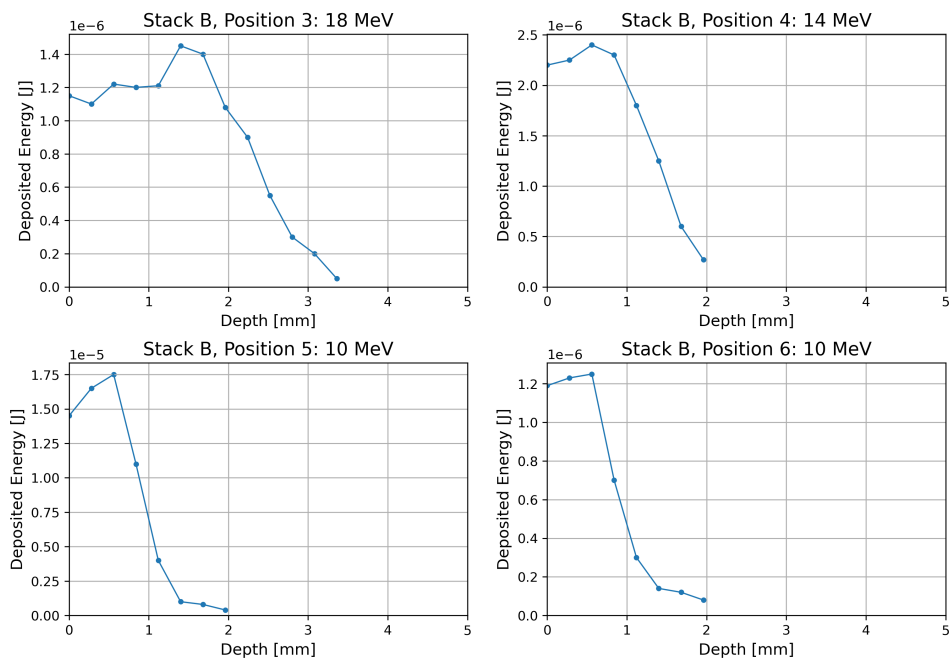


Figure 104: Depth-dose curves calculated by integrating the deposited energy within the irradiated sections across each layer of RCF Stack B.

8.4 Liquid Scintillator and Transducers

In subsequent experiments, the scintillating fibre detectors were removed from the SmartPhantom and the liquid scintillator was inserted through the tubes located on the top lid, shown in Figure 9. The detector was left undisturbed for a few minutes to allow air bubbles to dissipate, as their presence could affect the acoustic measurements.

The imaging systems were replaced with ones composing of two bi-convex lenses each. The piston hydrophone was mounted on the Kapton window opposite the entrance window and the Olympus V303 transducer was attached inside the SmartPhantom at the bottom. To secure the transducers and to reduce movement, the transducers were 3D-scanned and casings were 3D-printed to ensure a precise fit. The SmartPhantom was then mounted onto the motorized staging to enable horizontal and vertical movements and align it with the beam axis. Images of the experimental set-up are shown in Figure 105.

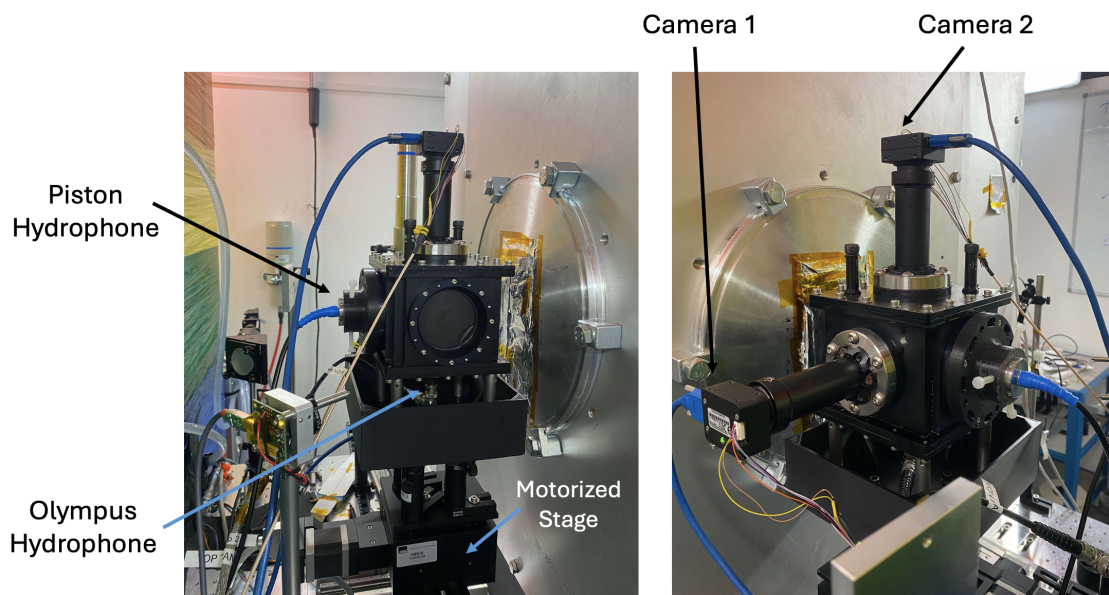


Figure 105: Experimental setup showing the SmartPhantom mounted on a motorized translation stage located at the accelerator's exit window. The Piston hydrophone is aligned with the beam axis and the Olympus V303 transducer is positioned at the bottom.

The transducer wires were connected to the picoscope, while the blue wires from the cameras were connected to the central computer. Three trigger signals were sent through the trigger box: one to each camera via GPIO connectors and one to the picoscope to activate the two transducers simultaneously. In addition, acoustic matching gel was applied between the Piston hydrophone and the black Kapton foil to ensure effective coupling and maximum signal transfer.

To evaluate the effect of the beam width on the scintillation light patterns and the shapes of the acoustic signals, collimators of various sizes were placed between the accelerator's exit window and the entrance window of the SmartPhantom. The collimators used are shown in Figure 106 and feature circular apertures with diameters of 1, 2, 3 and 4 mm.

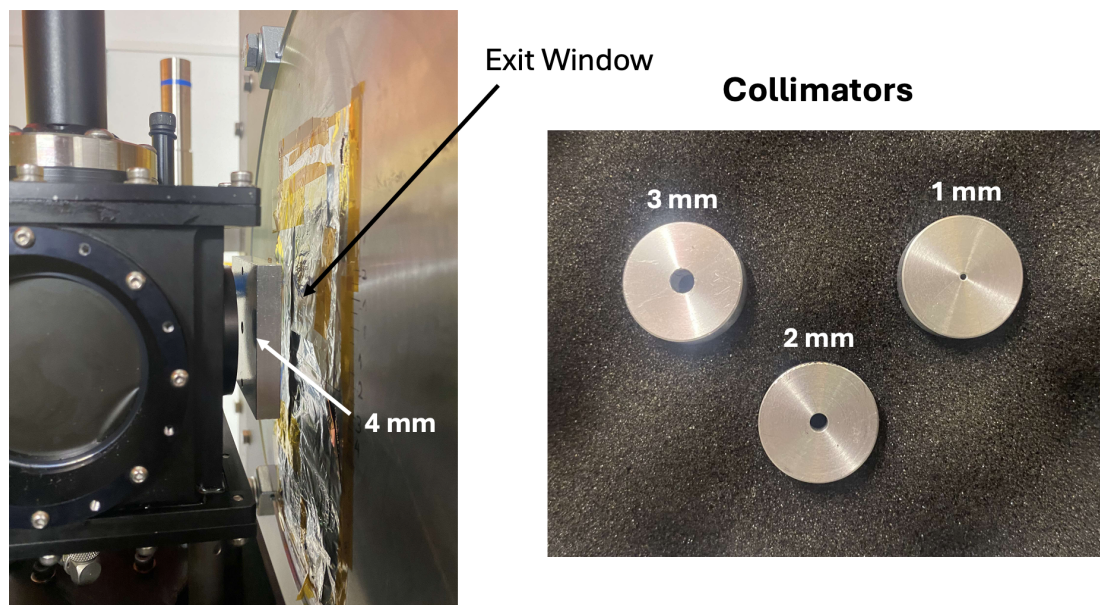


Figure 106: Location of the collimators relative to the SmartPhantom and the accelerator's exit window (left) and image of the collimators showing their respective diameters (right).

No Collimator

Initially, no collimator was placed in front of the SmartPhantom, with the only collimation coming from the 15 mm entrance tube. Simultaneous optical data from the two cameras and ultrasound data from the two transducers were collected using proton beams at design energies of 10, 12, 14, 16, 18 and 20 MeV. The background-corrected grayscale images captured by the top and side cameras are shown in Figures 107 and 108, respectively.

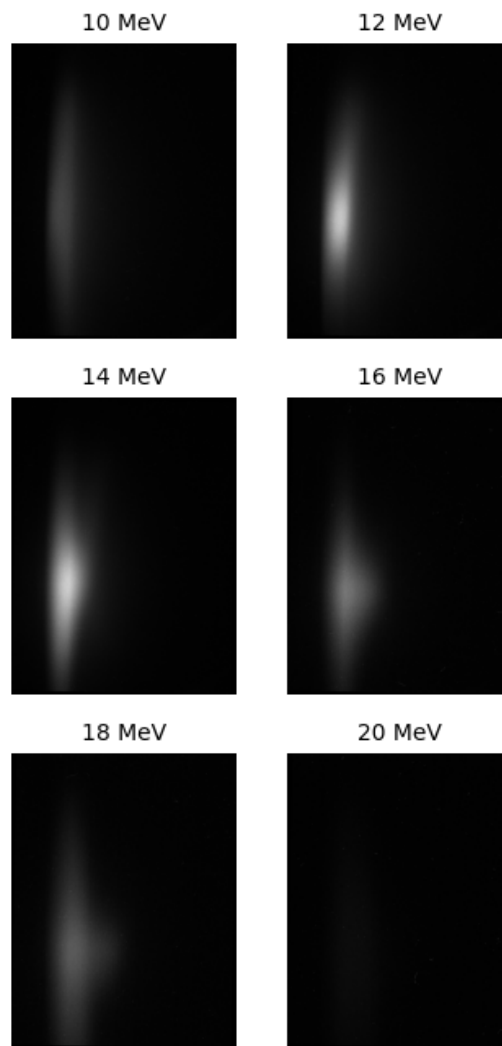


Figure 107: Averaged, background-corrected grayscale images captured using Camera 2 from the setup depicted in Figure 105, with no collimator placed at the front. The beam is incident from the left.

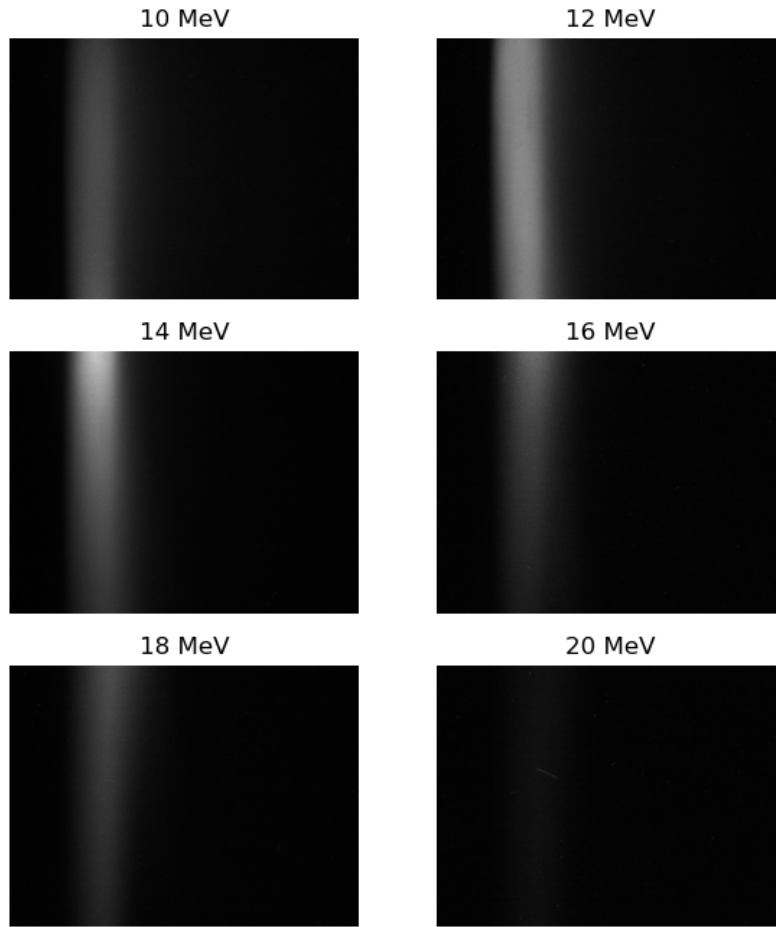


Figure 108: Averaged, background-corrected grayscale images captured using Camera 1 from the setup depicted in Figure 105, with no collimator was placed at the front. The beam is incident from the left.

The images were processed to produce colourmap plots of the pixel intensity distributions. Figure 109 presents the results based on the data obtained at a proton design energy of 14 MeV, captured using the top camera (left) and the side camera (right). In the plots, the yellow regions correspond to high-intensity pixels and the blue regions correspond to pixels with low-intensity values.

In addition, black lines are overlaid on the images to indicate the cross sections used in the subsequent analysis. In the colourmap from the top camera (Figure 109 (a)), the

horizontal line represents the z-profile that is along the beam propagation axis, while the vertical line denotes the profile in the defined x-direction. In the colourmap from the side camera (Figure 109 (b)), the vertical line represents the y-profile of the energy depositions, providing complementary information on the three-dimensional distribution.

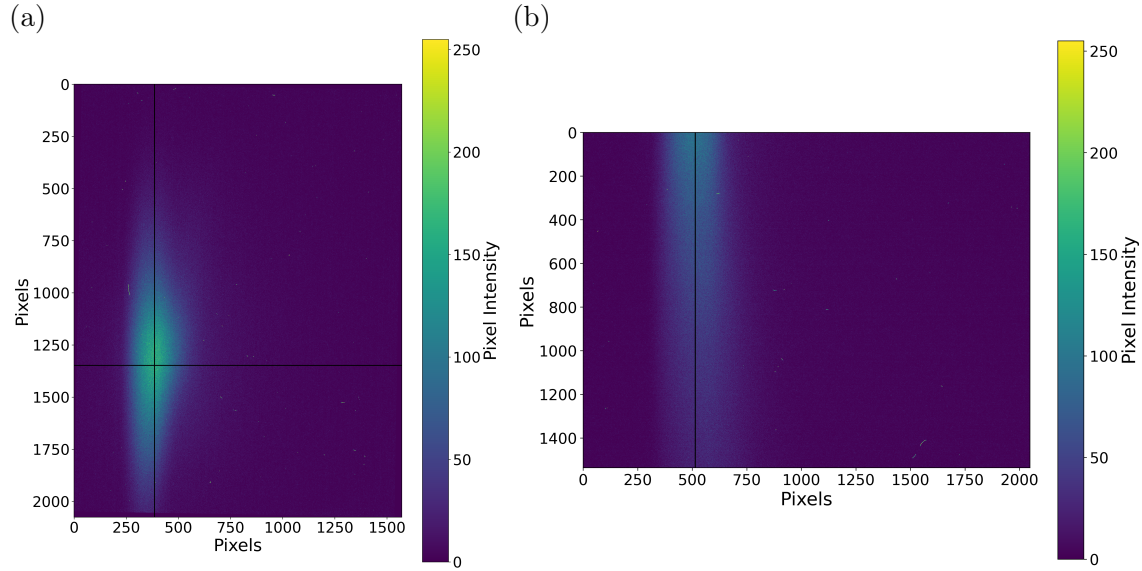


Figure 109: Colourmaps of the pixel intensities from the images obtained using the setup depicted in Figure 105 when a 14 MeV proton beam passes through the liquid scintillator. Colourmap of the averaged image captured using the top camera: (a). Colourmap of the averaged image captured using the side camera: (b).

The pixel dimensions were converted to millimeters using the physical pixel width of $3.45 \mu\text{m}$ and the magnification factor of the imaging system, -0.94 , determined through an optical simulation developed in ZEMAX Optics Studio [125]. The images were then analyzed by averaging 60 pixels along the defined axes, indicated by the black lines in the colormaps shown above. The resulting z-, x- and y-profiles are depicted in Figures 110, 111 and 112 respectively. The standard deviation, presented as a light-blue band, reflects variations across multiple measurements. The relatively large deviation values are likely

attributed to large particle number variations between shots.

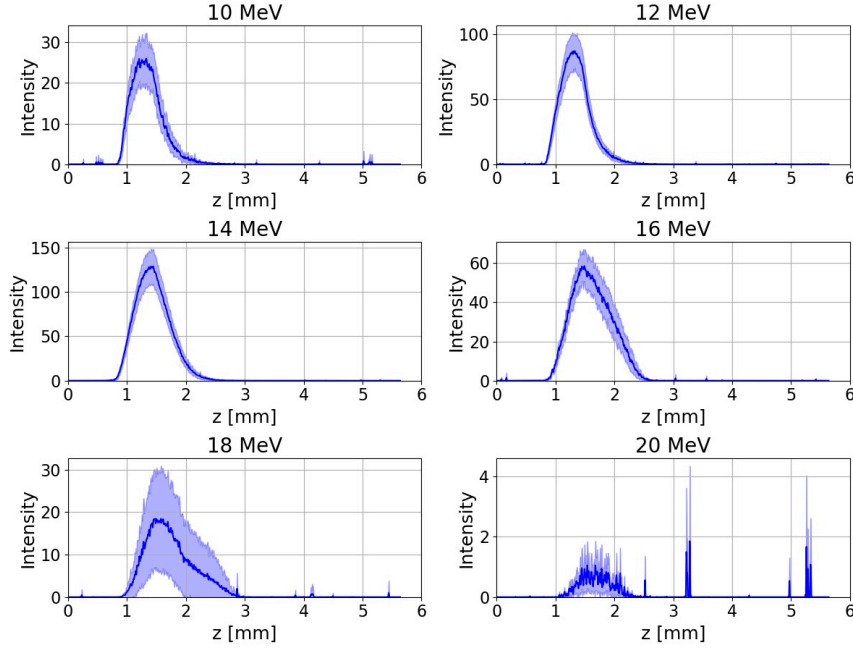


Figure 110: Z-profile average of 60 pixels, defined by the horizontal line in Figure 109 (a), from images obtained at various LION proton energies transversing the liquid scintillator.

The plots in Figure 110 show a distinct peak for all energies, with the peak location shifting to the right as the beam energy increases. In addition, the peak broadens with increasing energy and noise becomes more prominent. However, the peaks taper off gradually and do not fall sharply to zero, suggesting that the beam comprises of particles with a wide range of energies. Furthermore, no sharp rising edge is observed when the beam enters the liquid scintillator, with the light intensity gradually rising at approximately 1 mm. Upon investigation, it was concluded that this results from the entrance window flange occluding the scintillation light from the first few millimeters of the energy depositions.

Figure 111 presents the beam's transverse profile along the x-direction. The plots reveal a central peak with the intensity gradually decreasing towards the edges, suggesting good particle focus and a symmetric beam. However, the plots appear shifted and off-

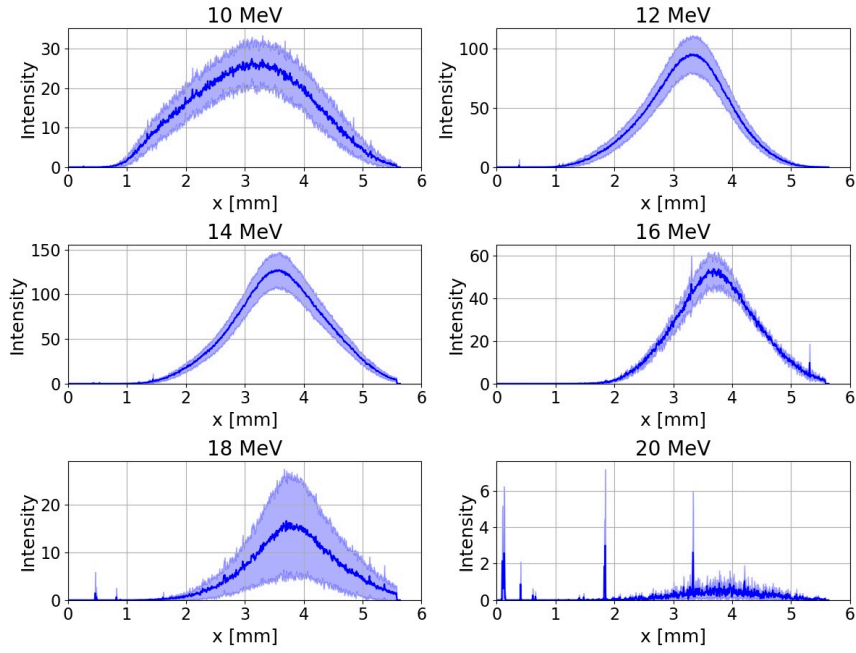


Figure 111: X-profile average of 60 pixels, defined by the vertical line in Figure 109 (a), from images obtained at various LION proton energies transversing the liquid scintillator.

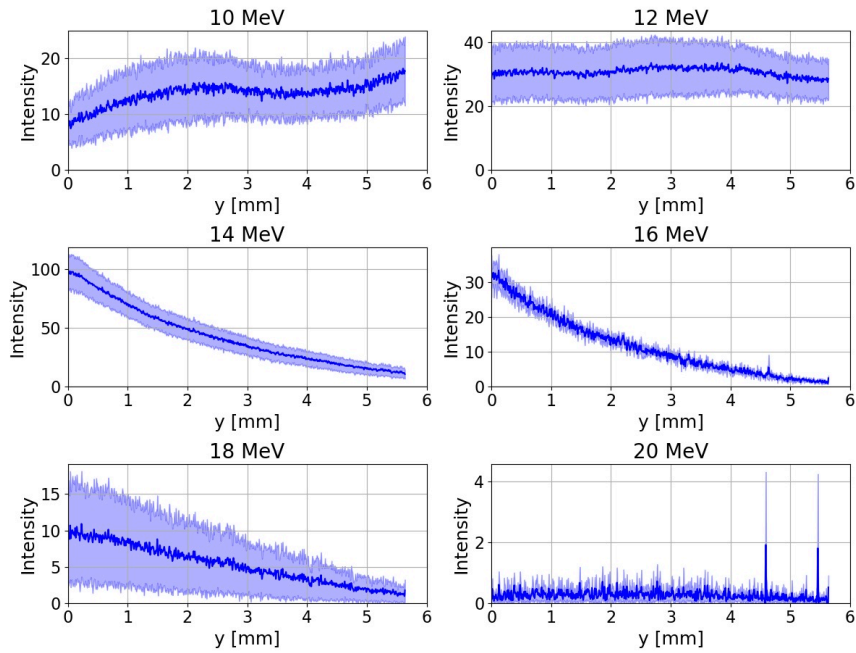


Figure 112: Y-profile average of 60 pixels, defined by the vertical line in Figure 109 (b), from images obtained at various LION proton energies transversing the liquid scintillator.

centered, possibly due to misalignment between the collimator's center and the center of the SmartPhantom. Similarly to the z-profile plots, noise dominates at higher beam energies.

In Figure 112 the beam profiles along the y-direction are presented. Unlike the x-profiles, the y-profiles do not exhibit a central peak, appearing incomplete. This could be because a significant fraction of the energy depositions occurs outside the field of view of the imaging system.

Simultaneous acoustic measurements were obtained using the Piston hydrophone and Olympus V303 transducer. Before recording the ultrasound signals, acoustic measurements of the background noise, originating from nearby cables and devices, were made. The frequency components of the noise were identified and the transducer signals were filtered to remove them. The resulting acoustic traces, for the Piston hydrophone and the Olympus transducer are shown in Figures 113 and 114, respectively.

The acoustic signals from the Piston hydrophone exhibit clear patterns, featuring the three distinct peaks observed in the simulations: the first originates from the Bragg peak, the second is the window signal and the third comes from the Bragg peak reflected off the Kapton foil. As the beam energy increases, these peaks spread apart, due to the effective range moving further from the entrance window. Consequently, the first peak arrives sooner to the transducer, the middle peak remains stationary due to the fixed distance between the foil and the transducer, and the third peak is delayed due to the additional distance the wave needs to cover to reach the Kapton foil and back. In addition, as the beam energy increases, the signals weaken and noise becomes increasingly important. As a result, features of the signal become harder to distinguish.

The acoustic signals from the Olympus transducer are more distorted, possibly due to weak particle focusing in the observed direction. The irregular signal shapes make it

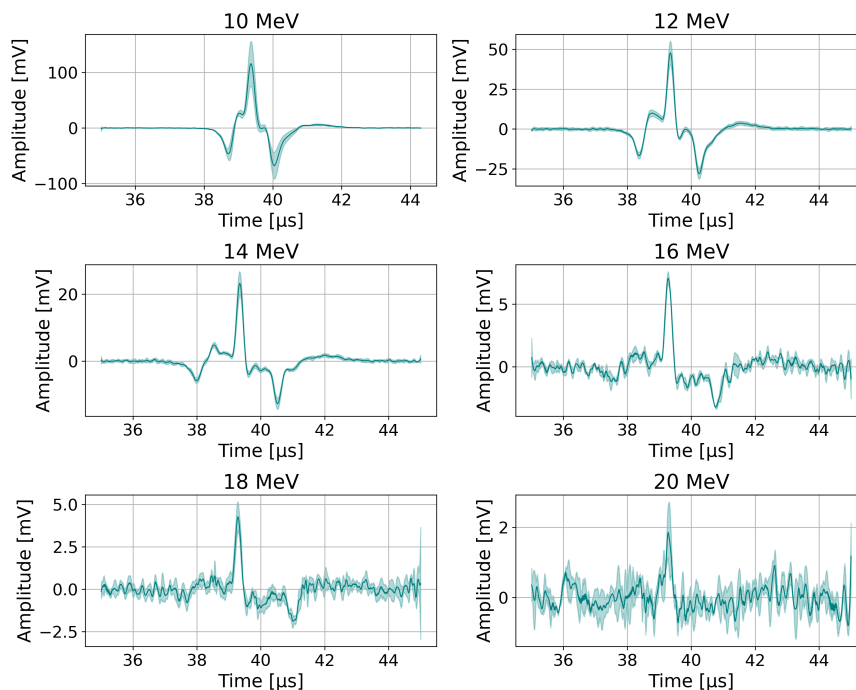


Figure 113: Acoustic waveforms recorded by the Piston hydrophone, positioned on-axis with the beam, with various LION beam energies. No collimator was used in the setup.

challenging to identify clear patterns in the peaks, limiting the amount of useful information. In addition, similar to the Piston hydrophone data, the signals become increasingly noisy as the beam energy increases.

4 mm Collimator

In the next set of experiments, a 4 mm circular collimator was placed at the front of the SmartPhantom, mounted on a holder fixed to the optical bench. The averaged, background-corrected images obtained using the top and side cameras, for the various beam energies, are shown in Figures 115 and 116 respectively.

The images show that the collimator reduces the cross-sectional area of the beam, as expected due to its small aperture. As a result, most of the energy depositions, and hence

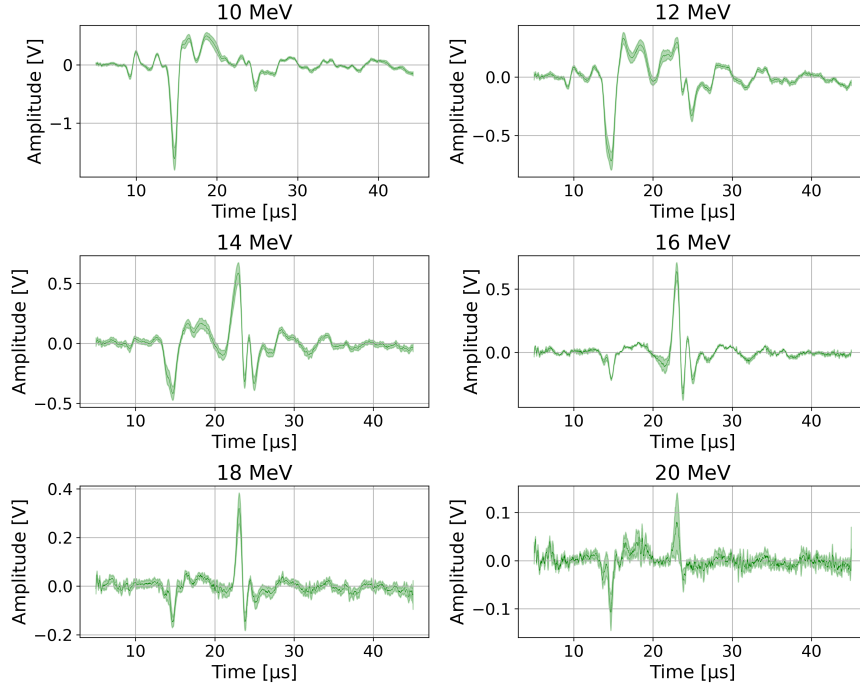


Figure 114: Acoustic waveforms recorded by the Olympus V303 transducer, immersed at the bottom, with various LION beam energies. No collimator was used in the setup.

scintillation light, occur within the cameras' field of view. In addition, the offset between the energy depositions and the center of the imaging plane is possibly due to misalignment between the collimator and imaging system. Moreover, the intensity fluctuations can be attributed to large particle number variations between shots.

The beam profiles were extracted from the images by averaging 60 pixels along the black lines shown in the colourmaps in Figure 117. As in the case of the previous datasets, the horizontal and vertical lines in the left plot indicate the z- and x-axis, respectively, and the vertical line in the right plot corresponds to the y-axis. The resulting z-, x- and y-profiles across the respective lines are presented in Figures 118, 119 and 120.

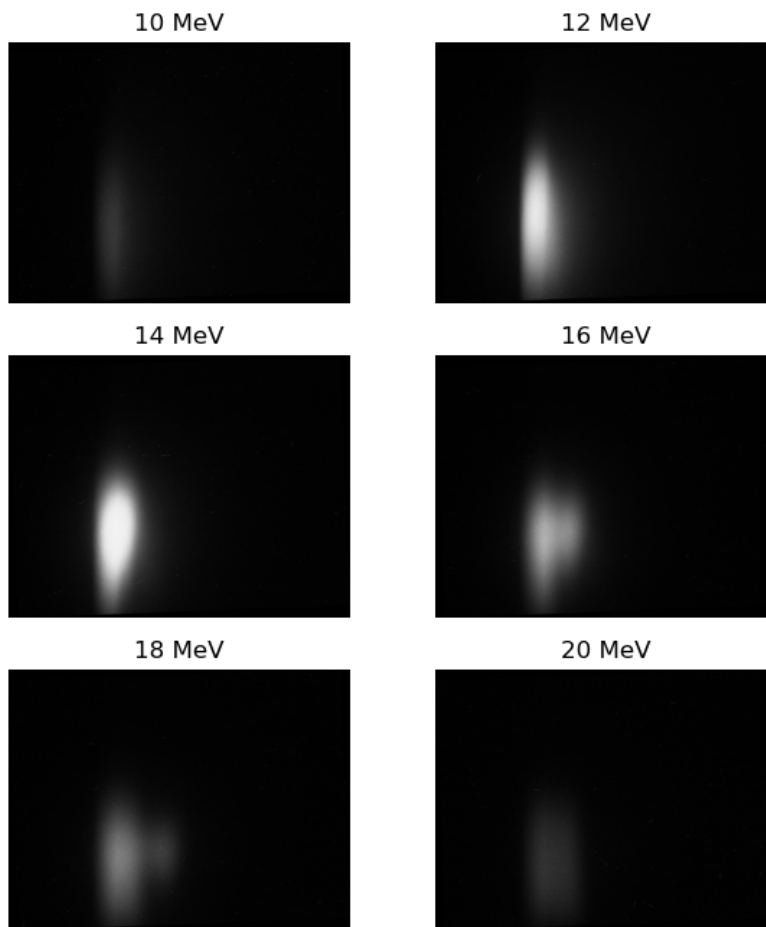


Figure 115: Averaged, background-corrected grayscale images obtained using Camera 2 from the setup shown in Figure 105. A 4 mm collimator was placed at the front.

The z-profile plots with the 4 mm collimator exhibit sharper peaks compared to the z-profiles without a collimator. This can be because the collimator filters out particles found in the outer radius of the beam that do not have the desired energy. As a result, the collimator sharpens the energy spectrum of the focused particles and hence the Bragg peak appears narrower. Furthermore, as the beam energy increases, a second peak begins to emerge. A possible explanation for this might be the non-optimized drifts between the quadrupole magnets in the accelerator configuration.

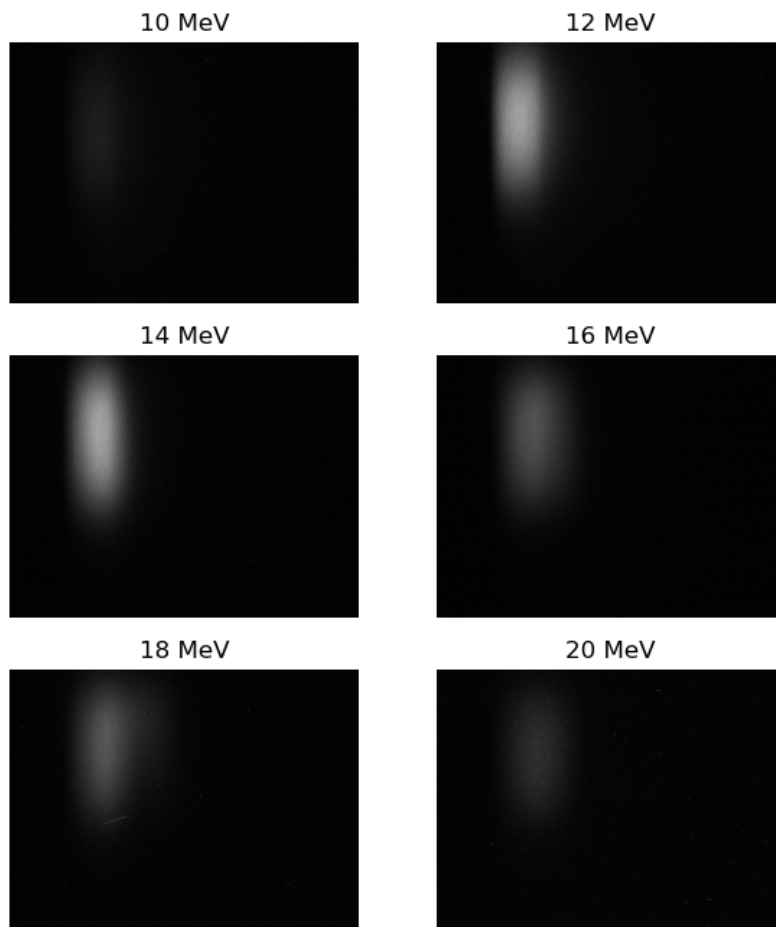


Figure 116: Averaged, background-corrected grayscale images obtained using Camera 1 from the setup shown in Figure 105. A 4 mm collimator was placed at the front.

The x- and y-profile plots are narrower when the collimator is placed in front of the detector. Consequently, the camera imaging the y-plane is able to capture a larger fraction of the energy depositions. In addition, as with the previous results, the beam is not centered in either plane due to misalignment between the collimator and the detector's center. Furthermore, saturation observed in the x-plane when the 14 MeV beam propagates through the liquid scintillator, possibly due to a large particle count. The saturation is also evident in the colourmap in Figure 117 (a).

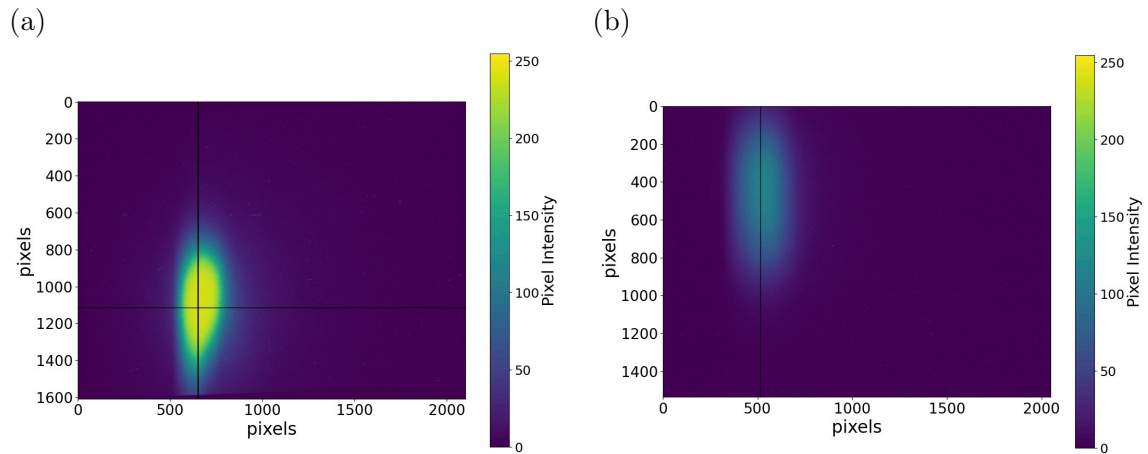


Figure 117: Colourmaps of pixel intensities from the images obtained using the top camera (a) and side camera (b) when a 14 MeV proton beam passes through the liquid scintillator. The setup included a 4 mm collimator in front of the SmartPhantom.

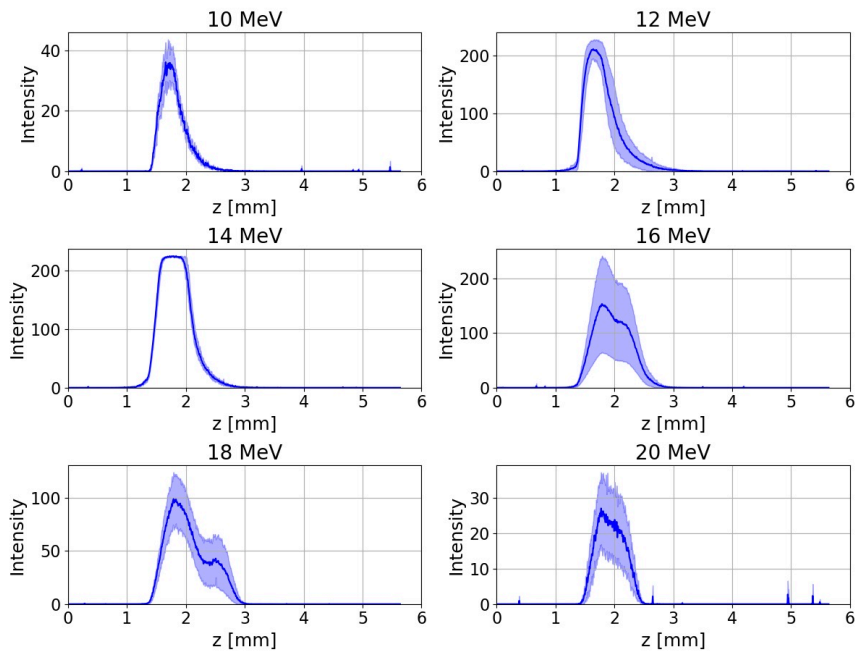


Figure 118: Z-profile average of 60 pixels from images obtained at various proton energies transversing the liquid scintillator, with 4 mm collimator at the front of the SmartPhantom.

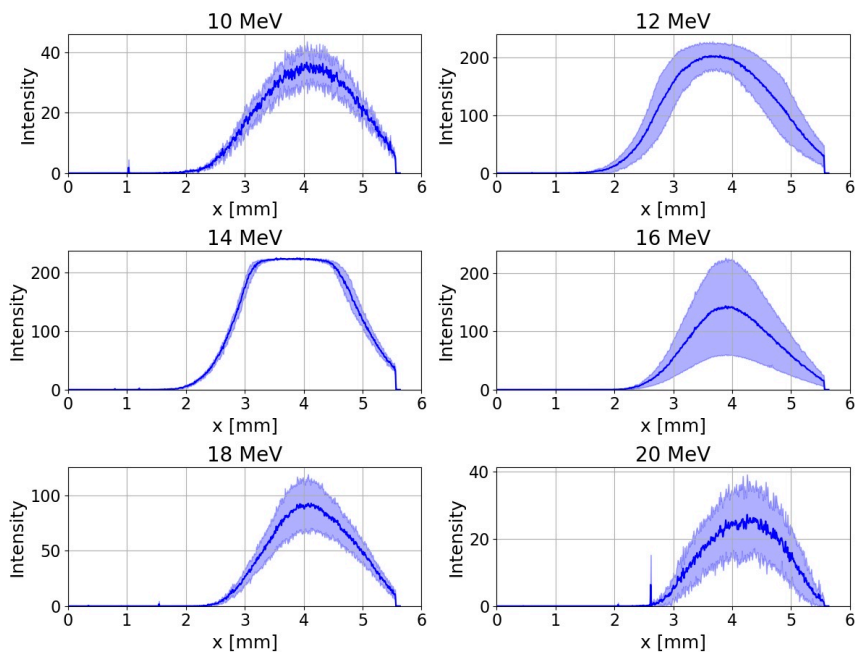


Figure 119: X-profile average of 60 pixels from images obtained at various proton energies transversing the liquid scintillator, with 4 mm collimator at the front of the SmartPhantom.

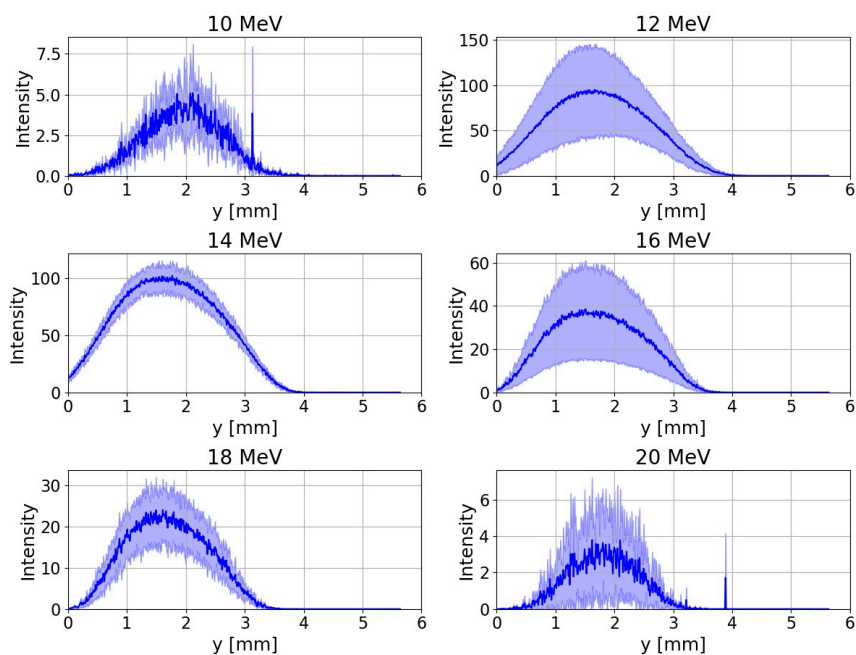


Figure 120: Y-profile average of 60 pixels from images obtained at various proton energies transversing the liquid scintillator, with 4 mm collimator at the front of the SmartPhantom.

The acoustic signal traces recorded by the Piston hydrophone and Olympus transducer with the 4 mm collimator in front of the SmartPhantom are shown in Figures 121 and 122.

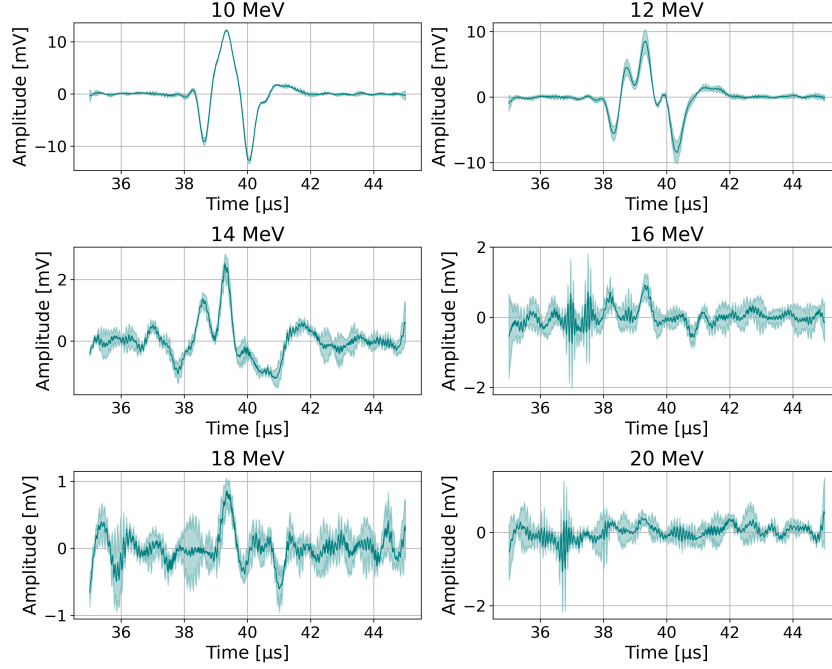


Figure 121: Acoustic waveform recorded by the Piston hydrophone, on-axis with the beam, with a 4 mm collimator placed in front of the SmartPhantom.

The waveform recorded by the Piston hydrophone appears noisier compared to the corresponding waveform without a collimator. While the peaks appear at the same time intervals, the amplitudes are significantly smaller due to the lower number of particles entering the detector. As a result, the signal features are harder to distinguish, with the 16, 18 and 20 MeV waveforms being dominated by noise.

In contrast, the waveforms recorded by the Olympus transducer are significantly clearer compared to those obtained without a collimator, with two distinct peaks visible in the acoustic traces across all beam energies. This is possibly due to the the collimator filtering out particles found at the outer radius of the beam, thereby generating a more compact

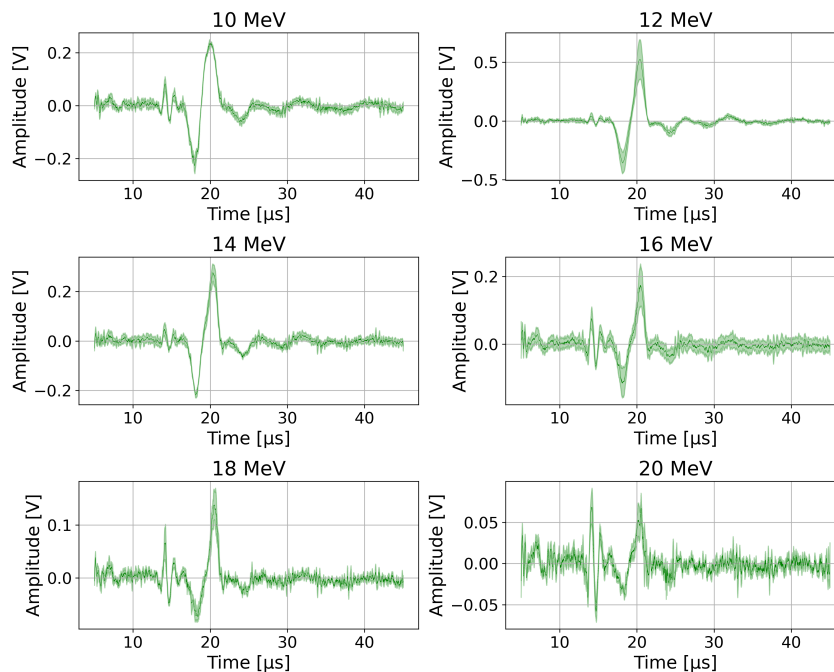


Figure 122: Acoustic waveform recorded by the Olympus V303 transducer, immersed from the bottom, with a 4 mm collimator placed in front of the SmartPhantom.

and well-defined sound wave. In addition, as with all acoustic traces, the signals become progressively noisier with increasing beam energy.

2 mm Collimator

In the final set of experiments, the 4 mm diameter collimator was replaced with a smaller one that had a 2 mm circular aperture. Due to time constraints, measurements were only taken with nominal 14 and 16 MeV proton beams. The averaged, background-corrected grayscale images using the top and side cameras are shown in Figures 123 and 124, respectively. The images reveal that the width of the beam decreases significantly with the smaller collimator aperture, with the scintillation light entirely contained within the camera's field of view. In addition, colourmaps of the images obtained with a 14 MeV proton beam are displayed in Figure 125.

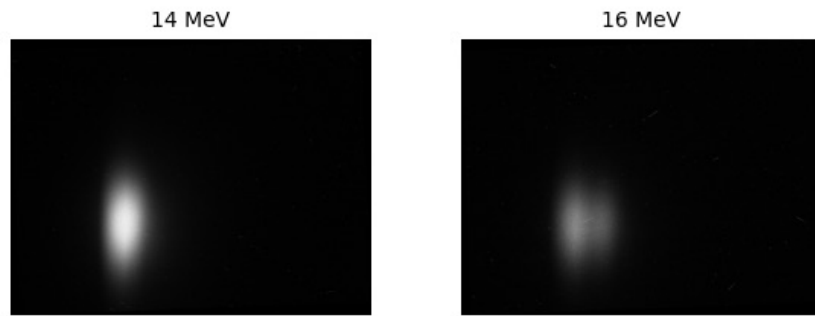


Figure 123: Averaged, background-corrected grayscale images obtained using Camera 1 from the setup shown in Figure 105. A 2 mm collimator was placed at the front.

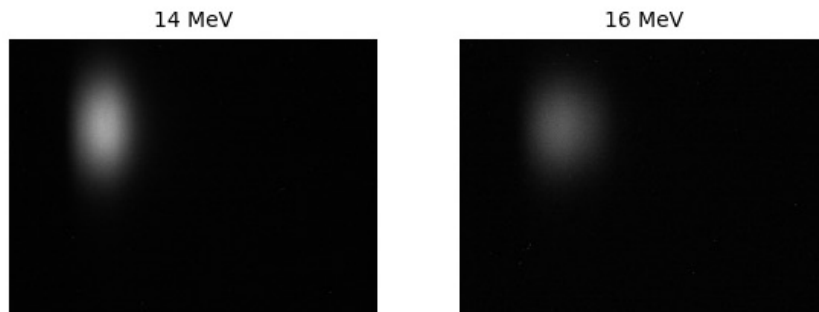


Figure 124: Averaged, background-corrected grayscale images obtained using Camera 2 from the setup shown in Figure 105. A 2 mm collimator was placed at the front.

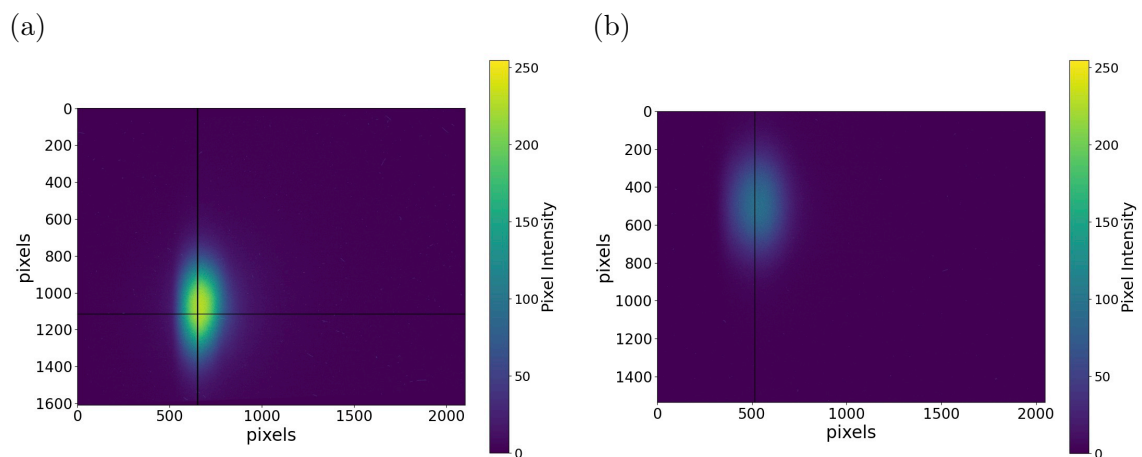


Figure 125: Colourmaps of pixel intensities from the images obtained with a 14 MeV proton beam. The setup included a 2 mm collimator in front of the SmartPhantom.

The z-, x- and y-profiles across the black lines illustrated in the colourmaps, for the different proton beam energies, are shown in Figures 126, 127 and 128, respectively.

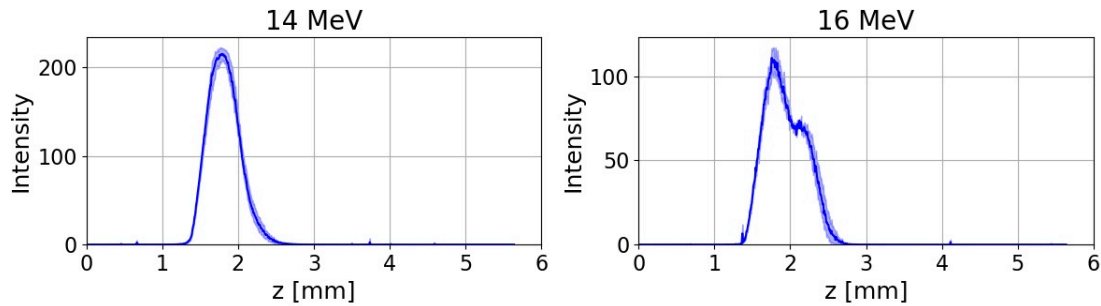


Figure 126: Z-profile average of 60 pixels from images obtained at various proton energies transversing the liquid scintillator, with 2 mm collimator at the front of the SmartPhantom.

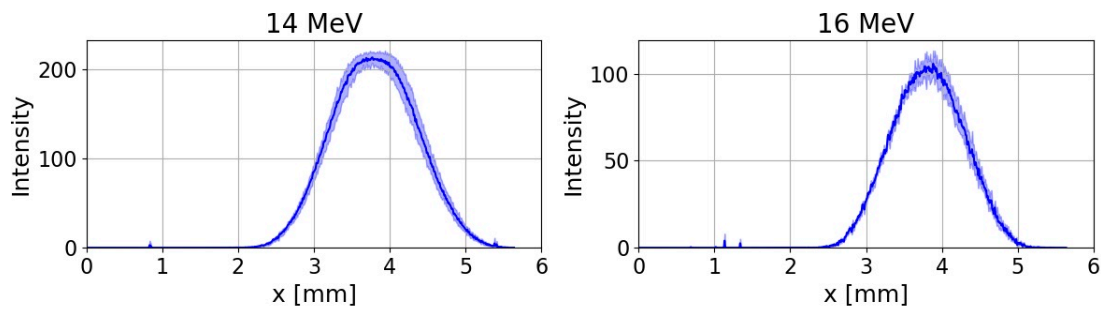


Figure 127: X-profile average of 60 pixels from images obtained at various proton energies transversing the liquid scintillator, with 2 mm collimator at the front of the SmartPhantom.

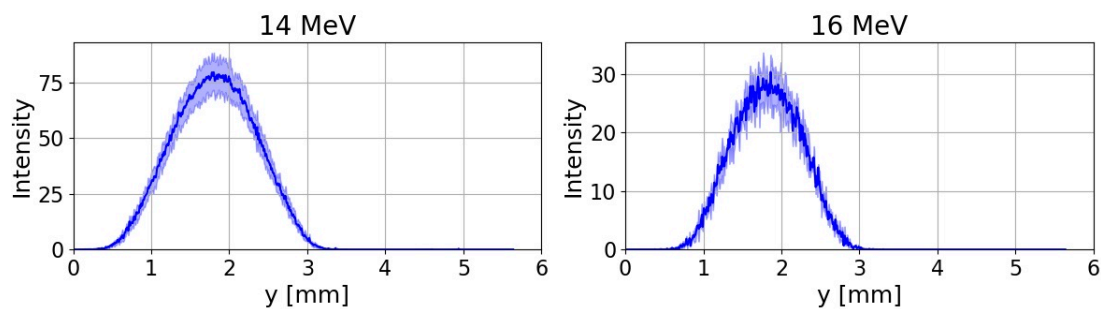


Figure 128: Y-profile average of 60 pixels from images obtained at various proton energies transversing the liquid scintillator, with 2 mm collimator at the front of the SmartPhantom.

The plots indicate that the central peaks in the z-profiles become narrower, while an emerging second peak at 16 MeV is observed. In addition, the beam width in both the x- and y-directions is significantly smaller. Overall, the errors bands with the 2 mm collimator are significantly smaller, making features in the profiles easier to identify.

Lastly, the acoustic traces recorded by the two transducers are presented in Figures 129 and 130. The traces from the Piston hydrophone appear noisy and of low amplitude, while the traces from the Olympus transducer appear clearer and more distinct.

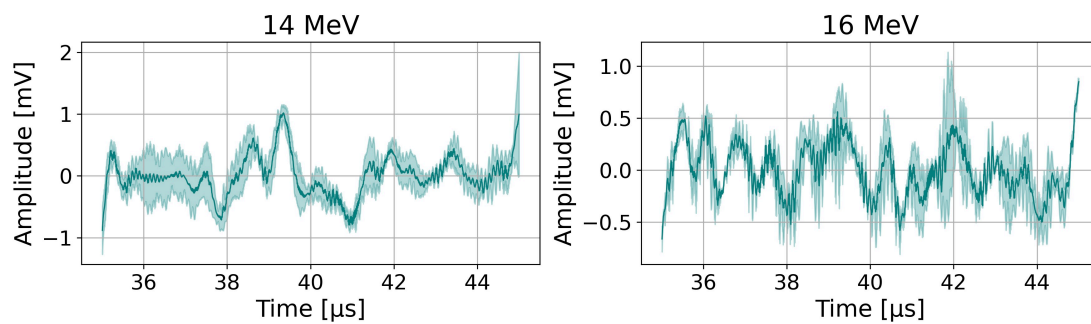


Figure 129: Acoustic waveform recorded by the Piston hydrophone, on-axis with the beam. It's position is shown in Figure 105. A 2 mm collimator was used in this configuration.

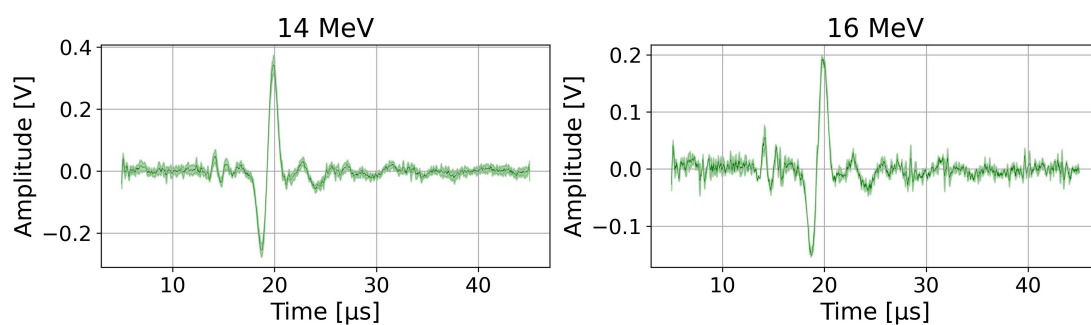


Figure 130: Acoustic waveform recorded by the Olympus V303 transducer, immersed from the bottom. It's position is shown in Figure 105. A 2 mm collimator was used in this configuration.

8.4.1 Effective Range

The effective range of the beam can be determined using both the optical and acoustic data. A comparison of the values determined by the two methods can provide valuable insights into the degree of correlation between the optical and the acoustic systems.

Initially, the z-profile data were corrected by identifying the location of the entrance window in the images, as it is also imaged by the optical system. This was done by analyzing the slope of the dark blue curves shown in Figures 110, 118 and 126. The point of greatest curvature change was identified by finding the peak of the second derivative of the curves. The peak remained consistent across all energies. Subsequently, the data preceding it were disregarded.

A significant portion of the scintillation light was occluded by the mechanical structure of the entrance window seal. To account for this effect, an optical simulation was developed in ZEMAX Optics Studio, by Professor Peter Hobson, incorporating the design of the SmartPhantom as well as key optical properties of both the structure's materials and the liquid scintillator [125]. The optical simulation was performed with a 0.1 mm diameter beam that emits a uniform intensity in all directions. Two separate simulations were run: one with the SmartPhantom entrance window sealed by a flat Kapton foil and another where the entrance window also includes the flange shown in Figure 11. The results without and with the entrance window seal are shown in Figure 131 top and bottom, respectively, where 0 mm is the center of the SmartPhantom.

The plot reveals that the first few millimeters are shadowed by the mechanical structure of the seal, with the gradient of the curve appearing less steep compared when it is absent. In addition, the x-axis crossing is shifted by 0.5 mm. To compensate for the shadowing

effect, the z-axis values of the z-profiles were shifted by 0.5 mm to the right.

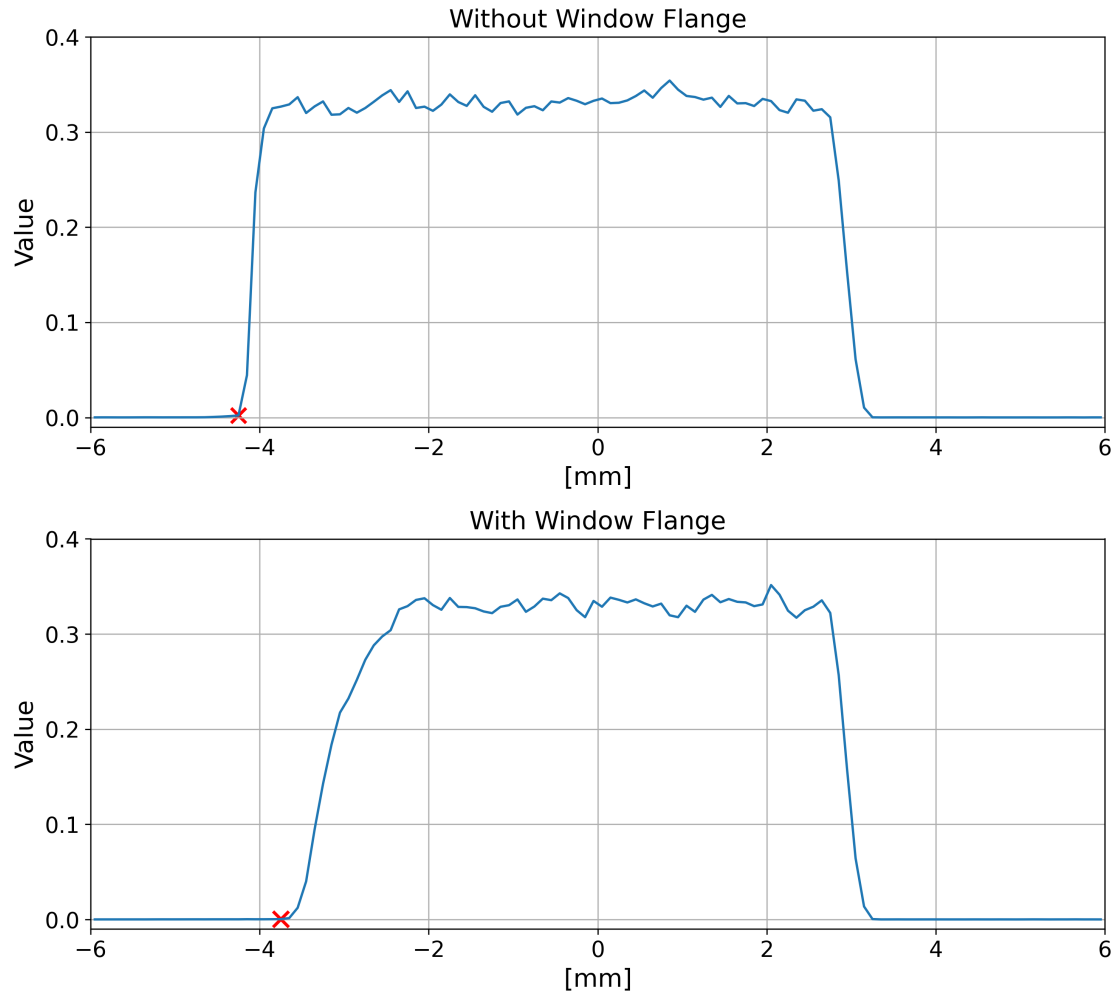


Figure 131: Optical simulation results developed in ZEMAX Optics Studio without (top) and with (bottom) the entrance window flange depicted in Figure 11 [125]. The simulation was performed using a 0.1 mm diameter beam emitting a uniform intensity in all directions.

The corrected z-profiles for the various beam energies and collimator sizes used in the experiment are shown in Figures 132, 133 and 134. In the plots, the vertical green lines indicate the location identified by the peak of the second derivative of the slope, which was used as an initial estimate of the entrance window, behind which the data were disregarded.

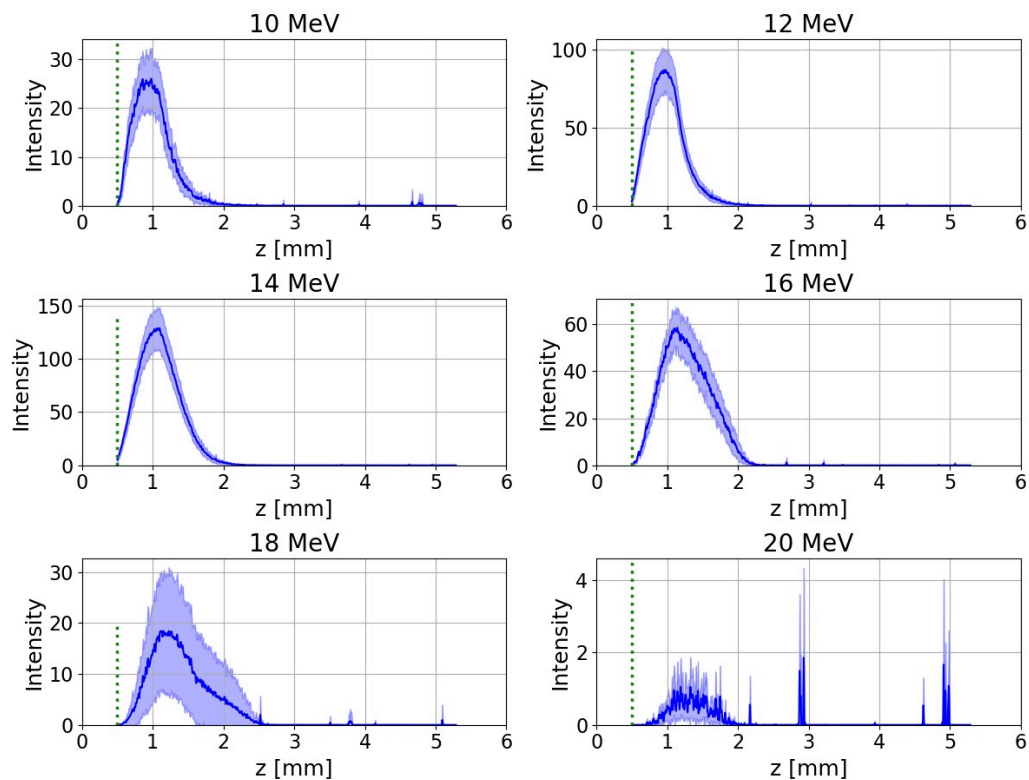


Figure 132: Z-profile average of 60 pixels, without any collimator, corrected for the 0.5 mm shift observed due to the entrance window flange. The green dotted line marks the initial estimate of the entrance window, determined by the peak of the second derivative of the curves.

The effective range was also estimated using the acoustic traces by calculating the signal envelope. The time difference between the first peak, corresponding to the signal from the Bragg peak, and the third peak, which corresponds to its reflection off the entrance window was then calculated. This time difference was multiplied by the speed of sound in the liquid scintillator to give twice the range. Figures 135, 136 and 137 display the envelope using gray lines, with the peaks marked by black dotted lines. Notably, the envelope calculation and beam range determination were only performed for datasets with clear and distinct signals.

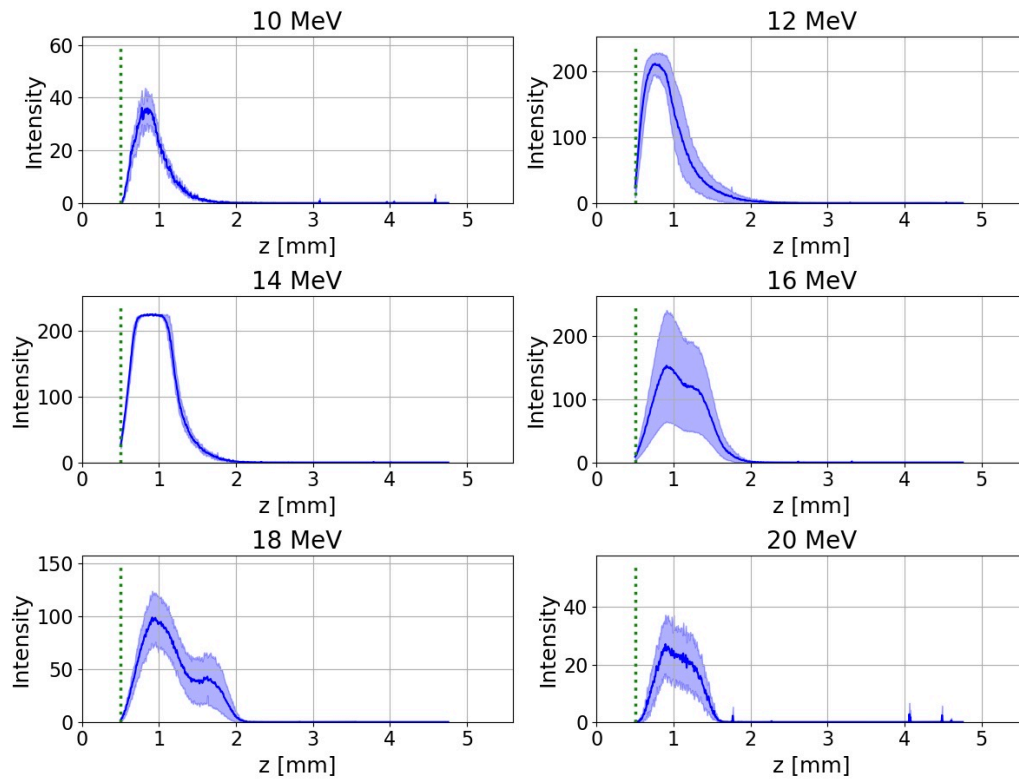


Figure 133: Z-profile average of 60 pixels, with a 4 mm collimator, corrected for the 0.5 mm shift observed due to the entrance window flange. The green dotted line marks the initial estimate of the entrance window, determined by the peak of the second derivative of the curves.

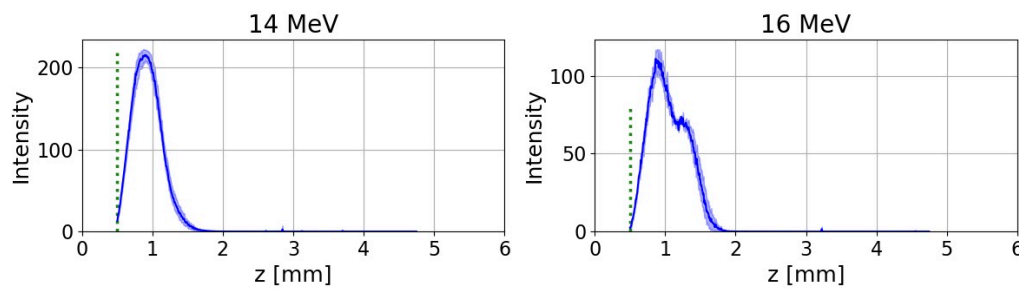


Figure 134: Z-profile average of 60 pixels, with a 2 mm collimator, corrected for the 0.5 mm shift observed due to the entrance window flange. The green dotted line marks the initial estimate of the entrance window, determined by the peak of the second derivative of the curves.

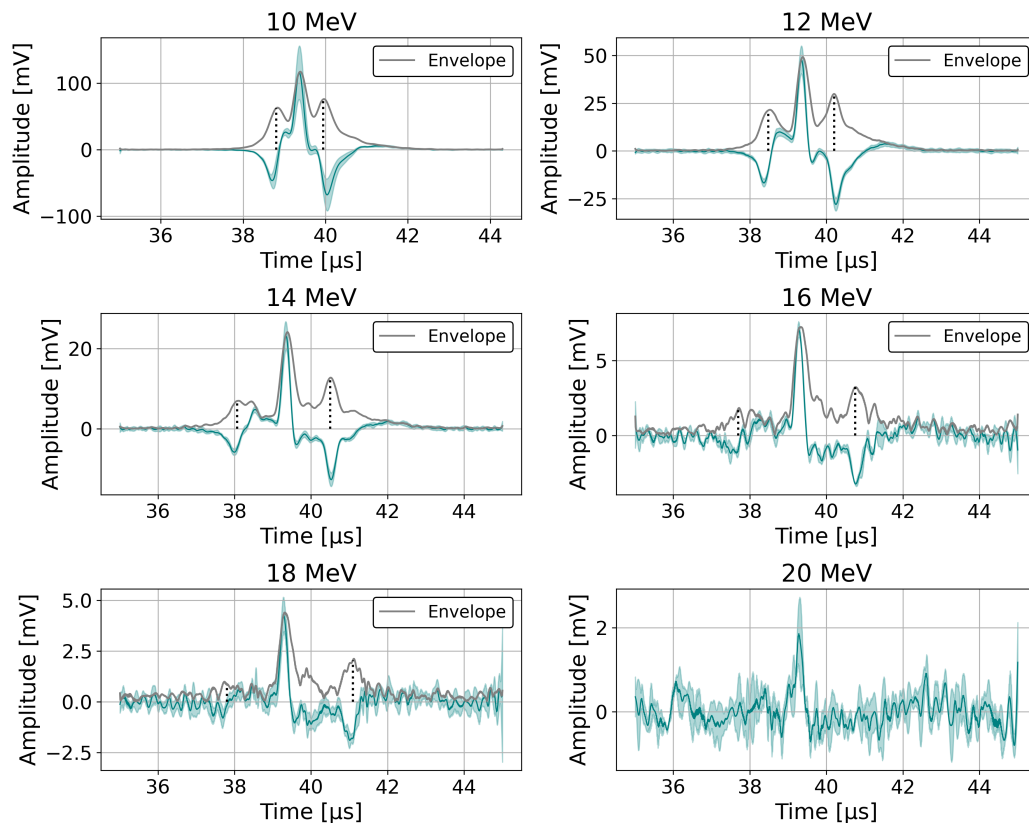


Figure 135: Acoustic waveforms recorded by the Piston hydrophone, without a collimator in the setup. The envelope is shown by the gray line, while the first and third peaks are marked by black dotted lines.

Unfortunately, the insufficient focusing of the particle beams prevented obtaining images of the scintillation light with distinct peaks for the accurate determination the effective range. Therefore, only the effective ranges determined by the acoustic data were retrieved and hence no comparison between the optical data was made. The results are presented in Figure 138. In the plots, the associated errors were calculated using the standard deviation at each peak.

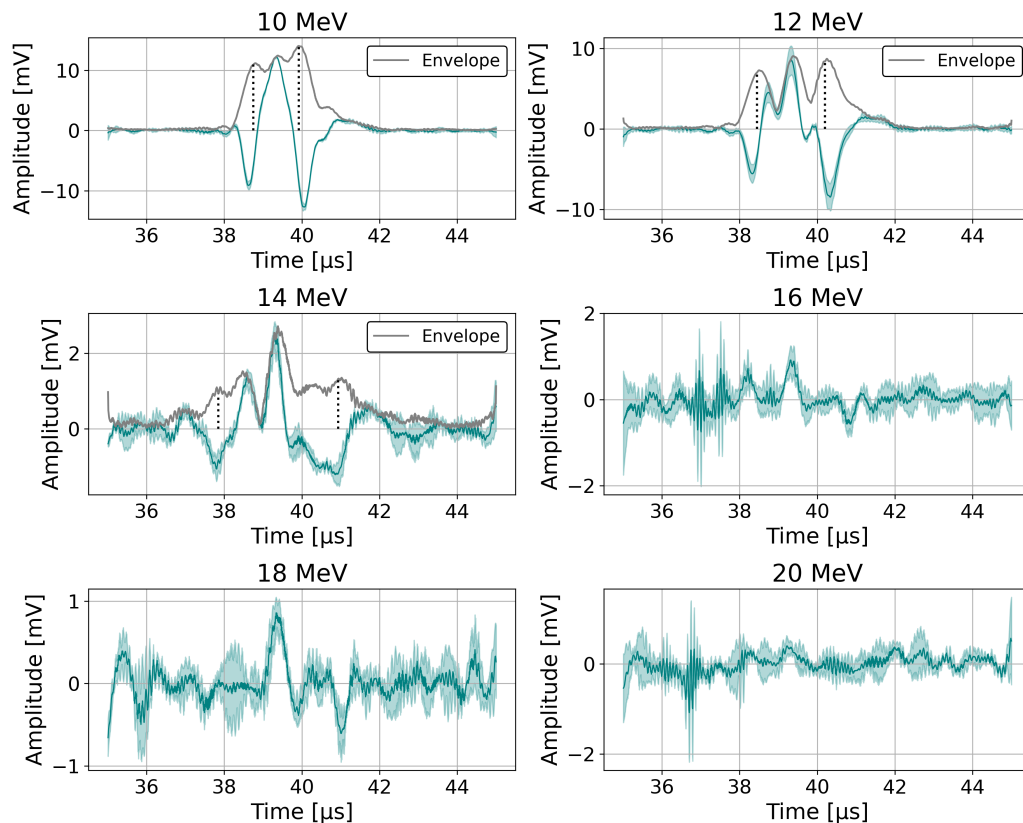


Figure 136: Acoustic waveforms recorded by the Piston hydrophone, with a 4 mm collimator in the setup. The envelope is shown by the gray line, while the first and third peaks are marked by black dotted lines.

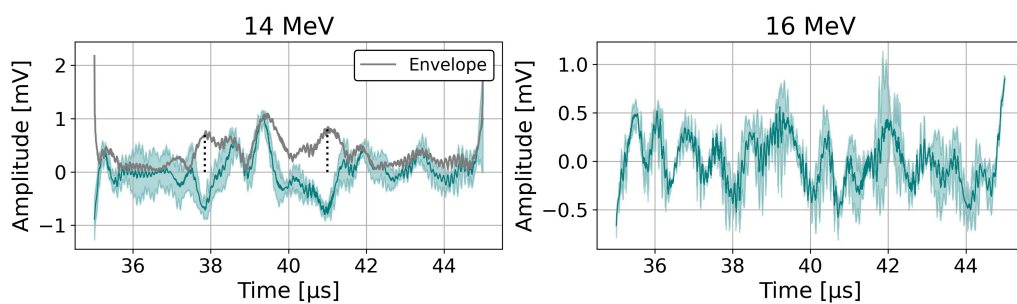


Figure 137: Acoustic waveforms recorded by the Piston hydrophone, with a 2 mm collimator in the setup. The envelope is shown by the gray line, while the first and third peaks are marked by black dotted lines.

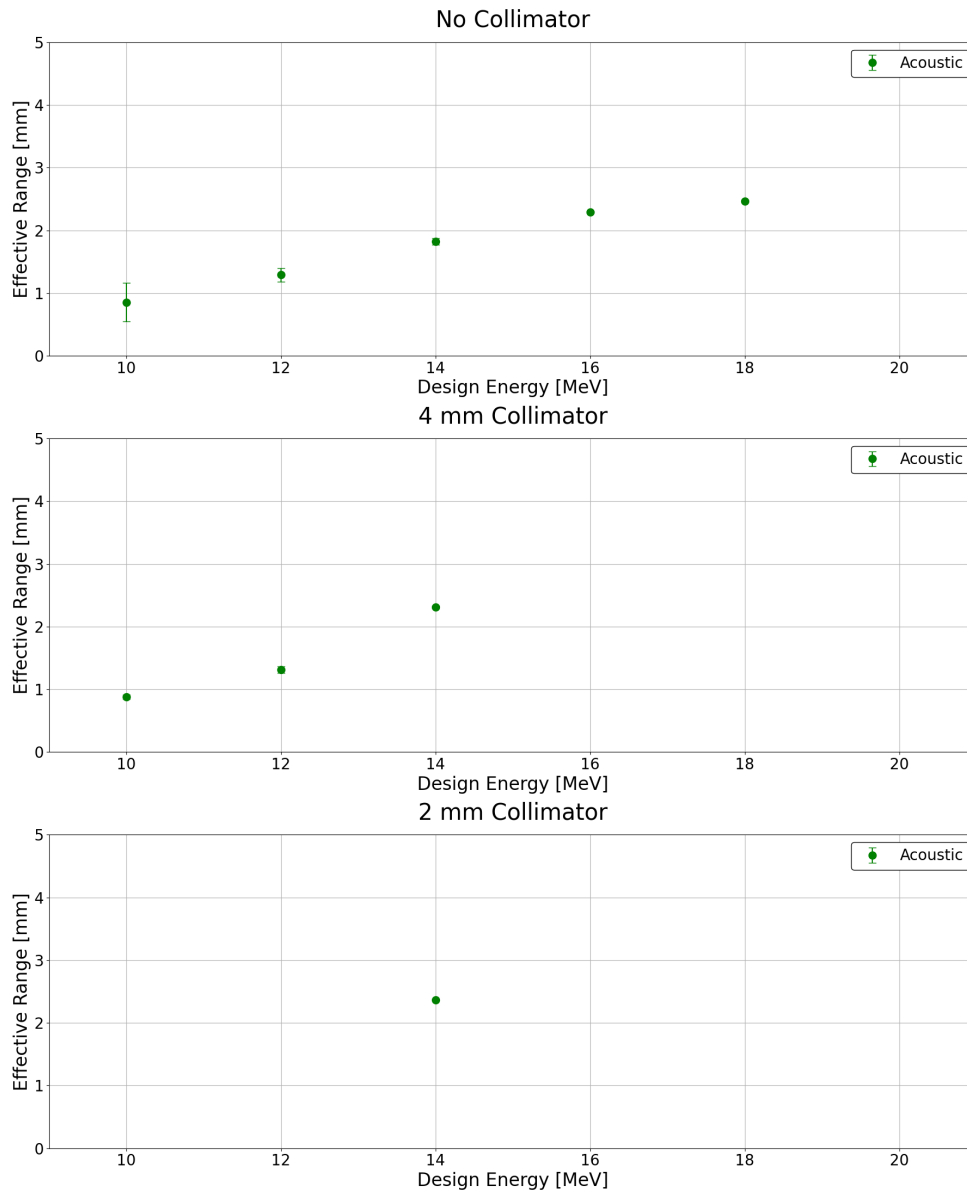


Figure 138: Effective range calculated using the peaks observed in the acoustic traces obtained by the Piston hydrophone positioned on axis with the beam.

8.4.2 Mean Energy

Furthermore, the mean energy of the beam was calculated using the Bragg-Kleeman formula (Equation 2.4), discussed in Section 2.1.2, which uses the Bragg peak range and known medium-dependent parameters. The data displayed in Figure 138 were therefore

used to calculate the mean energy of the beam for each case, with the results presented in Figure 139. In almost all cases, the calculated mean beam energy is lower than the design energy, aligning with observations from RCF Stack B.

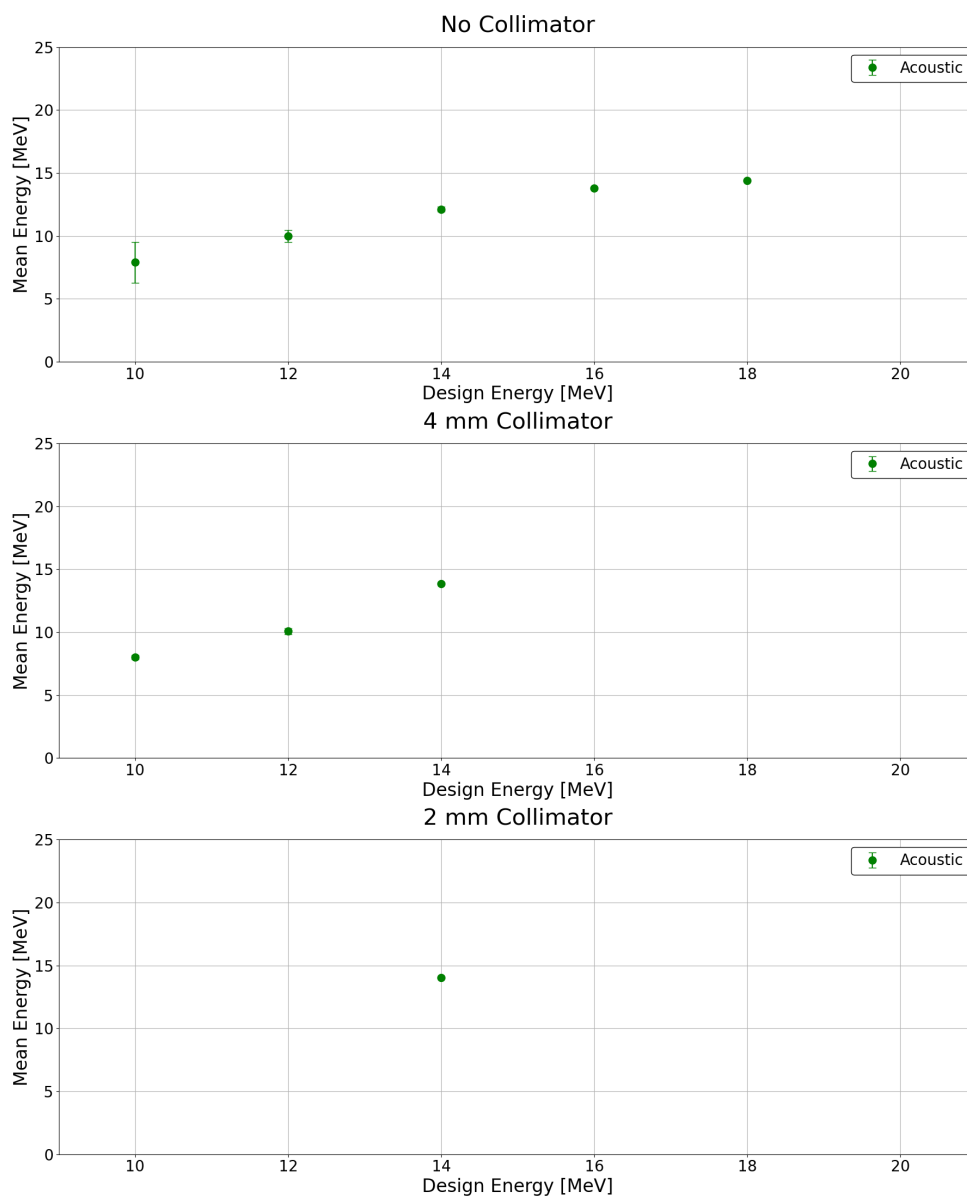


Figure 139: Mean beam energy calculated using the effective ranges shown in Figure 138 and the Bragg-Kleeman formula (Equation 2.4).

8.4.3 Beam Width

The beam width in the x- and y-directions was determined from the x- and y-profiles of the energy depositions along each axis. To calculate the FWHM, polynomial fits were applied to the data and the errors were calculated using the standard deviation derived from the error bands.

X-Profile

The energy deposition profiles along the x-direction for the different beam energies and collimators used are shown in Figures 140, 141 and 142, with the polynomial fits and FWHM indicated by the black dashed and dotted lines, respectively.

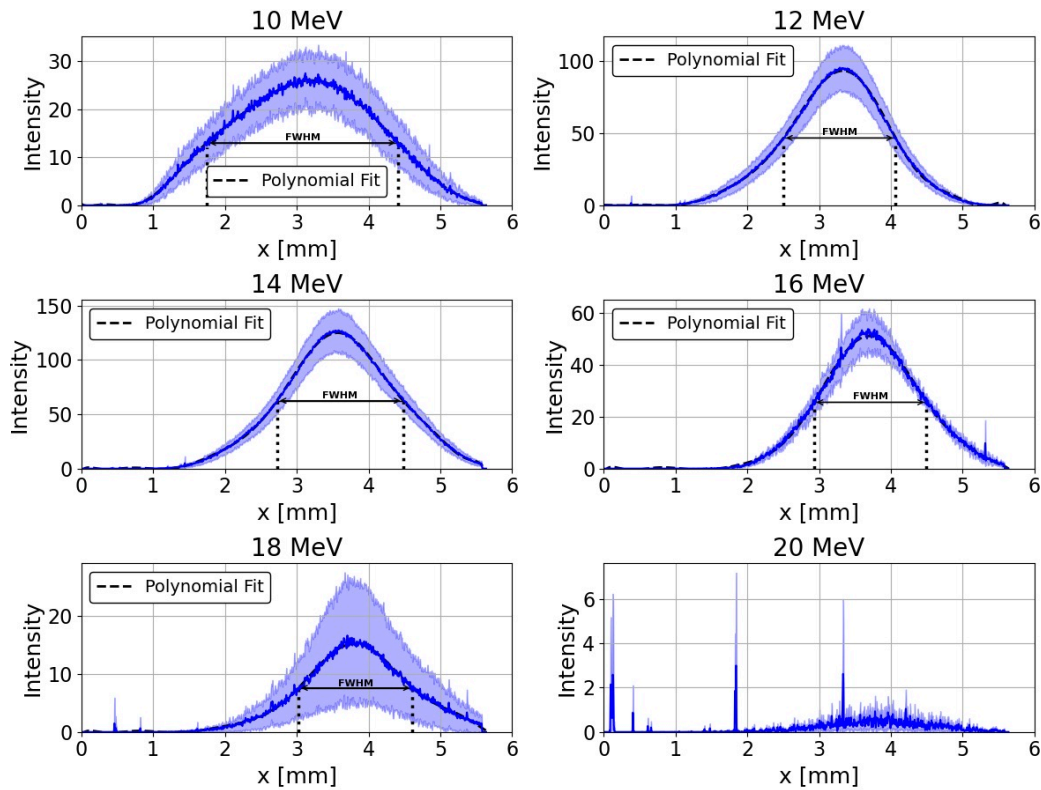


Figure 140: X-profile average of 60 pixels, from images obtained at various LION proton energies transversing the liquid scintillator. No collimator was used in the setup. A polynomial curve is fitted to the data for calculating the FWHM.

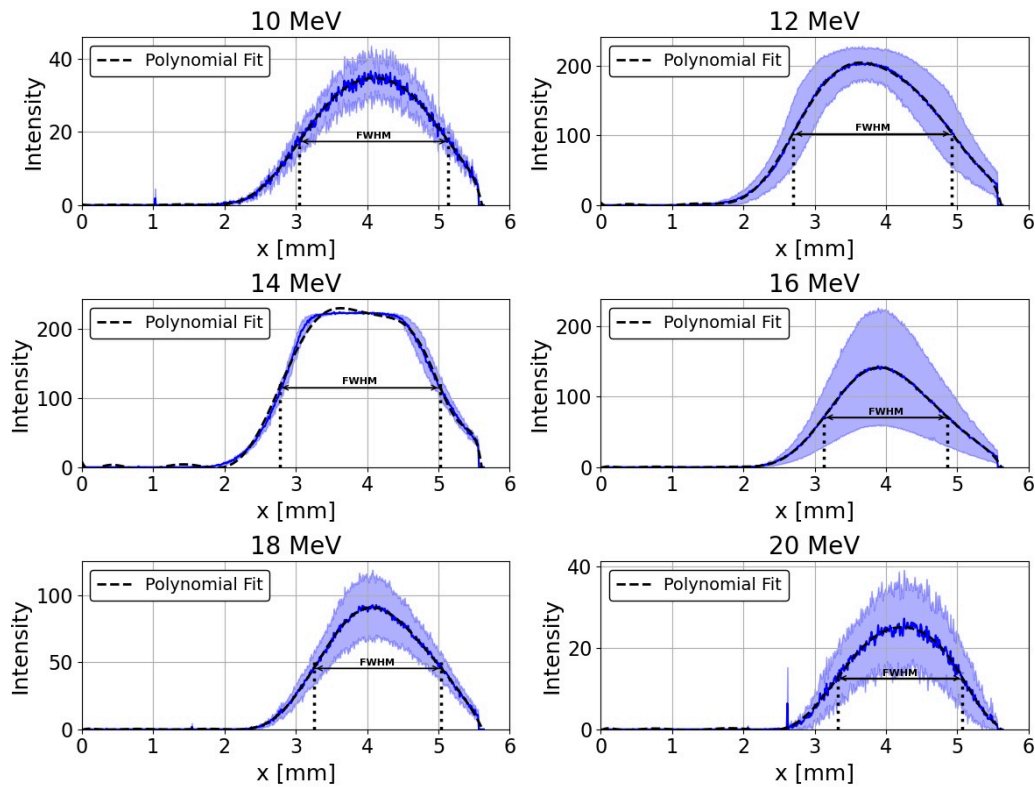


Figure 141: X-profile average of 60 pixels, from images obtained at various LION proton energies transversing the liquid scintillator. A 4 mm collimator was used in the setup. A polynomial curve is fitted to the data for calculating the FWHM.

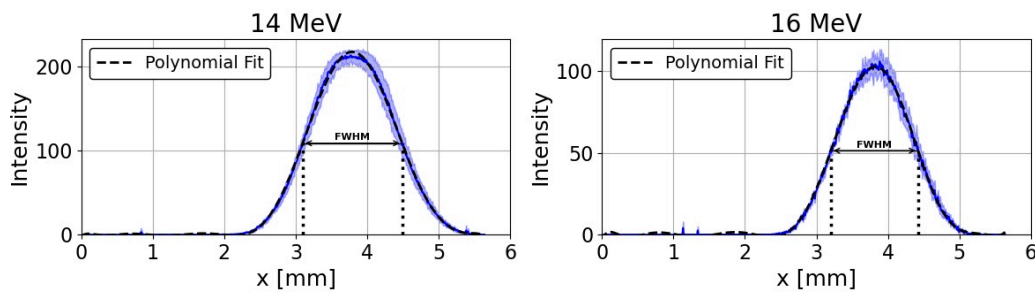


Figure 142: X-profile average of 60 pixels, from images obtained at various LION proton energies transversing the liquid scintillator. A 2 mm collimator was used in the setup. A polynomial curve is fitted to the data for calculating the FWHM.

Figure 143 shows the calculated FWHM of the beam width along the x-direction based on the optical data for the various collimators used. However, a comparison of the beam width between optical and acoustic data in this direction is not possible as no transducer was positioned facing the defined x-axis. From the plots, it is evident that the beam width decreases with the collimator size. In addition, a small decrease in width is also observed as the design energy increases.

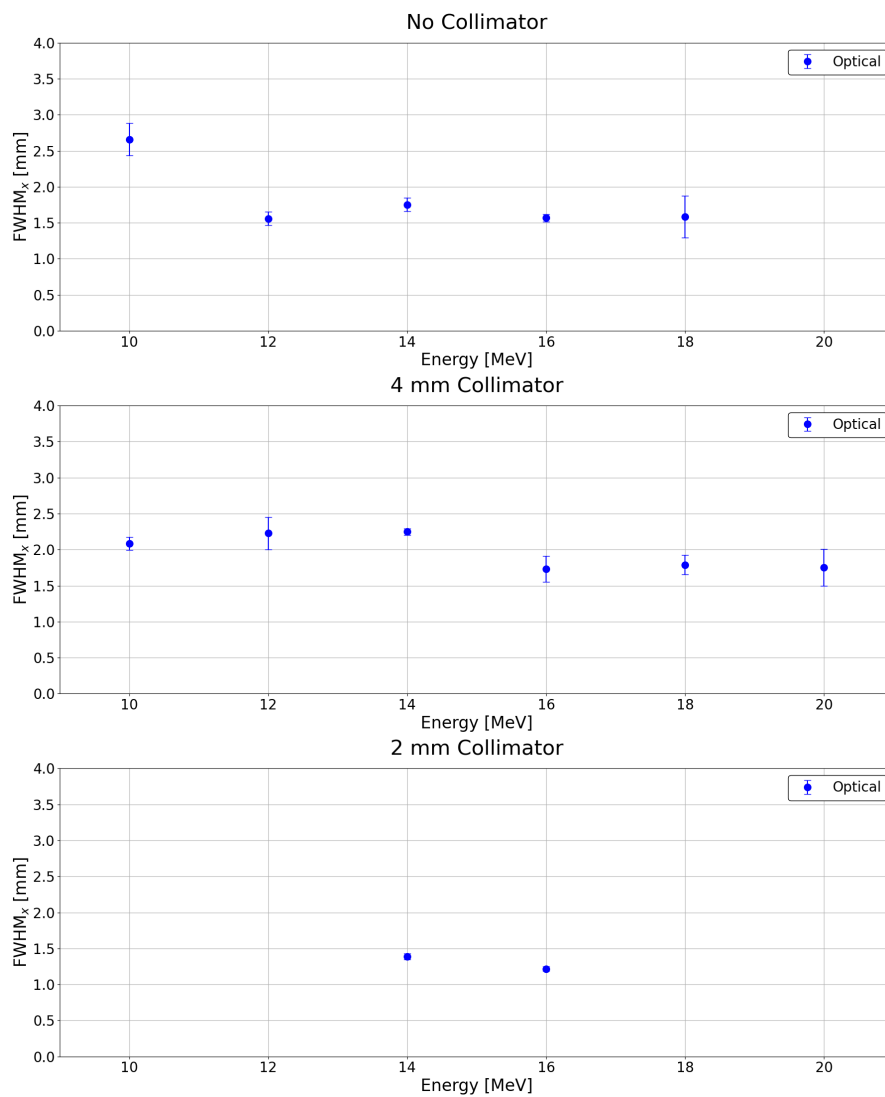


Figure 143: Full Width Half Maximum (FWHM) calculation along the x-direction of the beam depositions at the various proton energies and collimator sizes used in the setup.

Y-Profile

The beam width in the y-direction was calculated using the same approach as the width across the x-direction, by applying polynomial fits to the extracted profiles. Figures 144 and 145 present the y-profile averages over 60 pixels along the y-direction for the 4 mm and 2 mm data at the investigated energies, respectively. Unfortunately, the beam width along the y-direction without a collimator could not be determined, as a large fraction of the energy depositions were outside the camera's field of view. In addition, the polynomial fits are shown as black dashed lines. The FWHM for each case was calculated from the fits, with the associated errors calculated from the error bands shown by the lighter blue colour.

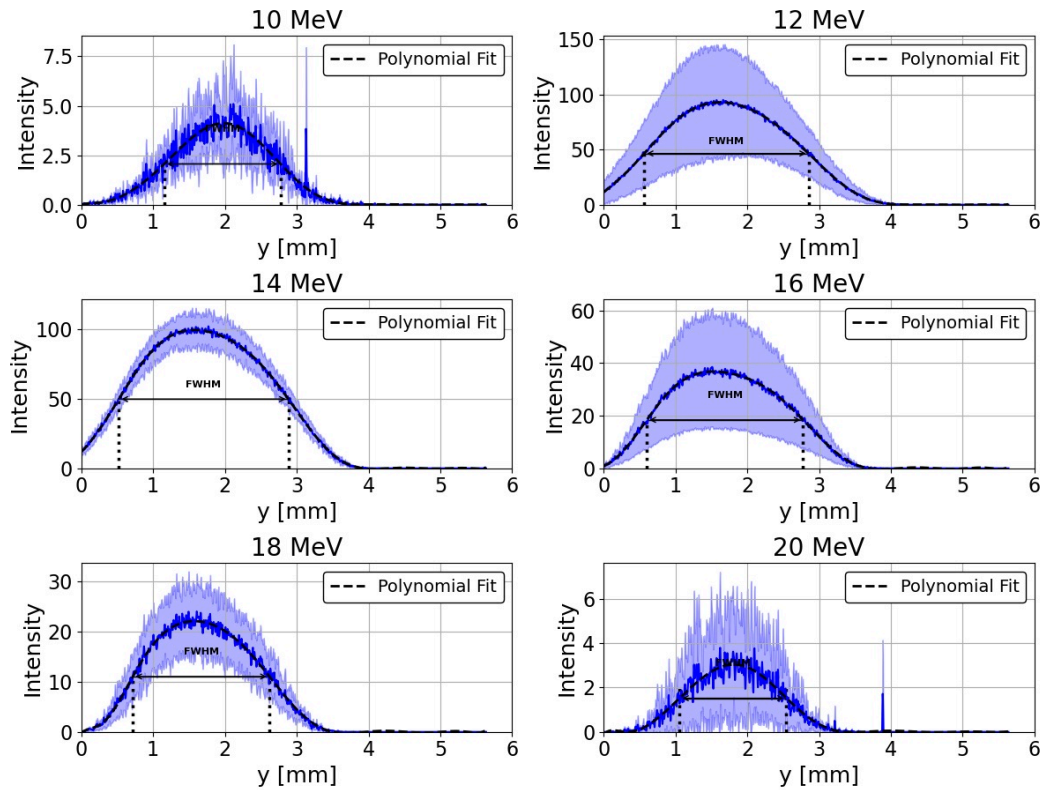


Figure 144: Y-profile average over 60 pixels from images obtained at various proton energies transversing the liquid scintillator, with a 4 mm collimator in the setup. A polynomial fit, shown by the dashed black line, is used to calculate the FWHM of the beam.

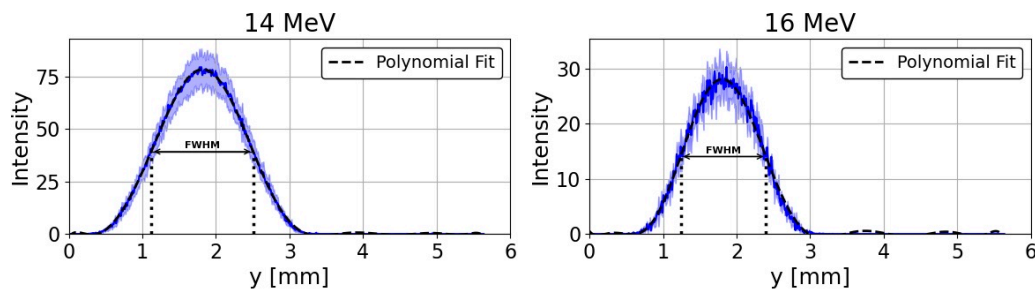


Figure 145: Y-profile average over 60 pixels from images obtained at various proton energies transversing the liquid scintillator, with a 2 mm collimator in the setup. A polynomial fit, shown by the dashed black line, is used to calculate the FWHM of the beam.

For comparison, the beam width in the y-direction was also calculated using the acoustic data. This was done using the acoustic traces obtained from the Olympus V303 transducer, which was positioned facing the y-direction. The beam width was estimated by calculating the signal envelope and identifying the two dominant peaks, corresponding to the compression and rarefaction waves. Subsequently, the time difference between them was calculated and multiplied by the speed of sound in the liquid scintillator to obtain the beam width in that direction. For the cases where the three signals from the Bragg peak, the entrance window and the Bragg peak reflection off the entrance window overlap, the FWHM of the envelope was used instead.

Figures 146, 147 and 148 display the acoustic traces, with the time differences, dt , marked and labeled. The traces at 10 and 12 MeV without a collimator, as well as at 18 and 20 MeV with a 4 mm collimator, were deemed unusable, as no distinct peaks could be identified. As before, the errors were estimated using the error bands.

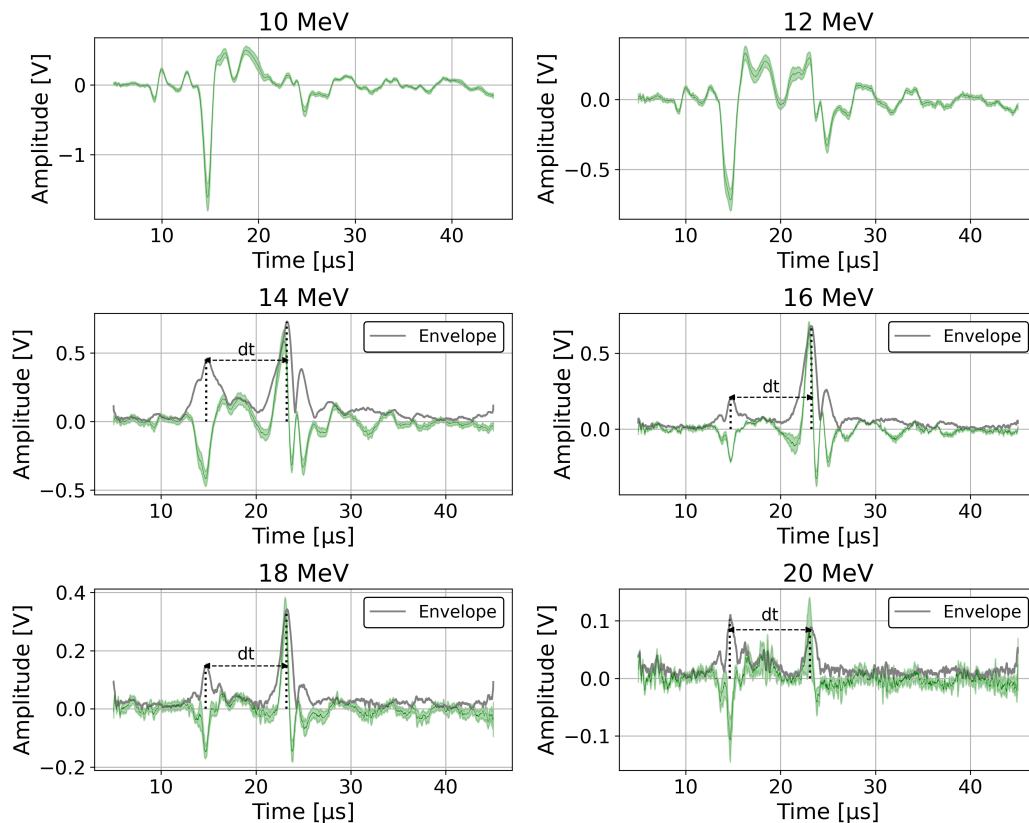


Figure 146: Acoustic waveforms recorded by the Olympus transducer, without a collimator in the setup. The compression and rarefaction peaks are indicated by vertical dashed lines and the time difference, dt , is marked by the horizontal line.

Figure 149 presents a comparison of the beam width in the y-direction using the various collimator sizes and proton energies investigated, calculated using the optical and acoustic data. The plots reveal that, at all energies, the FWHM of the beam decreases proportionally to the collimator size. In addition, a slight decrease in beam width is observed for a fixed collimator size and increasing modal beam energy—a trend also observed in the data along the x-direction. Furthermore, for the 4 mm and 2 mm collimator data, the calculated optical and acoustic beam widths are in strong agreement, within the associated errors.

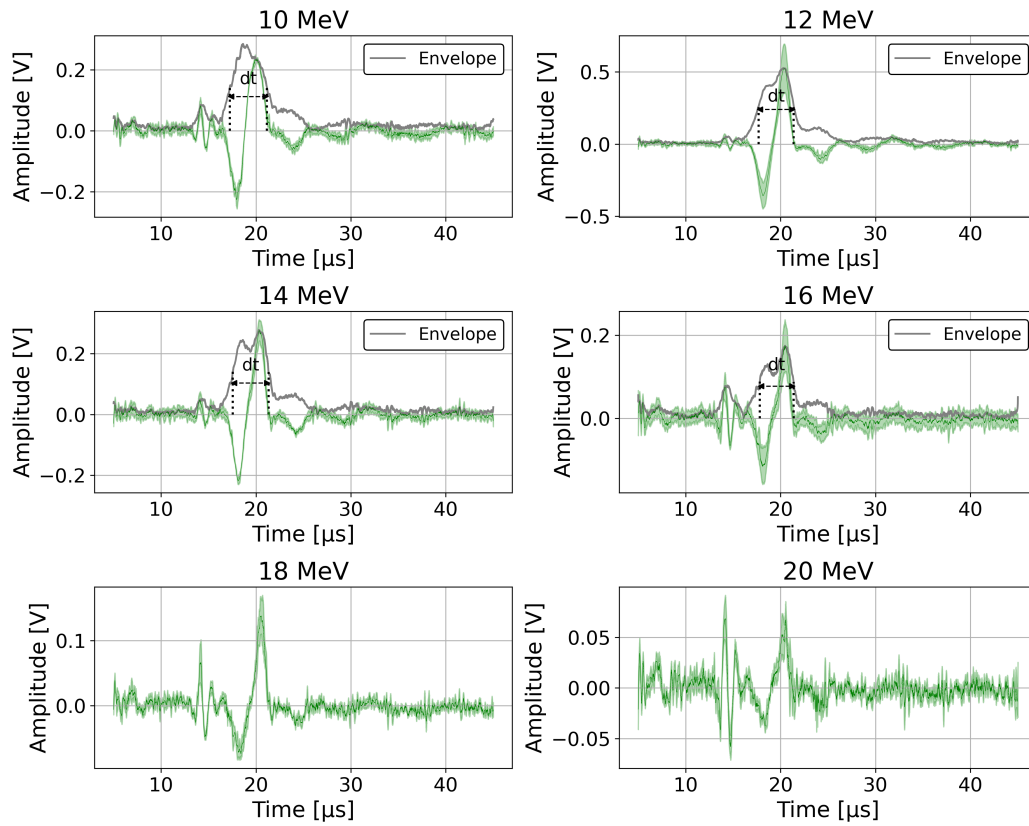


Figure 147: Acoustic waveforms recorded by the Olympus transducer, with a 4 mm collimator in the setup. The compression and rarefaction peaks are indicated by vertical dashed lines and the time difference, dt , is marked by the horizontal line.

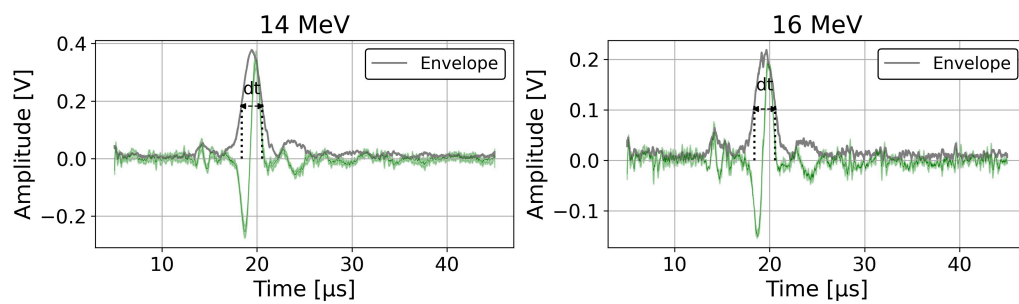


Figure 148: Acoustic waveforms recorded by the Olympus transducer, with a 2 mm collimator in the setup. The compression and rarefaction peaks are indicated by vertical dashed lines and the time difference, dt , is marked by the horizontal line.

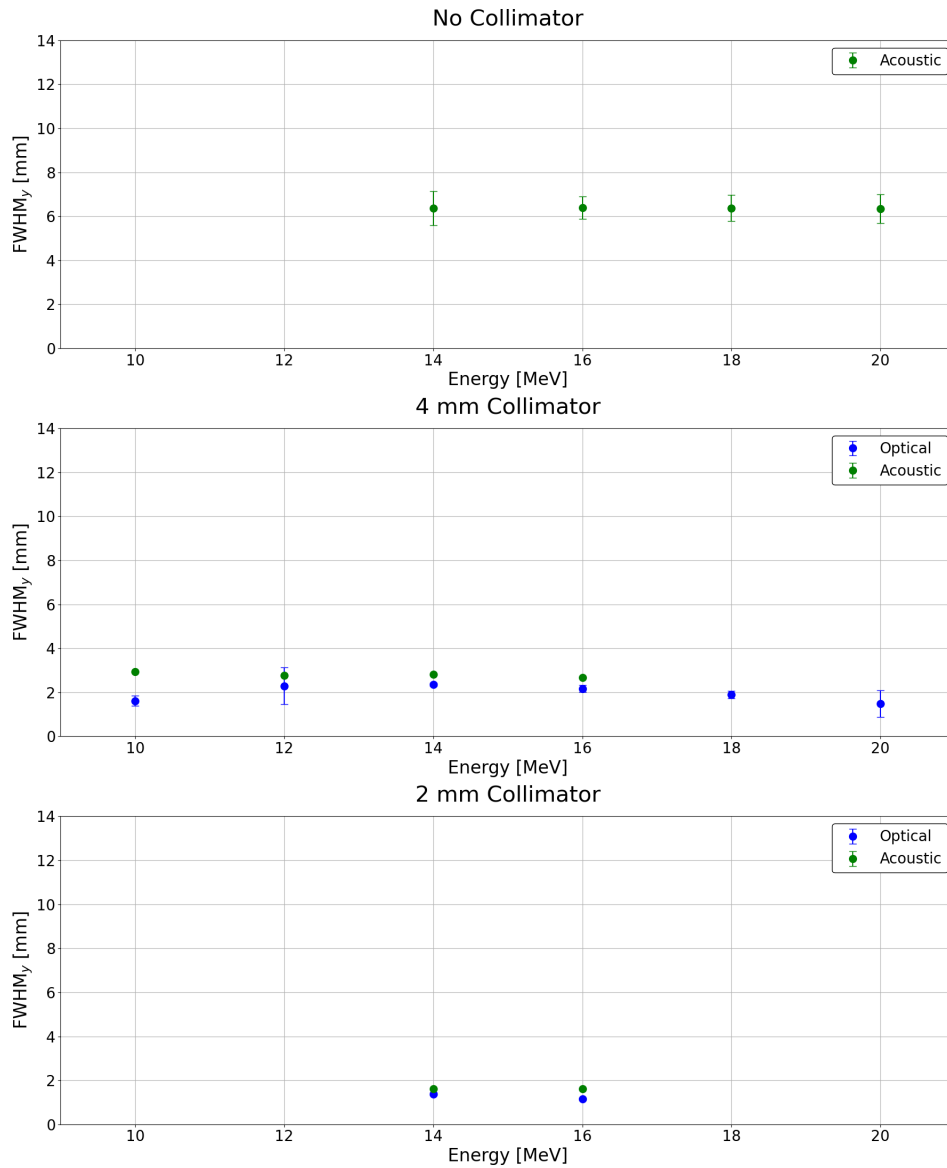


Figure 149: Full Width Half Maximum (FWHM) calculation along the y-direction of the beam depositions at the various proton energies and collimator sizes used in the setup.

8.4.4 Particle Number

Lastly, specific features retrieved from the optical and acoustic data are proportional to the particle number in each bunch, providing an additional way of establishing a correlation between the two [124].

In the images obtained, the particle count is directly proportional to the pixel intensity, assuming that no saturation is reached. This is because a higher particle count generates a greater total scintillation light emission as there are more particles to deposit energy. The average pixel intensity of each averaged, background-corrected image at each proton design energy and collimator size used was calculated and plotted in Figure 153.

In the acoustic signals, the number of particles in the bunch is proportional to the amplitude of the signal traces. This is because a greater particle count would give a larger beam current and hence picoscope voltage reading. Specifically, the waveforms recorded by the Piston hydrophone, placed on-axis with the beam, were used. However, since the first and third peaks originating from the Bragg peak are influenced by the beam's energy spread, the second peak, originating from the entrance window was selected for the measurement. The amplitude of this peak is marked by the black crosses in Figures 150, 151 and 152. The peak was only identified for the data where the peak was sufficiently distinct.

Figure 153 presents a comparison of the amplitude of the entrance window peak from the Piston hydrophone acoustic waveforms (green) with the average pixel intensity of the images captured during the same shots (blue). Both the average pixel intensity and the amplitude of the acoustic peak decrease as the size of the collimator is reduced. In addition, at a fixed collimator size, both the optical and acoustic data follow a decreasing pattern as the beam design energy increases. This is due to the lower number of particles being focused as a result of the quadrupole doublet focusing mechanism.

However, a significant discrepancy between the values obtained by the two methods is observed at 10 and 12 MeV. The average pixel intensities at those energies are much lower than expected based on the trend. This can be attributed to the entrance window flange, which occludes the first few millimeters of the energy depositions, resulting in a significant

loss of information.

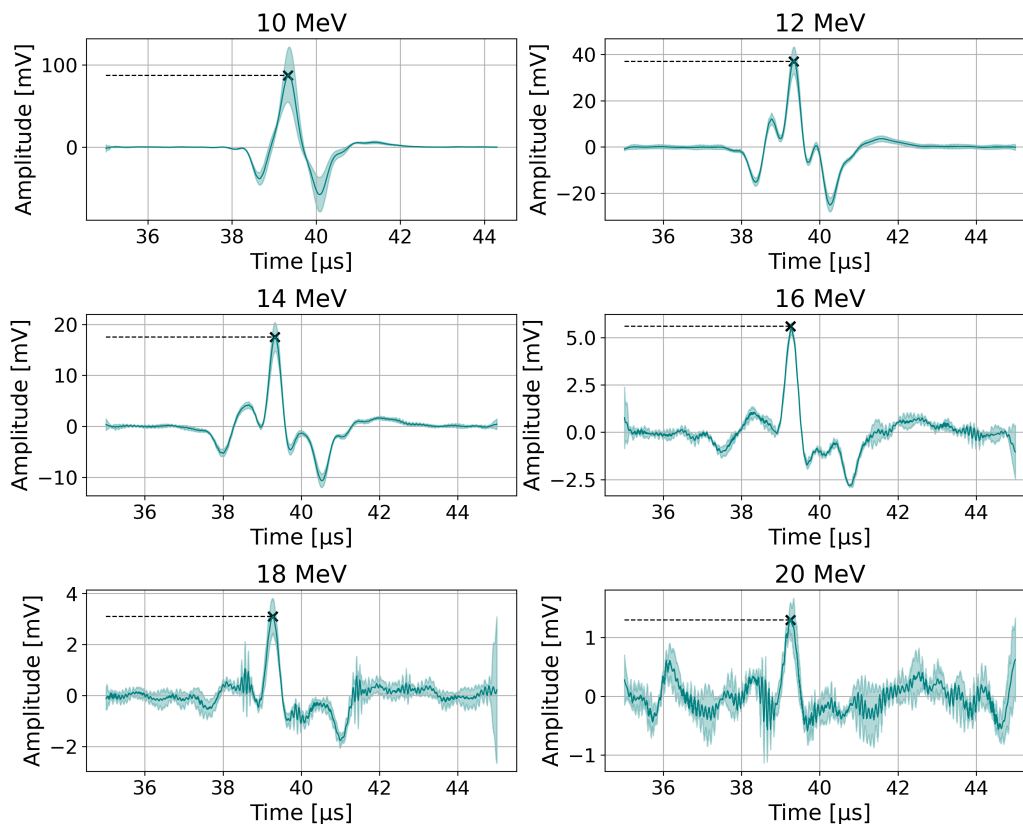


Figure 150: Acoustic waveforms recorded by the Piston hydrophone, without a collimator in the setup. The amplitude of the peak originating from the entrance window that is directly proportional to the particle number in the bunch is marked by a black cross.

In conclusion, a positive correlation appears to exist between the optical data coming from the scintillation light images and the acoustic data from the recorded acoustic waveforms as the beam propagates through the SmartPhantom. The shot-by-shot comparisons of the effective range, mean beam energy, beam width and bunch particle number revealed a promising relationship between the two methods. This comparison lays a strong foundation towards a calibration mechanism, in which the liquid scintillator will calibrate the acoustic response and yield an absolute determination of the deposited dose.

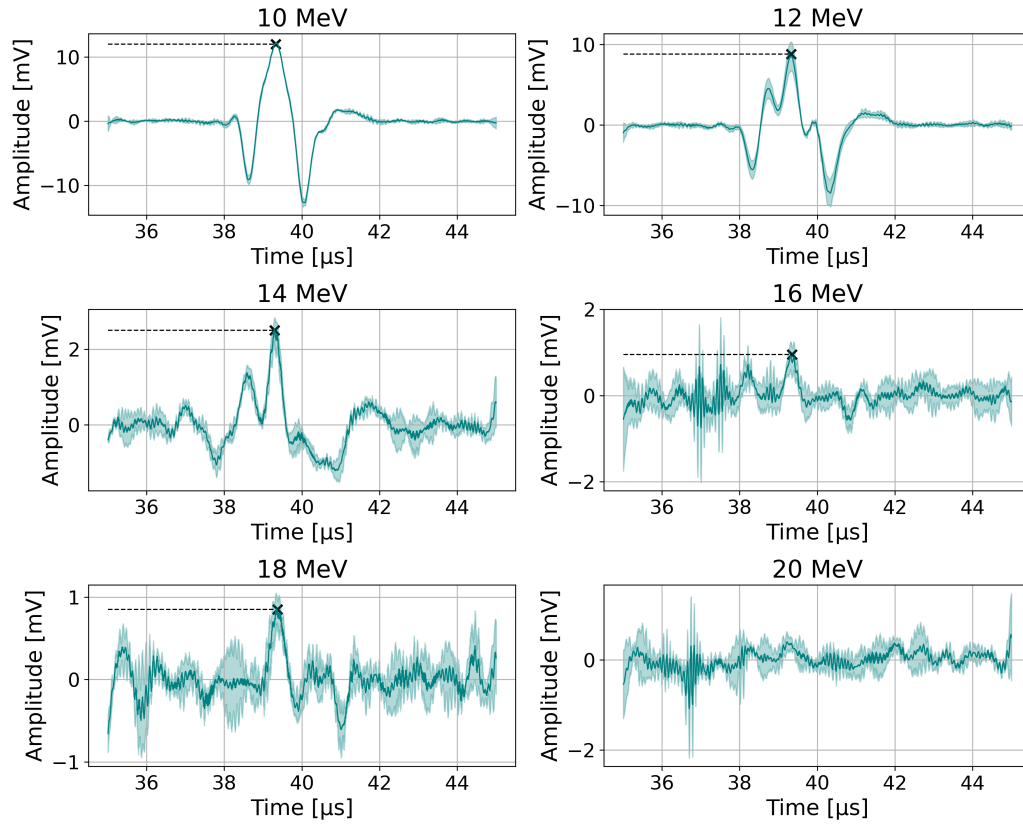


Figure 151: Acoustic waveforms recorded by the Piston hydrophone, with a 4 mm collimator in the setup. The amplitude of the peak originating from the entrance window that is directly proportional to the particle number in the bunch is marked by a black cross.

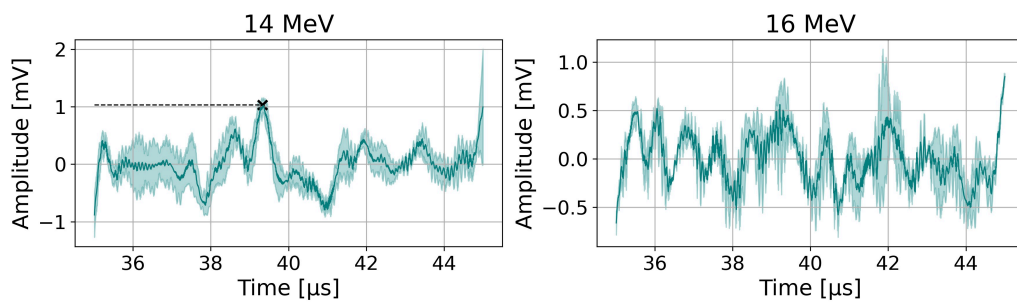


Figure 152: Acoustic waveforms recorded by the Piston hydrophone, with a 2 mm collimator in the setup. The amplitude of the peak originating from the entrance window that is directly proportional to the particle number in the bunch is marked by a black cross.

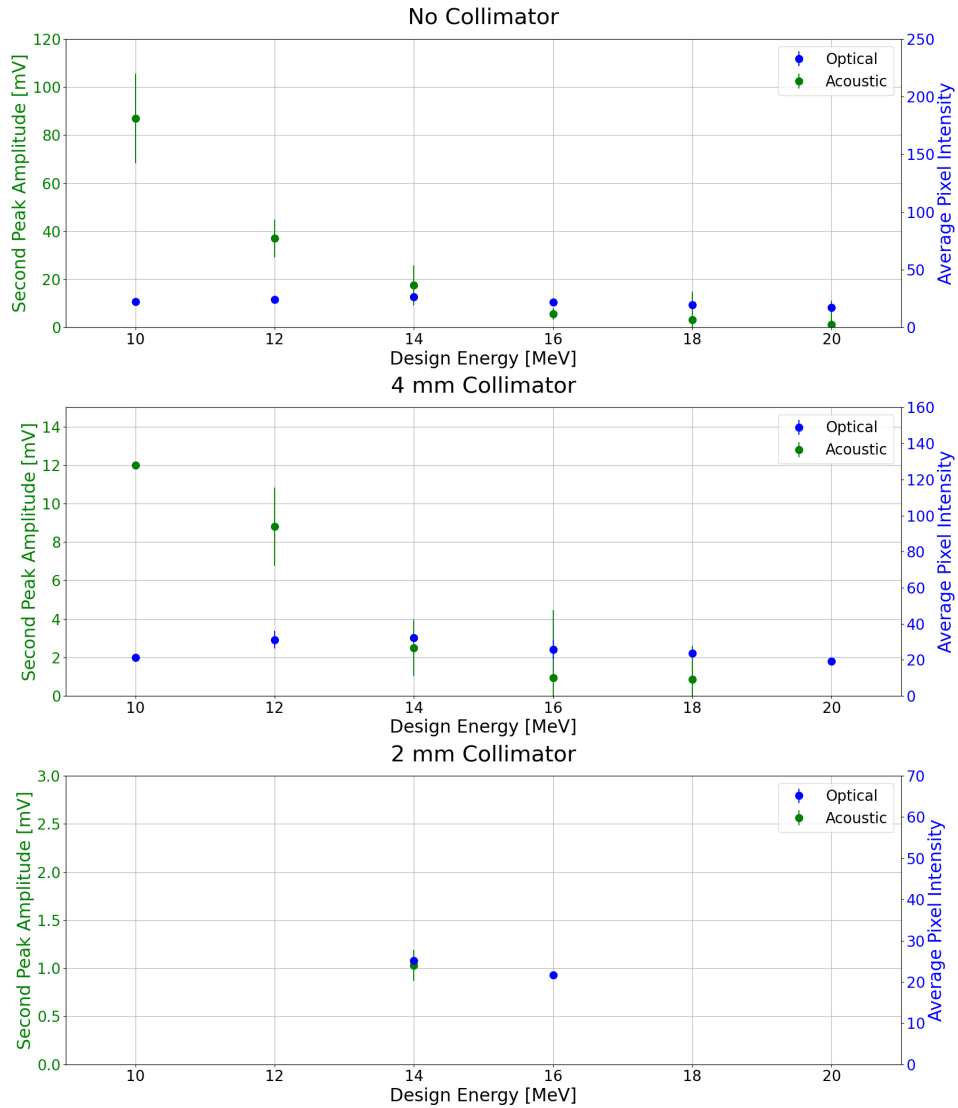


Figure 153: Comparison of the entrance window peak amplitude obtained from the Piston hydrophone waveforms (green) and the average pixel intensity from the images obtained during the same shot (blue). Both measurements are related to the particle number in the bunch.

Chapter 9

Conclusion

9.1 Discussion

Radiotherapy is a non-invasive cancer treatment technique used in more than 50% of cancer patients worldwide. Conventional radiotherapy uses photons (x-rays) to target tumours by damaging the DNA and stopping cell replication. However, ions are more effective than photons because they deposit most of their energy in a small volume of tissue at the end of their range, the "Bragg peak", rather than along the entire path of the beam from the skin surface to the tumour. This is advantageous as more dose is accumulated in the tumour region, while reducing the radiation received by the surrounding healthy cells and thereby reducing the risk of damage. In addition, FLASH radiotherapy, which delivers particles at ultra-high dose rates (>40 Gy/s), and the use of mini- and micro-beams have been shown to preserve the surrounding healthy cells.

Innovative and cost-effective cancer treatment facilities that will enable the study the radiobiological effects and therapeutic benefits of different beam characteristics should be built. The Laser Hybrid Accelerator for Radiobiological Applications (LhARA) collaboration, introduced in Chapter 3, aims to revolutionize radiotherapy by providing a highly flexible facility that will deliver proton and light-ion beams in the FLASH regime and at the mini-beam range. LhARA's next-generation features, including efficient ion generation through the Target Normal Sheath Acceleration (TNSA) mechanism, advanced ion capture and transport using Gabor lenses, and a flexible post-acceleration scheme through the Fixed Field Alternating gradient (FFA) accelerator, will surpass current technologies, making the

development of such a facility possible.

The accurate localization of the Bragg peak for LhARA, and particle radiotherapy in general, is crucial to ensure accurate dose delivery, enhance tumour targeting, improve treatment effectiveness and minimize uncertainties. To achieve this, a detector was designed, built and evaluated to serve as proof-of-principle for a real-time monitoring system of the three-dimensional dose accumulation as pulsed particle beams travel through matter. The proposed instrumentation has novel features such as providing real-time calibrated feedback, as opposed to other monitoring devices that provide a relative and not an absolute determination of the delivered dose. The proposed detector, named SmartPhantom, leverages the ultrasound waves induced as the beam propagates through matter and scintillation-based detection to calibrate the acoustic response. The detection systems, comprising of ultrasound transducers and several optical components, have several advantages including good resolution and real-time feedback. The SmartPhantom's performance and accuracy were evaluated at the Laser-driven Ion (LION) accelerator at the Center for Advanced Laser Applications (CALA) in Munich, Germany, where the generation of ion-acoustic signals was possible due to the very short beam pulses.

The design and optimization of the detector were carried out using a simulation pipeline, with the detector tailored for beams up to 20 MeV. The parametrization of the laser-driven source was crucial in understanding the energy and angular distributions of the beam to be transported through the beamline. The comprehensive simulation of the accelerator using the Beam Delivery Simulation (BDSIM) software, discussed in Chapter 4, provided valuable information about the transport of the generated particles along the various beamline elements. In addition, the simulation of the quadrupole system provided deep understanding of the accelerator's beam focusing mechanism and helped explore how particles with

different energies are focused within the system.

The precise simulation of particle generation at the laser-driven source and their transport through the LION beamline enabled the characteristics of the beam entering the SmartPhantom and the subsequent energy deposition distribution to be retrieved. This facilitated the optimization of the optical and acoustic detection systems by accurately simulating the expected acoustic traces and scintillation patterns, which were explored in the next stages of the simulation pipeline. Lastly, the parametrization and transport of source-generated electrons provided valuable insights into the expected background noise in the experiment.

The Geant4 simulation of the SmartPhantom, presented in Chapter 5, provided valuable information about the energy-deposited distribution of the particles in the three-dimensional space. This information was crucial in understanding the expected light distribution, the range of the depositions inside the liquid, as well as the characteristics of the induced waves. In addition, the Geant4 simulation enabled the comparison of various liquid candidates for filling the interior volume of the SmartPhantom. Three different liquids were investigated: water, the Ultima Gold XR liquid scintillator and 50-50% mixture of the two. The simulation revealed a 5% variation in the energy deposition range across them, suggesting that the size of the detector can remain unchanged, regardless of the liquid selected.

The three-dimensional energy deposition distribution served as a source for generating the acoustic waves in Matlab, using the k-Wave toolkit. K-Wave was very effective at modeling the expected ultrasound waves, successfully providing information about their frequency content and spatial characteristics. In addition, the k-Wave toolkit was used to simulate four ultrasound transducers (Vantage matrix array ultrasound transducer, GE 9L-D lin-

ear array ultrasound transducer, Olympus V303 immersion transducer, Precision acoustics LM4X50 Piston hydrophone) incorporating their shape, element size and frequency bandwidth. The acoustic simulation, described in Chapter 5, provided valuable insights into the expected waveforms to be recorded by each transducer, as well as the evaluation of their ability to reconstruct the three-dimensional pressure distribution. Furthermore, the implementation of the transducers' frequency response in k-Wave was essential for understanding the impact of each transducer on the recorded traces, which played a key role in optimizing their strategic placement and proximity to the source deposited energy.

Three different reconstruction algorithms were developed in Matlab and their ability to reconstruct the three-dimensional pressure distribution using the recorded acoustic waveforms was assessed. The algorithms written included iterative time-reversal, model-based minimization and back-projection. All three algorithms struggled to reconstruct the pressure distribution in the transverse direction due to the poor ability of the chosen transducers in detecting the lateral waves. As a result, the reconstructed x- and y-profiles exhibit significant inaccuracies, with the reconstructed profiles appearing almost flat and the reconstructed pressures nearing zero. However, in all three algorithms, the entrance window edge and the Bragg peak were reconstructed with relatively good accuracy, owing to the shape, placement and frequency bandwidth of the transducers.

The iterative time-reversal reconstruction was deemed the most successful reconstruction technique, as after approximately eight iterations, the reconstructed pressure distribution along the beam propagation direction was closer to the source pressure distribution, with the Bragg peak clearly identified. This algorithm also resulted in fewer artefacts, with the Bragg peak reconstructed with high accuracy. The model-based minimization reconstruction was also successful in reconstructing the Bragg peak but resulted in poorer

reconstruction compared to the iterative time-reversal for the same number of iterations. While it provides improved reconstruction accuracy in certain features such as the entrance window edge, it fails to reconstruct the sharpness of the Bragg peak, smearing its shape. Finally, the back-projection reconstruction technique appears to be the fastest algorithm as it does not require solving complex wave equations or performing multiple forward and backward propagations of the pressure field. However, this image reconstruction technique yields the least accurate pressure distribution reconstruction for the given sensor specifications. The reconstruction accuracy is expected to improve with the use of larger transducer elements, which would help increase the Signal-to-Noise Ratio (SNR) and minimize blurring effects.

Following the simulation of the generation and detection of acoustic waves, the optical system was evaluated in Chapter 6. The proposed liquid scintillator, Ultima Gold XR, was introduced and its properties were thoroughly examined to assess suitability for the proof-of-principle experiment using the SmartPhantom. A preliminary experiment was performed using a fluorescent dye and a UV source to gain practical experience with optical components and CMOS cameras, as well as to learn how to analyze scintillation images from such experiments. In addition, various correction techniques were discussed to mitigate artefacts in the images caused by reflection, refraction and background noise.

The optical absorption and attenuation length of the liquid scintillator, as well as a 50-50 mixture with water, were measured using a spectrophotometer. The results indicated that there is significant light scattering in the mixture and therefore it was concluded that the SmartPhantom should be filled with 100% liquid scintillator. In addition, the linearity of the response and the saturation level of Ultima Gold XR were evaluated at the MC40 cyclotron in Birmingham using proton beams. Images of the scintillation light

were captured using the proposed imaging system as proton beams propagated through the liquid. The images were analyzed and corrected for background noise, and subsequently, the energy deposition profiles in each direction were extracted. It was observed that across all investigated energies and particle numbers, the liquid scintillator exhibited a linear response to the deposited energy with no signs of saturation up to approximately 1×10^8 particles in the beam.

In Chapter 7, the use of scintillating fibre detectors was discussed and explored as an alternative to the liquid scintillator. Their design and simulation using Geant4 were presented and their construction process was described. In the simulation, the feedback from each fibre was used to reconstruct the two-dimensional profile at each depth. The results indicated that the area over which the energy was deposited increased with depth, as expected due to scattering when the beam interacts with the liquid. In addition, the deposited energy across the fibres in each detector was summed and an analytical approximation of the Bragg peak was fitted to the data to reconstruct the energy profile along the direction of the beam propagation. This approach resulted in reconstruction profiles with high accuracy.

However, the k-Wave implementation of the scintillating fibre detectors revealed significant acoustic wave distortion when optical and acoustic measurements are taken simultaneously, highlighting limitations in their use. As an alternative, the detector configuration was adjusted by spacing the detectors further apart to measure the divergence of the beam instead. In addition, linearity and saturation measurements were conducted at the MC40 cyclotron in Birmingham, following a similar approach to the liquid scintillator. The experimental results revealed a linear response with no signs of saturation up to approximately 1×10^9 particles in the beam. Lastly, although optical measurements of the scintillating

fibre detectors were successfully taken, the optical system needs refinement to expand the field of view and effectively capture all the fibres in all four detectors.

In Chapter 8, the final design of the SmartPhantom and its evaluation at the LION beamline are presented. A series of experiments were conducted, where the full hybrid system, which combined the acoustic and optical detection methods, was assessed on a pulse-to-pulse basis. Measurements obtained with Radiochromic Films (RCFs) revealed a weak particle focus, attributed to quadrupole alignment errors during configuration. As a result, the focused beam exhibited a "star" shaped cross-section rather than the expected tightly focused elliptical shape. The analysis of the RCF films also revealed proton spectra with a wide range of energies, with the modal energy of the beam estimated to be consistently lower than the design energy. Despite challenges with quadrupole alignment, which led to a weak particle focus, the experimental results demonstrated a strong correlation between the data recorded by the optical and acoustic systems. Both the acoustic waveforms and the scintillation images were able to provide valuable information about the characteristics of the emerging beam, including the Bragg peak range, mean beam energy, beam width and particle number.

In conclusion, the evaluation of the SmartPhantom at the LION beamline demonstrated that the proposed instrumentation effectively provides accurate real-time feedback on the characteristics of the energy depositions caused by the passage of a pulsed ion beam. The successful assessment of the proposed detector lays the foundation for developing a calibrated system that can be used in a clinical setting.

9.2 Future Work

Despite the successful experiment at the LION beamline and the positive correlation established between the optical and acoustic measurements, further work is needed to achieve the objectives of the LhaRA collaboration.

First, a deep understanding of quadrupole alignment errors and their impact on the shape and energy spectrum of the focused beam is needed to interpret and explain the energy deposition patterns observed in the experiment. The impact of vertical and horizontal offsets between the quadrupoles, tilts from their nominal orientations and minor adjustments to the ideal drift lengths between them should be carefully studied. To gain these insights, the simulation pipeline can be used to recreate the beams obtained in the experiment, by introducing offsets to various beamline elements as well as investigating different combinations to yield the obtained distributions.

For future experiments at the LION beamline, beyond obtaining better particle focus, a second version of the SmartPhantom with several modifications is essential. The recent experiment exposed various weaknesses in the current design, with the most significant one being the partial occlusion of the first few millimeters of scintillation light by the mechanical structure of the entrance window flange. To correct the results obtained, experiments with UV light can be performed in the lab to characterize the shape of the occluded region and develop effective scintillation light correction methods. In addition, the next version of the SmartPhantom should feature a redesigned entrance window seal that will minimize or completely eliminate the shadowing effect.

Moreover, future experiments should integrate the matrix and linear array transducers; therefore, the problems encountered in transporting the Verasonics system to Munich

should be addressed. The use of these transducers will offer significant advantages as three-dimensional reconstructions of the pressure distribution can be obtained, which will reveal important features that cannot be extracted from single time-series waveforms. In addition, the increased number of elements in these transducers will provide a higher SNR and improved signal quality.

In addition, the acoustic signal quality can be enhanced by immersing the transducer arrays closer to the energy deposition source, rather than coupling them with a Kapton foil located 5 cm away. A closer placement will not only record higher-amplitude signals but also reduce signal attenuation, as the waves will travel a shorter distance in the liquid scintillator before detection. To accomplish this, custom covers should be designed to protect the transducers from potential damage when in contact with the liquid scintillator, prevent air bubbles from being trapped and ensure effective acoustic coupling between the two media.

Furthermore, the k-Wave simulations revealed weaknesses in obtaining accurate reconstructions of the pressure distribution with the proposed transducer designs, shapes and sizes. Designing and customizing a sensor array with a greater angular coverage and a frequency bandwidth that covers the entire frequency spectrum of the induced signals would be highly beneficial, as it will ensure that no valuable information is lost.

Lastly, an analysis routine should be developed to calibrate the acoustic response using the obtained scintillation light images. A possible way to do this may be as follows: first, the pixel intensities from the images can be converted into deposited energy (MeV) using the known light yield of the liquid scintillator (11200 photons/MeV). To achieve this, the results from the MC40 cyclotron in Birmingham, obtained using monoenergetic beams, can be used, as the same imaging system and entrance window flange were used. The total

energy deposited in the liquid scintillator can be determined by integrating the scintillation light intensity and using the photon yield. Since various particle counts were investigated, a calibration curve of average light intensity against deposited energy can be plotted. Given that the acoustic signal amplitude also scales with deposited energy, the acoustic calibration factor can be determined by dividing the scintillator-measured deposited energy by the average acoustic signal amplitude. The method can be verified using the simulation pipeline. Determining this conversion factor will eliminate the need for the liquid scintillator in future experiments, enabling the development of a system that relies entirely on ultrasound transducers. In addition, the same process can be repeated with the scintillating fibre detectors, after adjusting the optical system to ensure that all the fibres in the detectors are imaged.

9.3 Towards Clinical Application

Although the proposed system has demonstrated its ability to provide calibrated feedback on the three-dimensional distribution of the deposited dose, several challenges should be addressed before it is implemented in a clinical setting.

Firstly, the SmartPhantom consists of a uniform liquid with no interface discontinuities. In contrast, the human body is composed of multiple organs, each with distinct speed of sound and signal attenuation coefficient. This results in multiple locations with impedance mismatch, presenting challenges for the propagation of ultrasound waves and the reconstruction of the deposited dose. These heterogeneities cause significant signal reflections and varying degrees of attenuation, introducing asymmetric energy depositions and major sources of random uncertainties. In addition, bone and air pockets trapped between organs are poor ultrasound transmitters and hence cause large reflections and high signal

attenuation.

Moreover, respiration and cardiac movements cause continuous anatomical fluctuations, leading to ion range variations within the body. To overcome these limitations and correct dose delivery on-the-fly, real-time ultrasound imaging can be used to co-register the patient's anatomy with live ion-acoustic measurements. This will ensure precise dose delivery accounting for motion, as well as eliminating the error related to the speed of sound and the body's heterogeneity.

However, co-registering live ultrasound images is extremely challenging as a single transducer is needed that is capable of registering both ultrasound and ion-acoustic signals. This is very challenging because ultrasound imaging typically operates at frequencies of a few MHz, whereas ion-acoustic signals at clinically relevant energies (>200 MeV) are in the order of a few kHz. To overcome this challenge, innovative ultrasound transducers should be developed that have a broadband frequency range. Lastly, ion-acoustic signals are extremely weak and low in amplitude. This poses a challenge not only for the transducer, as high sensitivity is needed, but also for the electronics and the amplification methods.

To conclude, new innovative transducers are needed which are not only broadband, to enable simultaneous ultrasound images and ion-acoustic measurements, but also exhibit high sensitivity at a wide range of frequencies, overcoming limitations of current transducer technologies.

Appendix A

Two-Dimensional Model

A two-dimensional acoustic simulation of the SmartPhantom was developed in k-Wave to investigate the impact of the aluminium walls and the immersion transducer on the acoustic signals [13]. This study was conducted in two dimensions because a three-dimensional model is extremely computationally heavy and k-Wave does not support video recording at this grid size and resolution.

The aluminium walls and the Olympus immersion transducer are expected to introduce acoustic reflections off their surfaces, as they act as additional interface discontinuities with differing acoustic impedances. If the signals are recorded for long enough, the reflections become visible on the acoustic trace. These reflections can be advantageous, as more information is recorded, or disadvantageous, as interference might occur, leading to artefacts in the reconstructed images.

To assess the impact of each interface, three different simulations were run: one that includes only the liquid scintillator, another with the liquid scintillator enclosed by aluminium walls, and a third with the liquid scintillator enclosed by aluminium walls and the Olympus transducer immersed in the liquid. Each medium was simulated by incorporating its respective density and speed of sound. In addition, the acoustic attenuation of the liquid scintillator was modeled by implementing the frequency-dependent acoustic absorption coefficient [74].

In the simulation, the signals were recorded by an ideal point detector transducer (zero dimensions and infinite bandwidth) placed within the SmartPhantom's volume. Figure

154 displays the acoustic wave generation and propagation of the acoustic waves within the SmartPhantom for the third investigated case, where both the aluminium walls and immersion transducer are included. The figure shows that the acoustic waves reflect off both the aluminium walls and the transducer's surface. As a result, the waves are repeatedly reflected within the SmartPhantom, gradually attenuating.

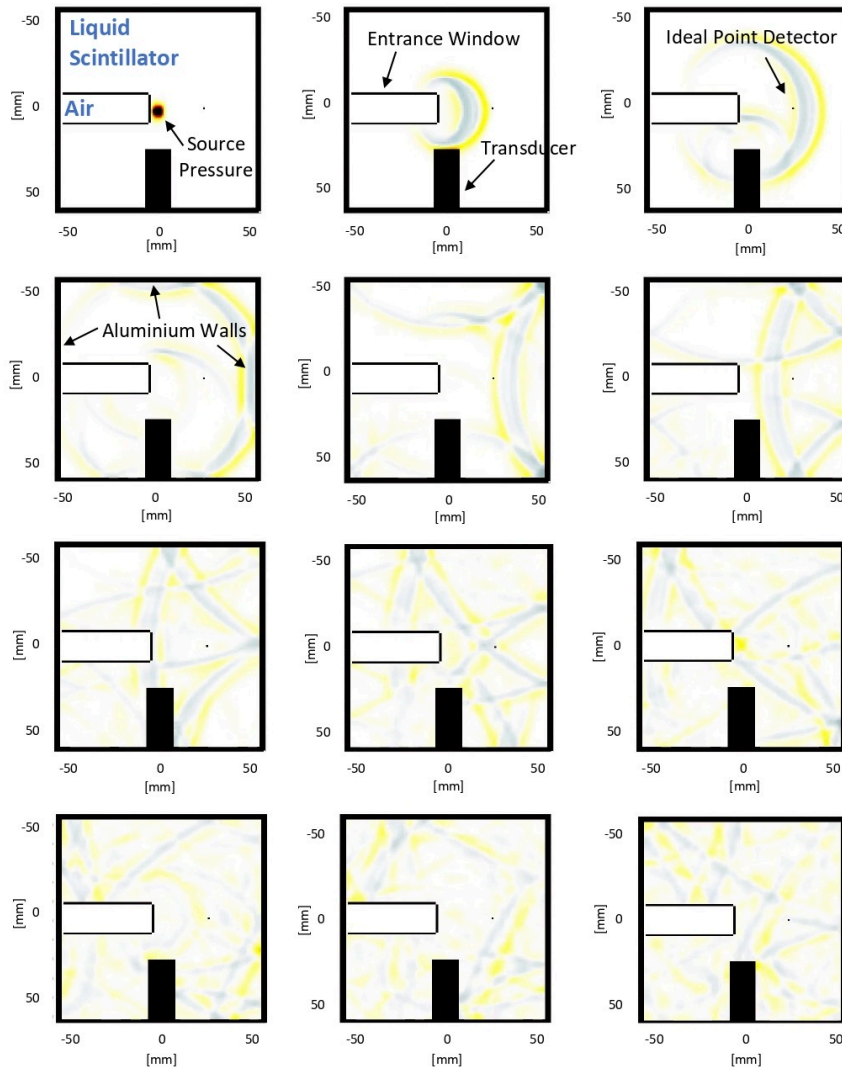


Figure 154: Acoustic wave generation and propagation in the two-dimensional model of the SmartPhantom. The liquid scintillator, which forms the detector's volume, is enclosed by aluminium walls and the Olympus transducer is immersed inside 2.49 cm from the center.

Figure 155 shows the acoustic traces of the signals recorded by the ideal point detector for the three different cases. The plot reveals that the simulation with solely the liquid scintillator displays the expected acoustic signals, resulting from the Bragg peak, the entrance window and the reflection of the Bragg peak signal off the entrance window. When the aluminium walls are added, additional peaks are observed due to multiple acoustic reflections off their surfaces. Moreover, when the immersion transducer is also introduced into the simulation, even more oscillations are observed as there is an extra interface to reflect off. In addition, the amplitude of the peaks in this case appear greater compared the signal in its absence. Lastly, in all cases, the amplitude of the oscillations gradually decreases over time due to the energy being absorbed by the liquid.

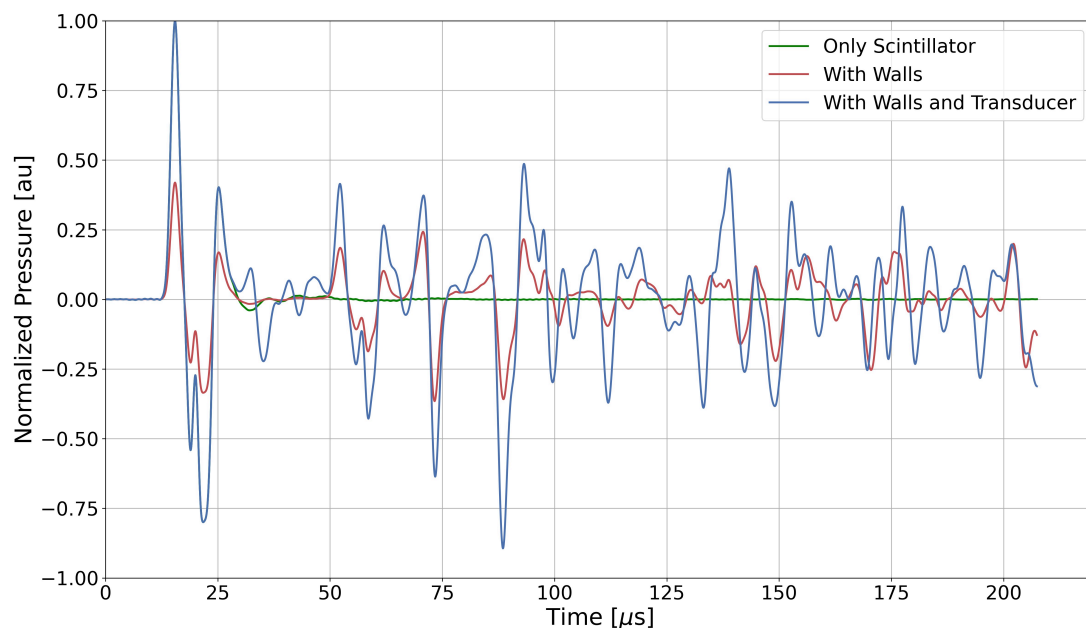


Figure 155: Acoustic waveform recorded by an ideal point detector placed on axis with the beam for three different cases: liquid scintillator alone (green), liquid scintillator enclosed by aluminium walls (red) and liquid scintillator enclosed by aluminium walls with the Olympus transducer immersed (blue).

The frequency content of the recorded signals is displayed in Figure 156. The plot reveals that in all cases, the frequency range of the signals is between 0.1 and 0.6 MHz. In the cases where the aluminium walls and immersion transducer are included, the additional reflections introduce more frequencies to be present, though they remain within that range. Since the overall frequency range is not altered, the impact of the aluminium walls and immersion transducer is expected to be minimal.

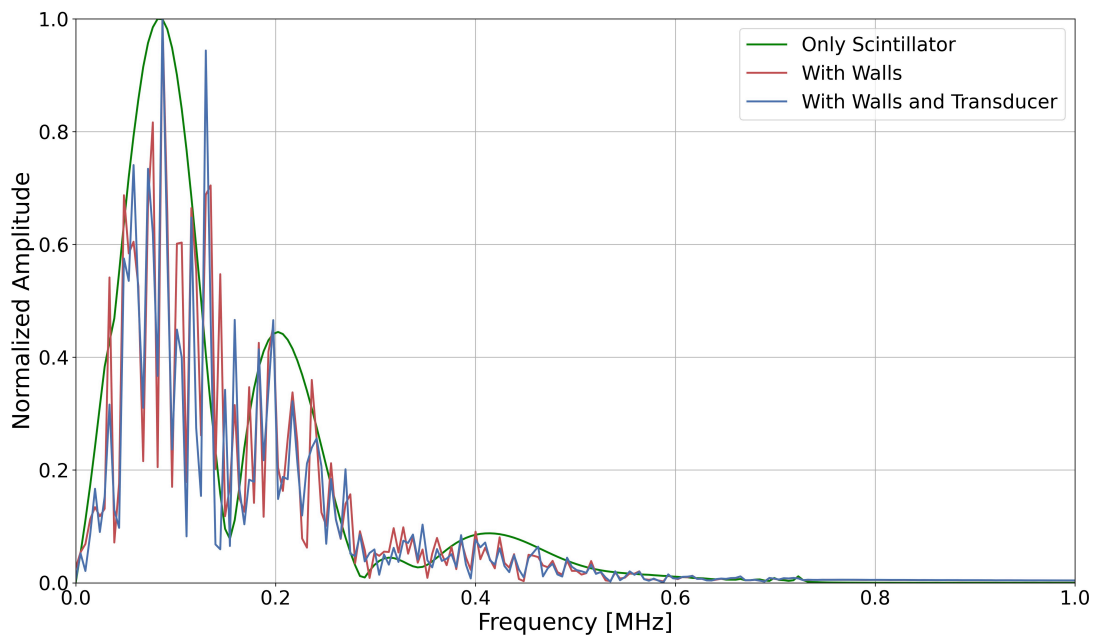


Figure 156: Frequency spectrum of the signals recorded by an ideal point detector placed on axis with the beam for three different cases: liquid scintillator alone (green), liquid scintillator enclosed by aluminium walls (red) and liquid scintillator enclosed by aluminium walls with the Olympus transducer immersed (blue).

Lastly, Figure 157 presents the acoustic trace recorded by the ideal point detector when the simulation including the aluminium walls and the immersion transducer is recorded for a longer period. The graph illustrates that even after approximately 0.003 seconds (3000 microseconds), the signal has not yet been fully absorbed by the medium.

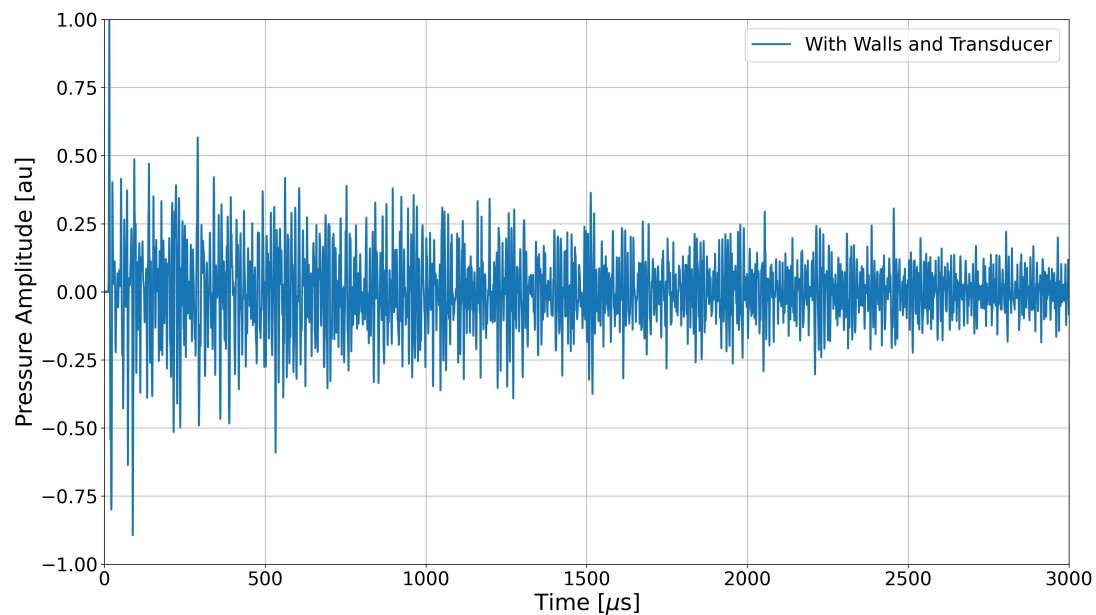


Figure 157: Acoustic waveform recorded by an ideal detector placed on axis with the beam, with the SmartPhantom filled with the liquid scintillator enclosed by aluminium walls and the Olympus transducer immersed inside.

Appendix B

Image Reconstruction: Hemispherical Cup

In Chapter 5, the reconstructed images obtained using the Vantage matrix array and the GE 9L-D linear array ultrasound transducers were extremely poor. To demonstrate that the iterative-time reversal algorithm functions correctly and that the poor reconstruction is solely due to factors such as the shape, proximity to the source pressure and frequency bandwidth of the transducers, an additional simulation was run in k-Wave.

In this simulation, a hemispherical cup array transducer was designed to maximize angular coverage and enable efficient detection of both axial and lateral waves. The designed transducer features a 7 mm radius and consists of 300 elements, each 0.7 mm in diameter, uniformly distributed on its surface [127]. In addition, the simulated hemispherical cup array transducer has infinite bandwidth and is positioned around the pressure source to minimize signal attenuation before detection. Each transducer element is oriented to face the center of the pressure source. The specified hemispherical cup array transducer and its position relative to the source pressure distribution caused by the passage of the LION beam in the SmartPhantom are shown in Figure 158.

For comparison, eight iterations of the time-reversal algorithm discussed in Chapter 5 were performed. Figure 159 depicts the source pressure distribution (a) and the reconstructed pressure distribution (b) using this transducer design. In addition, the difference between the source and reconstructed pressure distributions is shown in Figure 160 and the extracted x-, y- and z-profiles of the reconstruction are shown in Figure 161.

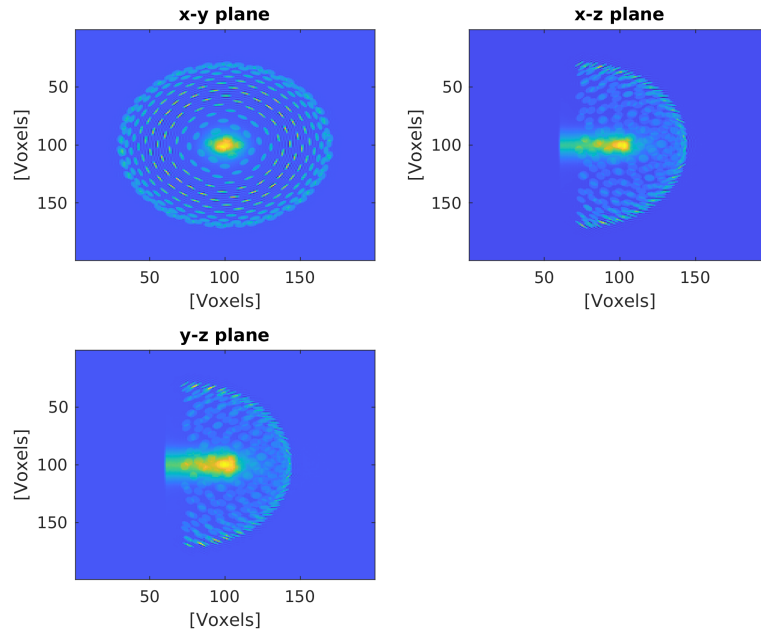


Figure 158: k-Wave simulation showing the designed hemispherical cup array transducer and its position relative to the beam energy depositions, indicated by the yellow region. The energy depositions depicted are generated by a proton beam exiting the LION beamline, optimized for a modal energy of 20 MeV, as it passes through the liquid scintillator.

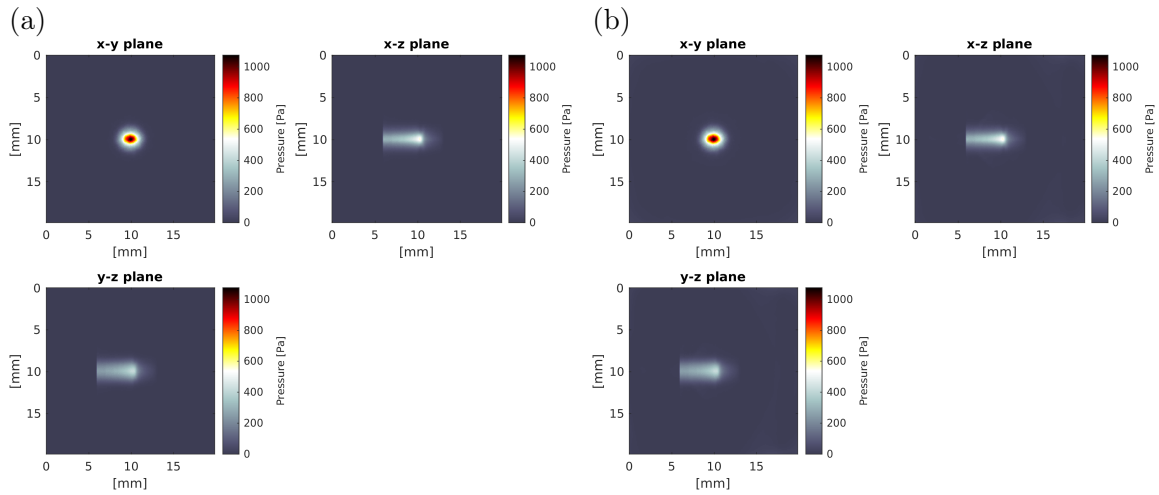


Figure 159: Source pressure distribution (a) and reconstructed pressure distribution (b) after eight iterations of the iterative time-reversal algorithm, using the data acquired from the specified hemispherical cup array transducer.

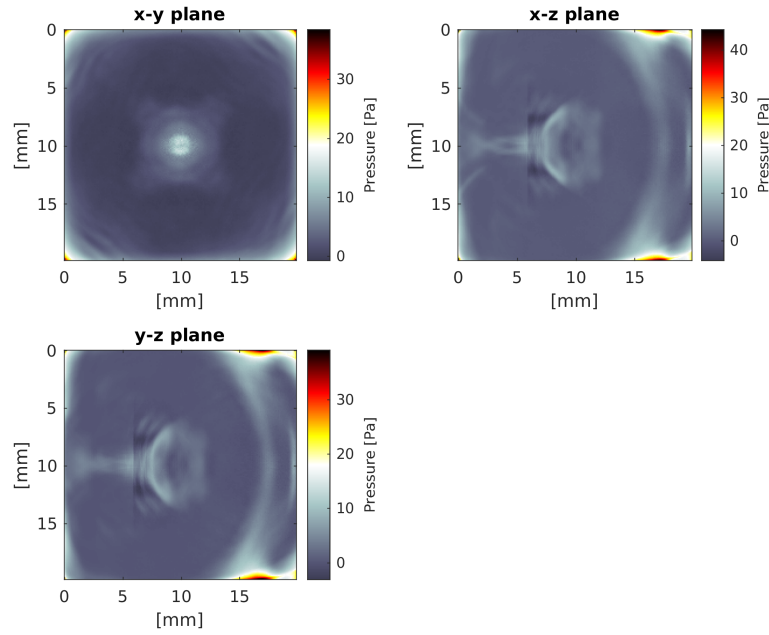


Figure 160: Difference between reconstructed pressure distribution and source pressure distribution, using the data recorded by the hemispherical cup and the iterative time-reversal algorithm.

The results reveal great precision in reconstructing the source pressure distribution. This confirms that the algorithm works as intended and demonstrates that the poor reconstructions obtained using the Vantage matrix array and GE 9L-D linear array transducers are entirely due to their shape, proximity to the pressure source and frequency bandwidth.

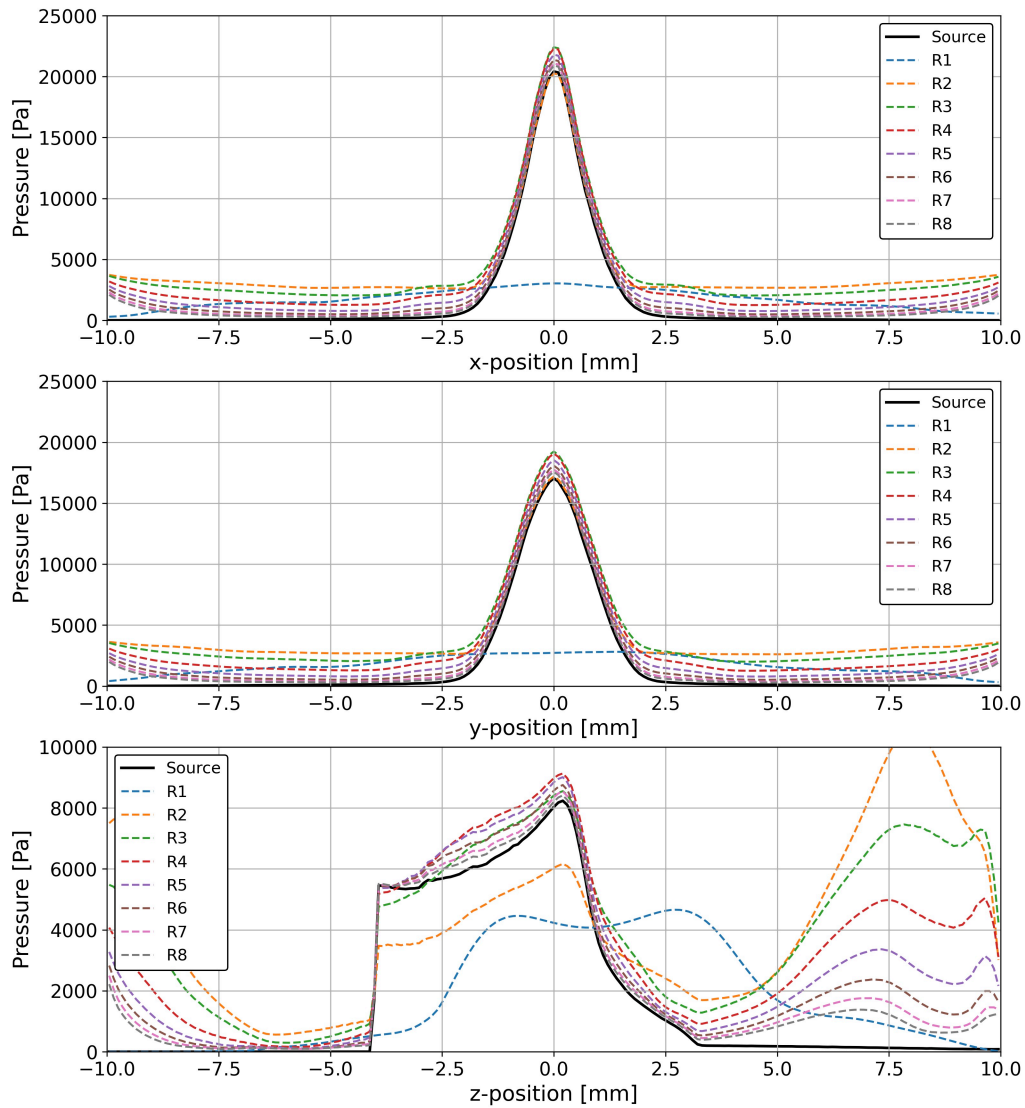


Figure 161: Reconstructed pressure distribution profiles along the x-(top), y-(middle) and z-(bottom) directions, using eight iterations of the iterative-time reversal algorithm and the specified hemispherical cup array transducer.

Appendix C

Ion-Acoustics in Human Physiology

The various structures within the human body are expected to produce distinct depth-dose curves and energy deposition patterns. This is because structures with varying densities and atomic masses exhibit different stopping powers and scattering behaviour as a function of depth. Consequently, the ion-acoustic signals generated within each medium are expected to have distinct characteristics.

To investigate the depth-dose curves and the characteristics of the ion-acoustic signals generated by different anatomical structures, the Geant4 simulation of SmartPhantom was recreated in Topas, a Geant4 extension tool that allows the simulation of various organs in the human body [128]. Topas provides significant advantages by offering pre-existing packages to simulate biological structures at the sub-atomic level.

Six distinct human body structures were investigated: water, soft tissue, blood, cortical bone and compact bone. In the simulation, these media constituted the inner volume of the SmartPhantom, enabling the three-dimensional energy depositions to be retrieved for each scenario. Figure 162 presents the energy deposition curves along the direction of beam propagation, generated using a monoenergetic 100 MeV proton beam consisting of 10000 particles, with the simulations split into 1 mm cubic voxels.

The figure reveals that for the same beam characteristics, the proton beam comes at rest at varying depths within each structure. In addition, both the energy deposited at the entrance window and the width of the Bragg peak vary between the media. Structures with higher densities, such as the cortical and compact bones, result in a higher entrance dose

delivery and a sharper Bragg peak, owing to their greater stopping power.

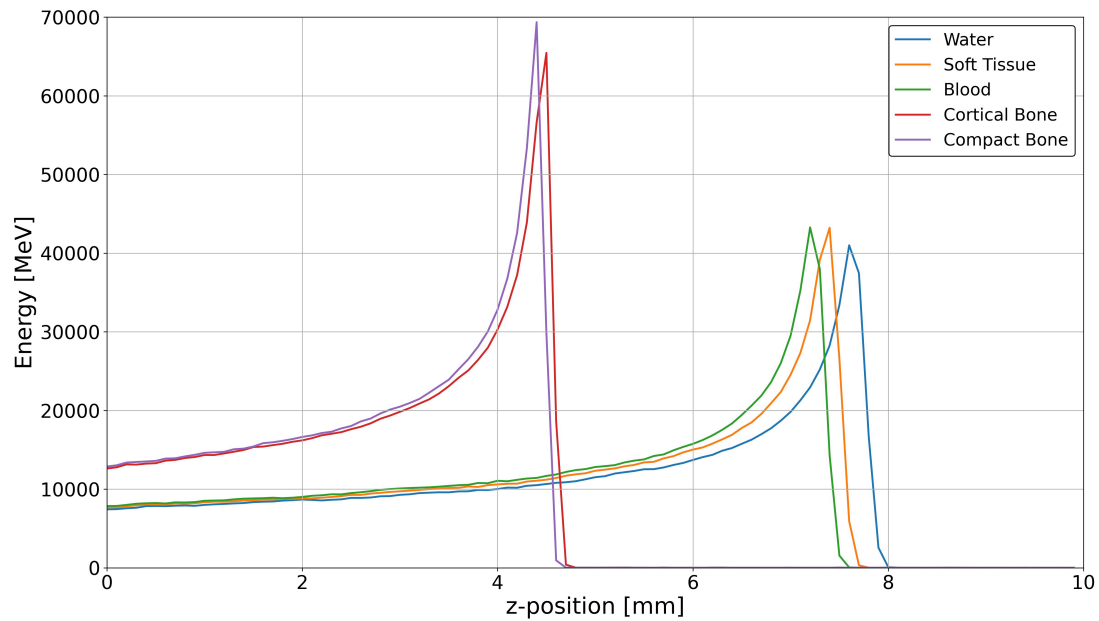


Figure 162: Deposited energy as a function of depth for a monoenergetic 100 MeV proton beam consisting of 10000 particles, propagating through various human body structures simulated in Topas [128].

The three-dimensional energy depositions obtained from the Topas simulation of each human structure were written in a Matlab file for import into k-Wave. In k-Wave, the ion-acoustic waves were generated based on the energy deposition distributions and propagated through the three-dimensional space. The simulation incorporated the speed of sound, attenuation coefficient and density of each medium.

Figure 163 displays the acoustic waveforms recorded by an ideal point detector positioned approximately 36 mm from the SmartPhantom's entrance window. The plot reveals significant variations in acoustic signal amplitude across the different structures, with denser materials generating ion-acoustic signals with greater amplitudes. In addition, due to the differing Bragg peak ranges among the materials, the compression and rarefaction peaks

are recorded with varying time delays.

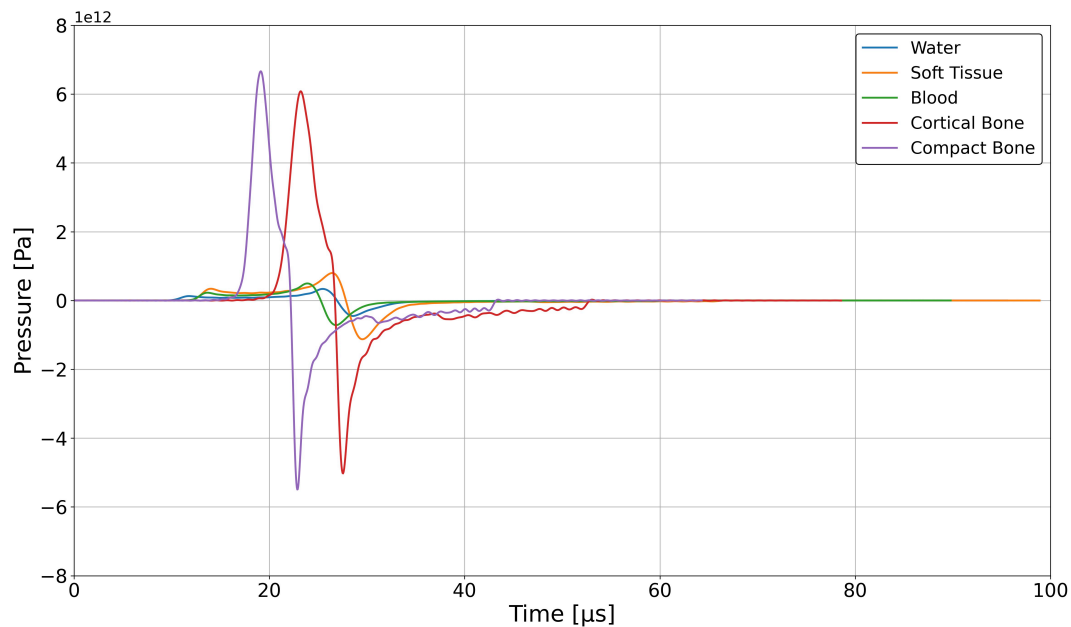


Figure 163: Simulated acoustic waveforms, recorded by an ideal point detector capturing the ion-acoustic signals induced by a monoenergetic 100 MeV proton beam consisting of 10000 particles propagating through various human body structures. The ion-acoustic wave generation, propagation and detection were simulated using k-Wave.

Lastly, the frequency spectra of the recorded signals are presented in Figure 164. The figure reveals that higher-density structures, such as the cortical and compact bones, generate ion-acoustic signals with higher frequency components, compared to lower-density structures such as water, soft tissue and blood. This suggests that denser materials are able to generate stronger pressure waves, possibly due to the steeper energy-deposition gradients resulting from their higher stopping powers.

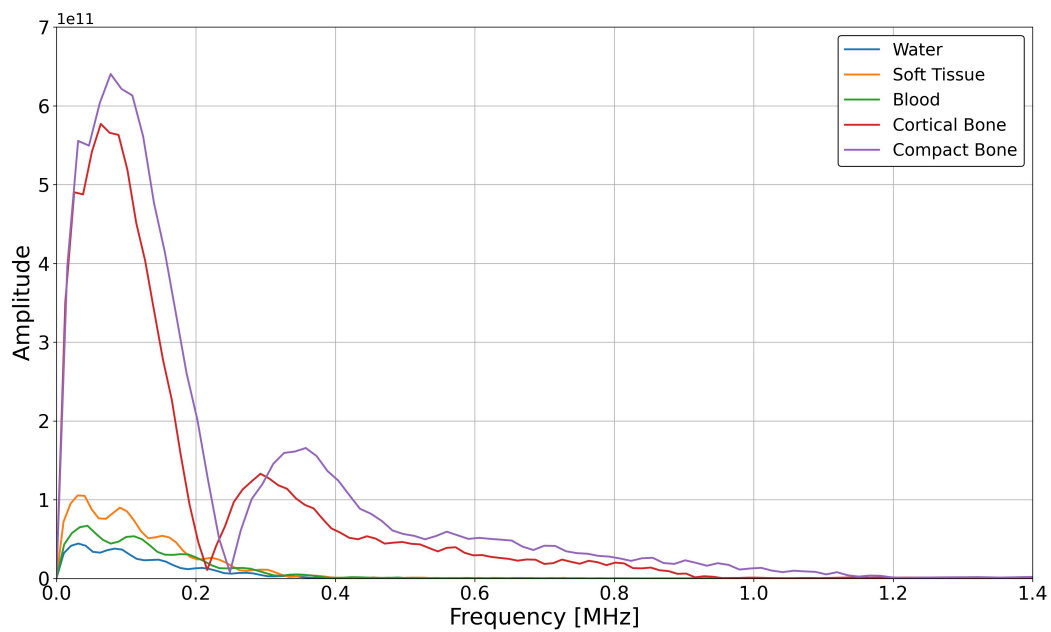


Figure 164: Frequency spectra of the simulated signals, recorded by an ideal point detector capturing the ion-acoustic signals induced by a monoenergetic 100 MeV proton beam consisting of 10000 particles propagating through various human body structures. The ion-acoustic wave generation, propagation and detection were simulated using k-Wave.

References

- [1] World Health Organization: WHO (2019). Cancer. [online] Who.int. Available at:
https://www.who.int/health-topics/cancer#tab=tab_1 [Accessed 20 Mar. 2022].
- [2] World Health Organization (2022). Cancer. [online] World Health Organization. Available at:
<https://www.who.int/news-room/fact-sheets/detail/cancer> [Accessed 20 Mar. 2022].
- [3] Cancerresearchuk.org. (2018). Radiotherapy | Cancer in general | Cancer Research UK.
[online] Available at: <https://www.cancerresearchuk.org/about-cancer/cancer-in-general/treatment/radiotherapy> [Accessed 8 Feb. 2022].
- [4] Aymar, G., et al. (2020). LhARA: The Laser-hybrid Accelerator for Radiobiological Applications. *Frontiers in Physics*, 8, 567738.
<https://doi.org/10.3389/fphy.2020.567738>
- [5] Richards, A. A. (2011). Acoustic imaging: Seeing with sound. In *Alien vision: Exploring the electromagnetic spectrum with imaging technology* (2nd ed., Chapter 5). SPIE Press.
<https://doi.org/10.1117/3.883085.ch5>
- [6] Lee, W., & Roh, Y. (2017). Ultrasonic transducers for medical diagnostic imaging. *Biomedical Engineering Letters*, 7(2), 91–97.
<https://doi.org/10.1007/s13534-017-0021-8>
- [7] Athanassopoulos, C., et al. (1997). The liquid scintillator neutrino detector and LAMPF neutrino source. *Nuclear Instruments and Methods in Physics Research Section A: Accelerators, Spectrometers, Detectors and Associated Equipment*, 388(1-2), pp.149–172.
[https://doi.org/10.1016/S0168-9002\(96\)01155-2](https://doi.org/10.1016/S0168-9002(96)01155-2).
- [8] Lo Presti, D., et al. (2019), Real-Time Particle Radiography by Means of Scintillating Fibers Tracker and Residual Range Detectors. *IntechOpen*,
<https://doi.org/10.5772/intechopen.81784>.
- [9] Rösch, T. F., et al. (2017). Laser-driven ION (LION) acceleration at the Centre for

-
- Advanced Laser Applications (CALA). In CLEO/Europe-EQEC, Munich, Germany, pp. 1–1.
<https://doi.org/10.1109/CLEOE-EQEC.2017.8087795>
- [10] Python Software Foundation (2019). Welcome to Python.org. [online] Python.org. Available at: <https://www.python.org> [Accessed 18 Apr. 2022].
- [11] L.J. Nevay, et al. (2020), BDSIM: An accelerator tracking code with particle–matter interactions, Computer Physics Communications, Volume 252, 2020, 107200,
<https://doi.org/10.1016/j.cpc.2020.107200>.
- [12] CERN. (2020). User Documentation. [online] Available at:
<https://geant4.web.cern.ch/support/user>. [Accessed 18 Apr. 2022].
- [13] www.k-wave.org. (n.d.). k-Wave: A MATLAB toolbox for the time domain simulation of acoustic wave fields. [online] Available at: <http://www.k-wave.org> [Accessed 19 Mar. 2022].
- [14] nl.mathworks.com. (n.d.). MATLAB - MathWorks. [online] Available at:
<https://nl.mathworks.com/products/matlab.html> [Accessed 18 Apr. 2022].
- [15] University of Birmingham. (n.d.). MC40 Cyclotron Facility - The Birmingham Centre for Nuclear Education and Research. [online] Available at: <https://www.birmingham.ac.uk/research/activity/nuclear/about-us/facilities/mc40-cyclotron-facility> [Accessed 30 Jul. 2024].
- [16] Maani, E.V. and Maani, C.V. (2022). Radiation Therapy. [online] PubMed. Available at:
<https://www.ncbi.nlm.nih.gov/books/NBK537036/> [Accessed 30 Jul. 2024]
- [17] Lehrer EJ, Prabhu AV, Sindhu KK, Lazarev S, Ruiz-Garcia H, Peterson JL, Beltran C, Furutani K, Schlesinger D, Sheehan JP, et al. Proton and Heavy Particle Intracranial Radiosurgery. Biomedicines. 2021; 9(1):31.
<https://doi.org/10.3390/biomedicines9010031>.
- [18] Hamad, Morad. (2021). Bragg-Curve Simulation of Carbon-Ion Beams for Particle-therapy Applications: a study with the GEANT4 toolkit. Nuclear Engineering and Technology.

-
- <https://doi.org/10.1016/j.net.2021.02.011>.
- [19] Lourenço, A., Subiel, A., Lee, N. et al. Absolute dosimetry for FLASH proton pencil beam scanning radiotherapy. *Sci Rep* 13, 2054 (2023).
<https://doi.org/10.1038/s41598-023-28192-0>.
- [20] Jan J. Wilkens, Uwe Oelfke, Direct Comparison of Biologically Optimized Spread-out Bragg Peaks for Protons and Carbon Ions, *International Journal of Radiation Oncology*Biography*Physics*, Volume 70, Issue 1, 2008, Pages 262-266,
<https://doi.org/10.1016/j.ijrobp.2007.08.029>.
- [21] Grimes, D.R., Warren, D.R. & Partridge, M. (2017) An approximate analytical solution of the Bethe equation for charged particles in the radiotherapeutic energy range. *Sci Rep* 7, 9781, <https://doi.org/10.1038/s41598-017-10554-0>.
- [22] protherapy.ru. (n.d.). Proton Centers Around the World. [online] Available at:
<https://protherapy.ru/page/view?id=4> [Accessed 30 Jul. 2024].
- [23] Particle Therapy Co-Operative Group. (2025). Facilities in operation (public). [online] Available at: <https://ptcog.site/index.php/facilities-in-operation-public> [Accessed 30 Jul. 2024].
- [24] B. B. Rossi, High-energy particles. Prentice-Hall physics series, New York, NY: Prentice-Hall, 1952.
- [25] W. R. Leo. Techniques for Nuclear and Particle Physics Experiments. Springer-Verlag Berlin Heidelberg, 1987.
- [26] Ziegler, J. F., Ziegler, M. D., & Biersack, J. P. (2010). SRIM – The stopping and range of ions in matter. *Nuclear Instruments and Methods in Physics Research Section B: Beam Interactions with Materials and Atoms*, 268(11–12), 1818–1823.
<https://doi.org/10.1016/j.nimb.2010.02.091>
- [27] Raza Qasim, M.H., & Baeg, S. (2020). Energy straggling and an experimental investigation

- of Bragg's rule for ^{241}Am alpha particles in air and its constituents. *Radiation Physics and Chemistry*, 176, 108987.
- [28] Mayles, P., Nahum, A., & Rosenwald, J.C. (Eds.). (2007). *Handbook of Radiotherapy Physics: Theory and Practice* (1st ed.). CRC Press.
<https://doi.org/10.1201/9781420012026>.
- [29] Ulmer, W., & Matsinos, E. (2010). Theoretical methods for the calculation of Bragg curves and 3D distributions of proton beams. *European Physical Journal–Special Topics*, 190(1), 1–81. <https://doi.org/10.1140/epjst/e2010-01335-7>.
- [30] Bortfeld T. An analytical approximation of the Bragg curve for therapeutic proton beams. *Med Phys*. 1997 Dec;24(12):2024-33. <https://doi.org/10.1118/1.598116>.
- [31] McGarrigle JM, Long KR, Prezado Y. The FLASH effect-an evaluation of preclinical studies of ultra-high dose rate radiotherapy. *Front Oncol*. 2024 Apr 22;14:1340190.
<https://doi.org/10.3389/fonc.2024.1340190>.
- [32] Wilson, P., Jones, B., Yokoi, T., Hill, M., & Vojnovic, B. (2012). Revisiting the ultra-high dose rate effect: implications for charged particle radiotherapy using protons and light ions. *The British Journal of Radiology*, 85(1018), e933–e939
<https://doi.org/10.1259/bjr/17827549>.
- [33] Nrc.gov. (2019). NRC: Glossary – Gray (Gy). [online] Available at:
<https://www.nrc.gov/reading-rm/basic-ref/glossary/gray-gy.html> [Accessed 15 Sep. 2022].
- [34] Schneider, T. (2022). Technical aspects of proton minibeam radiation therapy: Minibeam generation and delivery. *Physica Medica*, 100, 64–71.
<https://doi.org/10.1016/j.ejmp.2022.06.010>
- [35] CRR. (2018). Microbeam. [online] Available at:
<https://www.crr.columbia.edu/raraf/our-research/microbeam> [Accessed 15 Sep. 2022].

-
- [36] Prezado, Y., et al. (2017). Proton minibeam radiation therapy spares normal rat brain: Long-term clinical, radiological and histopathological analysis. *Scientific Reports*, 7, 14403. <https://doi.org/10.1038/s41598-017-14786-y>
- [37] H. Paganetti, Proton Therapy Physics. CRC Press, November 2018.
- [38] Casolaro, P., Campajola, L., Breglio, G. et al. Real-time dosimetry with radiochromic films. *Sci Rep* 9, 5307 (2019). <https://doi.org/10.1038/s41598-019-41705-0>.
- [39] Boag JW, Epp E, Fielden EM, Parker RP. 4. Calorimetric Dosimetry of Pulsed Radiation. Reports of the International Commission on Radiation Units and Measurements. 1982;os-18(1):22-30. https://doi.org/10.1093/jicru_os18.1.22.
- [40] Gray, L. H. (1936). An ionization method for the absolute measurement of gamma-ray energy. *Proceedings of the Royal Society of London. Series A, Mathematical and Physical Sciences, vol. 156, no. 889, pp. 578–596. <https://doi.org/10.1098/rspa.1936.0169>
- [41] Grusell E, Isacson U, Montelius A, Medin J. Faraday cup dosimetry in a proton therapy beam without collimation. *Phys Med Biol*. 1995 Nov;40(11):1831-40. <https://doi.org/10.1088/0031-9155/40/11/005..>
- [42] Parodi, Katia et al. PET/CT imaging for treatment verification after proton therapy: a study with plastic phantoms and metallic implants. *Medical physics* vol. 34,2 (2007): 419-35. <https://doi.org/10.1118/1.2401042>
- [43] Testa, Etienne Bajard, M. Chevallier, M. Dauvergne, Denis Foulher, Fabrice Freud, Nicolas Létang, Jm Poizat, J.C. Ray, Cédric Testa, Mauro. (2009). Dose profile monitoring with carbon ions by means of prompt-gamma measurements. *Nuclear Instruments and Methods in Physics Research Section B: Beam Interactions with Materials and Atoms*. 267. 993-996. <https://doi.org/10.1016/j.nimb.2009.02.031>.
- [44] Faraggi, Eshel & Wang, Shijun & Gerstman, Bernard. (2005). Stress confinement, shock wave formation, and laser-induced damage. *Proceedings of SPIE - The International Society*

-
- for Optical Engineering. 5695. <https://doi.org/10.1117/12.589469>.
- [45] Jones KC, Nie W, Chu JCH, et al. (2018) Acoustic-based proton range verification in heterogeneous tissue: simulation studies. *Phys Med Biol*.
<https://doi.org/10.1088/1361-6560/aa9d16>.
- [46] Lascaud J, Dash P, Wieser HP, Kalunga R, Würfl M, Assmann W, Parodi K. Investigating the accuracy of co-registered ionoacoustic and ultrasound images in pulsed proton beams. *Phys Med Biol*. 2021 Sep 9;66(18). <https://doi.org/10.1088/1361-6560/ac215e>.
- [47] WFSA Resource Library. (n.d.). The Physics Of Ultrasound – Part 1. [online] Available at: <https://resources.wfsahq.org/atotw/the-physics-of-ultrasound-part-1/#:~:text=PD%20%3D%20N%20> [Accessed 19 May 2024].
- [48] Robertson D, Hui C, Archambault L, Mohan R, Beddar S. Optical artefact characterization and correction in volumetric scintillation dosimetry. *Phys Med Biol*. 2014 Jan 6;59(1):23-42.
<https://doi.org/10.1088/0031-9155/59/1/23>.
- [49] G. F. Knoll, Radiation detection and measurement, 4th ed. Hoboken, N.J: John Wiley, 2010.
- [50] Chu, X., Wang, J., Wen, W. and Zhang, B. (2020). Development of novel water equivalent liquid scintillator. *Radiation Measurements*, 136, p.106391.
<https://doi.org/10.1016/j.radmeas.2020.106391>.
- [51] Knoll, G. F. (2010). Radiation detection and measurement. John Wiley & Sons.
- [52] www.ukri.org. (n.d.). Researching a new generation of technology to treat cancer. [online] Available at: <https://www.ukri.org/news/researching-a-new-generation-of-technology-to-treat-cancer/> [Accessed 19 May 2024].
- [53] Nonnenmacher, T., Dascalu, T. S., Bingham, R., Cheung, C. L., Lau, H. T., Long, K. R., Pozimski, J., & Whyte, C. (2021). Anomalous beam transport through Gabor (plasma) lens prototype. *Applied Sciences*, 11(10), 4357. <https://doi.org/10.3390/app11104357>

-
- [54] Hughes, J.R., & Parsons, J.L. (2020). FLASH Radiotherapy: Current Knowledge and Future Insights Using Proton-Beam Therapy. *International Journal of Molecular Sciences**, 21(18), 6492. <https://doi.org/10.3390/ijms21186492>
- [55] S. C. Wilks, A. B. Langdon, T. E. Cowan, M. Roth, M. Singh, S. Hatchett, M. H. Key, D. Pennington, A. MacKinnon, and R. A. Snavely, Energetic proton generation in ultra-intense laser–solid interactions *Physics of Plasmas*, vol. 8, no. 2, pp. 542–549, 2001, <https://doi.org/10.1063/1.1333697>.
- [56] Ferrario, M., Migliorati, M. and Palumbo, L. (n.d.). Space Charge Effects. [online] Available at: https://indico.cern.ch/event/361988/contributions/1775745/attachments/1157672/1678600/Space_Charge_Final.pdf [Accessed 10 Jun. 2022].
- [57] Fuchs, J., Antici, P., d’Humières, E. et al. Laser-driven proton scaling laws and new paths towards energy increase. *Nature Phys* 2, 48–54 (2006). <https://doi.org/10.1038/nphys199>.
- [58] Dover NP, Nishiuchi M, Sakaki H, Kondo K, Lowe HF, Alkhimova MA, et al. Demonstration of repetitive energetic proton generation by ultra-intense laser interaction with a tape target. *High Energy Density Phys.* (2020) 37:100847. <https://doi.org/10.1016/j.hedp.2020.100847>
- [59] Nürnberg F, Schollmeier M, Brambrink E, Blazević A, Carroll DC, Flippo K, Gautier DC, Geissel M, Harres K, Hegelich BM, Lundh O, Markey K, McKenna P, Neely D, Schreiber J, Roth M. Radiochromic film imaging spectroscopy of laser-accelerated proton beams. *Rev Sci Instrum.* 2009 Mar;80(3):033301. <https://doi.org/10.1063/1.3086424>.
- [60] H.T. Lau (2022). *Medical Applications for Particle Physics*, p.138.
- [61] Machida, S. (n.d.). Fixed field alternating gradient. [online] Available at: <https://arxiv.org/pdf/1302.2026.pdf> [Accessed 17 Sep. 2022].
- [62] Vallicelli, E.A., Tambaro, M., Cosmi, M.O. et al. 50-Channel Ionoacoustic Sensor for 60 MeV

-
- Proton Beam Characterization in Hadron Therapy Applications. SN COMPUT. SCI. 5, 224 (2024). <https://doi.org/10.1007/s42979-023-02502-9>
- [63] Thorlabs.com. (2024). N-BK7 High Precision Windows. [online] Available at: https://www.thorlabs.com/newgrouppage9.cfm?objectgroup_id=1117&gad_source=1&gclid=EAIaIQobChMI_rCYtNK9iwMVEGVBAh2mqSAyEAAAYASAAEgIRKfD_BwE [Accessed 12 Feb. 2025].
- [64] www.pulse.physik.uni-muenchen.de. (n.d.). ATLAS - Pulse. Petawatt Users, Lasers, Sources and Experiments - LMU Munich. [online] Available at: <https://www.pulse.physik.uni-muenchen.de/research/high-power/atlas/index.html> [Accessed 13 Mar. 2023].
- [65] Schreiber J, Bell F, Grüner F, Schramm U, Geissler M, Schnürer M, Ter-Avetisyan S, Hegelich BM, Cobble J, Brambrink E, Fuchs J, Audebert P, Habs D. Analytical model for ion acceleration by high-intensity laser pulses. Phys Rev Lett. 2006 Jul 28;97(4):045005. <http://doi.org/10.1103/PhysRevLett.97.045005>.
- [66] Cowan, G., 2019. Monte Carlo Techniques. [online] Pdg.lbl.gov. Available at: <https://pdg.lbl.gov/2020/reviews/rpp2020-rev-monte-carlo-techniques.pdf>.
- [67] Holzer, B. J. (2014). Introduction to Transverse Beam Dynamics. [online] CERN Accelerator School. CERN-2014-005. Available at: <https://cds.cern.ch/record/1693320/files/CERN-2014-005-p21.pdf> [Accessed 4 October 2020].
- [68] Sannibale, F. (2023). Lecture 6: Magnets. USPAS Winter 2023 – Fundamentals of Accelerator Physics & Technology with Simulations and Measurements Lab. Lawrence Berkeley National Laboratory. [online] Available at: https://www2.als.lbl.gov/als_physics/Fernando/USPASJan2023/Lectures/Fernando/USPAS_Winter2023_6_Magnets.pdf [Accessed 4 October 2020].

-
- [69] Holzer Cern, B., Geneva and Switzerland (2013). Lattice Design in High-Energy Particle Accelerators. [online] <https://doi.org/10.5170/CERN-2014-009.61>.
- [70] Rösch, T.F., Afshari, M., Balling, F., Doyle, L., Gerlach, S., Hartmann, J., Prasselsperger, A., Morris, S. and Schreiber, J. (2024). Transverse emittance growth of proton sources from laser-irradiated sub- μ m-thin planar targets. *Physical Review*, 109(2).
<https://doi.org/10.1103/physreve.109.025201>.
- [71] www.sciencedirect.com. (n.d.). Bremsstrahlung - an overview | ScienceDirect Topics. [online] Available at:
<https://www.sciencedirect.com/topics/physics-and-astronomy/bremsstrahlung>
[Accessed 17 Dec. 2024].
- [72] Liang TT, Bauer JM, Liu JC, Rokni SH. Radiation Protection Around High-intensity Laser Interactions with Solid Targets. *Health Phys.* 2018 Dec;115(6):687-697.
<https://doi.org/10.1097/HP.0000000000000927>.
- [73] Wright, G. (2022). What Is Nyquist Theorem? - Definition from WhatIs.com. [online] WhatIs.com. Available at:
<https://www.techtarget.com/whatis/definition/Nyquist-Theorem> [Accessed 17 Dec. 2024].
- [74] Insights provided by Prof. Peter Hobson and Prof. Jeff Bamber (personal communication, July 31, 2024)
- [75] Pollock, D.D. (1993). *Physical Properties of Materials for Engineers* (2nd ed.). CRC Press.
<https://doi.org/10.1201/9781003068082>
- [76] pmgroup (2015). Vantage Systems. [online] Verasonics. Available at:
<https://verasonics.com/vantage-systems/> [Accessed 17 Dec. 2024].
- [77] services.gehealthcare.com. (n.d.). 9L-D, Ultrasound | GE HealthCare Service Shop USA. [online] Available at: <https://services.gehealthcare.com/gehcstorefront/p/5499510>

- [Accessed 22 Jul. 2024].
- [78] www.olympus-ims.com. (n.d.). Immersion Transducers. [online] Available at: <https://www.olympus-ims.com/en/ultrasonic-transducers/immersion/> [Accessed 17 Dec. 2024].
- [79] Vallicelli, E., Cosmi, M., Baschiroto, A., & De Matteis, M. (2021). Front-end design optimization for ionoacoustic 200 MeV protons beam monitoring with sub-millimeter precision for hadron therapy applications. In Proceedings of the 14th International Joint Conference on Biomedical Engineering Systems and Technologies (BIODEVICES 2021) (pp. 77–87). <https://doi.org/10.5220/0010346600002865>
- [80] Precision Acoustics Ltd. (n.d.). ML4X50 Piston Hydrophone. [online] Available at: <https://www.acoustics.co.uk/product/piston-hydrophone/> [Accessed 2 Jun. 2025].
- [81] www.mathworks.com. (n.d.). Fast Fourier Transform (FFT). [online] Available at: <https://www.mathworks.com/discovery/fft.html> [Accessed 2 Jun. 2025].
- [82] www.fluke.com. (n.d.). Electrical Noise and Transients. [online] Available at: <https://www.fluke.com/en-us/learn/blog/power-quality/electrical-noise-and-transients> [Accessed 2 Jun. 2025].
- [83] Huang, C., Wang, K., Nie, L., Wang, L. V., & Anastasio, M. A. (2013). Full-wave iterative image reconstruction in photoacoustic tomography with acoustically inhomogeneous media. IEEE Transactions on Medical Imaging, 32(6), 1097–1100. <https://doi.org/10.1109/TMI.2013.2254496>
- [84] K-wave.org. (2022). model-based image reconstruction «k-Wave User Forum. [online] Available at: <http://www.k-wave.org/forum/topic/model-based-image-reconstruction> [Accessed 17 Dec. 2024].
- [85] www.sciencedirect.com. (n.d.). Backprojection - an overview | ScienceDirect Topics. [online] Available at: <https://www.sciencedirect.com/topics/engineering/backprojection>

-
- [Accessed 17 Dec. 2024].
- [86] www.icr.ac.uk. (n.d.). Help us to transform the future for people with hard-to-treat cancers - The Institute of Cancer Research, London. [online] Available at: <https://www.icr.ac.uk/support-us> [Accessed 23 Jun. 2024].
- [87] pmgroup (2015). Vantage Systems. [online] Verasonics. Available at: <https://verasonics.com/vantage-systems/> [Accessed 17 Dec. 2024].
- [88] www.sciencedirect.com. (n.d.). Hamming Window - an overview | ScienceDirect Topics. [online] Available at: <https://www.sciencedirect.com/topics/engineering/hamming-window> [Accessed 17 Dec. 2024].
- [89] 2.161 Signal Processing: Continuous and Discrete. (2008). Available at: https://ocw.mit.edu/courses/2-161-signal-processing-continuous-and-discrete-fall-2008/5af5cf66ca3148b1ef0c6d94284a3382_lecture_22.pdf [Accessed 22 Jun. 2024].
- [90] Nishizaki, L. (2019). Cross-correlation of 2 matrices. [online] Observable. Available at: <https://observablehq.com/@lemonnish/cross-correlation-of-2-matrices> [Accessed 23 Jun. 2024].
- [91] Messer, P. (2015). Calculating Signal Loss - CompTIA A+ 220-901 - 2.2. [online] Professor Messer IT Certification Training Courses. Available at: <https://www.professormesser.com/free-a-plus-training/220-901/calculating-signal-loss/> [Accessed 23 Jun. 2024].
- [92] PerkinElmer, Inc. (2020). Safety data sheet: Ultima Gold XR (Catalog No. 6013119) [PDF]. Revvity. <https://www.revvity.com/product/ultima-gold-xr-2x5-1-6013119>
- [93] Dianu, Magdalena & Podina, Corneliu. (2007). The safety of environment in final disposal of Ultima Gold scintillation liquid cocktail used for determination of radioactive content in various samples at Cernavoda Nuclear Power Plant. *Revue Roumaine de Chimie*. 52. 509-519.

-
- [94] Williams, K.J., Campbell, T.O., & Upton, R.J. (2013). Measurement of wavelength-dependent refractive indices of liquid media independent of opacity, viscosity and colour. *Applied Radiation and Isotopes*, 82, 382–388.
- [95] Hoertz, P.G., Mills, K., Davis, L., Baldasaro, N., Gupta, V. (2013). Response of organic liquid scintillators to fast neutrons and gamma radiation.**Radiation Physics and Chemistry*, 84, 59–65. <https://doi.org/10.1016/j.radphyschem.2012.06.044>
- [96] Robertson, D., Hui, C., Archambault, L., Mohan, R., & Beddar, S. (2014). Optical artefact characterization and correction in volumetric scintillation dosimetry. *Physics in Medicine and Biology*, 59(1), 23–42. <https://doi.org/10.1088/0031-9155/59/1/23>.
- [97] Liu, Y., Andrés Hernández, M. D., George, M., & Burrows, J. P. (2023). Experimental determination of Rayleigh scattering cross-sections at 408 nm. *Applied Physics B*, 129(82). <https://doi.org/10.1007/s00340-023-08025-8>.
- [98] Can Wang et al 2021 *Laser Phys.* 31 025801 <https://doi.org/10.1088/1555-6611/abd565>.
- [99] uk.rs-online.com. (n.d.). EOLD-365-525 OSA Opto, UV LED | RS. [online] Available at: <https://uk.rs-online.com/web/p/uv-leds/1736313> [Accessed 26 Sep. 2023].
- [100] www.edmundoptics.co.uk. (n.d.). CM3-U3-31S4M-CS 1/1.8" Chameleon®3 Monochrome Camera. [online] Available at: <https://www.edmundoptics.co.uk/p/cm3-u3-31s4m-cs-1-18inch-chameleon3-monochrome-camera/37029/> [Accessed 15 Sep. 2023].
- [101] Test Equipment Solutions Datasheet. (n.d.). [online] Available at: <https://www.testequipmenthq.com/datasheets/KEITHLEY-2010-Datasheet.pdf> [Accessed 28 Sep. 2023].
- [102] www.hellenicaworld.com. (n.d.). Attenuation length. [online] Available at: <https://www.hellenicaworld.com/Science/Physics/en/Attenuationlength.html> [Accessed 28 Sep. 2023].

-
- [103] Vo, K. (2022). Spectrophotometry. [online] Chemistry LibreTexts. Available at:
https://www.avantes.com/support/theoretical-background/introduction-to-spectrometers/?gad_source=1&gbraid=0AAAAAD-Bb4L_L9nIs3dC_9IXgbqFxp3X&gclid=CjwKCAiAjp-7BhBZEiwAmh9rBZC5zY8C1Kf02JeRBt_TzsQ2ZG_rpIg-9Gqqq8AAIy8ANSOmJAHz-BoCDPwQAvD_BwE [Accessed 28 Sep. 2023].
- [104] Edinburgh Instruments (2023). Beer Lambert Law | Transmittance & Absorbance. [online] Edinburgh Instruments. Available at:
<https://www.edinst.com/blog/the-beer-lambert-law/#:~:text=The%20Beer%2DLambert%20law%20state> [Accessed 28 Sep. 2023].
- [105] www.shimadzu.co.uk. (n.d.). UV-Vis-NIR Spectroscopy | SHIMADZU EUROPA. [online] Available at: https://www.shimadzu.co.uk/uv-vis-nir-spectroscopy?ppc_keyword=shimadzu%20uv&gclid=EAIaIQobChMI46XEvaH2gwMVE49QBh1k2QHDEAAYASAAEgKdZ_D_BwE [Accessed 24 Jan. 2024].
- [106] www.meetoptics.com. (n.d.). MEETOPTICS | Search & Compare Quality Optics. [online] Available at: <https://www.meetoptics.com/lenses/spherical/bi-convex-lens/s/thorlabs/p/LB1596-A> [Accessed 15 Sep. 2023].
- [107] www.thorlabs.com. (n.d.). Thorlabs, Inc. - Your Source for Fiber Optics, Laser Diodes, Optical Instrumentation and Polarization Measurement & Control. [online] Available at: <https://www.thorlabs.com> [Accessed 15 Sep. 2023].
- [108] Nettleton, D. (2014). Pearson Correlation - an overview. [online] www.sciencedirect.com. Available at:
<https://www.sciencedirect.com/topics/computer-science/pearson-correlation> [Accessed 15 Sep. 2023].
- [109] Chichester, D., Watson, S. and Johnson, J. (2012). Comparison of BCF-10, BCF-12, and

-
- BCF-20 Scintillating Fibers for Use in a 1-Dimensional Linear Sensor IEEE 2012 Nuclear Science Symposium Comparison of BCF-10, BCF-12, and BCF-20 Scintillating Fibers for Use in a 1-Dimensional Linear Sensor. [online] Available at:
<https://inldigitallibrary.inl.gov/sites/sti/sti/5532301.pdf> [Accessed 6 Oct. 2023].
- [110] MacIntosh-LaRocque, Anthea. Novel scintillating fibre detector developed for clinical proton beams. Master's thesis, Imperial College London, 2023, p. 37.
- [111] www.easycomposites.co.uk. (n.d.). IN2 Epoxy Infusion Resin - Easy Composites. [online] Available at: <https://www.easycomposites.co.uk/in2-epoxy-infusion-resin> [Accessed 6 Oct. 2023].
- [112] Lecture 9: Reflection, Transmission and Impedance 1 Boundary conditions at a junction. (n.d.). [online] Available at:
<https://scholar.harvard.edu/files/schwartz/files/lecture9-impedance.pdf>.
- [113] www.easycomposites.co.uk. (n.d.). AT30 Epoxy Hardener - Easy Composites. [online] Available at:
<https://www.easycomposites.co.uk/at30-epoxy-resin-hardener-fast-or-slow> [Accessed 6 Oct. 2023].
- [114] docs.opencv.org. (n.d.). OpenCV: Hough Circle Transform. [online] Available at:
https://docs.opencv.org/4.x/da/d53/tutorial_py_houghcircles.html [Accessed 6 Oct. 2023].
- [115] Tequipment.net. (2025). Available at:
<https://www.tequipment.net/Pico/6404D/PC-Based-Oscilloscopes/> [Accessed 16 Feb. 2025].
- [116] Indico. (2025). LPA Special Workshop on Intelligent Systems. [online] Available at:
<https://indico.physik.uni-muenchen.de/event/484/contributions/1959/> [Accessed

- 16 Feb. 2025].
- [117] Casolaro, P., Campajola, L., Breglio, G. et al. Real-time dosimetry with radiochromic films. *Sci Rep* 9, 5307 (2019). <https://doi.org/10.1038/s41598-019-41705-0>.
- [118] www.gafchromic.com. (n.d.). Gafchromic EBT Films - GAFchromicTM. [online] Available at: <http://www.gafchromic.com/gafchromic-film/radiotherapy-films/EBT/index.asp> [Accessed 16 Feb. 2025].
- [119] Epson.co.uk. (2025). Expression 11000XL Pro. [online] Available at: https://www.epson.co.uk/en_GB/products/scanners/document-scanner/expression-11000xl-pro/p/12308?srsId=AfmB0orE8mKIo--V20A31a4VIWaaG3sdqM936Vu3gT6aW6fZT4dfzvTq [Accessed 19 Feb. 2025].
- [120] Walcher, D.J. (2021). Absolute Calibration of Radiochromic Films. Bachelor's thesis. Ludwig Maximilians Universität, Faculty of Physics, Munich.
- [121] [lmu-klinikum.de](https://www.lmu-klinikum.de). (2023). LMU Klinikum. [online] Available at: <https://www.lmu-klinikum.de/> [Accessed 20 Feb. 2025].
- [122] Dover, N. (2024) Analysis of LMU stacks, Update 12/11/2024.
- [123] www.srim.org. (n.d.). James Ziegler - SRIM & TRIM. [online] Available at: <http://www.srim.org/>.
- [124] Gerlach, Sonja (2023): Ionoacoustics for three-dimensional particle bunch monitoring. Dissertation, LMU München: Faculty of Physics
- [125] www.ansys.com. (n.d.). Ansys Zemax OpticStudio | Optical Design and Analysis Software. [online] Available at: <https://www.ansys.com/products/optics/ansys-zemax-opticstudio> [Accessed 16 Feb. 2025].
- [126] PDG (n.d.). Passage of Particles Through Matter. [online] Available at:

<https://pdg.lbl.gov/2019/reviews/rpp2018-rev-passage-particles-matter.pdf>

[Accessed 11 Apr. 2022].

- [127] González, Á. (2010). Measurement of areas on a sphere using Fibonacci and latitude–longitude lattices. *Mathematical Geosciences*, 42(1), 49–64.

<https://doi.org/10.1007/s11004-009-9257-x>

- [128] www.topasmc.org. (n.d.). TOPAS Tool for Particle Simulation. [online] Available at:

<https://www.topasmc.org/> [Accessed 16 Feb. 2025].